Dissertation zur Erlangung des Doktorgrades

der Fakultät für Chemie und Pharmazie

der Ludwig-Maximilians-Universität München

Synthesis and characterization of novel electroactive metal-organic frameworks, especially based on the MOF-74 topology

Patricia Irene Scheurle

aus

Bonn, Deutschland

2021

Synthesis and characterization of novel electroactive metal-organic frameworks, especially based on the MOF-74 topology

Patricia Irene Scheurle

2021

Erklärung

Diese Dissertation wurde im Sinne von §7 der Promotionsordnung vom 28. November 2011 von Herrn Prof. Dr. Thomas Bein betreut.

Eidesstattliche Versicherung

Diese Dissertation wurde eigenständig und ohne unerlaubte Hilfsmittel erarbeitet.

München, den 20.12.2021

_____

(Patricia Scheurle)

Dissertation eingereicht am:	15.11.2021
1. Gutachter:	Prof. Dr. Thomas Bein
2. Gutachter:	Prof. Dr. Achim Hartschuh
Mündliche Prüfung am	14.12.2021

Acknowledgements

After finishing this thesis I want to say thank you to a couple of people, who have helped me with the completion of the dissertation.

My first big thank you goes to my PhD advisor Prof. Thomas Bein, for the opportunity to work on such an interesting research field in his group. Thank you for the freedom you gave me during the work on my different projects. But also for your scientific advice in the (sub)group meetings, the proof-reading of my publications and of this thesis. Furthermore, I am thankful for the opportunity to go to many national and international conferences, which I really enjoyed, as well as for the financial support.

Secondly, a special thanks goes to Prof. Achim Hartschuh for taking over the second evaluation of my thesis and for the many successful cooperations.

In this context I also want to thank the rest of my examination board: Prof. Stefan Wuttke, Prof. Karaghiosoff, Prof. Müller-Caspary and Prof. Klapötke.

A big thank you goes to Dr. Dana Medina. Thank you for our collaborations, your advice and for countless discussions and meetings during my time in the group. As well for the corrections of my publications and for always having an open ear.

Next, I want to thank all my collaboration partners. Alexander Biewald, thank you for your measurements and proof-readings, as well as for the nice coffee breaks. Dr. Andre Mähringer for the team work in the lab and on our MOF projects. Dr. Andreas Jakowetz, thank you for your help on the PL measurements during my first project. My cooperation partners at the University in Oldenburg for good collaboration, Dr. Pouya Hosseini, Lena Harms and Prof. Gunther Wittstock. Thank you to the whole MOF / COF subgroup and all the helpful discussions. Thank you to Sebastian Häringer for the ALD ZnO substrates.

In our department, we are pleased to have the opportunity to get our materials analyzed by SEM and TEM. Therefore, thank you Dr. Steffen Schmidt and Dr. Markus Döblinger for SEM and TEM measurements.

Thank you, Tina Reuther, for sorption measurements and your general work in our group, which made our work in the lab easier. Also thanks to Corinna Heidt for caring about all the paper work. Thank you for my interns Robert Calaminus, Kieran Rorie, Sebastian Ambach and Huiqi Li.

A big thank you to Vera Hiendl for the great cover picture.

I also want to thank the whole AK Bein for the great atmosphere, good collaborations and also for great (barbecue)partys (before Corona). I really enjoyed the time, the lunches at the Biomensa and the activities in the group. Thank you to my first office members Dr. Enrico Greul, Dr. Julian Rotter, Lisa Wehl, Jonathan Kampmann and Derya Bessinger and to my current ones Marina Schönherr, Shizhe Wang and Max Sirtl. Especially to Ed, for coming with me to the new office. I had a lot of fun in our office with searching memes or just talking. Thanks to the South Tyrol crew, Ed, Andi, Laura and Laura, for the great trips.

A special thanks to Laura Frey, not only for our good collaboration on the Marta MOF, but also for your general help, the fun we had on conferences and our friendship inside and outside of the university. Thank you Bettina for our hallway meetings and lunch breaks, as well as for your friendship, since almost the beginning of our studies.

Thank you to Sonja and Giulia for our long-lasting friendship and last but not least, I want to thank my family for their never ending support and love.

Abstract

Metal-organic frameworks (MOFs) are crystalline and porous materials, which are formed through the connection of organic ligands with inorganic nodes. Due to their high surface area, common applications are gas storage, gas separation and drug delivery. However, MOFs feature a great structural flexibility, which allows for an individual design regarding ligands, metal ions, topologies and functional groups. As a consequence, a MOF can be built according to a modular principle for desired features, like pore size or specific functionalities.

The increasing (but still small) number of MOFs including the desired functionality of electrical conductivity has enabled new applications in the field of fuel cells, supercapacitors and sensing. To achieve significant electrical conductivity, it is necessary to combine the high surface areas of MOFs with good charge transport properties, high charge carrier densities and high mobilities. The free charge carriers can either come from the metal or the ligand. There are two ways to achieve a low energy pathway for charge transport. For the "through-space" approach, ligands with an extended π-system are needed. In the "through-bond" approach, an orbital overlap of the ligand and the metal is required. MOF-74 is a well-known MOF structure and has attracted much interest in recent years, due to its robust architecture, permanent porosity and high thermal stability. Moreover, MOF-74(Fe) already showed semiconducting behaviour and the hexagonal wall structure defining open channels can serve as path for charge carrier transport. In addition, MOF-74 can be expanded isoreticularly by the elongation of the ligands with phenyl (or other) groups, reaching pore apertures of up to 98 Å without pore collapse. All in all, it is an attractive MOF topology and a suitable platform for the implementation of functional, sterically more demanding ligands, to obtain MOF-74 analogs with attractive electroactive or photophysical properties.

Following this conceptual line of thought, the first research part of this thesis (Chapter 3) is based on the expansion of the MOF-74 topology by the incorporation of an electron donating organic building block, based on an anthracene core, into the backbone of the framework. Anthracene is an electron-rich molecule exhibiting interesting optical properties. Therefore, it is an optimal candidate for the implementation as organic ligand for the synthesis of an electroactive MOF structure. We synthesized five isostructural, highly crystalline and porous anthracene MOF-74 analogs exhibiting enlarged pore sizes. The electrical conductivity could be enhanced by up to six orders of magnitude, compared to the original MOF-74 with 2,5-dihydroxytherephtalic acid ligands. In addition, the MOFs show interesting photophysical properties, which were analyzed by means of UV-Vis spectroscopy, photoluminescence (PL) and time-correlated single-photon counting (TCSPC). In addition, the growth of the zinc MOF as thin film was studied.

To further enlarge the pore size of the MOF, we expanded the anthracene ligand with electron-rich ethyne groups (described in Chapter 4), which also positively affected the optical properties of the MOF. The band gap could be reduced, and the PL was redshifted. Surprisingly, the integration of the ethyne groups also influenced the crystal morphology. Helical rod-shaped crystallites in the µm range were formed, with the same amount of left- and right rotations.

In another approach, we used a derivative of the organic dye molecule perylene diimide (PDI) as ligand for the formation of a MOF-74 analog, which is discussed in Chapter 5. PDI and its derivatives feature remarkable optical properties, in combination with high electron mobilities and reversible redox-chemical behavior. Therefore, it is used in many areas ranging from organic photovoltaics to photoconduction. However, the synthesis of a PDI-based 3D MOF has been rarely reported. Here, we synthesized three isostructural MOF-74 analogs with the metal ions Zn^{2+}, Mg^{2+} and Ni^{2+}, comprising high crystallinity and porosity, by using a functionalized PDI building block. In the crystal structure, the PDI cores stack along the *c*-axis, enabling π-π-stacking between the ligands. This in principle could allow for a "through-space" charge transport along the PDI stacks, besides the "through-bond" transport. The PDI-MOF-74 series exhibits reasonable electrical conductivity, as well as photoluminescence in the orange and red spectral region. Moreover, the reduction potentials and the HOMO/ LUMO levels were analyzed by means of cyclic voltammetry (CV) measurements and UV-Vis spectroscopy.

The fourth research part of the thesis (Chapter 6) focuses on the thin film synthesis of MOF-74(Zn, Mg, Ni, Co) on different substrates *via* vapor-assisted conversion. The synthesis of crystalline and homogeneous thin films of MOFs is crucial for their implementation into device-type technologies for applications like chemical sensing, optoelectronics and gas storage/ separation. Therefore, a controlled MOF film growth is necessary, including tunable morphology and film thickness, as well as crystallite orientation. Vapor-assisted conversion (VAC) is a highly flexible direct on-surface growth method. The variation of many synthesis parameters enables the fabrication of defined architectures for the desired functionality. To date there are only few reports regarding MOF-74 film synthesis. In this chapter we address the remaining challenges and describe synthesis approaches for MOF-74 thin films with different metal ions on various substrates. In addition, we control the film thickness and obtain different crystallite orientations, depending on the metal ion.

The last research part of the thesis (Chapter 7) describes the synthesis and characterization of a novel cubic mesoporous Fe-Coronene MOF, which is built from hexahydroxy-cata-hexabenzocoronene and Fe^{III} ions. As indicated by its black color, it shows a broad absorption over the whole

visible and near infrared spectrum. In addition, this MOF features an electrical conductivity of 10^{-6} S/cm. The iron valency was studied by means of X-ray photoelectron spectroscopy (XPS).

In conclusion, this thesis has been focused on the development of novel electrically conductive porous metal-organic frameworks, with the main interest focused on MOFs based on the MOF-74 topology. Besides the electrical properties, the characterization of the optical properties of the MOF was also of major interest. Therefore, the synthesis of functionalized organic molecules with interesting (opto)electronic characteristics for their usage as ligands in metal-organic frameworks played a key role. In addition, the fabrication of thin MOF-74 films, intended for a future implementation into device-based technologies, was investigated.

Table of contents

List of abbreviations

List of Abbreviations

ALD	atomic layer deposition
AFM	atomic force microscopy
ANMOF	anthracene-based MOF
2D	two-dimensional
3D	three-dimensional
BET	Brunauer-Emmett-Teller
COF	covalent organic framework
DMF	dimethyl formamide
DMSO	dimethyl sulfoxide
EAMOF	ethyne-anthracene based MOF
EtOH	ethanol
eq.	equivalents
GIWAXS	grazing-incidence wide angle X-ray scattering
H_2O	water
MeOH	methanol
MOF	metal-organic framework
PDI	perylene diimide
PDIMOF	perylene-diimide based MOF
PL	photoluminescence
PLQY	photoluminescence quantum yield
ppm	parts per million

PXRD	powder X-ray diffraction
N_2	nitrogen
QSDFT	quenched solid density functional theory
SEM	scanning electron microscopy
TCSPC	time-correlated single-photon counting
TEM	transmission electron microscopy
TGA	thermogravimetric analysis
THF	tetrahydrofuran
UV-Vis	ultraviolet-visible
VAC	vapor-assisted conversion
XPS	X-ray photoelectron spectroscopy

1 Introduction

1.1 Metal-organic frameworks (MOFs) - a new class of porous materials

Porosity is a structural feature that has always played a fundamental role in nature. It exists in many different materials, from natural sponges and corals all the way to inorganic materials like TiO_2.[1] The pores or rather voids of porous materials can have different sizes and shapes and are made of a continuous solid phase, acting as a frame. They are able to accommodate guest species such as gases, molecules and ions, rendering themselves useful as gas storage and ion exchange materials, as well as for the purification of liquids.[2–4] Due to their typically high surface area, porous materials can also be used as catalysts, in case that the active sites are exposed on the pore surface.[3] The diffusion of reactants in heterogeneous catalysts are influenced by the pore architecture, including pore size and pore size distribution, as well as pore volume.[5]

Due to their broad usage, it is strongly desirable to create "custom-made porous compounds" which can be designed for specific applications.[6] The term ´reticular chemistry´ came up in 2003 and defines a new synthesis approach to predict and pre-design the topology of a resulting porous solid state material. It describes the synthesis of crystalline, extended frameworks exhibiting suitable chemical stability via the linkage of molecular building units by strong bonds.[6] In other words: " the molecule becomes the framework, as the framework becomes the molecule".[6,7] The well-defined structure and geometry of the molecular building blocks provide control in the construction of the desired scaffold and also maintain its rigid structure during synthesis. This includes pore shape, pore size and functionality, which can be designed towards defined applications.[8]

In the year 1995, Yaghi *et al.* published a groundbreaking paper about a novel class of hybrid materials, called metal-organic frameworks (MOFs).[9] However, research interest began already in the eighteenth century when the first coordination compound Prussian blue was discovered. Notably, a publication by Hoskins *et al*. in 1990 about a new class of 3D scaffolding-like materials laid the foundation for more extensive studies.[10] Reticular ("net-like") chemistry had a tremendous impact on the design and properties of MOFs, leading to the synthesis and study of over eighty thousand MOFs and hundreds of covalent organic frameworks (COFs). Due to their crystalline nature, they can easily be studied by X-ray diffraction or electron-diffraction techniques.[6]

Although the field of MOFs has grown very rapidly in recent years, there is no clear and strict definition of a MOF. This has led to discussions about the differences between coordination pol-

ymers and MOFs. Various publications exist in which MOFs are referred to as coordination polymers.[11] Others mention that MOFs are a porous subgroup of coordination polymers.[11] According to IUPAC, coordination polymers are continuous networks extending through coordination bonds in one, two or three dimensions.[12] Furthermore, a coordination compound contains a coordination unit. This compromises a central atom (neutral or an ion), usually a metal, which is connected by surrounding atoms or groups, the ligands. MOFs, according to IUPAC, are coordination polymers that have an open framework and contain potential voids.[12]

Summarizing, metal-organic frameworks (MOFs) consist of inorganic and organic nodes that are linked by coordinate bonds, leading to crystalline porous 2D or 3D coordination networks.[9,13,14] The metal ions are fixed in their positions, which guarantees the rigidity of the inorganic nodes, the so called secondary building units (SBUs), and play the role of stiff vertices.[15] In 1999, the synthesis of MOF-5 followed, which would become the most studied MOF up to date.[16,17] The structure of MOF-5 is built of octahedral Zn-O-C clusters, which are connected by terephthalate ligands, yielding a primitive cubic framework structure with defined pores.[16] The structure of MOF-5 is shown in Figure 1-1.[18]

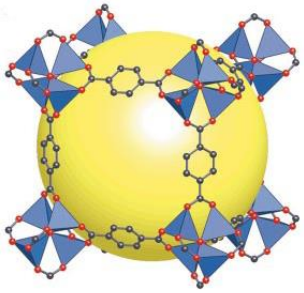

Figure 1-1: Structure of MOF-5: ZnO_4 tetrahedra (blue), oxygen (red) and carbon (black) of the organic linker, defining the pore (yellow).[18]

Zeolites have already demonstrated their ability to adsorb polar compounds and are being used at large scale for gas separation and purification applications.[19] Covalent organic frameworks (COFs), a closely related material class, where organic building blocks are connected by covalent bonds, also show good adsorption properties and are prominent candidates for gas storage and catalysis applications.[20] However, MOFs can be considered to be one of the most promising materials classes for adsorption applications, due to their stable periodic structure with permanent porosity and high surface area[13] of up to 7000 $m^2\ g^{-1}$ [13,21]. The (often) rigid structure of the MOF provides a selective and repeatable uptake and release of guest molecules into the well-defined and tunable pore spaces, by maintaining its framework or rather backbone structure.[7] Hence, Yaghi and his group added a new promising materials class to the family of porous materials.[22]

Depending on the organic building blocks and the respective metal species, the pore shapes and sizes can be tuned and the linker length is often directly correlated to the pore size. Adjusting the linker length allows for the synthesis of isoreticular MOFs (IRMOFs), which have a similar design principle and topology with variable pore sizes. Moreover, through the design of organic linker molecules, it is possible to incorporate different chemical compositions and functionalities into a MOF structure, to enable different structural connectivities with the metal nodes and to permit the generation of a large variety of possible topologies.[17,23,24,25]

Due to their structural diversity, a considerable number of different MOF families have evolved by combining different ligand types like carboxylate, imidazolate, pyridine, phosphonate, sulfonate and tetrazolate with different metal ions to generate new structures.[17,26,27] Some of the most popular MOF structures, besides MOF-5, are HKUST-1[28] (Hong Kong University of Science and Technologiy), MIL-53[29] (Matériaux de l'Institute Lavoisier) and MOF-74[30], which are often named after their discovering institute or working group. The lattice structures of a few examples of popular MOFs are shown in Figure 1-2.[31]

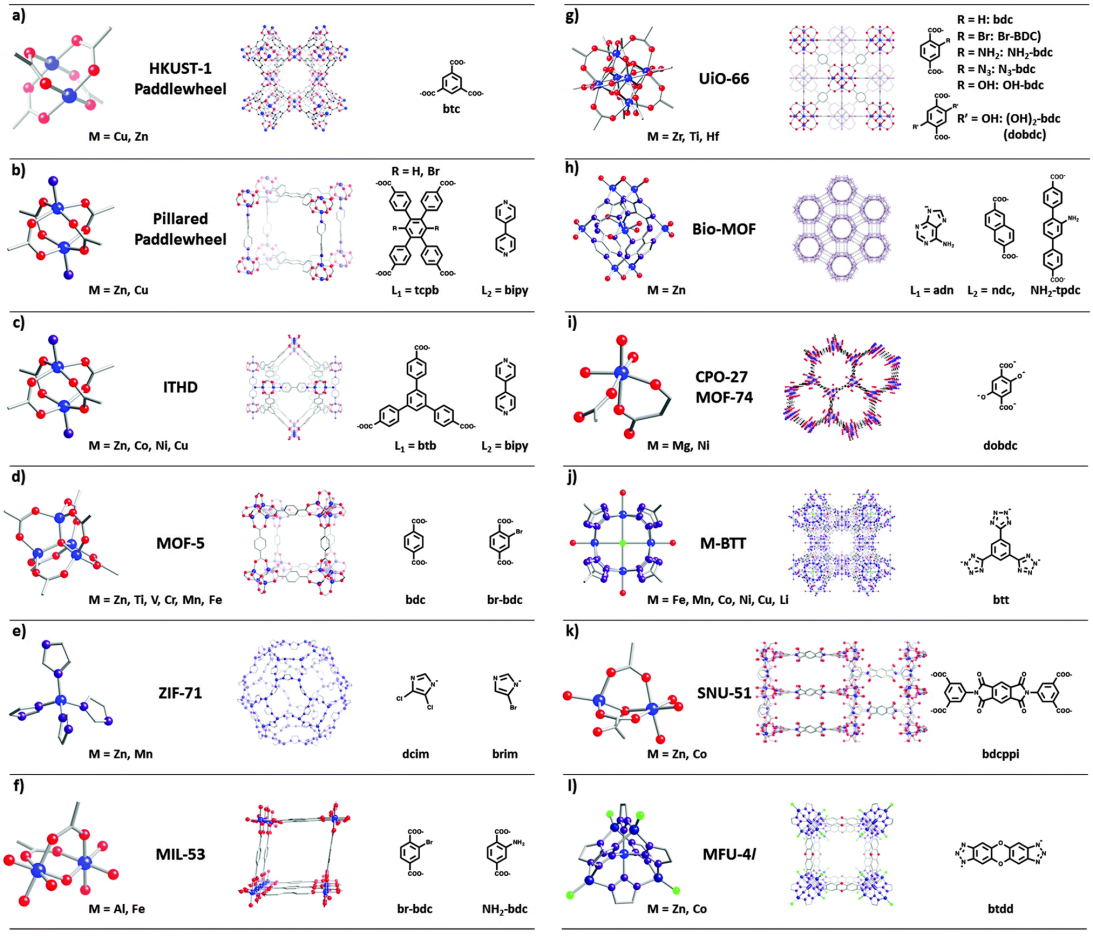

Figure 1-2: (Middle) lattice structure, (left) secondary building units (SBU), (right) organic ligands of a few popular MOFs. In blue the metal, in red oxygen, in purple nitrogen, in grey carbon and in green chlorine. Reproduced[31] with permission from the Royal Society of Chemistry.

This chemical and structural variety results in numerous possible chemical and physical properties of the synthesized MOFs.[24,32,33] It enables numerous potential applications like gas storage[34] and gas separation[35], chemical separation[35], heterogeneous catalysis[36], sensing[25], light harvesting and energy conversion[37], removal of toxic substances from air and water[38], drug delivery[14] and biomedical applications[39]. For example, one advantage of heterogeneous catalysis is the easy separation of the catalyst from the reaction mixture. This also avoids contamination from catalyst decomposition.[40] In addition, BASF is testing MOF-filled gas tanks to increase the storage density of natural gas, for example during transport, opening the usage of MOFs in industrial applications as well.[41]

1.1.1 MOF-74

This work mainly focuses on MOFs based on the MOF-74 topology, which was first synthesized by Rosi *et al.* in 2005.[30] MOF-74, or rather $M_2(DOBDC)(DMF)_2$ (M = divalent metal; H_4DOBDC = 2,5-dihydroxyterephthalic acid), crystallizes in the space group $R\bar{3}$ and was initially made with Zn^{II} as metal ion. It consists of one-dimensional 'infinite' rod-shaped metal oxide SBUs, linked by 2,5-dihydroxyterephthalic acid ligands, resulting in one-dimensional hexagonal pores with a dimension of 14 Å (see Figure 1-3 A).[30,42] The channels utilize metal to ligand connectivity and the walls can, in principle, serve as path for charge carrier transport. The SBUs consist of helical Zn-O-C rods with the composition $[O_2Zn_2](CO_2)_2$, comprising edge-sharing ZnO_6 octahedra.[30,43] Each Zn^{II} center is six-fold coordinated by oxygen, whereby three oxygens originate from carboxyl groups, two from deprotonated hydroxyl groups and one from the solvent DMF. This robust architecture offers permanent porosity and thermal stability up to 300 °C. In addition to the original structure with Zn^{II}, MOF-74 isostructures with the divalent metal ions Mg^{II}, Mn^{II}, Fe^{II}, Co^{II}, Ni^{II} and Cu^{II} have also been reported.[43–49]. Wang *et al.* even showed the synthesis of mixed metal MOF-74 analogs with 2, 4, 6, 8 and 10 different metal ions, ranging from MOF-74(Mg, Co), MOF-74(Mg, Co, Ni, Zn), MOF-74(Mg, Sr, Mn, Co, Ni, Zn), MOF-74(Mg, Ca, Sr, Mn, Fe, Co, Ni, Zn) to MOF-74(Mg, Ca, Sr, Ba, Mn, Fe, Co, Ni, Zn, Cd).[50]

Due to the good stability of MOF-74, in combination with high porosity and large surface area, MOF-74 exhibits very attractive adsorption properties. Besides N_2, the storage and separation performance of MOF-74 towards CO_2, SO_2, NH_3, C_6H_6 and HCl was studied.[51,52] Especially MOF-74(Mg) shows excellent performance for CO_2 capture and CO_2/ H_2 separation with a CO_2 adsorption capacity of 350 mg^2/g at 298 K.[53–56] MOF-74 has a high affinity towards CO_2, due to its unsaturated, or rather open metal sites. After synthesis, linker and also solvent molecules are coordinated to the metal. After removal of the solvent molecules, the structure of MOF-74 remains intact and open metal sites are created, which act like a Lewis acid, due to their electronic

deficiency. CO_2 acts as Lewis base and forms a strong interaction with the metal center.[57] However, adsorbed CO_2 can be displaced by H_2O, NO and SO_2, which feature higher binding energies at the metal site.[58] Besides adsorption, further publications report about the use of MOF-74(Co) and MOF-74(Co)-TTF as gas-sensing devices, due to conductivity changes with respect to the adsorbed gases.[57,59] MOF-74 was also used as catalyst, for example for the reduction of NO_x.[60]

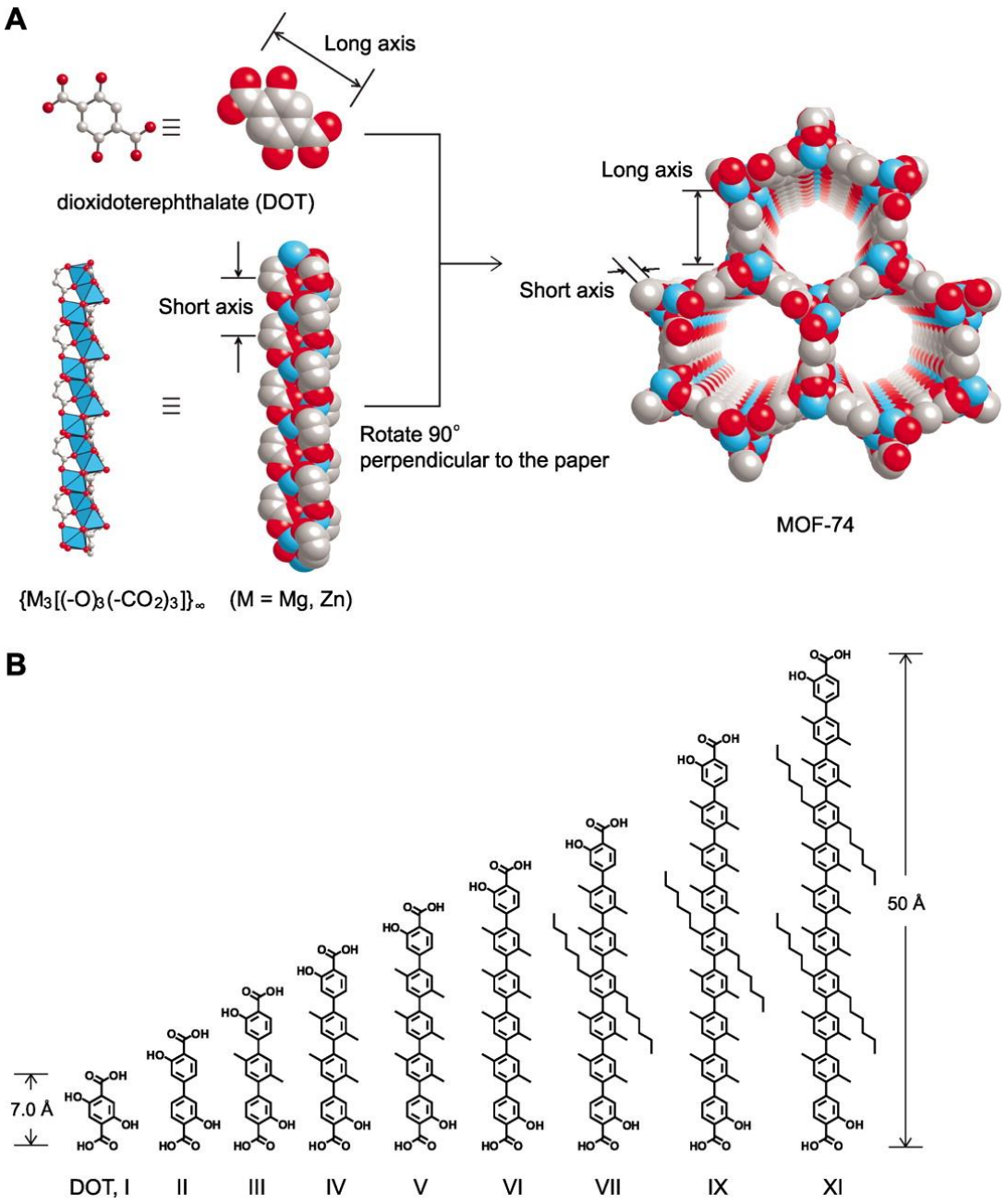

Figure 1-3: (A) Crystal structure of MOF-74. The metal-oxide SBU form, together with the DOT ligand, the three-dimensional MOF-74, creating one-dimensional hexagonal channels. (B) Organic ligands used for the isoreticular MOF-74 series (IRMOFs). From[42], reprinted with permission from AAAS.

MOF-74(Zn, Mg) can also be expanded isoreticularly, by elongating the linear 2,5-dihydroxyterephthalic acid linker with phenyl groups (see Figure 1-3 B).[42] Thereby, the pore size was increased

up to 98 Å without pore collapse, representing the largest one reported for MOF-74 topologies in the literature to date.[42] Thus, MOF-74 offers a high degree of synthetic versatility.

It also demonstrates the possibility to synthesize new MOFs with MOF-74 topology, by exchanging the organic ligand with other linear building blocks comprising different functional groups in the core, as long as they exhibit the terminal carboxy- and hydroxy functional groups. This was firstly shown by AlKaabi *et al*., who incorporated a naphtalene-diimide-based ligand into the MOF-74 topology.[61] The ligand *N*,*N*′-bis(3-carboxy-4-hydroxyphenyl)-1,4,5,8-naphthalenetetradicarboximide (H_4NDISA) utilizes terminal para-hydroxy and ortho-carboxy groups, which are reversed in comparison to the original MOF-74 with a 2,5-dihydroxyterephthalic acid ligand. However, together with Mg^{II} and Ni^{II} it forms the mesoporous MOFs Mg/Ni-NDISA, which crystallize in the MOF-74 topology. They exhibit pore widths of 3.3 nm, which were confirmed by N_2 type IV isotherms. Cyclic voltammetry showed two quasi-reversible one-electron redox couples of Mg-NDISA and Ni-NDISA films, coming from the formation of a radical anion $[NDI]^{\cdot-}$ and dianion $[NDI]^{2-}$, respectively. On Ni-NDISA films, a fast electrochromic switching from transparent to dark color was observed between the neutral ligand state to the reduced states of $[NDI]^{2-}$.[61]

Guo *et al.* used the regioisomer of the NDISA ligand, namely DSNDI, where the relative positions of the hydroxy- and carboxy groups are switched, thus matching the positions of traditional MOF-74 ligands.[62] Together with Zn^{2+} it forms the mesoporous DSNDI-based MOF-74, exhibiting pore apertures of about 3.1 nm. After intercalation of TTF molecules between the parallel NDI ligands, the bandgap was lowered from 2.1 eV to 1.0 eV, due to π-donor/ acceptor stacks, which were formed between the electron rich TTF molecules and electron deficient DSNDI ligands. This results in an efficient orbital overlap between NDI and TTF. Electron paramagnetic resonance (EPR) spectroscopy confirmed the coexistence of TTF radical cations together with DSNDI radical anions.[62]

1.2 Electroactive MOFs

The potential combination of the high surface area of MOFs with good charge transport properties (high charge carrier densities and mobilities for significant electrical conductivity) would open new applications in the field of chemical sensing[25], charge storage, semiconductors and fuel cells.[25,63–69]

However, porous MOFs often feature low electrical conductivity, due to their lack of free charge carriers and low-energy pathways for charge carrier transport. This is a direct consequence of the binding of hard metal ions and redox-inactive linker molecules *via* hard oxygen or nitrogen atoms.

However, in the past decade, an increasing interest as well as first developments of porous MOFs exhibiting electrical conductivity have emerged.

A high concentration of mobile charge carriers can be provided by the use of transition metal ions and the incorporation of stable radicals serving as organic ligands. The charge transfer between metal nodes can be facilitated with redox-active molecular building blocks. Depending on the design of the MOF, different low-energy and long-range charge delocalization pathways are possible. In the "through-bond" approach, charge transport occurs over an internal pathway *via* covalent bonds. This requires a symmetry-based and energetically favorable orbital overlap between the metal nodes and the organic ligands.[44,45] For example, the use of sulfur instead of oxygen or nitrogen atoms as functional groups of the organic linker, can cause orbital overlap with the metal nodes.[44,70] In the "through-space" approach, charge carrier percolation occurs between electroactive fragments of the organic ligand *via* π-π-stacking interactions [71] Another effective method is the incorporation of electroactive guest molecules into the pores, which can provide free charge carriers. Mobile charge carriers can also be injected by doping the MOF with guest molecules, which oxidize or reduce the organic building blocks while maintaining the porosity of the MOF framework.

An increasing number of electroactive 2D and 3D MOFs have been reported since 2009, realizing different approaches of introducing electrical conductivity.[72] Especially 2D MOFs show high electrical conductivity values in combination with high crystallinity. $Cu_3(BHT)_2$ (BHT = benzenehexathiol) films show the highest reported electrical conductivity of a MOF, with 2500 S/cm, but feature only low porosity.[73] 2D MOFs exhibit a graphite-like molecular stack and in-plane conjugation, which offer good electron delocalization and low-energy charge carrier transport pathways. However, the construction of different 2D MOFs is limited by strict design rules. A rigid organic building block with a distinct symmetry and a planar linking motif is necessary to form extended sheets with the metal ions.[74] Furthermore, the stacking of 2D layers could lead to a limited surface area, as well as non-accessible metal sites.[75]

In recent years, an increased number of electroactive 3D MOFs were published, showing different approaches to induce electrical conductivity. In comparison to 2D MOFs, 3D MOFs offer a multifaceted platform for the construction of potentially conductive MOFs. In addition, 3D MOFs often exhibit better adsorption and diffusion properties, which is crucial for the intercalation of potential dopants to tune the electronic properties.[76] However, only a few of them exhibit the combination of electrical conductivity with high surface-areas, which is essential for desired applications like chemical sensing or charge storage.[44] In this review, we focus on electroactive 3D MOFs and 3D porous coordination polymers (PCP), which in principle offer a vast portfolio of

organic building blocks, bonding schemes and topologies. This leads to diverse MOF platforms and different charge transport pathways, enriching the library of 3D electroactive MOFs.

1.3 3D electrically conducting MOFs

Takaishi and coworkers published one of the first electrically conductive MOFs in 2009, namely $Cu[Cu(pdt)_2]$(pdt = 2,3-pyrazinedithiolate) (see Figure 1-4).[72] $[Cu^{III}(pdt)_2]^-$ shows a reversible redox process to $[Cu^{II}(pdt)_2]^{2-}$ and acts as electron acceptor unit in the MOF. The N atoms of the pyrazine units coordinate to copper ions, the electron donor moiety and form an infinite tetragonal lattice. The 3D MOF exhibited temperature dependent electrical conductivity values of 1×10^{-4} S/cm at room temperature and 6×10^{-4} S/cm at 300 K (pellet, method not stated), as well as an activation energy of 193 meV. The charge bistability between $Cu^I[Cu^{III}(pdt)_2]$ and $Cu^{II}[Cu^{II}(pdt)_2]$ with a resulting redox hopping between the copper centers was claimed as reason for the relatively high conductivity.

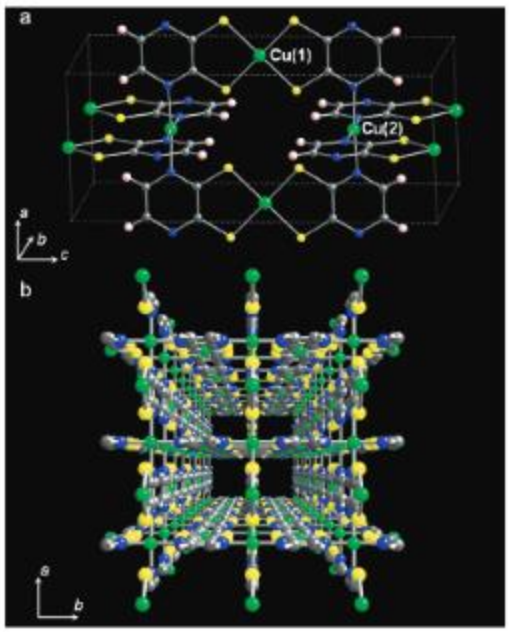

Figure 1-4: (a, b) Crystal structure of $Cu[Cu(pdt)_2]$. Reprinted (adapted) with permission[72]. Copyright {2009} American Chemical Society.

However, Kobayashi *et al.* reported that the one-dimensional pores of this compound collapse after desolvation, which destroys the crystallinity of the MOF.[77] They successfully exchanged Cu^{II} with Ni^{II}, which led to the permanently porous MOF analog $Cu[Ni(pdt)_2]$, exhibiting a BET surface area of 385 m^2/g. However, the room temperature conductivity of a $Cu[Ni(pdt)_2]$ film (two-point probe method, film, rt) was measured to be 1×10^{-8} S/cm. [77] In a later report, $Cu[Ni(pdt)_2]$ showed an electrical conductivity value of 2.6×10^{-6} S/cm (guest-free pellet, two-

point probe method, rt).[78] Notably, partial oxidation of the framework with a stream of I_2 vapor as oxidant at 50 °C achieved an electrical conductivity enhancement up to 1 x 10^{-4} S/cm (two-point probe method, film, rt).[77] The conductivity increase after oxidation with I_2 is based on the newly formed, reversible $[Ni(pdt)_2]^{2-/1-}$ couple in the MOF, which enables redox hopping.

1.3.1 Intercalation of guest molecules into 3D MOFs and 3D PCPs

Further publications on 3D conductive MOFs reported doping processes or the intercalation of guest molecules in order to increase the electrical conductivity values of MOFs. For example the intercalation of iodine and 7,7,8,8-tetracyanoquinodimethane (TCNQ) have been investigated.

1.3.1.1 Iodine intercalation

Lin *et al.* doped the orthorhombic porous coordination polymer (PCP) ($[Na_2)I_2CB[6])\cdot 8H_2O]_n$) (CB[6] = cucurbit[6]uril) with I_2, resulting in iodine molecules encapsulated in-between iodide ions in the pore channels. However, due to a change of the crystal lattice of the PCP during the iodine insertion, the framework loses its crystallinity. An electrical conductivity value of 7.46 x 10^{-7} S/cm (two-point probe method, pellet, rt) was measured for the PCP after iodine adsorption. A Grotthus-like charge transfer mechanism of $I^- + 2I_2 \rightarrow I_2 + I_3^-$, or a charge transfer by polyiodide units were invoked as reason for the measured electrical conductivity.[79]

Yin *et al.* synthesized a bi-pillared-bilayer MOF structure, with the formula $\{[Cu_6(pybz)_8(OH)_2]\cdot I_5^- I_7^-\}_n$ (pybz = 4-(4-pyridyl)benzoate), by adding iodine molecules to the MOF precursor solution.[80] They measured an electrical conductivity value of 8.11 x 10^{-7} S/cm (method not stated, film of crushed crystals, rt). Here, the authors assumed an $n \rightarrow \sigma^*$ charge-transfer, induced by the polyiodide chains in the well-ordered aromatic pore channels. Removal of I_2 from the polyiodides during soaking in methanol decreased the electrical conductivity to 8.04 x 10^{-9} S/cm in $[Cu_6(pybz)_8(OH)_2(I^-)_2]$, demonstrating the ability to tune the conductivity. However, the porosity of the iodine-loaded MOF was not determined.

Hao *et al.* used a similar strategy and incorporated iodine into the pores of the europium-based MOF $Eu_4(BPT)_4$ (BPT = biphenyl-3,4´,5-tricarboxylate).[81] A temperature-dependent electrical conductivity of 8.27 x 10^{-7} S/cm at room temperature and 2.71 x 10^{-5} S/cm at 80 °C (two-point probe method, pellets, rt) was observed. However, the porosity of the undoped $Eu_4(BPT)_4$ was already very low (maximal N_2 uptake of about 35 cm^3/g) and no sorption measurements of the iodine-loaded material were performed. Furthermore, Lee *et al*. noticed a conductivity increase after iodine doping of nonconductive $Co_3(NDC)_3DMF_4$ (NDC = 1,4-naphtalenedicarboxylic acid) MOF films, by dipping the films into a 0.1 M solution of I_2 in acetonitrile. [82]An electrical conductivity value of up to 1.88 x 10^{-6} S/cm (two-point probe, film, rt) was measured. XPS detection

of I_3^- in the MOF framework as well as a measured hole mobility of 21.2 cm^2/ Vs and a charge carrier concentration of 5 x 10^{11} cm^{-3} implied the formation of a charge transfer complex. This led to the oxidation of the aromatic ring of the ligand by iodine, leading from an insulator to a hole-doped framework exhibiting electrical conductivity.[82] In another report, a conductivity enhancement from 1.3 x 10^{-11} S/cm to 2.0 x 10^{-8} S/cm (pellet, two-contact probe method, rt) was observed in the MOF [DMA][In(TDC)$_2$] (DMA = dimethyl ammonium cation; TDC = 2,5-thiophene-dicarboxylic acid), doped with about 56 wt % I_2.[83] The iodine doping was confirmed by XPS measurements and lowered the band gap from 3.73 eV to 1.55 eV. The doping process was reversible by soaking the doped MOF in pure cyclohexane. However, intercalation of iodine into the pores caused the loss of the MOF's porosity.

1.3.1.2 Cation intercalation

Ogihara *et al*. used the non-conductive MOF naphtalene dicarboxylate dilithium [2,6-Naph(COOLi)$_2$] for the intercalation of Li^+ ions to form Li_2[2,6-Naph(COOLi)$_2$], which exhibited increased, temperature dependent electrical conductivity values (four-point probe method, pellet) of 10^{-6} S/cm (298 K) to 10^{-5} S/cm (333 K).[84] Furthermore, an actication energy of 190 meV as well as ionic conductivity was observed. In this MOF, tetrahedral LiO_4 units are connected by π-stacked naphtalene layers, forming a layered 3D structure in the monoclinic space group $P2_1/c$, which remained intact during the Li intercalation. The intercalation process, achieved by using a lithium naphthalenide THF solution, can be observed by a color change of the MOF powder from white to black. However, no sorption measurements of the MOF were examined. DFT calculations led to the conclusion that the intercalated Li ions are located in the organic layer of the naphtalene ligands, which caused an enhancement of the electron density and thus to a decreased band gap of 0.99 eV. Furthermore, it was proposed that the reductive lithium intercalation led to an anisotropic electron hopping, with the electron conduction pathway along the *b*-*c* planar direction in the 2D π-stacked naphtalene layers.

Rouhani *et al*. enhanced the electrical conductivity of the MOF TMU-60 ([Zn(OBA)(L*)·DMF], H_2OBA = 4,4´-oxybis(benzoic acid), L* = 5,6-di(pyridin-4-yl)-1,2,3,4-tetrahydropyrazine), by Cd^{II} ion intercalation.[85] TMU-60 crystallizes in the orthorhombic space group I_{bca}. It is built of $Zn_2(COO)_4$ paddle-wheel SBUs that are connected by the two different linkers, resulting in a two-fold interpenetrated structure. Metallic ion sorption with an aqueous Cd^{II} solution led to the intercalation of Cd^{II} ions into the 1D pores in the ratio of 1.5:1 (Zn:Cd). The appropriate orientation of the amine functions of L* led to supramolecular and electrostatic interactions with the Cd ions. The BET surface area of 171.5 m^2g^{-1} decreased after Cd intercalation, however no exact resulting BET surface area was mentioned. Electrical conductivity values (four-point probe method, pellet, 293 K) increased from 5.3 x 10^{-6} S/cm to 1.8 x 10^{-2} S/cm after Cd intercalation and could be

further tuned by the quantitiy of Cd intercalated into the MOF. The authors suggested an electron hopping process between the metal nodes and the Cd ions as reason for the conductivity enhancement. However, the effect of this remarkable conductivity increase by Cd^{II} intercalation could not be repeated with other MOF structures like UiO-66, MIL-100 and SBA-15. The authors emphasized that interactions of the Cd^{II} ions with suitable functional sites in the framework such as amino moieties as well as the small distances between metal nodes and Cd^{II} ions are mandatory for inducing a charge transfer.

Wang *et al.* incorporated Fe^{III} ions into MIL-177-LT (MIL = Materials from Institut Lavoisier, LT = low temperature form) to enhance the electrical conductivity in the MOF.[86] MIL-177-LT has the formula Ti_4O_5(mdip)(formate)$_2 \cdot 2.1H_2O$ (mdip = 3,3´,5,5´-tetracarboxydiphenylmethane) and crystallizes in the hexagonal space group *P*6/*mmm*. The SBU consists of $Ti_{12}O_{15}$ clusters, which are connected by mdip linkers and formate ions, resulting in hexagonal channels extending along the *c*-axis and featuring a BET surface area of 730 m^2g^{-1}. Thermally induced structural transformation led to the formation of MIL-177-HT (Ti_4O_6(mdip), HT = high temperature), including 1D $(Ti_6O_9)_n$ nanowires. The replacement of Ti atoms in the SBU with 11 % Fe^{III} ions, achieved by adding $FeCl_3$ during the synthesis, led to an increase of the electrical conductivity from an insulator character to 1.5 x 10^{-10} S/cm (two-point probe method, pellet, 373 K). The authors attributed the injection of free charge carriers through the addition of Fe^{III} as well as a facilitated charge carrier movement as reason for the conductivity enhancement.

1.3.1.3 7,7,8,8-tetracyanoquinododimethane (TCNQ) intercalation

7,7,8,8-Tetracyanoquinodimethane (TCNQ) is an electron acceptor and a widely used intercalation component for MOFs. On the one hand, it can form highly stable radical anions. On the other hand, , adjacent, parallel TCNQ molecules can build π-π stacked complexes, which induce charge transfer and electrical conductivity.[87]

Huang *et al.* synthesized single crystals of [Cu_2(TATAB)$_3$] $7.5H_2O$ (Cu-TATAB) (H_3TATAB = 4, 4´, 4´´-((1,3,5-triazine-2,4,6-triyl)tris(azane diyl)) tribenzoic acid), which crystallize in the cubic space group $Im\bar{3}$.[88] It contains an interpenetrated framework with paddlewheel SBUs. Three different rhombic and hexagonally shaped microchannels are present in the framework structure, but no sorption analysis was added. Soaking the MOF in a TCNQ methanol solution caused a crystal colour change from green to dark. Furthermore, the electrical conductivity value (two-point probe method, pellet, 293 K) increased during this intercalation process from 9.75 x 10^{-12} S/cm to 2.67 x 10^{-7} S/cm, up to 3.06 x 10^{-6} S/cm at 363 K. The authors attributed the increased conductivity after the intercalation of TCNQ molecules into the framework to the formation of a charge transport channel, which emerged due to the addition of unoccupied molecular orbitals in

the HOMO-LUMO gap of Cu-TATB. However, no discussion of the exact position of the TCNQ molecules in the framework or the interactions of TCNQ with the framework were presented.

The incorporation of TCNQ into the well-known cubic MOF HKUST-1 (($Cu_3(BTC)_2$, BTC = benzene-1,3-5-tricarboxylic acid), led to an electrical conductivity increase of over six orders of magnitude in comparison to the pristine MOF.[89] TCNQ molecules were intercalated into the pores of activated HKUST-1 films (see Figure 1-5), while retaining the crystal structure, by soaking them in a saturated TCNQ/CH_2Cl_2 solution for 72 h. The color of the activated MOF films changed from violet-blue to teal. Due to the loading of one TCNQ molecule per MOF cage, the BET surface area decreased frotcnq in m about 1844 $m^2\ g^{-1}$ to about 214 $m^2\ g^{-1}$. Electrical conductivity measurements (4-contact probe method, thin film, 300 K) gave values in the range of 10^{-8} S/cm for HKUST-1 and 7 x 10^{-2} S/cm for the TCNQ-loaded MOF. New absorption bands at about 700 nm and 850 nm in the UV-Vis spectrum of the TCNQ-loaded MOF were attributed to a partial charge-transfer of about 0.3e^- between Cu^{II} and TCNQ, which led to the increased conductivity. The presence of partially reduced TCNQ was also verified by Raman and infrared spectroscopy. Moreover, ab inito calculations confirmed the enhanced electronic coupling due to TCNQ molecules bridging the binuclear Cu^{II} paddlewheels (SBUs), hence forming a continuous charge transfer pathway. Several other groups reported a conductivity enhancement for TCNQ loaded HKUST-1 in a similar range.[90,91]

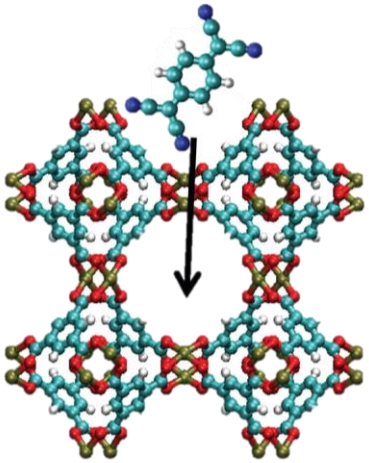

Figure 1-5: A $Cu_3(BTC)_2$ cage with a TCNQ molecule illustrated above, with an arrow pointing into the cage. From[89]. Reprinted with permission from AAAS.

Schneider *et al.* loaded one TCNQ molecule per $Cu_3(BTC)_2$ phase *via* a vapor phase infiltration process.[92] The electrical conductivity values (two-contact probe method, pellet, 298 K) increased exponentially with the TCNQ loading, up to 1.5 x 10^{-4} S/cm, in line with the classical percolation theory. However, a side phase of Cu(TCNQ) (in the form of nanowires) was also detected on the

MOF surface by SEM. Also, Thürmer *et al.* observed the complete conversion of HKUST-1 films during infiltration with TCNQ/MeOH solutions, resulting in Cu(TCNQ) films.[93] Cu(TCNQ) itself shows a room temperature conductivity of about 0.1 S/cm, inviting the question if the loaded MOFs or the conductive side phase is responsible for the improved conductivity of these hybrid materials.[93] As a consequence, the structural analysis of the phase composition of MOFs that were treated with redox-active species like TCNQ is essential for the determination of the origin of the conductivity.

1.3.2 Incorporation of redox-active and electroactive organic ligands

1.3.2.1 Naphthalene diimide (NDI) based ligands

The incorporation of electron-rich organic ligands to induce π-π-stacking as well as the incorporation of redox-active building blocks into the MOF framework are prominent ways to introduce charge carriers and charge transfer pathways.

Naphthalene diimide (NDI) is a widely used electron acceptor and a redox-active organic building block.[62] Furthermore, it can form the stable radical anions $NDI^{\bullet-}$. Wade *et al.* synthesized the microporous MOF ZnNDI, which contains naphthalenediimide ligands that are connected *via* pyrazolate groups with tetrahedral Zn^{2+} ions in a distorted breathing angle of 77°.[94] It comprises channels with a diameter of about 16 Å and exhibits a BET surface area of 1460 $m^2\ g^{-2}$. Wentz *et al.* performed n-doping of 90 % of the redox-active NDI ligands in ZnNDI with tetra-*n*-butylammonium fluoride (TBAF), causing a conductivity enhancement from 10^{-14} S/cm up to 6 x 10^{-7} S/cm (two-point probe method, pellet, rt).[95] The reduction of NDI to $NDI^{\bullet-}$ radical anions by soaking the MOF in DMF-based TBAF solutions was confirmed by UV-Vis measurements. It caused an increase of the charge carrier density and generated a charge transport pathway along the ordered $NDI^{\bullet-}$ stacks.

Guo *et al.* constructed a pillared-paddlewheel MOF with *N,N´*-bis(4-pyridyl)-2,6-dipyrrolidyl naphthalenediimide (BPDPNDI) pillars and 1,2,4,5-tetrakis-(4-carboxyphenyl)benzene (TCPB) struts.[96] The resulting BMOF [Zn_2(TCPB)(BPDPND)] crystallized in a noncatenated cubic architecture and was grown on a ZnO-coated glass substrate under solvothermal conditions. The porosity was confirmed by CO_2 adsorption analysis, showing an uptake of 65 cm^3g^{-1} at 273 K and 1 bar. Electrical conductivity measurements (four-point probe method, film, 298 K) gave a value of 6 x 10^{-7} S/cm. It was demonstrated that intercalation of the π-acidic guest methyl viologen (MV^{2+}), by soaking the films in a MV^{2+} solution, further increased the electrical conductivity to

2.3 x 10^{-5} S/cm. The authors attributed the conductivity enhancement to the induced π-donor/acceptor charge transfer between BPDPNDI ligands and intercalated MV^{2+}, activating long-range electron delocalization in the framework.

Qu *et al.* synthesized the porous coordination polymer $[Cd(NDI\text{-}py)(OH_2)_4](NO_3)_{1.3\pm0.1}\cdot n$ DMA (PMC-1 = porous molecular conductor-1) (NDI-py = N,N´-di(4-pyridyl)-1,4,5,8-naphthalenetetracarboxdiimide; DMA = *N*,*N*-dimethylacetamide) *via* electrocrystallization in the hexagonal space group *P*622.[97] NDI-py ligands and $[Cd(OH_2)_4]^{2+}$ form 1D linear coordination polymers and the NDI cores build face-to-face infinite helical columns along the *c*-axis *via* *π*-*π*-stacking. However, the porosity of PCM-1 was not confirmed by sorption measurements. The NDI cores have a distance of 3.18 Å to each other and the pyridyl groups are oriented in 60° increments. A part of the NDI-py ligands exist in the radical anion state $NDI^{\cdot -}$, which is confirmed by solid-state spectroelectrochemical measurements (SEC) in diffuse reflectance mode solid-state-absorption spectroscopyand ESR spectroscopy. Electrical conductivity measurements (two-point probe method, 300 K) showed semiconducting behavior and gave values between 1.0 – 3.3 x 10^{-3} S/cm for single crystals along the *c*-axis and 1.5 – 7.6 x 10^{-6} S/cm for pressed pellets. Removal of DMA molecules in the single crystals led to an electrical conductivity increase to 1.2 – 3.7 x 10^{-2} S/cm. The authors attributed the conductivity enhancement to a structural change of the 1D columnar π-stacking structures to 2D-like packing nodes, with high charge carrier mobility and lower grain boundary resistivity. The partially reduced *π*-stacked NDI columns along the *c*-axis were identified as through-space conduction pathway.

The porous coordination polymer $Cu(DPNDI)_2PF_6\cdot 4DMA\cdot CH_3CN$ (DPND = N,N´-di(4-pyridyl)-1,4,5,8-naphthalenetetracarboxydiimide, named (Cu^{I}-NDI), reported by Kuang *et al*., features an electrical conductivity of 1.2 x 10^{-5} S/cm (two-point probe method, single crystal, 298 K).[98] It forms a sixfold interprenetrated adamantane-like cage, including *π*-*π*-stacking of the NDI cores. The electrical conductivity was measured along the *c*-axis, representing the *π*-stacking direction and the electron hopping pathway. DFT calculations determined that electrons can also freely delocalize along the -Cu-N- bonds, inducing another conductivity pathway. The porosity of Cu^{I}-NDI was not confirmed, however, solid-state NMR enabled the detection of PF_6^- and solvent molecules inside the pores.

1.3.2.2 Anthracene based ligand

Another electroactive microporous MOF with ligand-induced conductivity was published by Chen *et al*.[99] The MOF $[ZnNa_2(AnBEB_2)(DEF)_2\cdot DEF$ (AnBEB = 4,4′-(anthracene-9,10-diylbis-(ethyne-2,1-diyl))dibenzoate)), named NNU-27, crystallizes in the tetragonal space group $P4_2/nbc$. The anthracene cores coordinate *via* terminal benzoic acid groups with tetrahedral Zn^{II}

ions. Na^{I} ions build a distorted octahedral geometry by coordinating four carboxylic oxygen atoms of the ligands and two oxygen atoms of DEF molecules. An infinite bimetal chain is built by Na^{I}/ Zn^{II} (ratio 2:1) and carboxylate groups. Due to π-π-interactions between anthracene-based ligands with an interplanar distance of about 3.4 Å, neighbouring metallic chains interact in a zigzag fashion along the *c*-axis. Pore channels along the *c*-axis have a diameter of 16 x 16 Å and are constituted of the zigzag chains of the ligands forming a double-wall. However, removal of coordinated solvent molecules inside the pores after activation led to a collapse of the pristine structure. Nevertheless, porosity was confirmed by encapsulation of the dye methylene blue. An electrical conductivity of 1.3 x 10^{-3} S/cm (two-point probe method, rt) was measured on single crystals. The long-range π-conjugation of the ligands along the *c*-axis enabled a through-space charge transport. The fact that the planes of the ligands are parallel to the *c*-axis and feature a close stacking distance facilitates a conjugated charge transport pathway in form of a zigzag chain, resulting in the high conductivity.

1.3.2.3 Tetrathiafulvalene (TTF) based ligands

Several electroactive MOFs based on tetrathiafulvalene (TTF) linkers have been reported. TTF derivatives feature delocalized π-orbitals, planarity, good electron donor character and they can form stable radical cations, which facilitates charge-transfer. Furthermore, TTF–based ligands can form π-π-stacks with short internal S···S distances for good charge transport properties.[100–102] TTF molecules can also be introduced as guest molecules into the MOF framework to induce charge transport and to lower the bandgap of MOFs, as previously reported for MOF-74 topologies.[57,62]

Reaction of tetrathiafulvalene tetrabenzoic acid (H_4TTFTB) with zinc nitrate led to the crystallization of the microporous MOF [Zn_2TTFTB(H_2O)$_2$]·H_2O·2DMF (Zn_2TTFTB) in the hexagonal space group $P6_5$, reported by Narayan *et al.*.[71] In the crystal structure (

Figure 1-6), one-dimensional helical π-stacks of TTF ligands connect helical zinc benzoate chains. They are built from two pseudo-octahedral zinc atoms, connected by six oxygen atoms, namely four carboxylates and two water molecules. Furthermore, the benzoate groups line one-dimensional cylindrical micropores. The 6_5 screw axis is slightly shifted from the central TTF ethylene unit and therefore the TTF units are alternated by 60° relative to one another. As a consequence, the planes of the TTF units are not exactly perpendicular to the *c*-axis and have a distance of 3.47 Å to each other (

Figure 1-6 A). Furthermore, Zn_2TTFTB exhibits a charge carrier mobility of 0.2 cm^2/Vs, which was measured by flash photolysis time-resolved microwave conductivity (FP-TRMC) and time of flight (TOF) current transient measurements.

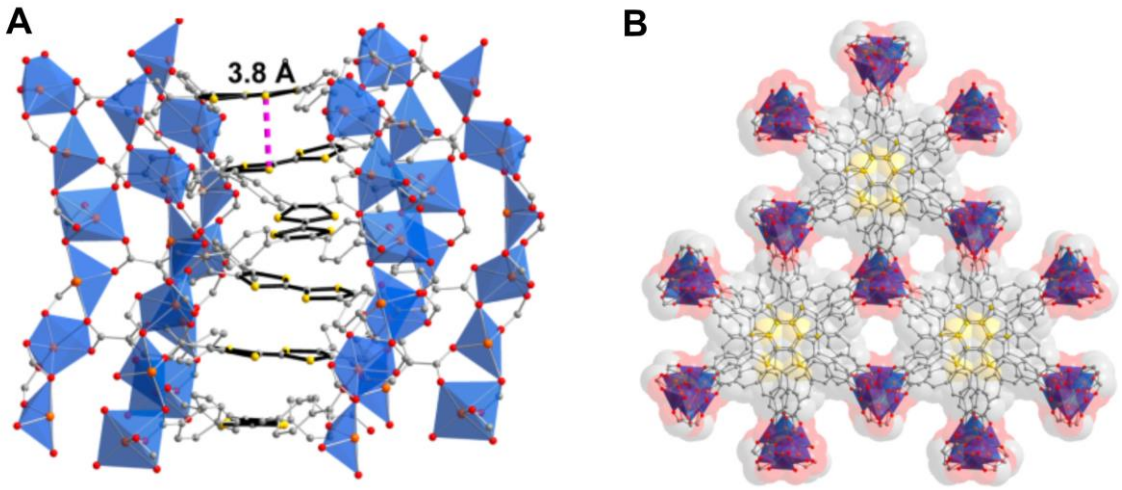

Figure 1-6: Crystal structure of [Zn_2TTFTB(H_2O)$_2$]·H_2O·2DMF (Zn_2TTFTB), (A) in side view, showing a helical TTF stack and the shortest intermolecular S···S contact. (B) Benzoate-lined infinite pores with view down the *c*-axis. Orange, yellow, red, and grey spheres represent Zn, S, O, and C atoms, respectively. Reprinted (adapted) with permission[71]. Copyright {2012} American Chemical Society.

Park *et al.* performed single crystals electrical conductivity measurements along the *c*-axis of Zn_2TTFTB and obtained an average value of 3.95 x 10^{-6} S/cm (two-point probe method, single crystal, rt).[103] The distance between two sulfur atoms among each pair of neighboring TTF units was calculated to be 3.757 Å (Figure 1-7). Moreover, MOF analogs of Zn_2TTFTB were synthesized with the metal ions cadmium, manganese and cobalt. They crystallize in the same space group and show microporous behavior with BET surface areas between 470 and 537 m^2/ mmol. While the SBUs of the manganese and cobalt MOFs exhibit corner-sharing pseudo-octahedra similar to the zinc MOF, the cadmium MOF reveals alternating seven- and six-coordinated cadmium ions. The effect of the different metal ions on the conductivity in the TTFTB-based MOF M_2TTFTB, was analyzed. An increase of the ionic radius of the metal ions in the TTFTB-based MOFs caused an enhanced electrical conductivity. The shortest S···S distance of neighboring TTF cores was observed in Cd_2(TTFTB) with 3.654 Å, also showing the highest single crystal conductivity value of 2.86 x 10^{-4} S/cm (two-contact probe method, single crystal, rt). Mn_2(TTFTB) and Co_2(TTFTB) with S···S distances of 3.654 Å and 3.773 Å exhibited conductivity values of 8.64 x 10^{-4} S/cm and 1.49 x 10^{-5} S/cm, respectively (two-contact probe method, single crystal, rt). Overall, it was concluded that larger cations in the TTFTB-based MOFs elongated the SBUs, which reduced the TTF-TTF distance in the π-stack and facilitated charge transport, due to an increased overlap between the sulfur $3p_z$ orbitals. However, the conductivity of Zn_2(TTFTB), measured parallel to the *ab* plane, was found to be 2.03 x 10^{-7} S/cm (two-point

probe method, single crystal, rt), in comparison to the measurement along the crystallographic *c*-axis giving a value of 3.95 x 10^{-6} S/cm, demonstrating an anisotropic conductivity.[103] Not surprisingly, the electrical conductivity measured with a pressed pellet of Cd_2(TTFTB) with the four-point probe and with the van der Pauw method on pressed pellets gave smaller values of of 4.39 x 10^{-6} S/cm and 2.70 x 10^{-6} S/cm, respectively, in comparison to the higher values measured with single crystals.[104] The study spotlights that different measurement methods, as well as different sample morphologies like single crystals and pressed pellets, can have a large impact on the observed conductivity values. Pressed pellets can feature different sizes and orientations of the crystallites within the pellet, due to the pressing process. Moreover, grain boundaries and gaps in pressed pellets can contribute to higher bulk resistances. In contrast, single crystal measurements are often more consistent and also enable the investigation of anisotropic conductivity.

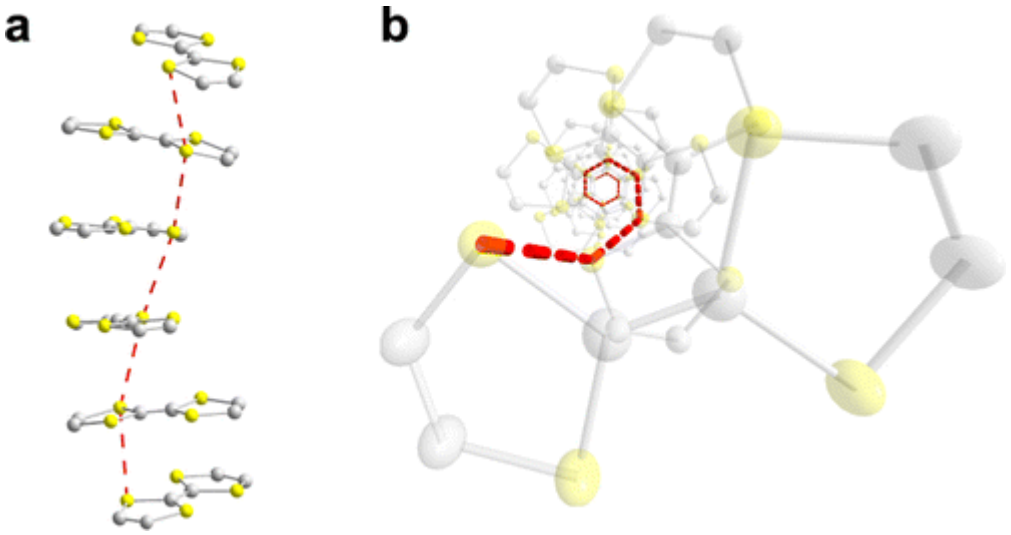

Figure 1-7: A view on the helical TTF stack, showing the shortest intermolecular S···S contacts (dashed red line),(a) along the ab plane, and (b) down the c-axis. In yellow: S atoms, in grey: C atoms.[103] (https://pubs.acs.org/doi/10.1021/ja512437u).

Su *et al.* synthesized an isostructural family of lanthanoid-based MOFs with the linker H_4TTFTB and the metal ions Ln = Tb^{III}, Dy^{III}, Ho^{III} and Er^{III}.[105] The obtained MOFs, $[Ln_2(TTFTB)_{1.5}(H_2O)_3]\cdot 3DMF\cdot 13H_2O$, crystallize in the triclinic space group *P*1. While the sorption behavior of the MOFs was not measured, partial oxidation of the TTF units to $TTF^{\cdot+}$, was achieved upon treatment with I_2, while I_3^- was incorporated into the pores during the process. Electrical conductivity values of the four MOFs were in the range of 1 x 10^{-8} S/cm to 1 x 10^{-9} S/cm (two-point probe method, pellet, rt). Partial oxidation of the TTF units led to marginally improved conductivity values between 4 x 10^{-8} S/cm to 8 x 10^{-9} S/cm, apparently due to the formation of defect states in the crystal structure. The relatively low coductivity was attributed to the lack of a favorable electronic band structure, leading to poor electron transfer in the MOF.

Xie *et al* used the linker H_4TTFTB to synthesize three different lanthanum MOFs. In all three MOFs, 1D chains of TTFTB ligands, which are coordinated by 1D chains of La atoms, formed solvent-filled pore channels.[106] Solvent mixtures with higher ratios of (H_2O:DMF) seemed to favor the formation of phases with increased ligand π-π-interactions. The degree of π-π-stacking as well as the intermolecular S···S distance between TTF units are different in all three MOFs and responsible for their respective electrical conductivity values. In addition, all three La-MOFs show permanent microporosity with BET surface areas of 596 m^2 g^{-1}, 454 m^2 g^{-1} and 362 m^2 g^{-1}, respectively. The first MOF, La_4(HTTFTB)$_4$, crystallizes in an orthorhombic system. Adjacent TTFTB ligands stack along [100] and are oriented at about 90° to each other. The arrangement facilitates the π-π-stacking, while the steric repulsion between benzoate groups is diminished. The intermolecular S···S distances between TTF units are between 3.581 Å and 3.892 Å, leading to an average electrical conductivity of 2.5 x 10^{-6} S/cm (two-point probe method, pellet, rt). The second MOF, La(HTTFTB), crystallizes in a monoclinic system and comprises diamond-shaped channels. Adjacent dimers, consisting of two stacked nearly parallel TTFTB ligands, are organized in a slightly offset orientation. The decreased overlap and the resulting S···S distances in the range of 3.897 Å and 5.208 Å led to a conductivity value of 9 x 10^{-7} S/cm (two-contact probe method, pellet, rt). The third MOF, La_4(HTTFTB)$_3$, crystallizes in a trichlinic system and also contains diamond-shaped channels. Three ligands stack offset to each other, forming trimers. Between adjacent trimers there is a large gap, resulting in longer intermolecular S···S distances of 3.809 Å to 7.650 Å. The resulting decreased π-π-overlap hinders charge hopping processes, which results in lower conductivity values in the MOF La_4(HTTFTB)$_3$ (1 x 10^{-9} S/cm, two-contact probe method, pellet, rt). Moreover, EPR spectroscopy data, optical band gaps and activation energies indicate an extrinsic doping of the three MOFs, assuming hole-doping and the generation of $TTFTB^{\cdot+}$.

Castells-Gil *et al.* synthesized five isostructural lanthanoid-based MOFs, namely MUV-5(Ln) (MUV = materials of University of Valencia; Ln = Gd, Tb, Dy, Ho, Er), with the linker H_4TTFTB.[107] Two different structure types, MUV-5a and MUV-5b were obtained by an alternative synthetic procedure. While the formation of orthogonal TTF dimers or large intermolecular S···S distances often limited a good orbital overlap between TTF units in TTF-Ln MOFs, MUV-5(Ln) features parallel-arranged TTF units, exhibiting relatively short S···S distances. MUV-5a, [Ln_3(TTFTB)$_2$($OOCCH_3$)(OH)(H_2O)] 2.5H_2O, crystallizes in the monoclinic space group *P2/c*. The crystal structure consists of partially oxidized and parallel-arranged TTFTB linker motifs, which are connected by Ln^{3+}-based SBUs. A partial oxidation of the TTF units forming the radical state $TTF^{\cdot+}$ was confimed by electron paramagnetic resonance (EPR). Furthermore, two crystallographically independent Ln^{3+} ions are present in the cyrstal structure, which comprises different

coordination environments. Infinite SBUs chains are present along the *a*-axis and the two types of 1D micropores are filled with water and acetate anions. Nitrogen sorption analysis shows no gas uptake, whereas a CO_2 uptake of 65 cm^3 g^{-1} was measured, indicating permanent porosity. MUV-5b [Ln(HTTFTB)(H_2O] (CH_3COOH) crystallizes in the space group $P2_1/m$. It has only one independent Ln^{3+} ion and a dimeric Ln_2 SBU. Two types of 1D micropores are formed and filled with acetic acid. No sorption measurements were performed with MUV-5b. Electrical conductivity measurements of MUV-5a(Gd, Dy, Ho, Er and Tb) showed values between 2.0 x 10^{-7} S/cm and 1.5 x 10^{-5} S/cm (four-point probe method, pellet, rt), with the shortest S···S distances between adjacent TTF units of 3.73 Å to 3.61 Å. MUB-5b(Dy) showed an average electrical conductivity of 3.3 x 10^{-8} S/cm with a S···S distance of 4.05 Å to 5.04 Å. The conductivity is one order of magnitude lower than that of MUB-5a(Dy). The shorter S···S distances in MUV-5a cause a better orbital overlap, resulting in a better charge delocalization, in comparison to the longer ones in MUV-5b. In combination with the partially oxidized TTF units in MUV-5a, the charge transport is optimized.

Zhuo *et al.* exchanged dimethylammonium in the redox-active MOF (Me_2NH_2)[In^{III}(TTFTB)]·0.7 C_2H_5OH·DMF, by the cations $TTF^{\cdot+}$ and MV^{2+} (*N*,*N'*-dimethyl-*4*,*4'*-bipyridinium) *via* post-synthetic cation-exchange.[102] The pristine MOF framework is doubly interpenetrated and comprises two different voids. They are formed by octacoordinated [$In^{III}(COO)_4]^-$ nodes bridged by the TTF moieties of the organic linker. No sorption measurements of the MOFs are provided, however, one cavity is filled with the respective cation. The single crystal to single crystal transformation during the cation-exchange led to the two MOFs ($TTF^{\cdot+}$)[In^{III}(TTFTB)]·5DMF and (MV^{2+})$_{0.5}$[In^{III}(TTFTB)]·2DMF. They crystallize in the centrosymmetric space group *Cccm*. The measured electrical conductivity values (two-contact probe method, pellet, 293 K) were 1.04 x 10^{-9} S/cm for the pristine MOF and increased to 1.06 x 10^{-7} S/cm and 1.02 x 10^{-7} S/cm for the $TTF^{\cdot+}$ and MV^{2+} exchanged MOFs. EPR, IR and solid-state UV-vis-NIR spectra indicate the presence of $TTF^{\cdot+}$ moieties in ($TTF^{\cdot+}$)[In^{III}(TTFTB)]·5DMF, as well as the formation of mixed-valence states TTFTB/ MV^{2+} and $TTFTB^{\cdot+}$/ $MV^{\cdot+}$ in (MV^{2+})$_{0.5}$[In^{III}(TTFTB)]·2DMF. The authors attributed the enhanced conductivity to the induced mixed-valence states and the resulting partial electron transfer between these states. However, the distances between TTFTB linker and the $TTF^{\cdot+}$ and MV^{2+} cations are quite far, inhibiting the formation of extended stacks.

Xie *et al.* exchanged the TTFTB linker with the metallolinker nickel(II)bis(dibenzoateglyoximate) ($Ni(dbg)_2$) and synthesized the MOFs $Mn_2[Ni(dbg)_2]$, $Zn_2[Ni(dbg)_2]$ and $Cd_2[Ni(dbg)_2]$ with the same topology as the previously reportetd TTFTB-based MOF Zn_2TTFTB.[108] The MOFs contain 1D rhombic pores and helical linker stacks along the *c*-axis. The coordination envi-

ronement of the metal ions in the SBU is different in all MOFs and causes altered Ni···Ni distances. However, the 1D SBUs are composed of two crystallographically independent M^{2+} ions, coordinated by linker carboxylates and solvent atoms, forming a three-fold screw axis alsong the *c*-axis. The SBUs of $Cd_2[Ni(dbg)_2]$ are built of edge-sharing polyhedra, resulting in an intermediate Ni···Ni distance of 3.770 Å and an electrical conductivity value of 2.7 x 10^{-6} S/cm along the stacking direction (two-point probe method, single crystal, rt). The authors attributed the lower conductivity value of 2.0 x 10^{-7} S/cm (two-point probe method, single crystal, rt) of $Mn_2[Ni(dbg)_2]$ to the longer Ni···Ni distance of 3.812 Å, caused by the SBU containing five-coordinated Mn^{II} centers forming corner-sharing polyhedra. Moreover, in comparison to the TTFTB-based analogs, the conductivity values are 2-3 orders of magnitude lower.[103] The SBUs of $Zn_2[Ni(dbg)_2]$ are built of alternating tetrahedra and pseudo-octahedra that do not share any oxygen atoms. The Ni···Ni distance (3.703 Å) is the shortest in the series, but no single crystals could be obtained. Pressed pellets (two-point probe method, rt) gave low conductivity values in the range of < 10^{-10} S/cm for all three MOFs, which may be associated with the anisotropic charge transport pathway. However, UV-Vis spectroscopy revealed π-π* transitions between the linkers, as well as metal-to-ligand charge-transfer (MLCT), which the authors assumed to occur between Ni 3d orbitals and π* states of the linker. Moreover, this MOF series features permanent porosity with BET surface areas in the range of 543 to 486 m^2 g^{-1}.[108]

Zhang *et al.* constructed four new 3D MOFs based on tetrathiafulvalene tetracarboxylate (TTFTC) ligands, during a solvothermal synthesis between TTFTC–Me_4 tetramethyl ester and the alkali metal ions Na^I, K^I, Rb^I and Cs^{+I}.[109] Despite the fact that the four MOFs are not strictly isostructural, they all exhibit planar TTFTC ligands that are stacked along the *c*-axis. $[Na_4(TTFTC)(H_2O)_2]\cdot 0.5H_2O$) crystallized in an orthorhombic *Ibam* space group, featuring the smallest π-π-distance between TTF layers of $d_{\pi-\pi}$ = 3.39 Å, $d_{S\cdots S}$ = 3.73 Å. Notably, the MOF was formed in its oxidized form, comprising charge delocalized $TTFTC^{\cdot+}$ radical cations and mixed-valent $TTFTC^{0/\cdot+}$ ligands resulting in intervalence charge transfer (IVCT), which was confirmed by ESR and DRS measurements. The potassium derivative ($[K_4(TTFTC)(H_2O)_2]\cdot 2H_2O$) crystallized in a monoclinic $P2_1/c$ space group. Here, the distances between TTF units are $d_{\pi-\pi}$ = 3.67 Å, $d_{S\cdots S}$ = 3.79 Å.

The Rb derivative ($[Rb_4(TTFTC)(H_2O)_3]\cdot H_2O$) crystallized in an orthorhombic *Pbcn* space group, exhibiting a TTFTC ligand stacking distance of $d_{\pi-\pi}$ = 3.67 Å with $d_{S\cdots S}$ = 3.82 Å. In contrast to the Na and K-MOF, the Rb-MOF has practically neutral ligands. Only after exposure to air for a few days, aerobically oxidized $TTFTC^{\cdot+}$ ligands were formed. The Cs-MOF ($[Cs_4(TTFTC)(H_2O)_2]$) crystallized in an orthorhombic $Pna2_1$ space group, exhibiting the longest ligand distances of $d_{\pi-\pi}$ = 3.71 Å and $d_{S\cdots S}$ = 3.77 Å. Similar to the Rb-MOF, the ligands became

aerobically oxidized only after exposure to air for a few days. All MOFs do not show any porosity. However, all MOFs feature electrical conductivity values between $1.34 \cdot 10^{-7}$ S/cm for the Cs-MOF and $3.4 \cdot 10^{-5}$ S/cm (two-point probe method, pellet, rt, air) for the Na-MOF. This is in good accordance with the TTFTC-TTFTC ligand distances and the $TTFTC^{\cdot+}$ radical cation concentration. The Na-MOF has the best π-surface overlap and is saturated with $TTFTC^{\cdot+}$ radical cations, which enable through-space charge delocalization *via* TTFTC/ $TTFTC^{\cdot+}$ IVCT. In case of the K-MOF and Rb-MOF, the electrical conductivity slightly increased after longer exposure to air, due to the formation of $TTFTC^{\cdot+}$ radical cations. However, as stated by the authors, the differences in the coordination environments between the four MOFs can also contribute to the different electrical conductivity values.

1.3.2.4 Tetracyanoquinodimethane (TCNQ) based ligands

Several conducting coordination polymers were reported with TCNQ serving as the key ligand.

The coordination polymer Cu(TCNQ) can be synthesized in two polymorphs. Phase 1 consists of distorted tetrahedra with one copper atom coordinated by four TCNQ molecules. Neighboring TCNQ molecules are rotated at a 90° angle to each other. The closest π-stacking distance between TCNQ molecules is 3.24 Å. The copper atoms in phase 2 have a nearly tetrahedral geometry with coplanar TCNQ molecules oriented in perpendicular planes. As a consequence, no π-stacking is possible.[110,111] Electrical conductivity values (two-point probe method, pellet, rt) of 2.5 x 10^{-1} S/cm of phase 1 and of 1.3 x 10^{-5} S/cm of phase 2 illustrating this difference were reported by Heintz *et al.*[110] In another study by Fernandez *et al.*, electrical conductivity values (metal/film/metal sandwich structure measurement, film, rt) of 4.8 x 10^{-3} S/cm for phase 1 and of 5.8 x 10^{-7} S/cm for phase 2 were measured.[111] The conductivity differences between the two phases were attributed to the different TCNQ distances and the resulting π-π-stacking of parallel TCNQ molecules in phase 1. Moreover, interactions beetween the *d* orbitals of copper atoms with the *sp* orbitals of the cyano group in TCNQ molecules were stated as reason for the relatively high conductivity of phase 1.[111] A similar arrangement of the TCNQ radicals in phase 1 can be found in phase 1 of Tl(TCNQ), but with alternating distances of 3.16 - 3.35Å between TCNQ molecules. It shows an electrical conductivity of 2.4 x 10^{-4} S/cm (method not stated, pellet, 300 K).[112] The TCNQ stacks, which are oriented parallel to each other in the coordination polymer Tl(TCNQ (phase 2), feature a distance of 3.22 Å between adjacent TCNQ molecules and show a slightly higher electrical conductivity of 5.4 x 10^{-1} S/cm (method not stated, pellet, rt)[112] Similar conductivity values in the range of 10^{-4} S/cm to 10^{-5} S/cm are observed in the analogs with the metal ions Na^{I}, K^{I}, Rb^{I} and Ag^{I}.[113–116]

Wang *et al.* combined the electron donor $TTF(py)_4$ with the electron acceptor TCNQ, in form of Li(TCNQ) or H_2(TCNQ), as organic building blocks, to build six isostructural MOFs with Zn^{II} and Cd^{II} ions in a monoclinic crystal system.[117] In the MOF frameworks, TCNQ units were part of the skeleton, as well as intercalated in the pores. $[M(TTF(py)_4(TCNQ^{\cdot-})_{0.5}](TCNQ^{\cdot-})_{0.5}(NO_3)\cdot 2CH_3OH/CH_2Cl_2$ M-**1**) (M = Zn, Cd) exhibited electrical conductivity values of 2.48 x 10^{-8} S/cm and 2.63 x 10^{-8} S/cm, respectively (two-point probe method, pellet, 298 K). $[Cd(TTF(py)_4)(TCNQ^{2-})_{0.5}](NO_3)\cdot CH_3OH$ and $[Cd(TTF(py)_4)(TCNQ^{2-})_{0.5}](TCNQ^{\cdot-})_{0.5}(NO_3)_{0.5}\cdot CH_2Cl_2\cdot 0.5\ CH_3OH$, which were synthesized in air, in comparison to the other reactions under N_2, showed conductivity values of 1.05 x 10^{-8} S/cm and 4.77 x 10^{-8} S/cm (two-point probe method, pellet, 298 K). The rather low conductivity was attributed to the lack of long-range charge delocalization, due to the long distance between TTF and TCNQ molecules, combined with their orthogonal alignment. Treatment of Cd-**1** with I_2 led to the replacement of $TCNQ^{\cdot-}$ by I_3^- in the pores. It caused an increase of the electrical conductivity to 2.16 x 10^{-7} S/cm (two-point probe method, pellet, 298 K).

1.3.2.5 Triphenylene based ligands

Possible ligating groups of triphenylene motifs are hydroxyl-, amino-, or thiol groups. The metal-catecholate M-CAT-1 series is a prominent group of 2D MOFs, based on the conjugated tricatecholate ligand 2,3,6,7,10,11-hexahydroxytriphenylene (HHTP) and the square-planar coordinated metal ions Ni^{II}, Co^{II} and Cu^{II}.[118] The MOFs form a layered structure with hexagonally shaped pores. Triphenylene-based 2D MOFs often feature high electrical conductivities of up to 40 S/cm for $Ni_3(HITP)_2$ (HITP = 2,3,6,7,10,11-hexaiminotriphenylene) (two-point probe method, thin film, rt).[118,119] Triphenylene ligands can engage in π-π stacking, they offer redox activity to form semiquinoid radicals, and they may generate strong π-*d* conjugation of the ligand with the metal ions.[118]

On the other hand, first examples of triphenylene-based 3D MOFs have recently been reported. Skorupskii *et al.* synthesized four isostructural lanthanide 3D MOFs with HHTP, namely $Ln_{1+x}HHTP(H_2O)_n$ (x = 0 to 2, Ln = La, Nd, Ho, Yb) (LnHHTP) featuring remarkable electrical conductivity values of up to 0.05 S/cm (two-point probe method, pellet, rt).[120] A honeycomb-like 2D net of HHTP ligands bound by Ln^{III} is formed, simular to the 2D transition-metal analogs. However, the Ln^{III} ions also connect the 2D sheets with each other by lying in-between the planes, resulting in a 3D MOF (Figure 1-8 b,c). The Ln^{III} ions are seven-fold connected by ligands and water molecules, forming infinite chains along the *c*-axis. Furthermore, all MHHTP MOFs feature permanent porosity with BET surface areas in the range of 208 to 452 $m^2\ g^{-1}$. Depending on the ionic radius of the lanthanides, different interlayer stacking distances between the 2D sheets were

obsereved, with 3.068 Å in LaHHTP and the smallest distance of 3.002 Å in YbHHTP. It was assumed that the π-π stacking of the ligands could promote charge transport along the *c*-axis. The smaller lanthanides also affected the optical band gaps, by narrowing the gap from 0.85 eV for LaHHTP to 0.73 eV for YbHHTP. The electrical conductivity (two-point probe method, pellet, 302 K) showed smaller values for LaHHTP (8.2 x 10^{-4} S/cm) and NdHHTP (8.0 x 10^{-4} S/cm) and higher values for HoHHTP (0.053 S/cm) and YbHHTP (0.01 S/cm). The latter two featured smaller organic interlayer distances, simplifying the charge transport. However, the higher electrical conductivity of HoHHTP in comparison to YbHHTP, with Yb having a smaller ionic radius than Ho, was not explained yet. The conductivity values show again the great impact of the metal ions on the electrical conductivity of the MOFs. Variable-temperature conductivity measurements gave activation energies of about 0.25 eV in all four MOFs.[120]

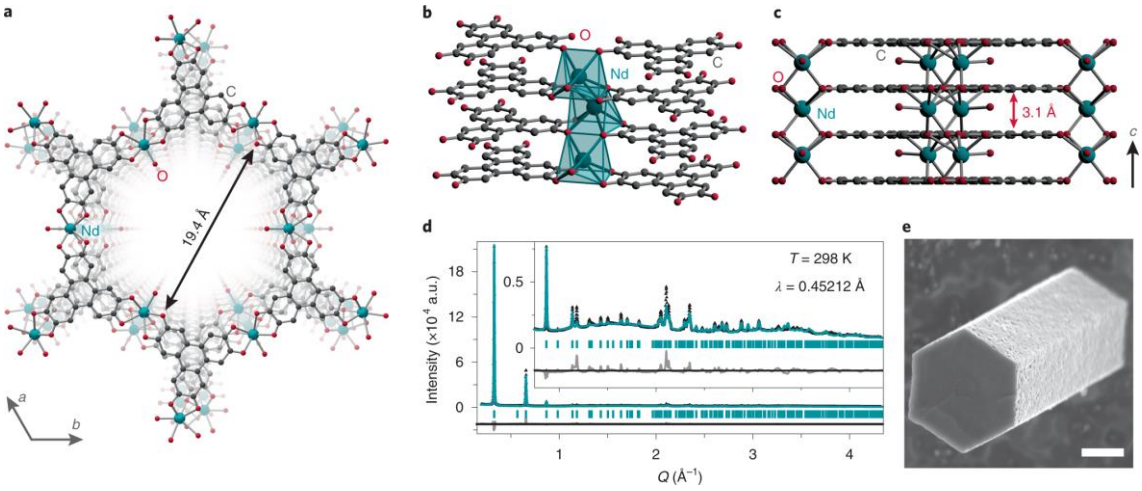

Figure 1-8: Crystal structure of NdHHTP (a) with view along the *c*-axis, (b) showing the metal-ligand connectivity, and (c) displaying the layer stacking. Hydrogen atoms are omitted for clarity. (d) Rietveld refinement of the NdHHTP structure to synchrotron PXRD data. Experimental data are shown as black triangles, the model fit in teal and the difference curve in grey. The tick marks denote the calculated peak positions. Fit statistics were $R_p = 5.80\%$, $R_{wp} = 7.74\%$ and GoF = 3.73. Triangle sizes are commensurate with error bars from standard deviations. (e) SEM image of a NdHHTP crystal. Scale bar, 1 µm. Reprinted by permission from [Springer nature Customer Service Centre GmbH]: [Springer Nature] [Nature Chemistry] [Efficient and tunable one-dimensional charge transport in layered lanthanide metal–organic frameworks, Grigorii Skorupskii *et al.*), [Copyright 2019].[120]

The reaction of HOTP (2,3,6,7,10,11-hexaoxytriphenylene) with the rare-earth metal ions yttrium, europium and lanthanum led to the formation of the 3D MOFs $[M_6\text{-}\mu_6\text{-}NO_3](HOTP)_2]^{5+}$ (M_6HOTP_2, M = Y, Eu, La), which crystallize in the cubic space group $Fd\bar{3}m$.[121] However, no phase pure La_6HOTP_2 crystallites could be obtained. The SBU, which are composed of six metal ions, six catecholate groups and one bridging nitrate ion, are connected into tetrahedral cages by HOTP ligands. The tetrahedral cages are linked at the vertices to build a *spn* topology. Y_6HOTP_2,

used as representative, featured permanent porosity with a BET surface area of 780 m^2 g^{-1}. However, storage under air of M_6HOTP_2 led to complete amorphization. On the other hand, storage over weeks or heating, both under inert conditions, maintained the crystallinity. In combination, a crystal colour change from yellow to darker bluish was observed, indicating (partial) oxidation of catechol moieties in $HOTP^{6-}$ to semiquinones, forming free charge carriers. The colour change was detected by in-situ UV-Vis spectroscopy, indicating a decrease of MLCT and of π-π* transitions within the catechol moieties. The rising of an absorption band at 1000 – 1200 nm was attributed to π-π* transitions in radical semiquinoid moieties, confirming the oxidation process. Electrical conductivity measurements of the partially oxidized samples (two-point probe method, pellet, 302 K) gave values of 2 x 10^{-5} S/cm for Y_6HOTP_2 and about 1.5 x 10^{-5} S/cm for Eu_6HOTP_2.[121]

Mähringer *et al*. synthesized a cubic 3D MOF with $Fe(BF_4)_2 \cdot 6H_2O$ and HHTP as precursors (see Figure 1-9).[122] In comparison to the 2D structure of the MCAT-1 (M = Ni, Co, Cu) series, the resulting FeCAT-1 MOF crystallizes in a 3D structure with the space group *F32*. It forms a diamond topology with supertetrahedral HHTP units and Fe^{III} ions. An iron-oxo cluster interconnects four triphenylene units, which build the facets of the tetrahedra. ^{57}Fe Mössbauer, SQUID, XPS and EPR measurements confirm high-spin Fe^{III} as only iron species, excluding a mixed valency state. FeCAT-1 MOF is a pitch-black and microporous material featuring a BET surface area of 1400 m^2 g^{-1}. Electrical conductivity measurements gave values of 5.6 x 10^{-3} S/cm (van der Pauw method, pellet, rt) and 1.1 x 10^{-4} S/cm (two-point probe method, pellet, rt). Quantum mechanical calculations determined a continuous electron transport path through the lattice via the iron centers and the connecting ligands. In contrast, no continuous hole transport path could be determined, confirming an electron conductor material.

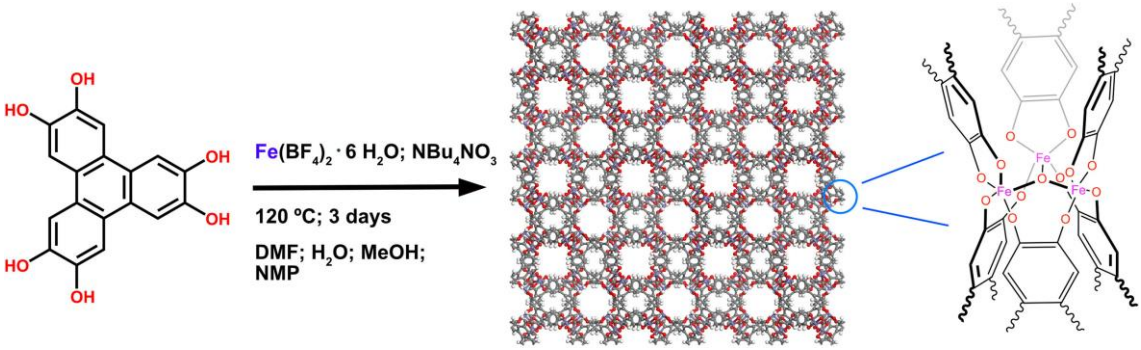

Figure 1-9: Synthesis scheme of 2,3,6,7,10,11-hexahydroxytriphenylene and an Fe^{II} precursor yielding FeCAT-1 MOF. The reaction was conducted under solvothermal synthesis conditions. FeCAT-1 MOF shows a cubic porous structure with iron oxo clusters bridging the triphenylene building blocks.[122]

Yadav *et al*. created a 3D MOF with the π-acidic *N*-heteroaromatic ligand 1,4,5,8,9,12-hexaazatriphenylene-2,3,6,7,10,11-hexacarbonitrile (HATHCN) and AgOTf.[123] The formed MOF

$[Ag_2(HATHCN)(CF_3SO_3)_2]_n$ crystallizes in the tetragonal space group $I\bar{4}2d$, featuring an electrical conductivity of 5 x 10^{-4} S/cm (two-point probe method, pellet, 297 K). Planar HATHCN molecules built π-stacks with an interlayer distance of 3.18 Å in an offset arrangement. DFT calculations predicted an overlap between $Ag^I(4p)$ and ligand($2p$) orbitals, indicating a facile charge movement along the staircase-like $[Ag^I\text{-HATHCN-}]_\infty$ chains. Moreover, anion-π-interactions between one HATHCN ligand and four Ag^+-bound TfO^- anions as well as a possible Ag^I/HATHCN MLCT led to the presence of $HATHCN^{\cdot-}$ radical anions, enhancing the electron density. This was confirmed by EPR analysis. However, sorption analysis showed a BET surface area of only 11.42 m^2/g, rendering $[Ag_2(HATHCN)(CF_3SO_3)_2]_n$ a nonporous coordination polymer rather than a MOF.

1.3.2.6 Hexaaminobenzene based ligand

Hexaaminobenzene (HAB) is an often-used organic ligand for the construction of electrically conductive 2D MOFs, with reported conductivities of up to 13 S/cm (van der Pauw method, pellet, 300 K)[124,125,126]. The 2D framework is formed together with d^8 and d^9 metal species like Ni^{II}, Co^{II} and Cu^{II}. Park *et al.* used the d^{10} metal ion Zn^{II} to create a 3D MOF with the ligand HAB.[76] Here, the metal ion adopts a tetrahedral geometry, in contrast to the square-planar geometry in the 2D frameworks. The synthesized microporous 3D MOF, named Zn-HAB, crystallizes in a body-centered tetragonal unit cell, exhibiting the space group $I4_122$. Furthermore, it shows a BET surface area of 145 m^2/g. However, the decrease of the BET surface area after activation at 80°C suggests a structural collapse at higher temperatures. Electrical conductivity measurements (four-point probe method, pellet, r.t., vacuum) gave a value of 8.6 x 10^{-4} S/cm. Moreover, Zn-HAB shows semiconducting behavior with a thermal activation energy of 170 meV for charge transport. In the measured range of 195 – 210 K, Zn-HAB exhibited a Seebeck coefficient of 195 – 220 μV/K. It is the first reported thermolelectric 3D MOF without added dopants. Moreover, the large Seebeck coefficient points toward a dominant hole charge transport in the MOF.

1.3.2.7 Phosphonate ligands

Phosphonate-based MOFs have been investigated much less than those with other ligands, but they show high thermal and chemical stability due to the strong ionic bonds between negatively (-2) charged phosphonates and, for example, divalent metal ions.[127,128,129] With their three oxygen groups, which are suitable for different metal-binding modes, phosphonate MOFs feature a high structural diversity leading to diverse 1D and 2D inorganic building units (IBU). [128,130] The 2D IBUs form pillared-layered networks featuring M-O-P polyhedra. The aromatic units in phophonate MOFs support electron hopping, while the M-O-P polyhedra can extend the conjugation.[128,129,134]

Bulut *et al.* synthesized the metal-organophosphonate MOF [{Cu_2(4,4'-bpy)$_{0.5}$}(1,4-NDPA)] with 1,4-naphtalenediphosphonic acid (1,4-NDPA-H_4), namely TUB75 (TUB = Technische Universität Berlin).[131] The SBU consists of zigzag, antiferromagnetically coupled copper dimer (Cu-O-P-O) chains. Copper is coordinated in a distorted octahedral environment in the SBU featuring three different Cu-Cu distances. The SBU is coordinated by 4,4'-bpy and 1,4-naphtalenediphosphonic acid ligands, forming rectangular voids due to the nearly 90° angle between the ligands.[130,131] The full deprotonation of the 1,4-naphtalenediphosphonic acid ligands causes electron delocalization in the SBU, according to electronic population analyses. Furthermore, TUB75 has a surface area of 132.1 m^2g^{-1}, which was predicted by Monte Carlo simulations. The MOF exhibits an indirect band gap of 1.4 eV. In a later study, Siemensmeyer *et al.*[130] measured the resistance of TUB75 by fixing the flat side of MOF crystals in between the circular gold surfaces of a relay. It yielded a remarkable maximum conductivity of 10 S/cm and a lowest value of 10^{-5} S/cm (single crystal, rt), depending on the orientation of the crystals, which was not explained in more detail.[130]

Another conductive phosphonate MOF was reported by Bulut *et al.*,[132] and further characterized by Peeples *et al.*.[128] [{Cu(H_2O)}(2,6-NDPA)$_{0.5}$] (NDPA = naphtalenediphosphonic acid), short TUB40, forms a 3D pillared-layered MOF structure with 2D SBUss connected via the aromatic 2,6-NDPA ligands. The 2D SBUs are built by corner-sharing polyhedra, including copper and phosphonate (Figure 1-10 a). The copper atoms are antiferromagnetically coupled, as demonstrated by DFT calculations and magnetization measurements. TUB40 exhibits an indirect band gap of 1.42 eV and the water-free TUB40 has an estimated helium-accessible pore volume of 0.032 cm^3/g (7% v/v void fraction), obtained via a Monte Carlo simulation. However, no experimental data are available here. Electrical conductivity measurements were performed on single crystals lying between two gold surfaces of a relay, giving an average value of 2 S/cm and a record value of 10 S/cm (impedance spectroscopy, single crystal, rt), making it one of the most conductive 3D MOFs reported in the literature. Impedance spectroscopy measurements on pelletized TUB40 under a mechanical load of 1 MPa, gave a value of 1.42 S/cm (impedance spectroscopy, pellet, rt.)[128] The electrical conductivity was attributed to the excitation between the HOMO on the naphtalene building units and the LUMO located on the Cu^{II} ions.[128]

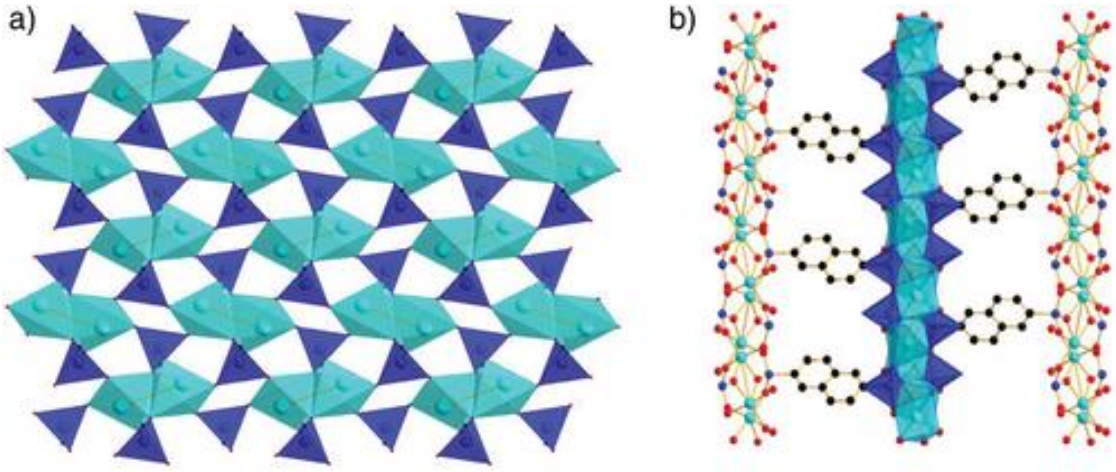

Figure 1-10: (a) View of TUB40's 2D copper phosphonate IBU composed of edge-sharing Cu-O-P-O-Cu-O-P-O polyhedra. (b) Crystal structure of the 3D pillared-layered network of TUB40.[128]

Zorlu *et al.* synthesized a zinc-phosphonate MOF, [Zn(Cu-*p*-H_4TPPA)]^2, known as GTUB3, with two charge balancing $(CH_3)_2NH_2^+$ ions in the pores and a Cu(II) ion in the square planar pyrrole ring of the *p*-H_8TPPA (5,10,15,20-tetrakis [*p*-phenylphosphonic acid])porphyrin) core.[133] Each tetrahedral zinc atom is coordinated to a mono-deprotonated phosphonic acid, which is part of the Cu-*p*-HyTPPA^{4-} ligand, resulting in ZnO_4 SBUs. GTUB3 has a predicted nitrogen accessible geometric surface area of 571 $m^2\ g^{-1}$. However, no experimental analyses were performed. Electrical conductivity measurements were carried out with a two-electrode jig system during impedance spectroscopy, giving a minimum conductivity value of 3 x 10^{-4} S/cm (randomly oriented crystals on a surface, rt). Single crystal DC measurements under an optical microscope yielded an average resistance of 200 Ω, resulting in an average non-directional electrical conductivity of 0.04 S/cm. The sp^2 hybridization of the phenylphosphonic acid around the porphyrin cores leads to an extended conjugation through the MOF lattice. It was postulated that the π-π-stacking distance of 4.2 Å between the planar porphyrin units possibly enables some electron hopping, hence acting as charge transport pathway.

Peplees *et al.* synthesized the MOF $Cu_3(H_5\text{-MTPPA})_2$ (H_8-MTPPA = methane tetra-p-phenylphosphonic acid), named TUB1 (TUB = Technische Universität Berlin).[134] It is constructed of 1D IBUs, which are composed of corner-sharing eight-membered ((Cu1-O-P-O-Cu1-O-P-O and Cu2-O-P-O-Cu2-O-P-O rings containing Cu^{II} ions in square-planar and distorted trigonal bipyramidal coordination environments. The IBUs are bridged by tri-deprotonated H_5-MTPPA^{3-} ligands. TUB1 exhibits a predicted BET surface area of 766 m^2/ g (calculated with Monte Carlo simulations), as well as an indirect band gap of 2.4 eV and a direct band gap of 2.7 eV. The electrical conductivity was determinded by measuring the resistance of a single crystal, without directional selectivity that was fixed between two gold surfaces of a relay resulting in high values between 0.3 and 0.75 S/cm (2-point probe setup, single-crystal, rt). DFT calculations suggest that

the square planar copper atoms promote the electrical conductivity by reducing the HOMO-LUMO gap.

1.3.2.8 Chiral ligand

Huizi-Rayo *et al.* synthesized an enantiopure 3D MOF Dy-L with the formula {($Dy_2(\mu_4\text{-tar})_2(\mu\text{-tar})(H_2O)_2]\cdot 3\ H_2O\}_n$), performing as electron spin filtering material at room temperature.[135]

Dy-L is built from Dy(III) and *L*-tartrate ligands, crystallizing in the nonenantiogenic triclinic *P*1 space group. The crystals exhibit microchannels filled by crystal water. However, the porosity was not confirmed by sorption measurements. Furthermore, the crystals consist as highly anisotropic multihelical system, where the helices are oriented in different crystallographic directions.

Electrical conductivity values were obtained *via* current-voltage (*I*-*V*) measurements on a drop-cast film of MOF crystals on an ITO substrate. For the measurement, a current of nonpolarized electrons was inserted *via* a nonmagnetized conducting Co/Cr tip of an AFM setup at room temperature. Afterwards, an electric bias was applied between the tip and the MOF-ITO substrate. The tip could also be magnetized in a predefined orientation with an external permanent magnet. As a consequence, the spin of the electrons that were injected into the MOF could be controlled. On the tip-, the magnetic dipoles were oriented arbitrarily south and on the tip+, arbitrarily north. The magnetization of the tip influenced the electrical conductivity of the MOF. With the nonmagnetized tip, an electrical conductivity of 6.45 x 10^{-9} S/cm was measured. With tip-, a value of 2.2 x 10^{-10} S/cm and with tip+ a value of 2.9 x 10^{-7} S/cm was measured, with an *I*-*V* curve showing a clear S-shape behavior. The spin-polarized charge transport in the MOF proved the existence of polarized currents. The spin polarization reached almost 100 % at room temperature (± 10 V bias range) coming from the CISS effect, which is an enantiospecific conduction of electrons with spin selectivity.

1.3.3 MOFs based on the MOF-74 topology

In the past years, structures based on the MOF-74 topology were introduced as electrically conductive MOF platform.[24,45,136] The electrical conductivity of [M_2(DOBDC)$(DMF)_2$] (M = Zn^{2+}, Mg^{II}, Mn^{II}, Co^{II}, Ni^{II}, Cu^{II}, $DOBDC^{4-}$ = 2,5-dioxido-1,4-benzenedicarboxylate) shows values in the range of 10^{-12} S/cm to 10^{-14} S/cm (two-point probe method, pellet, 300 K).[45,136,137] In order to overcome the energy mismatch between the orbitals of the hard metal ions and the hard oxygen atoms and to facilitate charge transfer, Sun *et al.* replaced the phenol groups of the H_4DOBDC linker by thiophenol groups, leading to 2.5-disulfhydrylterephthalic acid (H_4DSBDC).[44] In the resulting Mn_2(DOBDC) analog, [Mn_2(DSBDC)$(DMF)_2$]·0.2 DMF, carboxylate and thiophenoxide groups of the ligands are connected to Mn^{II} chains and build hexagonal pores with a diameter

of about 16 Å. In contrast to M_2(DOBDC), the sulfur analog contains two crystallographically independent Mn^{2+} ions. Whereas one Mn^{2+} ion is coordinated by four carboxylate oxygen atoms and two thiophenoxide groups, the other one is coordinated by two carboxylate oxygen atoms, two phenoxide groups and two DMF molecules (Figure 1-11). The sulfur atoms on both crystallographic Mn sites coordinate with the same d orbital of Mn. This symmetry overlap is an important prerequisite for charge delocalization along the $(\text{-M-S-})_\infty$ chain. The Mn-S distances are 2.493 Å and 2.632 Å, respectively, with the sulfur atoms oriented trans to each other. Sorption measurements of Mn_2(DSBDC) confirmed permanent porosity upon solvent exchange with methanol followed by activation, and gave a BET surface area of 978 m^2/g. Moreover, a charge carrier mobility of 0.01 $cm^2V^{-1}s^{-1}$ was measured for the activated sample by flash-photolysis time-resolved microwave conductivity measurements (FP-TRMC). Furthermore, electrical conductivity measurements of $[Mn_2(DOBDC)(DMF)_2]\cdot x$(DMF) and $[Mn_2(DSBDC)(DMF)_2]\cdot x$(DMF) (two-point probe method, pellet, 297 K) gave values of 3.9 x 10^{-13} S/cm and 2.5 x 10^{-12} S/cm, respectively.[45] The increase of the electrical conductivity of the sulfur analog by one order of magnitude suggests the formation of more favorable intrachain charge transfer in the $(\text{-M-S-})_\infty$ chains. Removal of mobile DMF guest molecules from the pores upon soaking in DCM followed by activation at 100°C under vacuum resulted in remaining DMF molecules coordinated to Mn ions. As a result, slightly lower conductivity values of 3.0 x 10^{-13} S/cm for $Mn_2(DOBDC)(DMF)_2$ and 1.2 x 10^{-12} S/cm for $Mn_2(DSBDC)(DMF)_2$ were observed.[45] The authors suggested the formation of grain boundaries or defects during activation as reason for the decreased conductivity.

Exchange of the Mn^{2+} ions with Fe^{2+} in $[Mn_2(DSBDC)(DMF)_2]\cdot x$(DMF) led to the formation of $[Fe_2(DSBDC)(DMF)_2]\cdot x$(DMF), which is isostructural to $[Mn_2/Fe_2(DOBDC)(DMF)_2]$.[45] $[Fe_2(DSBDC)(DMF)_2]\cdot x$(DMF) features the coordination of three carboxylate groups, two trans thiophenoxide groups and one DMF molecule to one Fe ion (Figure 1-11). The Fe-S bond lengths are 2.444 Å and 2.446 Å and the sulfur atoms on both crystallographip Fe sites interact with the same d orbital of Fe^{II}, simular to the Mn_2(DSBDC) analog. In contrast to Mn_2(DSBDC), Fe_2(DSBDC) has only one crystallographically independent Fe^{II} ion. Removal of loosely bound DMF molecules in the pores yielded a reversibly distorted structure of $Fe_2(DSBDC)(DMF)_2$. Apparently due to the distortion, a lower BET surface area of 54 m^2/g was obtained. Electrical conductivity measurements (two-point probe method, pellet, at 297 K, N_2) gave values of 3.2 x 10^{-7} S/cm and 3.9 x 10^{-6} S/cm for $[Fe_2(DOBDC)(DMF)_2]\cdot x$(DMF) and $[Fe_2(DSBDC)(DMF)_2]\cdot x$(DMF), respectively.[45] For activated samples of $Fe_2(DOBDC)(DMF)_2$ and $Fe_2(DSBDC)(DMF)_2$, again slightly lower values of 4.8 x 10^{-8} S/cm and 5.8 x 10^{-7} S/cm were

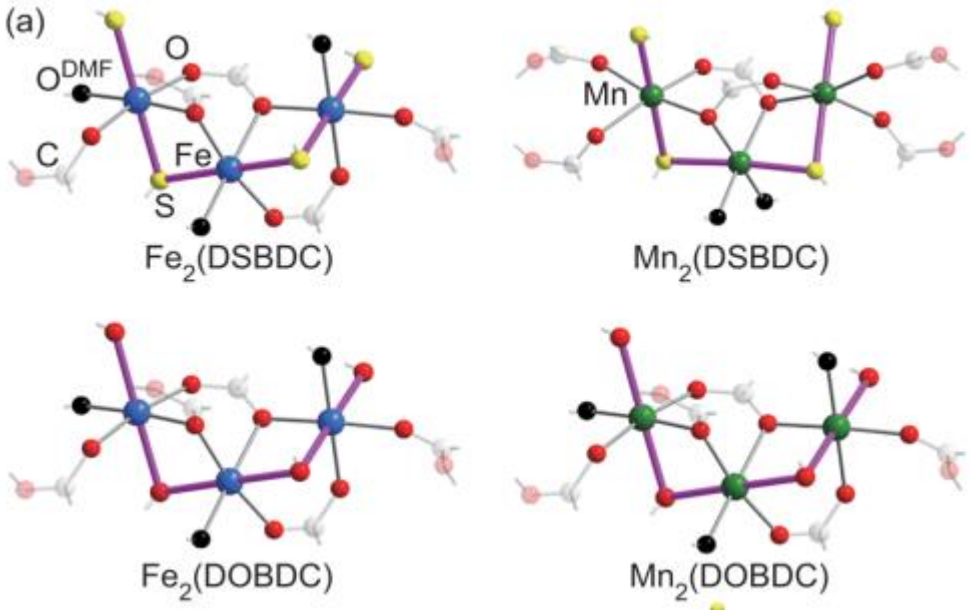

Figure 1-11: (a) Parts of the infinite secondary building units in $M_2(DEBDC)(DMF)_2 \cdot x(DMF)$ (M = Fe, Mn; E = S, O). The $(–M–E–)_\infty$ chains are represented in purple.[44] (https://pubs.acs.org/doi/abs/10.1021/jacs.5b02897.)

obtained. As described above, the conductivity increased by six orders of magnitude through the exchange of manganese with iron in both MOFs. The authors proposed the presence of electrons in the *β*-spin *d* band in d^6 Fe^{II} - in comparison to the empty one in d^5 high spin Mn^{II} - as reason for the higher conductivites in the Fe-based MOFs, because these electrons have low binding energies. Furthermore, the Fe-based MOFs have a lower conduction band, resulting in smaller band gaps, which suggest higher charge-carrier densities and higher conductivites. Moreover, the enhanced orbital overlap between Fe und S cause a lowered charge hopping barrier in $Fe_2(DSBDC)$ and facilitate charge transfer through $(-Fe-S-)_\infty$ chains. In addition, ^{57}Fe Mössbauer spectra revealed the presence of only high-spin Fe^{II}, excluding a potential oxidation to Fe^{III} in both Fe-based MOFs.[45] However, further EPR spectroscopy studies revealed the presence of high-spin Fe^{III}.[137] Due to the low reduction potential of the $Fe^{II/III}$ couple, adventitious oxidation of a few Fe^{II} centers is plausible. Exposure to air generated large amounts of Fe^{III} in $Fe_2(DSBDC)(DMF)_2$, which were detected in Mössbauer studies. In a following study, Sun *et al.* investigated the effect of coordinated DMF molecules in $Fe_2(DSBDC)$ on the electrical conductivity.[45] Soaking of $[Fe_2(DSBDC)(DMF)_2] \cdot x(DMF)$ in MeOH and afterwards in THF, followed by an activation under vacuum at 170°C, yielded solvent-free $Fe_2(DSBDC)$. The PXRD pattern confirmed the formation of the regular hexagonal lattice, but showed a distortion along the *c*-direction, as well as low crystallinity. The distortion was reversible by soaking the material in DMF/DCM. The BET surface area of the soaked and recovered materialof 624 m^2 g^{-1} is higher than that of the distorted $Fe_2(DSBDC)(DMF)_2$ sample. The measured electrical conductivity value of $Fe_2(DSBDC)$ (two-point probe method, pellet, 297 K, N_2) was 1.5 x 10^{-9} S/cm, two magnitudes

lower than that of $Fe_2(DSBDC)(DMF)_2$. While soaking $Fe_2(DSBDC)(DMF)_2$ in DMF recovered the previous conductivity (of $[Fe_2(DSBDC)(DMF)_2]\cdot x(DMF)$), this effect was not observed by soaking of $Fe_2(DSBDC)$ in DCM. However, the PXRD pattern of DCM-soaked material confirmed the recovery of the framework structure simular to $[Fe_2(DSBDC)(DMF)_2]\cdot x(DMF)$. DFT calculations showed a domination of Fe and S orbitals in the valence band and indicated a partial electron transfer from Fe to DMF. The holes created this way could act as charge carriers, improve the charge-carrier density in the MOF skeleton and thus enhance the electrical conductivity.

1.3.4 MOFs with mixed valence states

Recently, a drastically increased electrical conductivity of MOFs was achieved by the introduction of mixed-valency states. Manumpil *et al.* presented a Prussian blue analogue with the approximate formula $Co[VO(CN)_4]$.[138] It crystallizes in the cubic space group $Fm\bar{3}m$ and is colored dark blue in the dehydrated form. According to EPR spectroscopic data, the MOF contains high-spin Co^{II} as well as V^{IV} centers. Upon exposure of the MOF powder to a flow of water-saturated O_2 gas, the colour changed from blue to green. Partial oxidation of the V^{IV} centers to V^{V} produced a mixed-valence framework. After the exposure of the MOFs to an O_2 gas flow for 20 days, ICP-AES data and EPR spin quantification resulted in a V^{IV}/V^{V} ratio of 0.87/1. Electrical conductivity measurements of $Co[VO(CN)_4]$ gave values of $\sim 10^{-10}$ S/cm (van der Pauw method, pellet, 298 K, N_2). Upon oxidation of the V^{IV} centers, the conductivity increased up to 7.2×10^{-5} S/cm for the MOF with the V^{IV}/V^{V} ratio of 0.87/1. The conductivity could be further increased to 6.2×10^{-4} S/cm at 373 K. The increased electrical conductivity was attributed to IVCT transfer between V^{IV}/V^{V} centers (which was confirmed by UV-vis-near-IR spectroscopy), as well as thermally activated electron hopping. Moreover, N_2 adsorption measurements gave BET surface areas of 340 $m^2\ g^{-1}$ and 370 $m^2\ g^{-1}$, respectively, before and after oxidation, which confirms the retention of permanent porosity of the MOFs.

1.3.4.1 Iron-based MOFs

As already discussed for MOF-74(Fe), iron-based MOFs often exhibit significantly higher electrical conductivites in comparison to their MOF analogs with different metal ions. On the one hand, the loosely bound electrons in the β-spin *d* band in d^6 Fe^{II} cause higher charge densities. On the other hand, iron-based MOFs often exhibit a mixed valency $Fe^{III/II}$ system, due to the air sensitivity of Fe^{II}, which induces inter-valence charge transfer (IVCT). This can result in an improved charge-carrier mobility in the MOF.

Rieth *et al.* synthesized three isostructural mesoporous MOFs with the ligand bis(1H-1,2,3-triazolo[4,5-b], [4´5´-i])dibenzo-[1,4]dioxin (H_2BTDD).[139] The MOFs $M_2Cl_2(BTDD)(H_2O)_2$ (M =

Mn, Co, Ni), crystallize in the trigonal space group *R*3*m*. Each metal ion is connected with three nitrogen atoms of $BTDD^{2-}$ linkers, two chloride ligands and one water molecule, forming 1D SBUs chains. The SBUs are bridged by the triazolate linkers, forming a honeycomb like structure, with pores along the *c*-axis. BET surface areas in the range of 1762 to 1917 $m^2\ g^{-1}$ illustrate the high permanent porosity of these MOFs.[139] Sun *et al.* synthesized the isostructural $Fe_2Cl_2(BTDD)(DMF)_2$ and measured the electrical conductivity values of the whole $M_2Cl_2(BTDD)(DMF)_2$ series (two-contact probe method, pellet, 300 K, N_2).[137] $M_2Cl_2(BTDD)(DMF)_2$ (M = Mn, Co, Ni) gave values in the range of 3.7×10^{-13} S/cm to 1.3×10^{-14} S/cm, whereas $Fe_2Cl_2(BTDD)(DMF)_2$ gave a drastically higher value of 1.1×10^{-7} S/cm. ^{57}Fe Mössbauer spectroscopy revealed the presence of high-spin Fe^{II} centers. After exposure to air, over 70 % Fe^{III} was detected immediately, pointing to the air-sensitivity of the Fe^{II}-MOF. The authors suggest that, in comaparison to the other metal ions studied here, the valence electrons in high-spin Fe^{II} have the highest energy, due to the small Coulomb attraction between its nucleus and its valence electrons. DFT calculations revealed that Fe orbitals in $Fe_2Cl_2(BTDD)(DMF)_2$ dominated the VB, which raises the E_{VBM} and reduces the band gap, leading to the increased detected electrical conductivity.

Using 1*H*-1,2,3-triazolate as ligand, six isostructural MOFs, namely ($M(C_2N_3H_2)_2$, M = Mg, Zn, Mn, Fe, Co, Cu) were synthesized.[140,141] They crystallize in the cubic space group $Fd\bar{3}m$. The divalent metal ions coordinate to the nitrogen atoms of the triazolates, resulting in a near-octahedral coordination environment. Five metal centers form a tetrahedral SBU through the bridging of triazolate ions. The SBUs constitute the vertices of a diamond-type structure. Depending on the size of the metal ions, BET surface areas in the range of 370 m^2g^{-1} (for the Cu-MOF) to 890 m^2g^{-1} (for the Mn-MOF) were obtained.[141] Electrical conductivity measurements of $Fe(C_2N_3H_2)_2$ (four-point probe method, pellet, at 298 – 325 K, HV) gave a value of 7.7×10^{-5} S/cm. Doping of $Fe(C_2N_3H_2)_2$ with I_2 further enhanced the conductivity to 1.0×10^{-3} S/cm. The increased conductivity was attributed to the formation of a mixed valency Fe^{II}/Fe^{III} system, enabling intervalence charge transfer (IVCT) through the action of the oxidation agent I_2.[141] Sun *et. al*. measured the electrical conductivity values of ($M(C_2N_3H_2)_2$, M = Mg, Zn, Mn, Co, Cu, Fe, Cd) (two-point probe method, pellet, 300 K, N_2), which are in the range of 9.9×10^{-15} S/cm (Mg-MOF) to 1.4×10^{-13} S/cm (Cd-MOF), with the notable exception of the F-MOF.[137] The drastically higher conductivity of $Fe(C_2N_3H_2)_2$ (with a value of 3.0×10^{-6} S/cm), was lower in comparison to Gandara *et al.*.[137,141] However, the measurements of Sun *et al.* underscore the drastic effect of the metal ion iron on the electrical conductivity of the MOF. Quantum chemical calculations suggested that the Fe^{2+} centers in $Fe(C_2N_3H_2)_2$ are in the low-spin state, which does not enable them to provide high-energy charge carriers.[137] Instead, the authors suggested a $Fe^{III/II}$ mixed valency

state already present in the as-synthesized $Fe(C_2N_3H_2)_2$. ^{57}Fe Mössbauer spectroscopy showed isomer shifts that were assigned to either Fe^{III} or low-spin Fe^{II}. The isomer shifts were attributed to low-spin Fe^{II} based on the DFT calculations. However, broad signals in the EPR spectrum also hinted towards the presence of small amounts of high-spin Fe^{III} centers. Again, based on the assumption that low-spin Fe^{II} ions do not donate significant numbers of charge carriers, the authors suggested the presence of a mixed valence $Fe^{III/II}$ system in the Fe-MOF. The resulting inter-iron charge hopping processes were suggested to enhance the charge-carrier mobility and thereby increase the electrical conductivity.[137]

Wu *et al*. synthesized the three isostructural MOFs M-THBQ with the metals M = Fe, Co, Mn and the ligand tetrahydroxybenzoquinone (THBQ) from the respective precursor solutions in H_2O and diethylene glycol. The MOFs crystallize in the cubic space group $Pm\overline{3}$.[142] Regarding the example of Co-THBQ, each cubic cage-shaped cluster $Co_{12}(C_6O_6)_6(H_2O)_8$ comprises eight Co atoms with a distorted octahedral coordination geometry as well as four disordered Co^{2+} ions in the pores acting as charge-balancing counterions. Electrical conductivity measurements (four-point probe, pressed pellets, 300 K) gave values of 2.7 x 10^{-4} S/cm, 6 x 10^{-8} S/cm and 3.5 x 10^{-8} S/cm for Fe-THBQ, Co-THBQ and Mn-THBQ, respectively. An increase of the electrical conductivities was measured at 400 K, with the respective values of 2.7 x 10^{-3} S/cm, 5.4 x 10^{-6} S/cm and 3.7 x 10^{-6} S/cm. Moreover, activation energies, for conductivity as a function of temperature, of 0.23 eV, 0.46 eV and 0.48 eV were stated for Fe-THBQ, Co-THBQ and Mn-THBQ, respectively. Furthermore, an air-stable n-type Seebeck coefficient of -130 μVK^{-1} identified Fe-THBQ as an n-type semiconducting MOF. XPS measurements at room temperature confirmed Co^{II} and Mn^{II} as the only species present in Co-THBQ and Mn-THBQ. On the other hand, a mixed valence of Fe^{II} and Fe^{III} was indicated in Fe-THBQ. ^{57}Mössbauer spectroscopy confirmed the mixed Fe valence and detected two high-spin Fe^{II} states with 28.3 % at 77 K and 16.2 % at 300 K, as well as one high-spin Fe^{III} species with 71.7 % at 77 K and 83.8 % at 300 K. The Mössbauer spectra confirmed the mixed iron valency enabling an inter-iron electron hopping process, leading to increased charge-carrier mobility. In addition to the higher charge-carrier density and mobility of the mixed valency iron system, a further explanation for the higher conductivity of Fe-THBQ, in comparison to Co/Mn-THBQ, is the $3d^5$ electronic configuration of Fe^{III}, which could introduce mid-gap states, accelerating electrons, coupled with the formation of holes in the VB. Moreover, a through-space charge transport could also take place between neighboring parallel-stacked C_6O_6 rings.[142]

Chen *et al.* also synthesized the 3D MOF Fe-THBQ from a DMF/H_2O, tetrahydroxy-1,4-quinone (THQ) and iron(II)sulfate solution at 80°C.[75] It is a porous material with a BET surface area of 163 $m^2\ g^{-1}$. In contrast to the results of Wu *et al.* regarding Fe-HTBQ, no charge balancing ions

were detected in the pores. Electrical conductivity measurements were performed on pressed pellets and gave a value of about 3.3 x 10^{-3} S/cm (four-point probe method, pellet, 300 K, inert gas). An activation energy of 270 meV in the range of 240–340 K and of 150 meV in the range of 200 -240 K was interpreted as indication of a thermally-activated hopping process. After exposing the MOF to ambient air conditions for two weeks, the electrical conductivity decreased to 6.6 x 10^{-4} S/cm (four-point probe method, pellet, 300 K, air). XPS and ^{57}Fe Mössbauer measurements at 80 K confirmed a mixed valence state of high-spin Fe^{III} (68.2 %), high-spin Fe^{II} (28.5 %) and another Fe^{II} species (3.3 %). To achieve charge balancing, it is suggested that THQ also exhibits mixed valence states, leading to a dual mixed valence MOF. The slightly higher initial conductivity value of Fe-THBQ, in comparison to the results of Wu *et al.*,[142] could result from the handling under inert gas. In contrast, Wu *et al.*[142] did not state the ambient conditions. After two weeks of Fe-THBQ in air, some of the Fe^{II} ions were oxidized to Fe^{III}, leading to 85.9 % Fe^{III} in the MOF. Due to the increased ratio of Fe^{III}/Fe^{II}, the redox hopping process between the ions is apparently less efficient, leading to a decrease in electrical conductivity.

Park *et al*. synthesized the MOF $Fe(C_2N_3H_2)_2$, named $Fe(tri)_2$ (tri^- = 1,2,3-triazolate), previously reported by Gandara[141]and Sun[137] and partially oxidized Fe^{II} postsynthecially with different equivalents of thianthrenium tetrafluoroborate.[143] The obtained MOFs $Fe(tri)_2(BF_4)_x$, with x = 0.09, 0.22, 0.33, exhibited BET surface areas of 230, 70 and 50 $m^2\ g^{-1}$, respectively. $Fe(tri)_2(BF_4)_{0.33}$ showed nearly nonporous sorption behaviour, due to the stoichiometric filling of each pore in the framework with a single BF_4^- ion. The PXRD pattern of $Fe(tri)_2(BF_4)_{0.33}$ revealed the still-preserved parent framework structure. However, the Fe1-N1 distance of the iron ions at the corners of the tetrahedral pentanuclear SBUs decreased slightly, indicating a partial oxidation of low-spin Fe^{II} to Fe^{III}. On the other hand, the Fe2-N2 distance, of the crystallographyically distinct Fe iron in the center of the SBUs, hardly changed. Thus, the authors suggested a preferential oxidation of the corner Fe1-ions to form low spin Fe^{III}, which distorts the ideal octahedral coordination geometry. ^{57}Fe Mössbauer spectroscopy at 290 K confirmed the presence of pseudo-octahedral low-spin Fe^{II} as only species in $Fe(tri)_2$ when it was synthesized under completely oxygen-free conditions. The spectra of $Fe(tri)_2(BF_4)_x$ with x = 0.09, 0.22, 0.33 show an additional increasing absorption coming from low-spin Fe^{III} centers, with amounts of 16.2%, 50.8% and 66.67%, respectively (Figure 1-12). Electrical conductivity measurements (two-point probe method, pellet, 293 K) of pure $Fe(tri)_2$ gave values in the range of 7 x 10^{-9} S/cm to 1 x 10^{-10} S/cm. These values are much lower than the previously reported one of 7.7 x 10^{-5} S/cm of Gandara *et al*. for the nominally same MOF.[141]

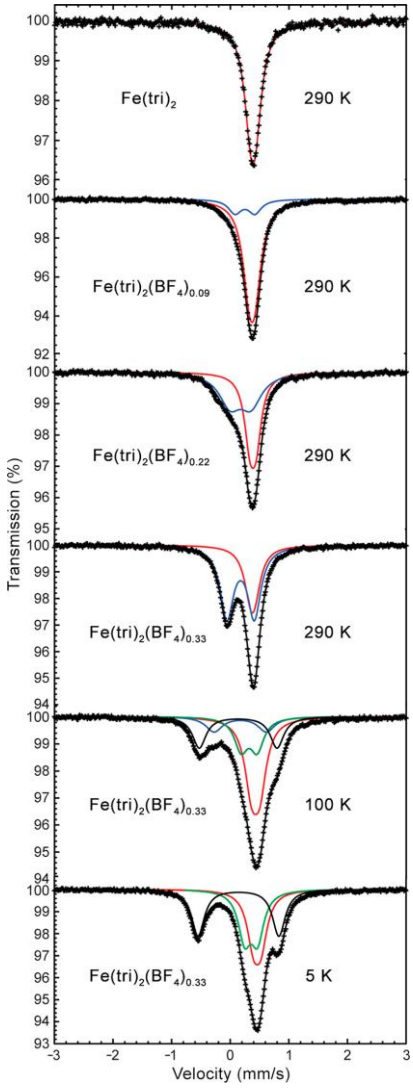

Figure 1-12: Mössbauer spectra of $Fe(tri)_2$ and $Fe(tri)_2(BF_4)_x$ obtained at the indicated temperatures. The component doublets correspond to low-spin iron(II) (red trace), valence-delocalized low-spin iron(II/III) (blue trace), localized low-spin iron(II) (green trace), and localized low-spin iron(III) (black trace). Reprinted (adapted) with permission.[143] Copyright {2018} American Chemical Society.

Thus Park *et al.* suggested that the samples of Gandera *et al.* suffered already partial oxidation of Fe^{II} in their MOF due to handling under air.[143]Strikingly, electrical conductivity values of 0.03, 0.2 and 0.3 S/cm were reported for the partially oxidized $Fe(tri)_2(BF_4)_x$ with x = 0.09, 0.22, 0.33, showing a remarkable conductivity enhancement by about eight orders of magnitude. UV-vis-NIR spectroscopy indicated an increasing intervalence charge transfer (IVCT), coupled with a decreasing metal-to-ligand charge transfer (MLCT) and an increasing oxidation level of iron ions. It was suggested that delocalization of the increasing charge-carrier density occured between octahedral low-spin Fe^{II} and Fe^{III}.

Building a MOF with dipyrazolate ligands, Aubrey *et al.* achieved an electrical conductivity enhancement of up to 0.025 S/cm by inducing a mixed valency state of Fe^{II}/Fe^{III}.[144] The MOF

$Fe_2(BDP)_3$ (BDP_2- = 1,4-benzenedipyrazolate) consists of 1D chains of μ^2-pyrazolate-bridged Fe^{III} octahedra extending parallel to the 001 direction. It features permanent porosity with triangular pores and a BET surface area of 1230 $m^2\ g^{-1}$. The low-spin Fe^{III} centers were partially reduced to high-spin Fe^{II} by potassium naphtalenide, resulting in $K_xFe_2(BDP)_3$ ($0 \leq x \leq 2$), featuring charge balancing cations inside the pores. This was confirmed by ^{57}Fe Mössbauer spectroscopy. Notably, $K_{1.1}Fe_2(BDP)_3$ still featured permanent porosity with a BET surface area of 430 $m^2\ g^{-1}$. Electrical conductivity values were measured by incorporating single microcrystals into FET devices by means of dropcasting the MOF crystals onto microelectrodes on a pre-patterned substrate. Electrical conductivity values of 3.5×10^{-7} (two-point probe method, single crystal, 293 K) and 9.6×10^{-3} S/cm (four-point probe, single crystal, 300 K) were measured for $Fe_2(BDP)_3$. After reducing about half of the Fe^{III} centers to Fe^{II}, which corresponds to the formula $K_{0.98}Fe_2(BDP)_3$, the conductivity increased to 0.025 S/cm (two-point probe method, single cyrstal, 293 K). Moreover, the charge mobility increased from 2×10^{-3} $cm^2V^{-1}s^{-1}$ for $Fe_2(BDP)_3$ to 0.84 $cm^2V^{-1}s^{-1}$ for $K_{0.98}Fe_2(BDP)_3$ (measured by flash-photolysis time-resolved microwave conductivity (FP-TRMC)). The lower conductivity of $Fe_2(BDP)_3$ measured with the two-contact probe device was attributed to contact resistances between crystals and electrodes – which would suggest that the conductivity of $K_{0.98}Fe_2(BDP)_3$ is underestimated because it could only be measured with the two-contact probe method. Band calculations (DFT) show a strong coupling between Fe-*dπ* and pyrazolate *π*-orbitals, indicating an anisotropic charge transfer *via* hopping along the 1D iron-pyrazolate chains.

Xie *et al*. used a similar method to achieve an increased electrical conductivity in an Fe^{II}-MOF by inducing mixed-valence $Fe^{II/III}$ states.[145] The MOF $Fe_2(H_{0.67}BDT)_3 \cdot 17H_2O \cdot 0.5(^iPrOH)$ (H_2BDT = 5,5´-(1,4-phenylene)bis(1*H*-tetrazole)), named $Fe_2(BDT)_3$, was synthesized in a solvothermal reaction of H_2BDT, $FeSO_4 \cdot 74H_2O$ and NaSCN in H_2O/ isopropyl alcohol. The procedure was previously published by Yan *et al.*, reporting a black-coloured MOF with mixed high-spin/low-spin Fe^{II} centers.[146] It crystallizes in the orthorhombic space group *Cmmm* (Figure 1-13 a). The Fe^{II}-ions are located in $[FeN_6]$ coordination spheres and form 1D (Fe-N-N-)*n* chains along the *a*-axis via the bonding of triple-bridged tetrazolate-N atoms. The Fe-N bond lengths are typical for low-spin Fe^{II} centers.[145] Xie *et al.* synthesized $Fe_2(BDT)_3$ under completely anaerobic conditions and observed a colour change from deep orange-red to black upon exposure to air, which was attributed to the oxidation of Fe^{II} to Fe^{III}.[145] However, the PXRD pattern of the air-exposed sample did not show any structural distortion or degradation. The air-exposed sample exhibited permanent porosity with a BET surface area of 614 $m^2\ g^{-1}$. Single crystal electrical conductivity measurements (two-point probe method, 296 K, N_2) along the *a*-axis gave an average value of 6×10^{-5} S/cm of the as-synthesized air-free samples. DFT calculations point to the (Fe-N-N-)*n* chains as

charge transport pathway (Figure 1-13 b). After seven days in air, the average conductivity increased to 0.3 S/cm and further to 1.2 S/cm after 30 days and up to seven months in air, with a single crystal champion conductivity of 1.8 S/cm. An activation energy of 160 meV was stated for the temperature-dependent conductivity. UV-vis-NIR spectroscopy of the as-synthesized MOF revealed the presence of low-spin Fe^{II} centers with ligand-to-metal charge transfer and d-d transitions of low-spin Fe^{II}. Upon exposure to air, the UV-Vis-NIR spectra showed the rise of a new absorbance band at 690 nm, which was attributed to intervalence charge transfer between Fe^{II} and Fe^{III} centers. Furthermore, the optical bandgap changed from 2.0 eV in the as-synthesized sample to 1.4 eV after exposure to air for 21 h, which was attributed to the population of mid-gap states. In addition, DFT band structure calculations predicted the formation of Fe^{3+} defect states upon exposure to air, stated as reason for the increased conductivity by the authors.

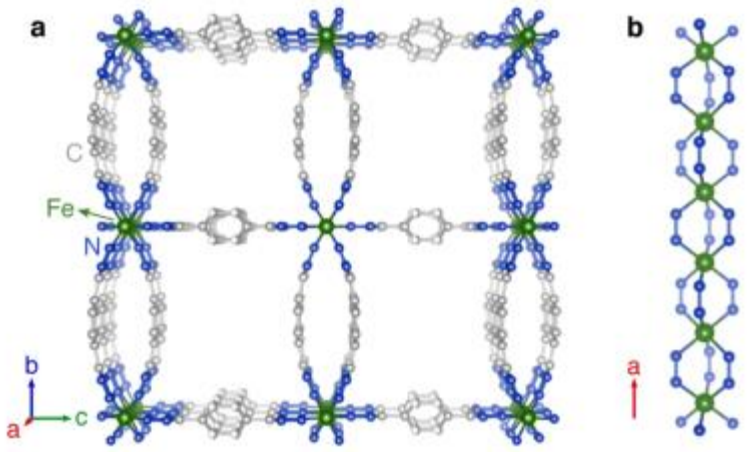

Figure 1-13: (a) Crystal structure of $Fe_2(BDT)_3$. (b) $Fe–N–N–)_\infty$ chains, which serve as the presumed charge transport pathways in this material. Reprinted (adapted) with permission.[145] Copyright {2018} American Chemical Society.

Mixed-valency states cannot only be introduced into a MOF by the metal ions, but also by the organic ligands. For example, in previously reported MOFs or coordination solids, three different valence states of 2,5-dihydroxybenzoquinone have been detected: $dhbq^{2-}$, the radical trianion $dhbq^{3-}$, and thb^{4-}(tetrahydoxybenzol anion). Darago *et al.* used the redox-active ligand 2,5-dihydroxybenzoquinone, an Fe^{II}-containing precursor and tetrabutylammonium bromide to synthesize the 3D MOF $(NBu_4)_2Fe^{III}_2(dhbq)_3$ (NBu_4 = tetrabutylammonium; $dhbq^{2-/3-}$ = 2,5-dioxidobenzoquinone/1,2-dioxido-4,5-semiquinone) with a mixed valency state.[147] It crystallizes in the cubic space group $I\bar{4}3d$ with two interpenetrated networks. In each lattice, neighboring metal centers contain the same chirality. Sorption measurements revealed the absence of porosity, due to the filling of the pores with tetrabutylammonium counterions. The authors proposed an electron transfer during the synthesis from Fe^{II} to $dhbq^{n-}$. In the crystal structure, shorter Fe-O distances of 2.008 Å and 2.031 Å were observed in comparison to related Fe^{II}-based complexes. Additionally,

^{57}Fe Mössbauer spectroscopy (across the temperature range 20 - 300 K) showed isomer shifts that are characteristic for high-spin Fe^{III}. Furthermore, the C-O distances in the crystal structure are longer than in typical $dhbq^{2-}$ coordination complexes. Thus, the authors presume a reduction of some $dhbq^{n-}$ ligands by Fe^{II} (in order to generate charge-balance) with a 2:1 ratio of $dhbq^{3-}$ and $dhbq^{2-}$. A chemical reduction of $(NBu_4)_2Fe^{III}_2(dhbq)_3$, with a stoichiometric amount of the reduction agent sodium naphtalenide led to the formation of $Na_{0.9}(NBu_4)_{1.8}Fe_2(dhbq)_3$. Both MOF states feature a sharp absorption edge at very low energy (4500 cm^{-1}), revealing the presence of Robin-Day Class II/III mixed-valency. Moreover, the ^{57}Fe Mössbauer spectrum confirmed the exclusive reduction of the ligands and not of the Fe^{III} centers, and a 2.7 : 0.3 ratio of $dhbq^{3-}$ and $dhbq^{2-}$ was calculated in $Na_{0.9}(NBu_4)_{1.8}Fe_2(dhbq)_3$. Electrical conductivity measurements (two-contact probe method, pellet, 298 K) gave a value of 0.16 S/cm for $(NBU_4)_2Fe^{III}_2(dhbq)_3$ and a lower value of 0.0062 S/cm for $Na_{0.9}(NBu_4)_{1.8}Fe_2(dhbq)_3$. Temperature-dependent conductivity measurements resulted in activation energies of 110 meV and 180 meV were, respectively. The authors suggested a charge transfer process between radical $dhbq^{3-}$ linkers and neighboring $dhbq^{2-}$ units due to electron hopping. While the charge-carrier density increased in $Na_{0.9}(NBu_4)_{1.8}Fe_2(dhbq)_3$, removal of $dhbq^{2-}$ units led to a decreased carrier mobility, which was assumed to have a dominant effect on the resulting lower conductivity.

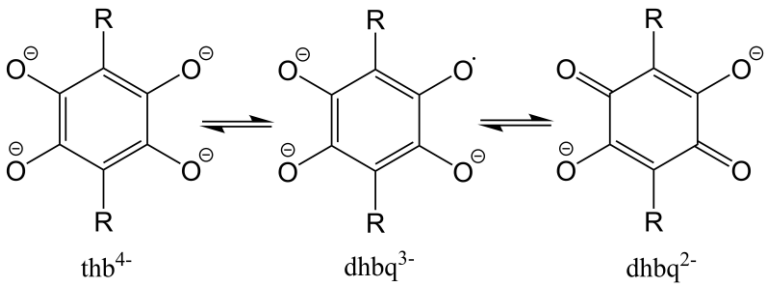

Figure 1-14: The linker 2,5-dihydroxybenzoquinone ($dhbq^{2-}$) and its redox states, $dhbq^{3-}$(1,2-dioxido-4,5-semiquinone) and thb^{4-} (tetrahydroxybenzol anion).

1.3.5 World record electrical conductivity of MOF single crystals

Pathak *et al.* integrated (-Cu-S-)*n* sheets into a MOF and achieved the highest single crystal electrical conductivity reported for MOFs to date.[148] Here, the reaction of 6,6´-dithiodinicotinic acid and Cu^{II} led to the formation of $\{[Cu_2(6\text{-Hmna})(6\text{-mn})]\cdot NH_4\}_n$, (6-Hmna = 6-mercaptonicotinic acid, 6-mn = 6-mercaptonicotinate), which crystallizes in the orthorhombic space group $Pna2_1$. Two crystallographically independent Cu^{I} centers form CuS_3N units with a tetrahedral geometry (Figure 1-15). The presence of Cu^{I} centers was confirmed by XPS analysis.The three sulfur atoms are originating from two 6-Hmna ligands and one 6-mn ligand, the nitrogen atoms from another 6-mn ligand. Vertical arrays of alternating Cu and S atoms, with Cu-S bond lenghts of 2.303 - 2.384 Å, form a honeycomb-like structure in the *ab* plane. The parallel-arranged (-Cu-S-)*n* sheets

are connected by the 6-Hmn and 6-mn ligands with a distance of 14.4 Å and build a layered MOF structure, including ammonium ions as counter ions. However, $\{[Cu_2(6\text{-Hmna})(6\text{-mn})]\cdot NH_4\}_n$ is considered to be a quite dense MOF by the authors, indicated by a low BET surface area. Thus, it should be considered a coordination polymers rather than a MOF. Notably, single crystal electrical conductivity measurements (four-point probe method, single crystal, 300 K) gave record high values of up to 10.96 S/cm. Moreover, an activation energy of only 6 meV was obtained for $\{[Cu_2(6\text{-Hmna})(6\text{-mn})]\cdot NH_4\}_n$ at low temperatures. The authors proposed the strong overlap between the Cu^I d-orbitals and the sulfur p-orbitals, which facilitate charge transport *via* the chemical bonds in the (-Cu-S-)*n* sheets, as reason for the high conductivity.

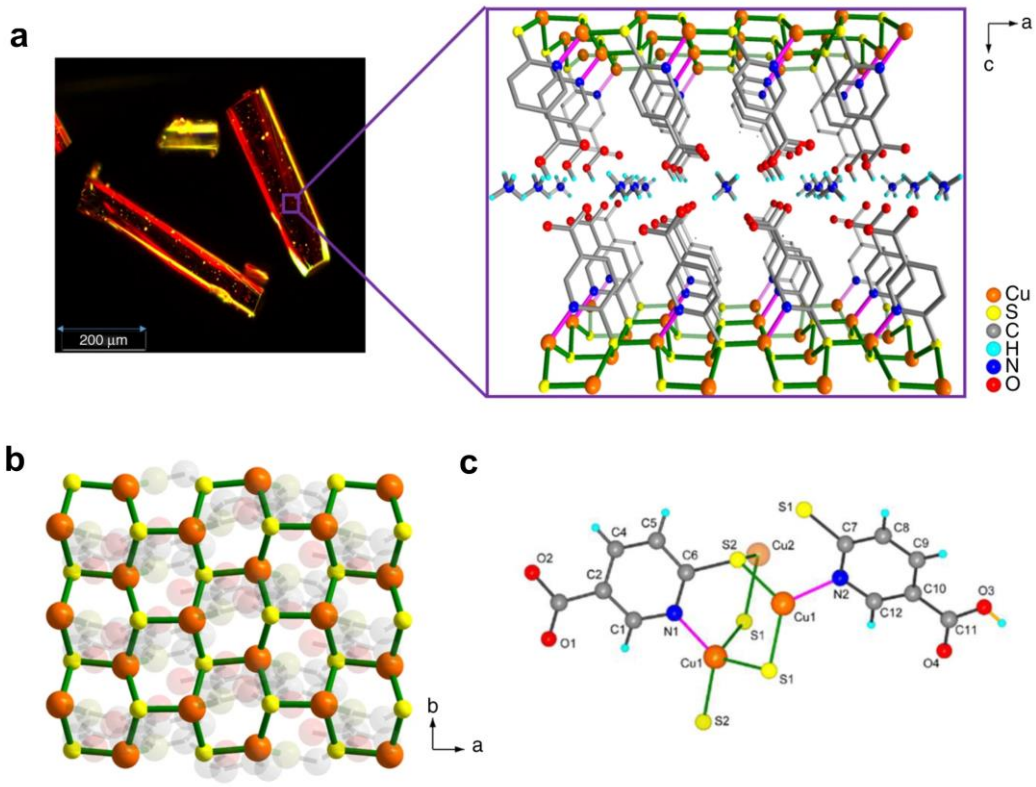

Figure 1-15: (a) Dark-field optical image and enlarged schematic view of the crystal structure of $\{[Cu_2(6\text{-Hmna})(6\text{-mn})]\cdot NH_4\}_n$ along the *c*-axis (Cu = orange, O = red, C = light gray, N = blue, S = yellow, H = cyan). (b) The corresponding 2D layer, visualizing the Cu-S arrangement. (c) Coordination environment of $\{[Cu_2(6\text{-Hmna})(6\text{-mn})]\cdot NH_4\}_n$.[148]

1.4 Conclusion and outlook

Metal-organic frameworks exhibiting the intriguing properties of crystallinity and porosity in combination with electrical conductivity have attracted increasing interest in recent years. Even if the group of such materials, in the form of 2D and 3D metal-organic frameworks, is still small,

it is growing at a significant rate. 2D MOFs are constructed as layered graphite-like sheets, providing two possible charge transfer pathways along the stacked layer as well as in the sheet plane.[74] In 3D MOFs, different charge transfer pathways are possible through the rational design of the MOF. Internal pathways along covalent bonds of the metal ions and organic ligands, as well as along π-π-stacked layers of the organic ligands are possible for charge transfer.[44,45,71] Several different strategies have been developed in the last years to enhance the electrical conductivity in three dimensional metal-organic frameworks. Low-energy charge transfer pathways as well as high concentrations of loosely bound charge carriers are key to induce electrical conductivity in the framework.

The incorporation of guest molecules into the pores is one possible way to provide freely-moving charge carriers. Iodine is a commonly used dopant that can form polyiodide chains in the pores and induce charge transfer between polyiodide units.[78,80] Moreover, iodine can oxidize a redox-active organic ligand and thus enable redox hopping in the framework.[82] TCNQ and TTF are also popular guest molecules in MOFs. TCNQ is an electron acceptor which can form stable radical anions.[87] Furthermore, parallel TCNQ molecules can form π-π-stacked complexes that open a charge transfer pathway through the whole framework.[87] For example, an electrical conductivity enhancement in HKUST-1 from 10^{-8} S/cm to 7 x 10^{-2} S/cm was achieved by TCNQ loading.[89] On the other hand, TTF is an electron donor with delocalized π-orbitals, enabling the formation of stable radical cations. Similar to TCNQ, adjacent TTF moieties can create π-π-stacks, thereby facilitating charge transfer.[100-102]

However, intercalation of guest molecules into the pores often causes the loss of the MOF's porosity. Therefore, another effective method to construct a low-energy charge transfer pathway *via* π-π-stacking is the design and incorporation of electroactive organic ligands like anthracene-based molecules.[99] Several MOFs were also constructed with redox-active NDI-based organic ligands, which can form stable radical anions and π-π-stacks.[62,94] Moreover, TTF is not only a prominent guest molecule, but it can also serve as a moiety in organic ligands. For example, several TTFTB-based (TTFTB = tetrathiafulvalene tetrabenzoate) MOFs were constructed, comprising a large number of different metal ions including lanthanides.[71,102,103,105-108] Not surprisingly, the MOFs exhibit different electrical conductivities depending on the metal ions, with Cd_2(TTFTB) showing the highest value of 2.86 x 10^{-4} S/cm (two-point probe method, single crystal, rt).[103] It has the shortest S···S distance of 3.654 Å between neighboring TTF cores in the π-π-stacks. This causes a good orbital overlap between sulfur atoms and thereby facilitates the charge transport in the MOF.[103] Additionaly, this MOF series exhibits micropores with BET surface areas in the range of 470 to 537 m^2/mmol. Organic ligands based on triphenylene are often used for the construction of electroactive 2D MOFs.[118,119] They feature the intriguing properties of ligand π-π

stacking, redox activity to form semiquinoid radicals, as well as strong π-*d* conjugation of the ligand with the metal ion.[118] Recently, the first 3D MOFs were constructed with triphenylene-based HHTP/HOTP ligands and rare earth metal ions.[120,121] They include examples with electrical conductivities ranging from 1.5 x 10^{-5} S/cm for Eu_6HOTP_2 to 0.053 S/cm for HoHHTP (two-point probe method, pellet, 302 K), as well as permanent porosity.[121]

A rare class of electrically conducting MOFs are based on phosphonate ligands, featuring high structural diversity and stable coordination to different metals.[128,131-134] Some of the highest reported electrical conductivity values are based on phosphonate MOFs. Especially the MOFs TUB75 and TUB40 feature high conductivity, reaching champion values of 10 S/cm (impedance spectroscopy, single crystal, rt).[128,131] TUB75 features a fully delocalized electronic system through the deprotonation of the 1,4-naphtalenediphosphonic acid ligands constituting the framework.[131] On the other hand, according to DFT calculations, TUB40 features an excitation between the HOMO of the naphthalene-based ligand and the LUMO of Cu^{II}.[128]

MOFs based on the MOF-74 topology were recently introduced as interesting electrically conductive MOF platform.[24,45,136] The exchange of the aromatic hydroxyl groups with thiophenol groups led to an electrical conductivity increase of one order of magnitude in Mn/Fe(DSBDC), which was attributed to an enhanced orbital overlap of the metal ion and the sulfur atom.[45] This led to a facilitated charge transfer through (-metal-S-)$_\infty$ chains. In general, the iron-based MOF-74 Fe_2(DOBDC) features the highest electrical conductivity of the MOF-74 series, with 3.2 x 10^{-7} S/cm (and 3.9 x 10^{-6} S/cm for Fe_2(DSBDC)) (two-point probe method, pellet, at 297 K, N_2).[45]

Not only the organic ligand can have a large impact on the electrical conductivity of the MOF, but also the metal ion used, as already discussed for MOF-74(Fe). Iron MOFs often exhibit higher conductivites in comparison to their MOF analogs with other metal ions.[45] Fe^{II} contains a relatively high charge density and can be easily oxidized to Fe^{III}, which results in mixed valence $Fe^{3+/2+}$ systems. As a consequence, IVCT improves the charge-carrier mobility and leads to higher conductivity values.[75,137,139,141] For example, purely Fe^{II}-based $Fe(C_2N_3H_2)_2$, named $Fe(tri)_2$, shows conductivity values in the range of 7 x 10^{-9} S/cm to 1 x 10^{-10} S/cm (two-point probe method, pellet, 293 K). Partial oxidation of the Fe^{II} centers with thianthrenium tetrafluoroborate led to a drastic electrical conductivity increase by about eight orders of magnitude, with a value of 0.3 S/cm for $Fe(tri)_2(BF_4)_x$ with x = 0.33.[143] In a dipyrazolate MOF, half of the Fe^{III} centers in $Fe_2(BDP)_3$ (BDP^{2-} = 1,4-benzenedipyrazolate) were partially reduced by potassium naphtalenide to $K_{0.98}Fe_2(BDP)_3$, while maintaining its permanent porosity.[144] The electrical conductivity increased by five orders of magnitude to 0.025 S/cm (two-point probe method, single cyrstal, 293 K).[144] The MOF $Fe_2(BDT)_3$ exhibits low-spin Fe^{II} centers and an electrical conductivity of 6

x 10^{-5} S/cm (two-point probe method, single crystal, 296 K, N_2), due to metal-to-ligand charge transfer. Exposure to air led to partial oxidation of Fe^{II} to Fe^{III} and to a champion conductivity of 1.8 S/cm, due to additional IVCT processes. This MOF exhibits the highest electrical conductivity in a 3D MOF reported to date, in combination with permanent porosity.[145]

The introduction of mixed-valency states into a MOF system is also possible through the incorporation of redox-active organic ligands. In the MOF $(NBu_4)_2Fe^{III}_2(dhbq)_3$ (NBu_4 = tetrabutylammonium; $dhbq^{2-/3-}$ = 2,5-dioxidobenzoquinone/1,2-dioxido-4,5-semiquinone),[147] the reduction of some $dhbq^{n-}$ ligands by Fe^{II} led to the formation of Robin-Day Class II/III mixed-valency states with a 2:1 ratio of $dhbq^{3-}$ and $dhbq^{2-}$. A high electrical conductivity of 0.16 S/cm (two-point probe method, pellet, 298 K) was measured, suggesting electron hopping between $dhbq^{3-}$ and $dhbq^{2-}$ units.[147]

The 3D MOF (or coordination polymer) $\{[Cu_2(6\text{-Hmna})(6\text{-mn})]\cdot NH_4\}_n$ was reported to have the highest electrical conductivity in MOF single crystals observed to date, with a value of 10.96 S/cm (4-contact probe method, single crystal, 300 K). The Cu^I centers and the ligand S atoms feature a strong orbital overlap, which led to a proposed charge transport *via* the (-Cu-S-)*n* sheets present in the structure. However, due to the absence of porosity, this material should be considered rather a coordination polymer than a MOF.[148]

As discussed in this review, a significant number of 3D metal-organic frameworks exhibiting electrical conductivity has been discovered in recent years. A wide range of structural elements and modifications such as doping or guest inclusion can be used to achieve significant conductivity and to further tune the charge-carrier dynamics in these remarkable molecular frameworks. It will be of great interest to explore their integration into operational devices, with possible applications in the field of chemical sensing and semiconductor materials. However, for the implemenation of MOFs into such devices, their controlled deposition on surfaces as thin films - instead of the synthesis as microcrystalline powders - is essential. [63,67,149,150] Developing control over the film morphology, thickness and crystallinity are important for achieving the desired performance of the resulting MOF films in the context of their potential applications. This also includes enhanced control over the crystallographic orientation in the films, especially for MOFs with highly anisotropic (opto)electronic properties. While thin film growth of MOFs is a subject beyond the scope of this review, we wish to direct the reader to a few key publications in this field.[151-158] Based on their intriguing features, suitable morphologies of electrically conducting (and semiconducting) MOFs are expected to be further developed and to be investigated in diverse (opto)electronic applications in areas such as chemical sensing, solar energy conversion or electrical energy storage.

1.5 References

(1) Su, B.-L.; Sanchez, C.; Yang, X.-Y. *Hierarchically Structured Porous Materials: From Nanoscience to Catalysis, Separation, Optics, Energy, and Life Science*; John Wiley & Sons: Weinheim, 2012.

(2) Liu, P.S.; Cgen, G. F. *Porous Materials: Processing and Applications,1st Edition*; Elsevier: Oxford, 2014.

(3) Xu, R.; Pang, W.; Yu, J.; Huo, Q.; Chen, J. *Chemistry of Zeolites and Related Porous Materials: Synthesis and Structure*; John Wiley & Sons: Singapore, 2007.

(4) Rouquerol, J.; Rouquerol, F.; Llewellyn, P.; Maurin, G.; Sing, K. S. W. *Adsorption by Powders and Porous Solids: Principles, Methodology and Applications, 2nd edition*; 1-18; Academic Press, 2013.

(5) Storck, H.B.S.; Maier, W. F. *Applied Catalysis A: Genera* **1998**, *174*, 137–146.

(6) Yaghi, O. M. Reticular Chemistry in All Dimensions. *ACS Cent. Sci.* **2019**, *5*, 1295–1300.

(7) Diercks, C. S.; Yaghi, O. M. The atom, the molecule, and the covalent organic framework. *Science* **2017**, *355(6328, article eaal1585)*.

(8) Jiang, H.; Alezi, D.; Eddaoudi, M. A reticular chemistry guide for the design of periodic solids. *Nat. Rev. Mat.* **2021**, *6*, 466–487.

(9) Yaghi, O. M.; Li, H. Hydrothermal Synthesis of a Metal-Organic Framework Containing Large Rectangular Channels. *J. Am. Chem. Soc.* **1995**, *117*, 10401–10402.

(10) Hoskins, B. F.; Robson, R. Design and construction of a new class of scaffolding-like materials comprising infinite polymeric frameworks of 3D-linked molecular rods. A reappraisal of the zinc cyanide and cadmium cyanide structures and the synthesis and structure of the diamond-related frameworks [N(CH3)4][CuIZnII(CN)4] and CuI[4,4',4",4"'-tetracyanotetraphenylmethane]BF4.xC6H5NO2. *J. Am. Chem. Soc.* **1990**, *112*, 1546–1554.

(11) Batten, S. R.; Champness, N. R.; Chen, X.-M.; Garcia-Martinez, J.; Kitagawa, S.; Öhrström, L.; O´Keeffe, M. O.; Suh, M. P.; Reedijk, J. Coordination polymers, metal-organic frameworks and the need for terminology guidelines. *CrystEngComm* **2012**, *14*, 3001.

(12) Connelly, N. G.; Hartshorn, R. M.; Damhus, T.; Hutton, A. T. *Nomenclature of Inorganic Chemistry IUPAC Recommendations 2005*; Cambridge, 2005.

(13) Furukawa, H.; Cordova, K. E.; O´Keeffe, M. O.; Yaghi, O. M. The Chemistry and Applications of Metal-Organic Frameworks. *Science* **2013**, *341*, 1230444.

(14) Feng, D.; Jiang, H. L.; Chen, Y. P.; Gu, Z. Y. Wei, Z.; Zhou H. C. Metal-Organic Frameworks Based on Previously Unknown Zr8/Hf8 Cubic Clusters. *Inorg. Chem.* **2013**, *52*, 12661–12667.

(15) Eddaoudi, M.; Moler, D. B.; Li, H.; Chen, B.; Reineke, T. M.; O´Keeffe, M. O.; Yaghi, O. M. Modular Chemistry: Secondary Building Units as a Basis for the Design of Highly Porous and Robust Metal-Organic Frameworks. *Acc. Chem. Res.* **2001**, *34*, 319–330.

(16) Li, H.; Eddaoudi, M.; O´Keeffe, M. O.; Yaghi, O. M. Design and synthesis of an exceptionally stable and highly porous metal-organic framework **1999**, *402*, 276–279.

(17) Stock, N.; Biswas, S. Synthesis of Metal-Organic Frameworks (MOFs): Routes to Various MOF Topologies, Morphologies, and Composites. *Chem. Rev.* **2012**, *112*, 933-969.

(18) Yaghi, O. M.; O´Keeffe, M. O.; Ockwig, N. W.; Chae, H. K.; Eddaoudi, M.; Kim, J. Reticular synthesis and the designof new materials. *Nature* **2003**, *423*, 705–714.

(19) Ackley, M.; Rege, S. U.; Saxena, H. Application of natural zeolites in the purification and separation of gases. *Microporous Mesoporous Mat.* **2003**, *61*, 25–42.

(20) Ding, S.-Y.; Wang, W. Covalent organic frameworks (COFs): from design to applications. *Chem. Soc. Rev.* **2013**, *42*, 548–568.

(21) Farha, O. K.; Eryazici, I.; Jeong, N. C.; Hauser, B. G.; Wilmer, C. E.; Sarjeant, A. A.; Snurr, R. Q.; Nguyen, S. T.; Yazaydın, A. Ö.; Hupp, J. T. Metal-organic framework materials with ultrahigh surface areas: is the sky the limit? *J. Am. Chem. Soc.* **2012**, *134*, 15016–15021.

(22) Yaghi, O. M.; Li, G.; Li, H. Selective binding and removal of guests in a microporous metal-organic framework. *Nature* **1995**, 703–706.

(23) James, S. L. Metal-organic frameworks. *Chem. Soc. Rev.* **2003**, *32*, 276.

(24) Kapelewski, M. T.; Geier, S. J.; Hudson, M. R.; Stück, D.; Mason, J. A.; Nelson, J. N.; Xiao, D. J.; Hulvey, Z.; Gilmour, E.; FitzGerald, S. A.; Head-Gordon, M.; Brown, C. M.; Long, J. R. M2(m-dobdc) (M = Mg, Mn, Fe, Co, Ni) metal-organic frameworks exhibiting increased charge density and enhanced H2 binding at the open metal sites. *J. Am. Chem. Soc.* **2014**, *136*, 12119–12129.

(25) Kreno, L. E.; Leong, K.; Farha, O. K.; Allendorf, M.; van Duyne, R. P.; Hupp, J. T. Metal-organic framework materials as chemical sensors. *Chem. Rev.* **2012**, *112*, 1105–1125.

(26) Eddaoudi, M.; Kim, J.; Rosi, N.; Vodak, D.; Wachter, J.; O´Keeffe, M. O.; Yaghi, O. M. Systematic Design of Pore Size and Functionality in isoreticular MOFs and Their Application in Methane Storage. *Science* **2002**, *295*, 469–472.

(27) Cohen, S. M. Postsynthetic methods for the Functionalization of Metal-Organic Frameworks. *Chem. Rev.* **2012**, *112*, 970–1000.

(28) Chui, S. S.-Y.; Lo, S. M.-F.; Charmant, J. P. H.; Orpen, A. G.; Williams, I. D. A chemically functionalizable nanoporous material. *Science* **1999**, *283*, 1148–1150.

(29) Loiseau, T.; Serre, C.; Huguenard, C.; Fink, G.; Taulelle, F.; Henry, M.; Bataille, T.; Férey, G. A rationale for the large breathing of the porous aluminum terephthalate (MIL-53) upon hydration. *Chem. Eur. J.* **2004**, *10*, 1373–1382.

(30) Rosi, N. L.; Kim, J.; Eddaoudi, M.; Chen, B.; O'Keeffe, M.; Yaghi, O. M. Rod packings and metal-organic frameworks constructed from rod-shaped secondary building units. *J Am Chem Soc* **2005**, *127*, 1504–1518.

(31) Deria, P.; Mondloch, J. E.; Karagiaridi, O.; Bury, W.; Hupp, J. T.; Farha, O. K. Beyond post-synthesis modification: evolution of metal-organic frameworks via building block replacement. *Chem. Soc. Rev.* **2014**, *43*, 5896–5912.

(32) Dolgopolova, E. A.; Shustova, N. B. Metal–organic framework photophysics: Optoelectronic devices, photoswitches, sensors, and photocatalysts. *MRS Bull.* **2016**, *41*, 890–896.

(33) Feng, D.; Gu, Z. Y.; Li, J. R.; Jiang, H. L.; Wei, Z.; Zhou, H. C. *Angew. Chem. Int. Ed. Engl.* **2012**, *51*, 10307–10310.

(34) Murray, L. L.; Dincă, M.; Long, J. R. Hydrogen storage in metal-organic frameworks. *Chem. Soc. Rev.* **2009**, *38*, 1294–1314.

(35) Li, J.-R.; Sculley, J.; Zhou, H.-C. Metal-Organic Frameworks for Separations. *Chem. Rev.* **2012**, *112*, 869–932.

(36) Lee, J.; Farha, O. K.; Roberts, J.; Scheidt, K. A.; Nguyen, S. T.; Hupp, J. T. Metal-organic framework materials as catalysts. *Chem. Soc. Rev.* **2009**, *38*, 1450–1459.

(37) Wang, J.-L.; Wang, C.; Lin, W. Metal–Organic Frameworks for Light Harvesting and Photocatalysis. *ACS Catal.* **2012**, *2*, 2630–2640.

(38) DeCoste, J. B.; Peterson, G. W. Metal-organic frameworks for air purification of toxic chemicals. *Chem. Rev.* **2014**, *114*, 5695–5727.

(39) Keskin, S.; Kızılel, S. Biomedical Applications of Metal Organic Frameworks. *Ind. Eng. Chem. Res.* **2011**, *50*, 1799–1812.

(40) Feng, D.; Chung, W.-C.; Wei, Z.; Gu, Z.-Y.; Jiang, H.-L.; Chen, Y.-P.; Darensbourg, D. J.; Zhou, H.-C. Construction of ultrastable porphyrin Zr metal-organic frameworks through linker elimination. *J. Am. Chem. Soc.* **2013**, *135*, 17105–17110.

(41) BASF Metal Organic Frameworks (MOFs): Innovative Fuel Systems for Natural Gas Vehicles (NGVs). *Chem. Soc. Rev.* **2014**, *43*, 6173–6174.

(42) Deng, H.; Grunder, S.; Cordova, K. E.; Valente, C.; Furukawa, H.; Hmadeh, M.; Gándara, F.; Whalley, A. C.; Liu, Z.; Asahina, S.; Kazumori, H.; O'Keeffe, M.; Terasaki, O.; Stoddart, J. F.; Yaghi, O. M. Large-pore apertures in a series of metal-organic frameworks. *Science* **2012**, *336*, 1018–1023.

(43) Rosi, N. L.; Kim, J.; Eddaoudi, M.; Chen, B.; O'Keeffe, M.; Yaghi, O. M. Rod packings and metal-organic frameworks constructed from rod-shaped secondary building units. *J. Am. Chem. Soc.* **2005**, *127*, 1504–1518.

(44) Sun, L.; Miyakai, T.; Seki, S.; Dincă, M. Mn2(2,5-disulfhydrylbenzene-1,4-dicarboxylate): a microporous metal-organic framework with infinite (-Mn-S-)∞ chains and high intrinsic charge mobility. *J Am Chem Soc* **2013**, *135*, 8185–8188.

(45) Sun, L.; Hendon, C. H.; Minier, M. A.; Walsh, A.; Dincă, M. Million-Fold Electrical Conductivity Enhancement in Fe2(DEBDC) versus Mn2(DEBDC) (E = S, O). *J. Am. Chem. Soc.* **2015**, *137*, 6164–6167.

(46) Caskey, S. R.; Wong-Foy, A. G.; Matzger, A. J. Dramatic tuning of carbon dioxide uptake via metal substitution in a coordination polymer with cylindrical pores. *J. Am. Chem. Soc.* **2008**, *130*, 10870–10871.

(47) Cozzolino, A. F.; Brozek, C. K.; Palmer, R. D.; Yano, J.; Li, M.; Dincă, M. Ligand redox non-innocence in the stoichiometric oxidation of Mn2(2,5-dioxidoterephthalate) (Mn-MOF-74). *J. Am. Chem. Soc.* **2014**, *136*, 3334–3337.

(48) Sanz, R.; Martínez, F.; Orcajo, G.; Wojtas, L.; Briones, D. Synthesis of a honeycomb-like Cu-based metal-organic framework and its carbon dioxide adsorption behaviour. *Dalton Trans.* **2013**, *42*, 2392–2398.

(49) Queen, W. L.; Hudson, M. R.; Bloch, E. D.; Mason, J. A.; Gonzalez, M. I.; Lee, J. S.; Gygi, D.; Howe, J. D.; Lee, K.; Darwish, T. A.; James, M.; Peterson, V. K.; Teat, S. J.; Smit, B.; Neaton, J., B.; Long, J. R.; Brown, C. M. Comprehensive study of carbon dioxide adsorption in the metal–organic frameworks M 2 (dobdc) (M = Mg, Mn, Fe, Co, Ni, Cu, Zn). *Chem. Sci.* **2014**, *5*, 4569–4581.

(50) Wang, L. J.; Deng, H.; Furukawa, H.; Gándara, F.; Cordova, K. E.; Peri, D.; Yaghi, O. M. Synthesis and characterization of metal-organic framework-74 containing 2, 4, 6, 8, and 10 different metals. *Inorg Chem* **2014**, *53*, 5881–5883.

(51) Britt, D.; Tranchemontagne, D.; Yaghi, O. M. Metal-organic frameworks with high capacity and selectivity for harmful gases **2005**, *108*, 11623–11627.

(52) Glover, G. T.; Peterson, G. W.; Schindler, B. J.; Britt, D.; Yaghi, O. MOF-74 building unit has a direct impact on toxic gas adsorption. *Chem. Eng. Sci.* **2011**, *66*, 163–170.

(53) Herm, Z. R.; Swisher, J. A.; Smit, B.; Krishna, R.; Long, J. R. Metal-organic frameworks as adsorbents for hydrogen purification and precombustion carbon dioxide capture. *J. Am. Chem. Soc.* **2011**, *133*, 5664–5667.

(54) Bao, Z.; Yu, L.; Ren, Q.; Lu, X.; Deng, S. Adsorption of CO2 and CH4 on a magnesium-based metal organic framework. *J. Colloid Interface Sci.* **2011**, *353*, 549–556.

(55) Millward, A. R.; Yaghi, O. M. Metal-organic frameworks with exceptionally high capacity for storage of carbon dioxide at room temperature. *J. Am. Chem. Soc.* **2005**, *127*, 17998–17999.

(56) Yang, D.-A.; Cho, H.-Y.; Kim, J.; Yang, S.-T.; Ahn, W.-S. CO 2 capture and conversion using Mg-MOF-74 prepared by a sonochemical method. *Energy Environ. Sci.* **2012**, *5*, 6465–6473.

(57) Strauss, I.; Mundstock, A.; Treger, M.; Lange, K.; Hwang, S.; Chmelik, C.; Rusch, P.; Bigall, N. C.; Pichler, T.; Shiozawa, H.; Caro, J. Metal-Organic Framework Co-MOF-74-Based Host-Guest Composites for Resistive Gas Sensing. *ACS Appl. Mater. Interfaces* **2019**, *11*, 14175–14181.

(58) Tan, K.; Zuluaga, S.; Gong, Q.; Gao, Y.; Nijem, N.; Li, J.; Thonhauser, T.; Chabal, Y. J. Competitive Coadsorption of CO 2 with H 2 O, NH 3 , SO 2 , NO, NO 2 , N 2 , O 2 , and CH 4 in M-MOF-74 (M = Mg, Co, Ni): The Role of Hydrogen Bonding. *Chem. Mater.* **2015**, *27*, 2203–2217.

(59) Strauss, I.; Mundstock, A.; Hinrichs, D.; Himstedt, R.; Knebel, A.; Reinhardt, C.; Dorfs, D.; Caro, J. The Interaction of Guest Molecules with Co-MOF-74: A Vis/NIR and Raman Approach. *Angew. Chem. Int. Ed.* **2018**, *57*, 7434–7439.

(60) Jiang, H.; Wang, Q.; Wang, H.; Chen, Y.; Zhang, M. MOF-74 as an Efficient Catalyst for the Low-Temperature Selective Catalytic Reduction of NOx with NH3. *ACS Appl. Mater. Interfaces* **2016**, *8*, 26817–26826.

(61) AlKaabi, K.; Wade, C. R.; Dincă, M. Transparent-to-Dark Electrochromic Behavior in Naphthalene-Diimide-Based Mesoporous MOF-74 Analogs. *Chem* **2016**, *1*, 264–272.

(62) Guo, Z.; Panda, D. K.; Gordillo, M. A.; Khatun, A.; Wu, H.; Zhou, W.; Saha, S. Lowering Band Gap of an Electroactive Metal-Organic Framework via Complementary Guest Intercalation. *ACS Appl. Mater. Interfaces* **2017**, *9*, 32413–32417.

(63) Campbell, M. G.; Dincă, M. Metal-Organic Frameworks as Active Materials in Electronic Sensor Devices. *Sensors* **2017**, *17*, 1108.

(64) Campbell, M. G.; Sheberla, D.; Liu, S. F.; Swager, T. M.; Dincă, M. Cu_3(hexaiminotriphenylene)$_2$: an electrically conductive 2D metal-organic framework for chemiresistive sensing. *Angew. Chem.* **2015**, *54*, 4349–4352.

(65) Stavila, V.; Talin, A. A.; Allendorf, M. D. MOF-based electronic and opto-electronic devices. *Chem. Soc. Rev.* **2014**, *43*, 5994–6010.

(66) Zhang, Z.; Yoshikawa, H. I.; Awaga, K. Monitoring the solid-state electrochemistry of Cu(2,7-AQDC) (AQDC = anthraquinone dicarboxylate) in a lithium battery: coexistence of metal and ligand redox activities in a metal-organic framework. *J. Am. Chem. Soc.* **2014**, *136*, 16112–16115.

(67) Yi, F.-Y.; Chen, D.; Wu, M.-K.; Han, L.; Jiang, H.-L. Chemical Sensors Based on Metal-Organic Frameworks. *ChemPlusChem* **2016**, *81*, 675–690.

(68) Kim, H.; Rao, S. R.; Kapustin, E. A.; Zhao, L.; Yang, S.; Yaghi, O. M.; Wang, E. N. Adsorption-based atmospheric water harvesting device for arid climates. *Nat. Commun.* **2018**, *9*, 1191.

(69) Gérard, F.; Millange, F.; Morcrette, M.; Serre, C.; Doublet, M.-L.; Grenèche, J.-M.; Tarascon, J.-M. Mixed-valence li/fe-based metal-organic frameworks with both reversible redox and sorption properties. *Angew. Chem.* **2007**, *46*, 3259–3263.

(70) Holliday, B. J.; Swager, T. M. Conducting metallopolymers: the roles of molecular archoitecture and redox matching. *Chem. Commun.* **2005**, 23–26.

(71) Narayan, T. C.; Miyakai, T.; Seki, S.; Dincă, M. High charge mobility in a tetrathiafulvalene-based microporous metal-organic framework. *J. Am. Chem. Soc.* **2012**, *134*, 12932–12935.

(72) Takaishi, S.; Hosoda, M.; Kajiwara, T.; Miyasaka, H.; Yamashita, M.; Nakanishi, Y.; Kitagawa, Y.; Yamaguchi, K.; Kobayashi, A.; Kitagawa, H. Electroconductive porous coordination polymer CuCu(pdt)2 composed of donor and acceptor building units. *Inorg. Chem.* **2009**, *48*, 9048–9050.

(73) Jin, Z.; Yan, J.; Huang, X.; Xu, W.; Yang, S.; Zhu, D.; Wang, J. Solution-processed transparent coordination polymer electrode for photovoltaic solar cells. *Nano Energy* **2017**, *40*, 376–381.

(74) Rodriguez-San-Miguel, D.; Amo-Ochoa, P.; Zamora, F. MasterChem: cookung 2D-polymers. *Chem. Commun.* **2016**, *52*, 4113–4127.

(75) Chen, G.; Gee, L. B.; Xu, W.; Zhu, Y.; Lezama-Pacheco, J. S.; Huang, Z.; Li, Z.; Babicz, J. T.; Choudhury, S.; Chang, T.-H.; Reed, E.; Solomon, E. I.; Bao, Z. Valence-Dependent Electrical Conductivity in a 3D Tetrahydroxyquinone-Based Metal–Organic Framework. *J. Am. Chem. Soc.* **2020**, *142*, 21243–21248.

(76) Park, J.; Hinckley, A. C.; Huang, Z.; Chen, G.; Yakovenko, A. A.; Zou, X.; Bao, Z. High Thermopower in a Zn-Based 3D Semiconductive Metal-Organic Framework. *J. Am. Chem. Soc.* **2020**, *142*, 20531–20535.

(77) Kobayashi, Y.; Jacobs, B.; Allendorf, M. D.; Long, J. R. Conductivity, Doping, and Redox Chemistry of a Microporous Dithiolene-Based Metal−Organic Framework. *Chem. Mater.* **2010**, *22*, 4120–4122.

(78) Aubrey, M. L.; Kapelewski, M. T.; Melville, J. F.; Oktawiec, J.; Presti, D.; Gagliardi, L.; Long, J. R. Chemiresistive Detection of Gaseous Hydrocarbons and Interrogation of Charge Transport in CuNi(2,3-pyrazinedithiolate)2 by Gas Adsorption. *J. Am. Chem. Soc.* **2019**, *141*, 5005–5013.

(79) Lin, J.-X.; Liang, J.; Feng, J.-F.; Karadeniz, B.; Lü, J.; Cao, R. Iodine uptake and enhanced electrical conductivity in a porous coordination polymer based on cucurbit[6]uril. *Inorg. Chem. Front.* **2016**, *3*, 1393–1397.

(80) Yin, Z.; Wang, Q.-X.; Zeng, M.-H. Iodine Release and Recovery, Influence of Polyiodide Anions on Electrical Conductivity and Nonlinear Optical Activtiy in an Interdigitated and Interprenetarted Bipillared-Bilayer Metal-Organic Framework. *J. Am. Chem. Soc.* **2012**, *134*, 4857–4863.

(81) hao, Z.; Yang, G.; Song, X.; Zhu, M.; Meng, X.; Zhao, S.; Song, S.; Zhang, H. A europium(III) based metal-organic framework:bifunctional properties related to sensing and electronic conductivity. *J. Mater. Chem. A* **2014**, *2*, 237–244.

(82) Lee, D. Y.; Kim, E.-K.; Shrestha, N. K.; Boukhvalov, D. W.; Lee, J. K.; Han, S.-H. Charge Transfer-Induced Molecular Hole Doping into Thin Film of Metal-Organic Frameworks. *ACS Appl. Mater. Interfaces* **2015**, *7*, 18501–18507.

(83) Mani, P.; Mandal, N.; Roopesh, M.; Gopalakrishnan, H.; Datta, A.; Mandal, S. Enhancement in electrical conductivity of a porous indium based metal–organic framework upon I 2 uptake: combined experimental and theoretical investigations. *J. Mater. Chem. C* **2020**, *8*, 4836–4842.

(84) Ogihara, N.; Ohba, N.; Kishida, Y. On/off switchable electronic conduction in intercalated metal-organic frameworks. *Sci. Adv.* **2017**, *3*, e1603103.

(85) Rouhani, F.; Rafizadeh-Masuleh, F.; Morsali, A. Highly Electroconductive Metal-Organic Framework: Tunable by Metal Ion Sorption Quantity. *J. Am. Chem. Soc.* **2019**, *141*, 11173–11182.

(86) Wang, S.; Kitao, T.; Guillou, N.; Wahiduzzaman, M.; Martineau-Corcos, C.; Nouar, F.; Tissot, A.; Binet, L.; Ramsahye, N.; Devautour-Vinot, S.; Kitagawa, S.; Seki, S.; Tsutsui, Y.; Briois, V.; Steunou, N.; Maurin, G.; Uemura, T.; Serre, C. A phase transformable ultrastable titanium-carboxylate framework for photoconduction. *Nat. Commun.* **2018**, *9*, 1660.

(87) Zhang, X.; Wang, Z.-X.; Xie, H.; Li, M.-X.; Woods, T. J.; Dunbar, K. R. A cobalt(ii) spin-crossover compound with partially charged TCNQ radicals and an anomalous conducting behavior. *Chem. Sci.* **2016**, *7*, 1569–1574.

(88) Huang, Q.-Q.; Lin, Y.-J.; Zheng, R.; Deng, W.-H.; Kashi, C.; Kumar, P. N.; Wang, G.-E.; Xu, G. Tunable electrical conductivity of a new 3D MOFs: Cu-TATAB. *Inorg. Chem. Commun.* **2019**, *105*, 119–124.

(89) Talin, A. A.; Centrone, A.; Ford, A. C.; Foster, M. E.; Stavila, V.; Haney, P.; Kinney, R. A.; Szalai, V.; El Gabaly, F.; Yoon, H. P.; Leonard, F.; Allendorf, M. D. Tunable Electrical Conductivity in Metal-Oragnic Framework Thin Film Devices. *Science* **2014**, *343*, 66–69.

(90) Neumann, T.; Liu, J.; Wächter, T.; Friederich, P.l.; Symalla, F.; Welle, A.; Mugnaini, V.; Meded, V.; Zharnikov, M.; Wöll, C.; Wenzel, W. Superexchange Charge Transport in Loaded Metal Organic Frameworks. *ACS Nano* **2016**, *10*, 7085–7093.

(91) Chen, X.; Wang, Z.; Hassan, Z. M.; Lin, P.; Zhang, K.; Baumgart, H.; Redel, E. Seebeck Coefficient Measurements of Polycrystalline and Highly Ordered Metal-Organic Framework Thin Films. *ECS J. Solid State Sci. technol.* **2017**, *6*, 150–153.

(92) Schneider, C.; Ukaj, D.; Koerver, R.; Talin, A. A.; Kieslich, G.; Pujari, S. P.; Zuilhof, H.; Janek, J.; Allendorf, M. D.; Fischer, R. A. High electrical conductivity and high porosity in a Guest@MOF material: evidence of TCNQ ordering within Cu3BTC2 micropores. *Chem. Sci.* **2018**, *9*, 7405–7412.

(93) Thürmer, K.; Schneider, C.; Stavila, V.; Friddle, R. W.; Léonard, F.; Fischer, R. A.; Allendorf, M. D.; Talin, A. A. Surface Morphology and Electrical Properties of Cu3BTC2 Thin Films Before and After Reaction with TCNQ. *ACS Appl. Mater. Interfaces* **2018**, *10*, 39400–39410.

(94) Wade, C. R.; Corrales-Sanchez, T.; Narayan, T. C.; Dincă, M. Postsynthetic tuning of hydrophilicity in pyrazolate MOFs to modulate water adsorption properties. *Energy Environ. Sci.* **2013**, *6*, 2172.

(95) Wentz, H. C.; Skorupskii, G.; Bonfim, A. B.; Mancuso, J. L.; Hendon, C. H.; Oriel, E. H.; Sazama, G. T.; Campbell, M. G. Switchable electrical conductivity in a three-dimensional metal-organic framework via reversible ligand n-doping. *Chem. Sci.* **2019**, *11*, 1342–1346.

(96) Guo, Z.; Panda, D. K.; Maity, K.; Lindsey, D.; Parker, T. G.; Albrecht-Schmitt, T. E.; Barreda-Esparza, J. L.; Xiong, P.; Zhou, W.; Saha, S. Modulating the electrical conductivity of metal–organic framework films with intercalated guest π-systems. *J. Mater. Chem. C* **2016**, *4*, 894–899.

(97) Qu, L.; Iguchi, H.; Takaishi, S.; Habib, F.; Leong, C. F.; D'Alessandro, D. M.; Yoshida, T.; Abe, H.; Nishibori, E.; Yamashita, M. Porous Molecular Conductor: Electrochemical Fabrication of Through-Space Conduction Pathways among Linear Coordination Polymers. *J. Am. Chem. Soc.* **2019**, *141*, 6802–6806.

(98) Kuang, X.; Chen, S.; Meng, L.; Chen, J.; Wu, X.; Zhang, G.; Zhong, G.; Hu, T.; Li, Y.; Lu, C.-Z. Supramolecular aggregation of a redox-active copper-naphthalenediimide network with intrinsic electron conduction. *Chem. Commun.* **2019**, *55*, 1643–1646.

(99) Chen, D.; Xing, H.; Su, Z.; Wang, C. Electrical conductivity and electroluminescence of a new anthracene-based metal-organic framework with π-conjugated zigzag chains. *Chem. Commun.* **2016**, *52*, 2019–2022.

(100) Bryce, M. R. Recent Progress on Conducting Organic Charge-Transfer Salts. *Chem. Soc. Rev.* **1991**, *20*, 355–390.

(101) Wudl, F.; Smith, G. M.; Hufnagel, E. J. Bis-1,3-dithiolium chloride: an unusually stable organic radical cation. *J. Chem. Soc. D* **1970**, 1453.

(102) Zhou, Y.; Yu, F.; Su, J.; Kurmoo, M.; Zuo, J.-L. Tuning Electrical- and Photo-Conductivity by Cation Exchange within a Redox-Active Tetrathiafulvalene-Based Metal-Organic Framework. *Angew. Chem. Int. Ed. Engl.* **2020**, *132*, 18922–18926.

(103) Park, S. S.; Hontz, E. R.; Sun, L.; Hendon, C. H.; Walsh, A.; van Voorhis, T.; Dincă, M. Cation-dependent intrinsic electrical conductivity in isostructural tetrathiafulvalene-based microporous metal-organic frameworks. *J. Am. Chem. Soc.* **2015**, *137*, 1774–1777.

(104) Sun, L.; Park, S. S.; Sheberla, D.; Dincă, M. Measuring and Reporting Electrical Conductivity in Metal-Organic Frameworks: Cd2(TTFTB) as a Case Study. *J. Am. Chem. Soc.* **2016**, *138*, 14772–14782.

(105) Su, J.; Hu, T.-H.; Murase, R.; Wang, H.-Y.; D'Alessandro, D. M.; Kurmoo, M.; Zuo, J.-L. Redox Activities of Metal-Organic Frameworks Incorporating Rare-Earth Metal Chains and Tetrathiafulvalene Linkers. *Inorg. Chem.* **2019**, *58*, 3698–3706.

(106) Xie, L. S.; Alexandrov, E. V.; Skorupskii, G.; Proserpio, D. M.; Dincă, M. Diverse π-π stacking motifs modulate electrical conductivity in tetrathiafulvalene-based metal-organic frameworks. *Chem. Sci.* **2019**, *10*, 8558–8565.

(107) Castells-Gil, J.; Mañas-Valero, S.; Vitórica-Yrezábal, I. J.; Ananias, D.; Rocha, J.; Santiago, R.; Bromley, S. T.; Baldoví, J. J.; Coronado, E.; Souto, M.; Mínguez Espallargas. Electronic, Structural and Functional Versatility in Tetrathiafulvalene-Lanthanide Metal-Organic Frameworks. *Chem. Eur. J.* **2019**, *25*, 12636–12643.

(108) Xie, L. S.; Park, S. S.; Chmielewski, M. J.; Liu, H.; Kharod, R. A.; Yang, L.; Campbell, M. G.; Dincă, M. Isoreticular Linker Substitution in Conductive Metal-Organic Frameworks with Through-Space Transport Pathways. *Angew. Chem.* **2020**, *132*, 1–5.

(109) Zhang, S.; Panda, D. K.; Yadav, A.; Zhou, W.; Saha, S. Effects of intervalence charge transfer interaction between π-stacked mixed valent tetrathiafulvalene ligands on the electrical conductivity of 3D metal–organic frameworks. *Chem. Sci.* **2021**, *120*, 8536.

(110) Heintz, R. A.; Zhao, H.; Ouyang, X.; Grandinetti, G.; Cowen, J.; Dunbar, K. R. New Insight into the Nature of Cu(TCNQ): Solution Routes to Two Distinct Polymorphs and Their Relationship to Crystalline Films That Display Bistable Switching Behavior. *Inorg. Chem.* **1999**, *38*, 144–156.

(111) Fernandez, C. A.; Martin, P. C.; Schaef, T.; Bowden, M. E.; Thallapally, P. K.; Dang, L.; Xu, W.; Chen, X.; McGrail, B. P. An electrically switchable metal-organic framework. *Sci Rep* **2014**, *4*, 6114.

(112) Avendano, C.; Zhang, Z.; Ota, A.; Zhao, H.; Dunbar, K. R. Dramatically different conductivity properties of metal-organic framework polymorphs of Tl(TCNQ): an unexpected room-temperature crystal-to-crystal phase transition. *Angew. Chem. Int. Ed. Engl.* **2011**, *50*, 6543–6547.

(113) Kobayashi, H. *Bull. Chem. Soc. Jpn.* **1981**, *54*, 3669.

(114) Konno, M.; Saito, Y. *Acta Crystallogr. Sect. B* **1974**, *30*, 1294.

(115) Kumai, R.; Okimoto, Y.; Tokura, Y. *Science* **1999**, *284*, 1645.

(116) Shields, L. *J. Chem. Soc. faraday Trans. 2* **1985**, *81*, 1.

(117) Wang, H.-Y.; Su, J.; Ma, J.-P.; Yu, F.; Leong, C. F.; D'Alessandro, D. M.; Kurmoo, M.; Zuo, J.-L. Concomitant Use of Tetrathiafulvalene and 7,7,8,8-Tetracyanoquinodimethane within the Skeletons of Metal-Organic Frameworks: Structures, Magnetism, and Electrochemistry. *Inorg. Chem.* **2019**, *58*, 8657–8664.

(118) Hmadeh, M.; Lu, Z.; Liu, Z.; Gándara, F.; Furukawa, H.; Wan, S.; Augustyn, V.; Chang, R.; Liao, L.; Zhou, F.; Perre, E.; Ozolins, V.; Suenaga, K.; Duan, X.; Dunn, B.; Yamamto, Y.; Terasaki, O.; Yaghi, O. M. New Porous Crystals of Extended Metal-Catecholates. *Chem. Mater.* **2012**, *24*, 3511–3513.

(119) Sheberla, D.; Sun, L.; Blood-Forsythe, M. A.; Er, S.; Wade, C. R.; Brozek, C. K.; Aspuru-Guzik, A.; Dincă, M. High electrical conductivity in Ni_3(2,3,6,7,10,11-hexaiminotriphenylene)$_2$, a semiconducting metal-organic graphene analogue. *J. Am. Chem. Soc.* **2014**, *136*, 8859–8862.

(120) Skorupskii, G.; Trump, B. A.; Kasel, T. W.; Brown, C. M.; Hendon, C. H.; Dincă, M. Efficient and tunable one-dimensional charge transport in layered lanthanide metal-organic frameworks. *Nat. Chem.* **2020**, *12*, 131–136.

(121) Skorupskii, G.; Dincă, M. Electrical Conductivity in a Porous, Cubic Rare-Earth Catecholate. *J. Am. Chem. Soc.* **2020**, *142*, 6920–6924.

(122) Mähringer, A.; Döblinger, M.; Hennemann, M.; Gruber, C.; Fehn, D.; Scheurle, P. I.; Hosseini, P.; Santourian, I.; Schirmacher, A.; Rotter, J. M.; Wittstock, G.; Meyer, K.; Clark, T.; Bein, T.; Medina, D. D. An electrically conducting three-dimensional iron-catecholate porous framework. *Angew. Chem.* **2021**, *133*, 18213–18220.

(123) Yadav, A.; Panda, D. K.; Zhang, S.; Zhou, W.; Saha, S. Electrically Conductive 3D Metal-Organic Framework Featuring π-Acidic Hexaazatriphenylene Hexacarbonitrile Ligands with Anion-π Interaction and Efficient Charge-Transport Capabilities. *ACS Appl. Mater. Interfaces* **2020**, *12*, 40613–40619.

(124) Dou, J.-H.; Sun, L.; Ge, Y.; Li, W.; Hendon, C. H.; Li, J.; Gul, S.; Yano, J.; Stach, E. A.; Dincă, M. Signature of Metallic Behavior in the Metal-Organic Frameworks M3(hexaiminobenzene)2 (M = Ni, Cu). *J. Am. Chem. Soc.* **2017**, *139*, 13608–13611.

(125) Feng, D.; Lei, T.; Lukatskaya, M. R.; Park, J.; Huang, Z.; Lee, M.; Shaw, L.; Chen, S.; Yakovenko, A. A.; Kulkarni, A.; Xiao, J.; Fredrickson, K.; Tok, J. B.; Zou, X.; Cui, Y.; Bao, Z. Robust and conductive two-dimensional metal-organic frameworks with excep-tionally high volumetric and areal capacitance. *Nat. Energy* **2018**, *1*, 30–36.

(126) Park, J.; Lee, M.; Feng, D.; Huang, Z.; Hinckley, A. C.; Yakovenko, A.; Zou, X.; Cui, Y.; Bao, Z. Stabilization of Hexaaminobenzene in a 2D Conductive Metal-Organic Framework for High Power Sodium Storage. *J. Am. Chem. Soc.* **2018**, *140*, 10315–10323.

(127) Yücesan, G.; Zorlu, Y.; Stricker, M.; Beckmann, J. Metal-organic solids derived from arylphosphonic acids. *Coord. Chem. Rev.* **2018**, *369*, 105–122.

(128) Peeples, C. A.; Kober, D.; Schmitt, F.-J.; Tholen, P.; Siemensmeyer, K.; Halldorson, Q.; Çoşut, B.; Gurlo, A.; Yazaydin, A. O.; Hanna, G.; Yücesan, G. A 3D Cu-Naphthalene-Phosphonate Metal–Organic Framework with Ultra-High Electrical Conductivity. *Adv. Funct. Mater.* **2021**, *31*, 2007294.

(129) Siemensmeyer, K.; Peeples, C. A.; Tholen, P.; Schmitt, F.-J.; Çoşut, B.; Hanna, G.; Yücesan, G. Phosphonate Metal-Organic Frameworks: A Novel Family of Semiconductors. *Adv. Mater.* **2020**, *32*, e2000474.

(130) Siemensmeyer, K.; Peeples, C. A.; Tholen, P.; Schmitt, F.-J.; Çoşut, B.; Hanna, G.; Yücesan, G. Phosphonate Metal-Organic Frameworks: A Novel Family of Semiconductors. *Adv. Mater.* **2020**, *32*, e2000474.

(131) Bulut, A.; Zorlu, Y.; Wörle, M.; Çetinkaya, A.; Kurt, H.; Tam, B.; Yazaydın, A. Ö.; Beckmann, J.; Yücesan, G. Short Naphthalene Organophosphonate Linkers to Microporous Frameworks. *ChemistrySelect* **2017**, *2*, 7050–7053.

(132) Bulut, A.; Zorlu, Y.; Wörle, M.; Paşa, S.; Kurt, H.; Zubieta, J.; Beckmann, J.; Yücesan, G. Rational Design of Two-Dimensional Bimetallic Wave Structures from Zigzag Chains via Site-Specific Coordination around the 2,6-Naphthalenediphosphonic Acid Motif. *Eur. J. Inorg. Chem.* **2016**, *2016*, 3506–3512.

(133) Zorlu, Y.; Tholen, P.; Ayhan MM.; Ceyda, B.; Hanna, G.; Yazaydin, A. O.; Yavuzcetin, O.; Yücesan, G. High Electrical Conductivity in Three-Dimensional Porphyrin-Phosphonate Metal Organic-Frameworks. *ChemRxiv. Cambridge: Cambridge Open Engage; 2021;*.

(134) Peeples, C. A.; Çetinkaya, A.; Schmitt, F.-J.; Tholen, P.; Zorlu, Y.; Yu, K.; Yazaydin, A. O.; Beckmann, J.; Hanna, G.; Yücesan, G. A 3D Cu-Phosphonate Metal-Organic Framework with Cu-Coordination-Enhanced Electrical Conductivity. *ChemRxiv. Cambridge: Cambridge Open Engage; 2021;*.

(135) Huizi-Rayo, U.; Gutierrez, J.; Seco, J. M.; Mujica, V.; Diez-Perez, I.; Ugalde, J. M.; Tercjak, A.; Cepeda, J.; San S., E. An Ideal Spin Filter: Long-Range, High-Spin Selectivity in Chiral Helicoidal 3-Dimensional Metal Organic Frameworks. *Nano Lett.* **2020**, *20*, 8476–8482.

(136) Scheurle, P. I.; Mähringer, A.; Jakowetz, A. C.; Hosseini, P.; Richter, A. F.; Wittstock, G.; Medina, D. D.; Bein, T. A highly crystalline anthracene-based MOF-74 series featuring electrical conductivity and luminescence. *Nanoscale* **2019**, *11*, 20949–20955.

(137) Sun, L.; Hendon, C. H.; Park, S. S.; Tulchinsky, Y.; Wan, R.; Wang, F.; Walsh, A.; Dincă, M. Is iron unique in promoting electrical conductivity in MOFs? *Chem Sci* **2017**, *8*, 4450–4457.

(138) Manumpil, M. A.; Leal-Cervantes, C.; Hudson, M. R.; Brown, C. M.; Karunadasa, H. I. Electronic Conductivity in a Porous Vanadyl Prussian Blue Analogue upon Air Exposure. *Inorg. Chem.* **2017**, *56*, 12682–12686.

(139) Rieth, A. J.; Tulchinsky, Y.; Dincă, M. High and Reversible Ammonia Uptake in Mesoporous Azolate Metal-Organic Frameworks with Open Mn, Co, and Ni Sites. *J. Am. Chem. Soc.* **2016**, *138*, 9401–9404.

(140) Zhou, X.-H.; Peng, Y.-H.; Du, X.-D.; Zuo, J.-L.; You, X.-Z. Hydrothermal syntheses and structures of three novel coordination polymers assembled from 1,2,3-triazolate ligands. *CrystEngComm* **2009**, *11*, 1964.

(141) Gándara, F.; Uribe-Romo, F. J.; Britt, D. K.; Furukawa, H.; Lei, L.; Cheng, R.; Duan, X.; O'Keeffe, M.; Yaghi, O. M. Porous, conductive metal-triazolates and their structural elucidation by the charge-flipping method. *Chem. Eur. J.* **2012**, *18*, 10595–10601.

(142) Wu, X.; Qiu, Y.; Chen, Z.; Guan, B.; Hao, X.; Rykov, A. I.; Sun, Y.; Liu, L.; Zou, Y.; Sun, J.; Xu, W.; Zhu, D. Paramagnetic Conducting Metal-Organic Frameworks with Three-Dimensional Structure. *Angew. Chem. Int. Ed. Engl.* **2020**, 20873–20878.

(143) Jesse G. Park, Michael L. Aubrey, Julia Oktawiec, Khetpakorn Chakarawet, Lucy E. Darago, Fernande Grandjean, Gary J. Long, and Jeffrey R. Long. Charge Delocalization and Bulk Electronic Conductivity in the Mixed-Valence Metal-Organic Framework Fe(1,2,3-triazolate)2(BF4)x. *J. Am. Chem. Soc.* **2018**, *140*, 8526–8534.

(144) Aubrey, M. L.; Wiers, B. M.; Andrews, S. C.; Sakurai, T.; Reyes-Lillo, S. E.; Hamed, S. M.; Yu, C.-J.; Darago, L. E.; Mason, J. A.; Baeg, J.-O.; Grandjean, F.; Long, G. J.; Seki, S.; Neaton, J. B.; Yang, P.; Long, J. R. Electron delocalization and charge mobility as a function of reduction in a metal-organic framework. *Nat. Mater.* **2018**, *17*, 625–632.

(145) Xie, L. S.; Sun, L.; Wan, R.; Park, S. S.; DeGayner, J. A.; Hendon, C. H.; Dincă, M. Tunable Mixed-Valence Doping toward Record Electrical Conductivity in a Three-Dimensional Metal-Organic Framework. *J. Am. Chem. Soc.* **2018**, *140*, 7411–7414.

(146) Yan, Z.; Li, M.; Gao, H.-L.; Huang, X.-C.; Li, D. High-spin versus spin-crossover versus low-spin: geometry intervention in cooperativity in a 3D polymorphic iron(II)-tetrazole MOFs system. *Chem. Commun.* **2012**, *48*, 3960–3962.

(147) Darago, L. E.; Aubrey, M. L.; Yu, C. J.; Gonzalez, M. I.; Long, J. R. Electronic Conductivity, Ferrimagnetic Ordering, and Reductive Insertion Mediated by Organic Mixed-Valence in a Ferric Semiquinoid Metal-Organic Framework. *J. Am. Chem. Soc.* **2015**, *137*, 15703–15711.

(148) Pathak, A.; Shen, J.-W.; Usman, M.; Wei, L.-F.; Mendiratta, S.; Chang, Y.-S.; Sainbileg, B.; Ngue, C.-M.; Chen, R.-S.; Hayashi, M.; Luo, T.-T.; Chen, F.-R.; Chen, K.-H.; Tseng, T.-W.;

Chen, L.-C.; Lu, K.-L. Integration of a (-Cu-S-)n plane in a metal-organic framework affords high electrical conductivity. *Nat. Commun.* **2019**, *10*, 1721.

(149) Wuttke, S.; Median, D. D.; Rotter, J. M.; Begun, S.; Stassin, T.; Ameloot, R.; Oschatz, M.; Tsotsalas, M. Bringing Porous Organic and Carbon-Based Materials toward Thin-Film Applications. *Adv. Funct. Mater.* **2018**, *28*, 1801545.

(150) Cruz, A. J.; Stassen, I.; Krishtab, M.; Marcoen, K.; Stassin, T.; Rodriguez-Hermida, S.; Teyssandier, J.; Pletincx, S.; Verbeke, R.; Rubio-Gimenez, V.; Tatay, S.; Mart-Gastaldo, C.; Meersschaut, J.; Vereecken, P. M.; Feyter, S. de; Hauffman, T.; Ameloot, R. Integrated Cleanroom Process for the Vapor-Phase Deposition of Large-Area Zeolitic Imidazolate Framework Thin Films. *Chem. Mater.* **2019**, *31*, 9462–9471.

(151) Rotter, J. M.; Weinberger, S.; Kampmann, J.; Sick, T.; Shalom, M.; Bein, T.; Melville, J. F. Covalent Organic Framework Films through Electrophoretic Deposition—Creating Efficient Morphologies for Catalysis. *Chem. Mater.* **2019**, *31*, 10008–10016.

(152) Hoppe, B.; Hindricks, K. D. J.; Warwas, D. P.; Schulze, H. A.; Mohmeyer, A.; Pinkvos, T. J.; Zailskas, S.; Krey, M. R.; Belke, C.; König, S. Fröba, M.; Haug, R.J.; Behrens, P. *CrystEngComm* **2018**, *20*, 6458-6471.

(153) Sheberla, D.;Sun, L.; Blood-Forsythe, Er, S.; Wade, C. R.; Brozek, C. K.; Aspuru-Guzik, A.; Dinca, M. *J.Am.Chem.Soc.* **2014**, *136*, 8859.

(154) Yao, M. S.; Lv, X. J.; Fu, Z. H.; Li, W. H.; Deng, W. H.; Wu, G. D.; Xu, G. *Angew. Chem. Int. Ed.* **2017**, *56*, 16510.

(155) Mähringer, A.; Hennemann, M.; Clark, T.; Bein, T.; Medina, D. D. Energy Efficient Ultrahigh Flux Separation of Oily Pollutants from Water with Superhydrophilic Nanoscale Metal-Organic Framework Architectures. *Angewandte Chemie* **2021**, *60*, 5519–5526.

(156) Mähringer, A.; Jakowetz, A. C.; Rotter, J. M.; Bohn, B. J.; Stolarczyk, J. K.; Feldmann, J.; Bein, T.; Medina, D. D. Oriented Thin Films of Electroactive Triphenylene Catecholate-Based Two-Dimensional Metal-Organic Frameworks. *ACS Nano* **2019**, *13*, 6711–6719.

(157) Mähringer, A.; Rotter, J. M.; Medina, D. D. Nanostructured and oriented metal-organic framework films enabling extreme surface wetting properties. *Beilstein J Nanotechnol* **2019**, *10*, 1994–2003.

(158) Virmani, E.; Rotter, J. M.; Mähringer, A.; Zons, T. von; Godt, A.; Bein, T.; Wuttke, S.; Medina, D. D. On-Surface Synthesis of Highly Oriented Thin Metal-Organic Framework Films through Vapor-Assisted Conversion. *J. Am. Chem. Soc.* **2018**, *140*, 4812–4819.

2 Characterization techniques

2.1 X-ray diffraction (XRD)

X-ray diffraction plays a key role in the characterization of the phase composition and in the structure determination of crystalline materials in form of powders, films or single crystals of several compound types. It is also useful for the study of unit cell dimensions, the determination of preferential orientations in crystalline films, as well as for the determination of the size of sub-micrometer crystallites in a solid. For the investigation of structural information on metal-organic frameworks, XRD analysis is crucial and can give information about the atomic arrangement within the crystal.

The construction of an X-ray diffractometer is divided into three basic elements: The X-ray tube, the sample holder and the X-ray detector. For producing X-rays in a cathode ray tube, a filament is heated, which generates electrons. By applying a voltage, these electrons are accelerated and bombard a metal target. Some electrons lose their energy when colliding with the metal, which leads to a continuous radiation (Bremsstrahlung). When the electrons have enough energy to displace electrons of the inner shells of the target material, higher energy levels fill the voids with electrons and characteristic X-ray radiation is created. The radiation has several components such as Kα and Kβ. Cobalt, molybdenum, iron, chromium and copper are popular target materials, with copper being a very common one, having a wavelength of Cu Kα radiation = 1.5418 Å. The high intensity, nearly monochromatic Kα X-rays can be used as a radiation source for XRD studies, by filtering the X-rays. During the measurement, the detector and sometimes also the sample are rotated. The monochromatic X-rays are bundled as an incident beam and focused onto the sample, where they interfere constructively with each other.[2] The crystalline phases in the sample diffract the beam according to Bragg´s law. However, only when parallel X-rays are phase-separated by an integer number *n*, constructive interference can occur: [3]

$$n\lambda = 2d\,sin\theta \qquad (1)$$

The law was established by the Braggs and awarded with the Nobel price in 1915.[4] It describes the constructive interference with: d = spacing between atomic planes in the crystalline phase; Θ = the incident angle and λ = X-ray wavelength. When each object in a periodic array scatters radiation in a coherent way, diffraction can occur, which generates distinct intensity patterns. The electrons of the irradiated atoms of the crystal scatter the light consistently and interact with the oscillating electric field of the light wavelength. If the wavelength of the X-rays, which is between 10 pm and 10 nm, corresponds approximately to the distance between the atoms in the periodic arrangement, then the effect of diffraction is greatest. As a result, diffraction from different planes

of atoms creates a diffraction pattern that contains information about the atomic arrangement in the crystal. The specific angles of diffraction in a pattern depend on the distance of the atoms, which enables the identification of the material. This signal is recoreded by the detector and converted to a count rate, which is output to a device such as a printer or a computer monitor.[2]

Due to the random crystallite orientation in a polycrystalline powder, the sample scan goes through a range of 2 Θ angles to obtain all possible diffraction directions of the lattice. However, amorphous materials do not have a periodic array with long range order and do not produce a diffraction pattern with diffferent intensities. For samples with a crystalline texture whose grains are preferentially oriented, e.g., crystalline films, the diffraction intensities of specific crystallographic reflections for these sample orientations are reduced compared to the intensities calculated for a randomly oriented polycrystal.

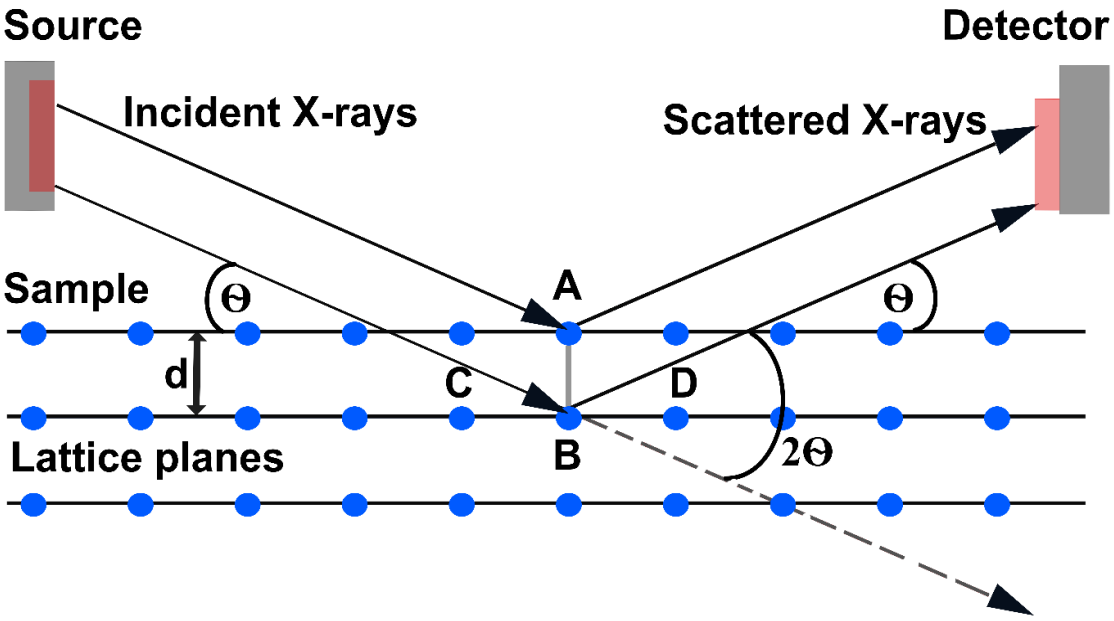

Figure 2-1: Schematic illustration of the Bragg diffraction: Two incident X-ray beams are focused on a crystalline sample, reflected by crystal planes and detected by a detector, which is placed in such a way that the angles of the incident and of the scattered X-rays are the same.

2.2 Grazing-incidence X-ray scattering (GIXS)

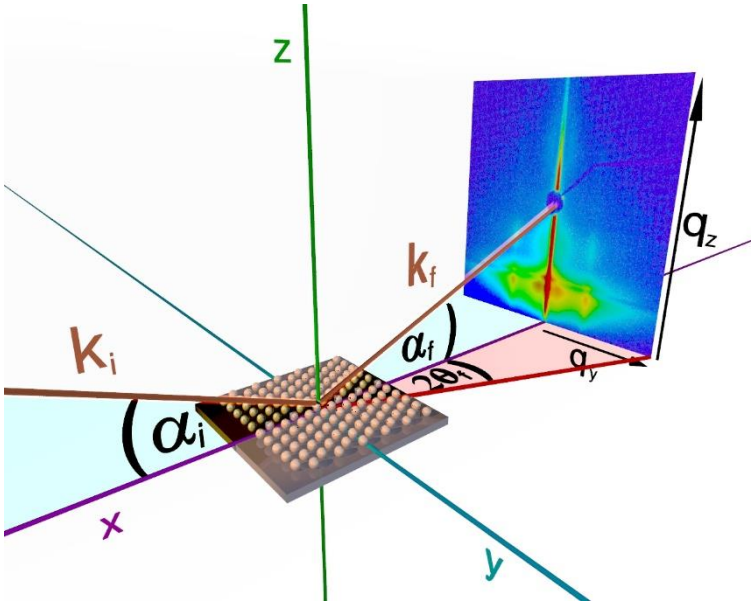

Figure 2-2: An image of the scattering geometry in a GISAXS experiment.[1]

Grazing-Incidence X-ray Scattering is a highly sensitive technique for the characterization of crystalline surfaces. It was first established in the year 1989 for the analysis of gold particles on a silicon substrate.[5,6] Compared to conventional XRD scanning methods, a planar sample is illuminated at grazing angle of incidence, with the angle of the incident beam below the critical angle of the substrate. As a consequence, even thin films with low sample thicknesses can be analyzed, in contrast to general X-ray scattering geometries. The scattering geometry in a grazing-incidence small-angle X-ray scattering measurement is shown in Figure 2-2. The sample-detector distance is often (although not in all instruments) over 2 m, in comparison to a much shorter distance in a grazing-incidence wide-angle X-ray scattering (GIWAXS) experiment.[7] A monochromatic X-ray beam, described by the wavevector k_i, is focused on a surface at a small incident angle α_i. The intensities of the scattered X-rays along the wavevector k_f are collected with a 2D area detector in the directions $2\Theta_f$ and α_f. As a result, the positions of the detected scattering spots are recorded as the wavelength independent scattering vector q.[1] These q values are related to 2Θ angles with the following equation:[1]

$$q = \frac{4\pi}{\lambda} \sin\frac{2\Theta}{2} \qquad (2)$$

The accessible length scales of GISAXS experiments are typically in the range of several nanometers to hundreds of nanometers, which makes them interesting for the study of materials with large unit cells, crystal morphology and domain sizes. Since the length scale in GIWAXS experiments can go down to the atomic range, the reflections in the scattering pattern originate from

crystal planes indicated by Miller indices (hkl) in the reciprocal lattice. It is an ideal technique to study the crystallinity and orientation of thin metal-organic framework layers on flat substrates. A preferential MOF crystallite orientation on the substrate is visualized with scattering spots in the 2D GIWAXS pattern, instead of the formation of Debye-Scherrer rings with homogeneous intensity distribution, which is typical for non-oriented materials.[7]

2.3 Gas sorption

The characteristic features of porous materials like MOFs, such as the surface area, pore size and pore volume, can be examined by gas sorption measurements. The porosity of a sample is defined as the ratio of the total pore volume to the particle volume or mass. During an adsorption process, molecules, atoms or ions accumulate in the proximity of an interface. Two types of adsorption can be distinguished. Firstly, chemisorption, which involves chemical bonding, and secondly, physisorption. During chemisorption, the chemisorbed molecules build bonds to parts of the surface, typically covering it as a monolayer. While this process is usually linked to high heats of adsorption, physisorption is associated only with a small heat exchange with the environment. In addition, surface coverage is not limited to one layer and occurs as a multilayer at higher relative pressures. Also, the chemical structure does not change during physisorption. The physical interactions between the inert gas (adsorptive) and the sample surface (adsorbent) are essentially van der Waals forces. The sample surface (adsorbent) can be covered by the adsorptive externally, outside of the pores, and internally, inside the pores. Another difference between the two sorption types is the fact that the physisorbed molecules (adsorbate) are in dynamic equilibrium with the adsorptive. Due to the reversible interaction between adsorptive and adsorbent, the fluid phase returns to the same form after desorption. In comparison, a chemisorbed molecule typically cannot be recovered by desorption due to reactions or dissociations during the adsorption process, rendering the sorption isotherms irreversible.[8] In order to categorize porous materials, the IUPAC has defined them in 1985 by their pore diameter, with macropores having pore widths exceeding about 50 nm, mesopores with intermediate sizes between 2 – 50 nm and micropores not exceeding 2 nm. [9] The IUPAC has defined eight types of physisorption isotherms, which can be created after plotting the relative pressure of the adsorptive against the amount of the adsorbed gas at standard pressure and constant temperature (see Figure 2-3). [9]

Reversible type I isotherms are typical for microporous adsorbents. They have a steep onset at low relative pressures. This micropore filling leads to saturation, which is defined by the micropore volume. Type I(a) isotherm is typical for narrow micropores (< ~1 nm) and type I(b) for materials exhibiting wider micropores, or rather narrow mesopores (< ~ 2.5 nm).

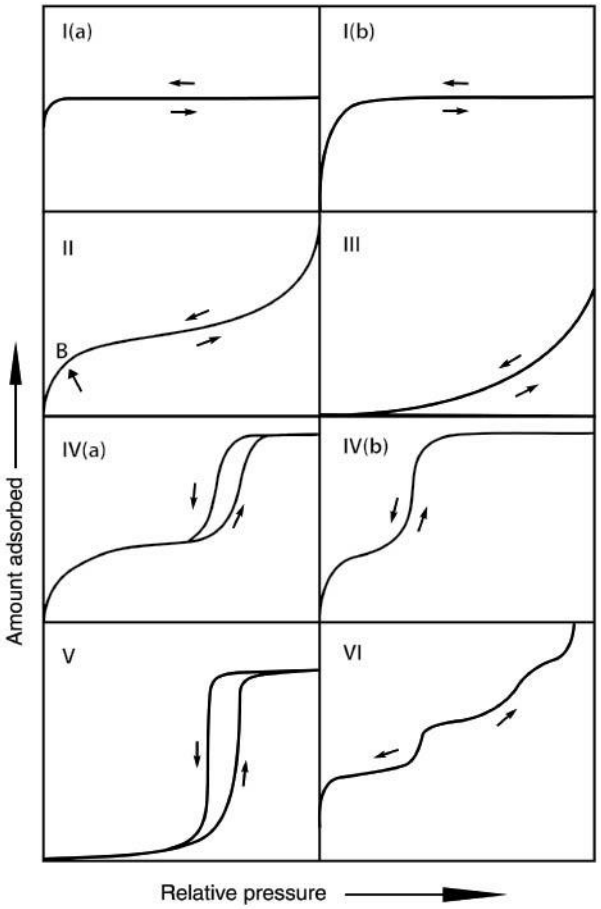

Figure 2-3: IUPAC classificiation of physisorption isotherms.[9]

The reversible type II isotherm comes with nonporous or macroporous adsorbents. The first uptake is due to monolayer coverage followed by multilayer adsorption. Point B marks the transition point between monolayer and multilayer adsorption.

Type III isotherms represent nonporous or microporous materials that show weak interactions with the adsorbate.

Type IV isotherms show the behaviour of mesoporous adsorbents. A monolayer coverage and multilayer adsorption are followed by pore condensation, which leads to a saturation of the adsorbate by pore filling. Pore condensation is the condensation of a gas inside a pore to a liquid-like phase. In type IV(a) isotherms, this capillary condensation leads to a hysteresis during the desorption process, with mesopores larger than the critical width of ~ 4 nm. In contrast, type IV(b) isotherms are fully reversible, without hysteresis, typical for mesopores under the critical width of ~ 4 nm, as well as for conical and cylindrical pores closed at one end.

Type V isotherms can be detected for water adsorption on hydrophobic microporous or mesoporous materials. Weak interactions between the adsorbent and the adsorbate are typical, in addition with pore filling and a hysteresis.

The reversible type VI isotherms are common for nonporous materials, exhibiting a highly uniform surface. Each step in the uptake is representative for an adsorbed monolayer.[9]

A first model for monolayer adsorption and surface coverage Θ was established by Langmuir. During monolayer adsorption, all potential adsorption sites are uniform and form a flat surface, without interactions between them or with particles.

$$\boldsymbol{\theta = \frac{n^a}{n_m^a} = \frac{K_p}{1 + K_p}} \qquad (3)$$

In this formula, n_a stands for the adsorbed amount of gas, $n^a{}_m$ for the monolayer capacity, K for a constant rate of the sorption process and p for the respective pressure. [9]

However, for the determination of the surface area, the Brunauer-Emmett-Teller model (BET) is the most common method, which is an extension of the Langmuir model and also considers multilayer adsorption by adding the following assumptions: The first monolayer has a different adsorption enthalpy in comparison to the following multilayers. The adsorbed molecules in the following multilayers have a liquid-like behaviour, whereby the layer right at the top and the vapour phase are in equilibrium with each other. Moreover, there are no interactions between the adsorption layers.[10]

After the transformation of the physisorption isotherm into the "BET plot", the BET monolayer capacity n_m can be obtained, with n_m and the molecular cross-section area σ and the BET-area α. The BET equation is applied in the linear form:

$$\frac{p/p^0}{n(1 - \frac{p}{p^0})} = \frac{1}{n_m C} + \frac{C - 1}{n_m C}(\frac{p}{p^0}) \qquad (4)$$

Here, with n the adsorbed amount at the relative pressure p/p^0, p the eqilibrium pressure, p^0 the saturation pressure, n_m the specific monolayer capacity and C the BET constant.[10]

The following equation gives the total surface area a_s, if the molecular cross-sectional area σ_m (the area occupied by the adsobring molecule) and the mass of the adsorbent m are known (N_A is the Avogadro constant).

$$\boldsymbol{a_s(BET) = \frac{N_A}{m} n_m \sigma_m} \qquad (5)$$

There are three definitions of relevant surfaces in sorption experiments (see Figure 2-4).[9] The first is the *van der Waals surface*, which is a computed surface constructed by spheres around atoms, where the radius of each sphere is equal to the van der Waals radius of the respective atom. The *Connolly surface area* comprises the area accessible by rolling a probe molecule of radius r over

the van der Waals surface. The *accessible suface area* is the area that is reachable to a solvent sphere, i.e., the area which is covered by the center of the probe molecule due the rolling process.[9]

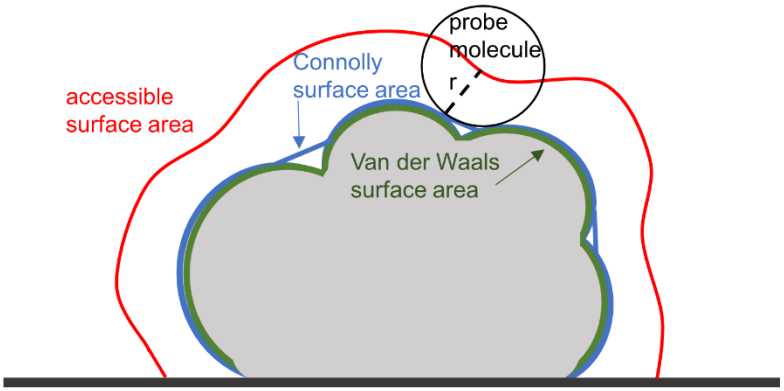

Figure 2-4: Schematic graphic of the possible hypothetical surfaces in sorption experiments.

From the obtained isotherms, the pore size distribution (PSD) can be determined:

$$\ln\left(\frac{p}{p_0}\right) = \frac{-2\gamma V_m}{RT(r_p - t_c)} \qquad (6)$$

In the formula, r_p is the pore radius, t_c describes the thickness of the adsorbed multilayer before condensation in the pores occurs, γ is the surface tension of the bulk fluid, and V_m is the molar liquid volume.[9,10] However, in narrow mesopores below a diameter of 10 nm, enhanced surface forces can occur, which could lead to an underestimation of the pore size by using the above equation.

The most traditional procedure for sorption measurements for MOF powders is the common nitrogen adsorption at 77 K, which is the temperature of liquid nitrogen. However, argon sorption measurements at 87 K are faster and more accurate, because argon has no quadrupole moment in comparison to nitrogen, which can show specific quadrupole interactions with the micropore surface. This leads to a direct correlation between argon pore filling pressures and the pore size of the material and therefore it is better suitable for microporous systems. Due to the monoatomic structure of argon, the orientation on the surface is consistent, leading to a clear cross-sectional area, which is important for the calculation of the surface area. The cross-sectional area is defined as the occupied area by an adsorbed molecule in a complete monolayer. In contrast, the specific interactions between nitrogen and polar hydroxyl groups can affect the orientation of the adsorbed nitrogen molecules. For materials with very low surface areas, for example MOF films, the use of krypton at 77 K is preferred due to its enhanced sensitivity. Krypton has a lower vapor pressure and low sublimation level at 77 K. In a measurement, the gas adsorption amount is calculated

from the difference between the number of dosed molecules and of molecules not adsorbed at equilibrium pressure. Due to the high saturation pressure of nitrogen at its boiling point, there is a large number of non-adsorbed molecules in the sample cell that can be reduced when using krypton. This results in a more accurate measurement of a larger relative pressure change.[9]

2.4 Thermogravimetric analysis

Thermogravimetric analysis (TGA) can be used to determine the thermal stability in MOFs. Furthermore, molecules trapped inside the pores like solvents or ligand residues can be detected. During an increasing temperature achieved with a heating program, the change in mass of the sample over a time period is analyzed. The sample can be investigated under different atmospheres while it is heated, including synthetic air, inert gases or vacuum. During the heating process, a precision balance detects the mass losses, or depending on the sample, the increase in mass. During this procedure, the sample can undergo different processes such as evaporation, decomposition, reduction and oxidation.[11]

2.5 Ultraviolet-visible (UV-Vis) spectroscopy

By irradiation of a sample with ultraviolet (UV) and visible (Vis) light, the valence electrons can be excited to energetically higher molecular orbitals. With σ-, π- and non bonding *n* electrons, the possible transitions are summarized in Figure 2-5.

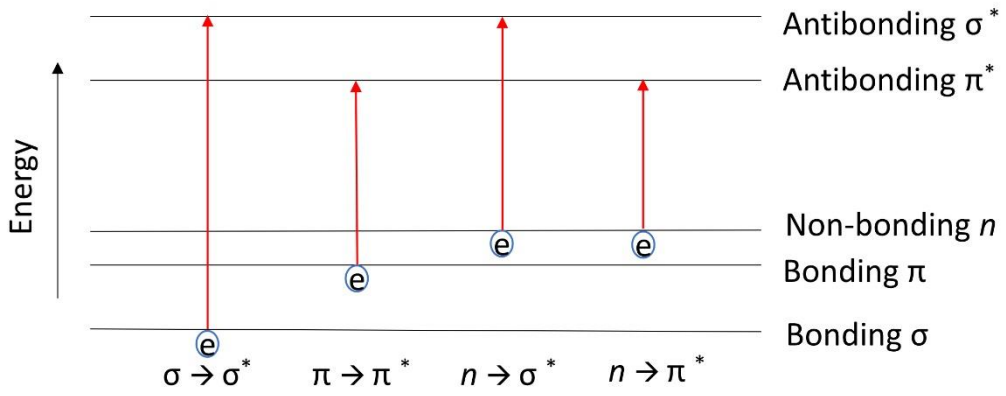

Figure 2-5: Possible electronic transitions of samples containing σ-, π- and *n*-electrons.

During a UV-Vis measurement, a sample is absorbing a certain ratio of the initial itensity I_0 at specific wavelengths. The Lambert-Beer law describes the correlation between the measured intensity of light transmitted by the sample, the concentration of the absorbing sample during the measurement and the sample thickness (best applicable for measurements on gases and dilute solutions:[12]

$$\boldsymbol{A = -log_{10}\frac{I}{I_0} = \varepsilon \cdot c \cdot L} \qquad (7)$$

With A = absorbance, I = intensity of transmitted light, I_0 = intensity of incident light, ε = extinction coefficient, c = concentration of the absorbing sample, L = length in medium.

The Lambert-Beer law does not fully cover the optical behavior of thin films, which are often synthesized on transparent substrates. Therefore, a different technique is necessary. The substrate causes reflection of the light at the interfaces between air, substrate and sample during the measurement. As a consequence, a procedure is necessary that does not neglect the reflectance and scattering processes. Therefore, the transmittance and the reflectance of the samples are measured separately. During the measurement of the transmittance, the film is located inside an integrating sphere in front of the transmission hole. For the reflectance measurement, the film is placed outside the integrating sphere. Under the assumption that 100 % of the light is either absorbed, reflected/scattered or transmitted, the percentage absorbance of the sample can be calculated with the formula:

$$\boldsymbol{\%T + \%R + \%A = 1} \qquad (8)$$

The absolute absorbance A can be calculated with:

$$\boldsymbol{A = -log_{10}(1 - \%A)} \qquad (9)$$

The optical band gap of a sample is the energy difference between the HOMO (highest occupied molecul orbital) energy level and the LUMO (lowest unoccupied molecule orbital) (here we simplify the discussion by considering excitations in molecules and semiconductors to be similar). To excite an electron from the HOMO to the LUMO, the absorbed photon needs to provide the same energy amount as the band gap, whereas the energy of the photon depends on the wavelength. An excitation into higher vibrational states is also possible with a higher energy amount than the band gap. By using the Tauc plot formalism, the absorbance can be used for the determination of the optical band gap E_g:

$$\boldsymbol{(\alpha h\nu)^{1/r} = A\,(h\nu - E_g)} \qquad (10)$$

With a = absorption coefficient/ absolute absorbance, ν = frequency of light, h = Planck´s constant, A = proportionality constant.

The value of *r* can vary between 0.5, 1.5, 2 and 3, which depends on the type of transition, ranging from direct allowed, direct forbidden to indirect allowed and indirect forbidden. For the MOFs investigated in this work, we assumed a direct band gap, causing the value of $r = 0.5$ for the bandgap calculations. A graph results where the first absorption band is rising in the absorbance spectrum. This absorption band has a linear region just before y = 0, which needs to be extrapolated to the abscissa, resulting in the estimated energy of the optical band gap of the sample (see Figure 2-6).[12]

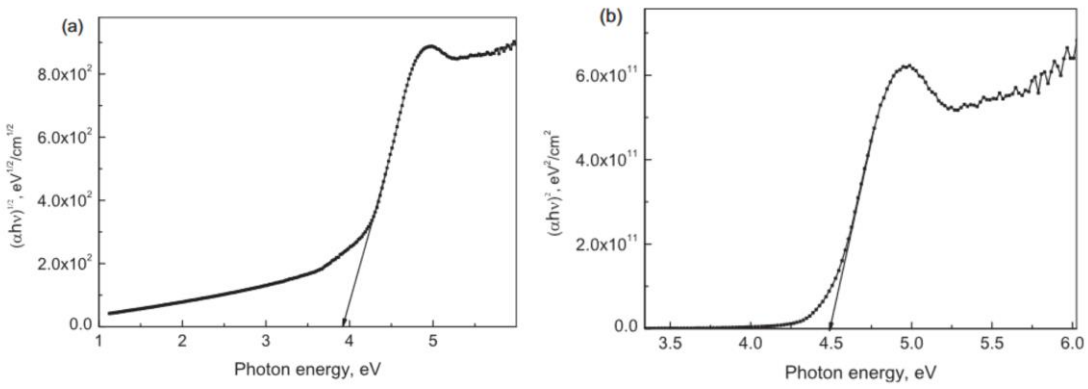

Figure 2-6: Exemplary Tauc plots for (a) indirect band gap and (b) direct band gap.[13]

For absorption measurements of non-tranlucent solids (powder samples), the diffuse reflectance of the sample can be evaluated by applying the Kubelka-Munk (KM) formalism. Here, the assumption is made that scattering is more common than absorption on solid materials and that reflection is insignificant on solid surfaces. Barium sulfate is used as white standard and the diffuse reflectance *R* of the sample is referenced to it. In order to obtain a spectrum of the absorption behaviour of the sample, the KM equation is used:[14]

$$\boldsymbol{KM = \frac{(1-R)^2}{2R}} \qquad (11)$$

2.6 Photoluminescence spectroscopy (PL)

Photoluminescence spectroscopy is a method for characterizing the electronic structure of materials, the optoelectronic properties of semiconductors and for observing defects in the interface region. Irradiated light is absorbed by the sample, followed by photoexcitation and relaxation under emission of light. The relaxation or recombination process typically describes the transition from the electronic excited state S_1 to the ground state S_0, which involves radiative and non-radiative processes. The radiative process describes the band-to-band recombination, whereby the excess energy is released by the emission of light, which means that a photon is emitted when an

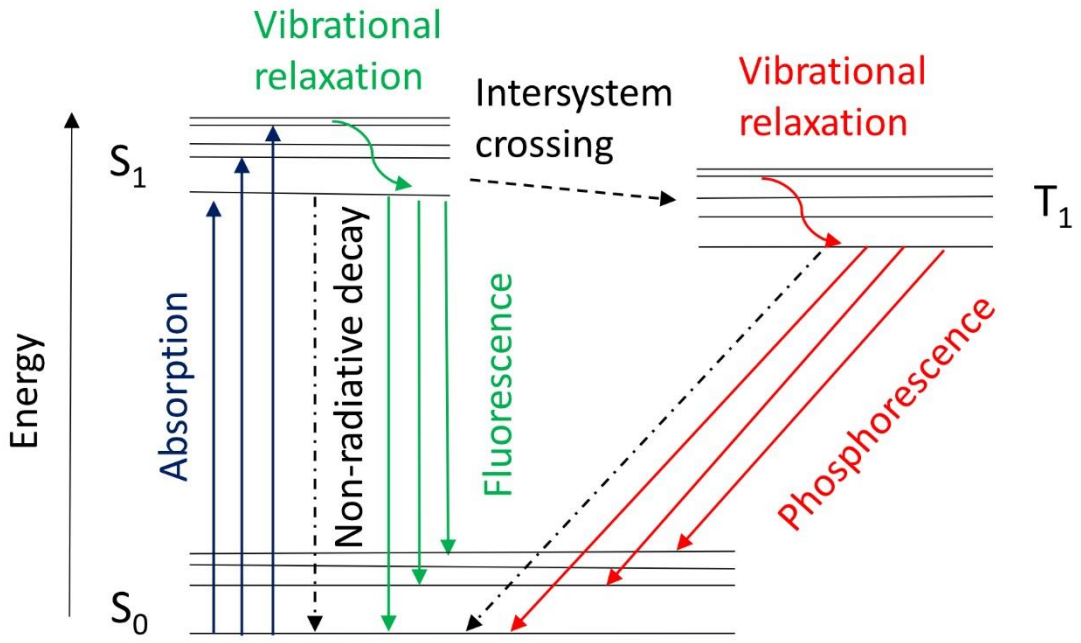

Figure 2-7: Simplified Jablonski diagram, describing the processes of absorption and emission of light between the ground state and the electronic excited state.

electron moves from the CB to the empty VB state. In contrast, electron-hole recombination can occur in non-radiative processes without any emission, which can be caused by surface states, bulk defects and traps. The direct band gap of semiconductors can also be detected by PL spectroscopy, since the photon energy of the emitted photon is directly related to the energy difference between the involved orbitals or bands. For the radiation of the sample, the used light source needs to provide photons that have a larger energy than the bandgap (or HOMO-LUMO gap) energy of the sample. After radiation, the electrons get excited from the valence band (VB) to the conduction band (CB) across the band gap. A fast decay of the fluorophore is called fluorescence, which occurs if the spin multiplicity is maintained during the relaxation process. Due to vibrational relaxations, which describe non-radiative transitions triggered by collisions between excited-state molecules, the emitted light of the fluorescence is red-shifted. As shown in the simplified Jablonski diagram in Figure 2-7, vibrational relaxation leads to the relaxation of the excited-state molecules to the lowest vibrational state of S_1, which is followed by fluorescence. The intersystem crossing describes a (often less dominant) non-radiative transition, which is coupled with a forbidden multiplicity change leading to a vibrationally excited triplet state T_1. This process is followed by the relaxation of the triplet state to the lowest vibrational state of T_1, followed by a symmetry-forbidden radiative transition to the ground state S_0. This process is called phosphorescence, which is typically characterized by a much longer lifetime than fluorescence.[15]

2.7 Time-correlated single photon counting (TCSPC)

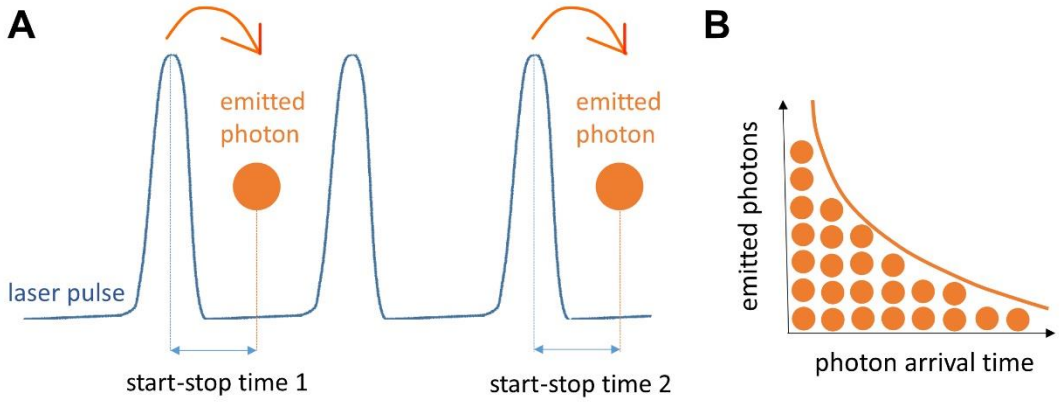

Figure 2-8: (A) Start-stop times during the TCSPC measurement. (B) Resulting histogram of the start-stop times.

For measuring the fluorescence time decays of samples, TCSPC is a commonly used technique. In contrast to the steady-state determination of the PL, TCSPC is a time-resolved spectroscopy. The lifetime of a fluorescent sample is defined as the average amount of time that a sample spends in the excited state. In a measurement, a laser pulse excites a sample and the detector measures the arrival time of the emitted photons in correlation to the timing of the laser pulse. The time periods between excitation and signal detection, or start-stop times, are recorded by the detector (see Figure 2-8 A). However, it is important that only one photon per excitation is measured. Due to the usage of a pulsed laser having a high repetition rate, the process can be often repeated. As a result, the intensity of the detected photons over the time difference from excitation to emission is plotted in a diagram as a decay curve (see Figure 2-8 B). [15]

2.8 Van der Pauw measurement

In 1958, Leo J. van der Pauw invented the van der Pauw method, which can be used for the investigation of the sheet resistance and the Hall coefficient of flat conductive layers, like films or pellets.[15] The conductive layer can have any shape, but needs to have a homogeneous thickness and a continuous form without holes or islands. It is a 4-point measurement arrangement with small contacts, located at four corners at the edge of the sample. A current is applied along one side, while the voltage is measured along the opposite side, to determine two resistances. For the conductivity value σ, the following formula is used:[16]

$$\sigma = \frac{ln2}{\pi t} \frac{2}{(R_{AB} + R_{AC})F_2} \qquad (12)$$

With the resistances R_{AB} and R_{AC} along two orthogonal sides, the tickness of the sample *t* and with the correction factor F_2.

The measurement of pelletized samples has some drawbacks, such as the high number of grain boundaries between crystallites. Furthermore, variations in the pelletization pressure, as well as in grain sizes, may cause reproducibility problems. In addition, no anisotropic charge transfer measurements can be carried out, due to random crystallite orientations in the pellet. Polycrystalline (or even epitaxial) films can be used as an alternative to pressed pellets. They are typically denser, resulting in higher conductivity values.

2.9 Cyclic voltammetry

For the investigation of the electrochemical properties of a material, cyclic voltammetry (CV) measurements can be performed. In a CV experiment, an electrode receives a linearly changing potential, while the current is measured during the potential scan. As a result, a current-potential curve is displayed, named CV curve. The potential varies lineary between an initial and a switching potential. After reaching the set potential, the potential of the working electrode is changed in the opposite direction, finishing with the initial potential. The potential scan can be repeated many times, with a fixed scan rate [V/s].[17]

CV measurements are performed with a three-electrode setup, consisting of a working electrode (WE) - in this work a stainless steel mesh with pressed MOF powder in it - a counter electrode (CE), made of platinum and a Ag/AgCl reference electrode (RE), which has a defined potential. An ionically conducting electrolyte solution connects all three electrodes. In this work we used tetrabutylammonium hexafluorophosphate in DMF. During the potential scan, the current between the WE and the CE electrode is measured, with potentials controlled by the RE.

With a CV measurement and the band gap in hand (which can be obtained from UV-Vis spectroscopic data evaluated by a Tauc plot), the oxidation onset potential against the HOMO energy of ferrocene can be used for the calculation of the absolute energy of the valence band edge against the vacuum scale (see equations 13, 14).

$$\boldsymbol{E_{HOMO} = -(E_{ox1}^{onset} + 4.8 - E_{FC/FC+})} \quad (13)$$

$$E_{LUMO} = E_{HOMO} + E_g \quad (14)$$

With the HOMO energy E_{HOMO}, the LUMO energy E_{LUMO}, the band gap E_g the oxidation onset potential E_{ox1}^{onset} and the HOMO energy of ferrocene $E_{FC/FC+}$.

2.10 Electron microscopy

Electron microscopy uses a beam of accelerated electrons to enable the characterization of the topography and composition of samples at the nanoscale. While a typical (classical) optical light microscope has a spatial resolution limit of approximately 200 nm (the Abbe limit), the electron miscroscope offers much better resolution. This is caused by the use of electrons with a de-Broglie-wavelength in the range of a few picometers, in comparison with visible light photons having wavelengths of several 100 nm. Electron microscpy can be also used for the characterization of MOFs, by imaging their morphology, crystalline domains, as well as pore systems. During operation, it is necesaary that the whole device is under vaccum. On the one hand, this avoids scattering of the high energy electrons by residual gas, on the other hand, it is important for the thermal and chemical stability of the electron gun.[2]

2.11 Scanning electron microscopy (SEM)

In the scanning electron microscope (SEM), a focused electron beam scans a sample on a surface in a grid pattern. The interaction of the electron beam with the sample leads to a detected signal of emitted electrons (and other signals), which in combination with the beam position can be used to create an image and to extract additional information. The data collection is performed point-by-point and line-by-line. The resolution of the image is typically possible in the nanometer range. Backscattered electrons (BSE), secondary electrons (SE), as well as X-rays and cathodoluminescence are part of the detected signals. BSE are primary electrons that are backscattered from the sample. In contrast, SE have a lower energy and are expelled from the sample due to the inelastic scattering of the primary beam. An SEM images the surface of a sample and has a lower resolution compared to the TEM, which can shows the inside of a sample. Therefore the electrons do not have to pass through the sample in an SEM, making sample preparation rather straighforward.[2]

2.12 Transmission electron microscopy (TEM)

The first electron microscopes with sub-micrometer resolution were developed primarly by Ruska in the 1930s in Berlin. Today, a TEM can image and analyze objects far below 10 nm, making it a very powerful analytical tool. For example, MOFs can be investigated by TEM to obtain information about the internal structure and for the imaging of the channel system. By using electron diffraction, it is also possible to obtain data of the samples in reciprocal space. An important requirement to analyze samples by TEM is the robustness of the samples. Due to the usage of high voltages between 60 kV and 400 kV during the measurement, less stable samples might degrade or decompose, leading to lower resolution and limited image quality. [2]

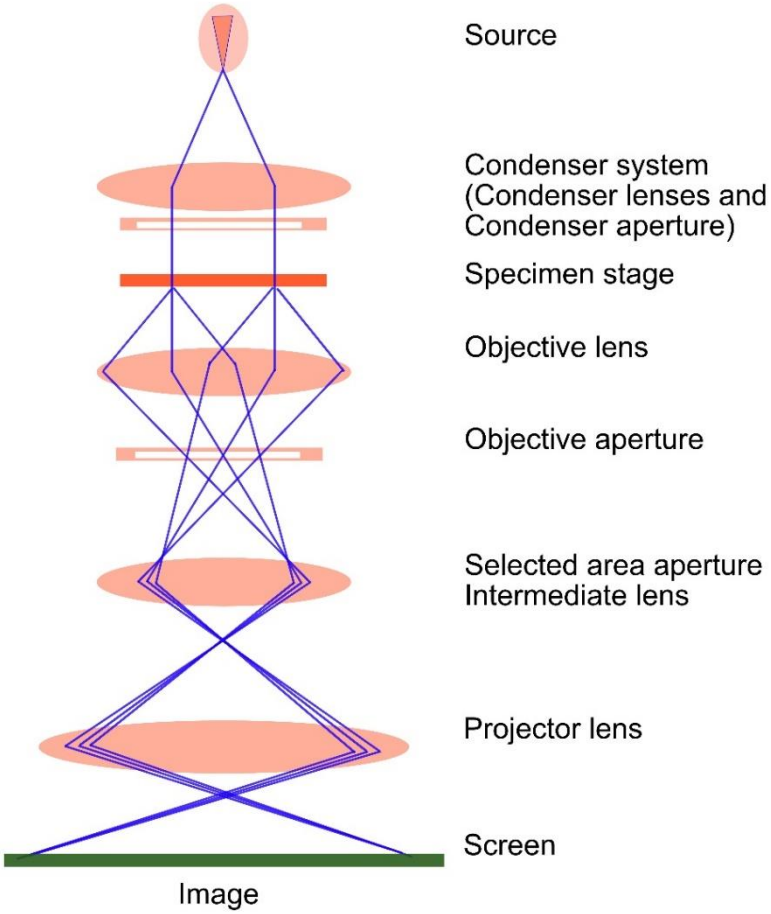

Figure 2-9: Schematic view of the imaging mode in a TEM.

A transmission electron microscope (TEM) is constructed of an electron gun (source), located at the top of the microscope, followed by an electromagnetic condenser lens system (see Figure 2-9). By varying the lens currents, the lens focus can be tuned. Next, a specimen stage with the specimen controls the axes and can be adjusted mechanically. The following objective lens produces an image of the specimen. The objective aperture and selected area aperture are optional to restrict the electron beam and to enhance the contrast. Further down, the image is enlarged by the intermediate and projector lenses. The final imaging system uses electromagnetic lenses and ultimately converts the high energy electron image into a visible image that appears on a fluorescent screen or is produced in an electronic image detector. Due to a path length limitation of an electron beam in air, the whole setup is kept under high vacuum.[18]

2.13 Atomic force microscopy (AFM)

Nanoscale surface structures and morphologies, for example of MOF films, can be measured with the atomic force microscope. It determines the topography, roughness and height distribution of film surfaces. During a measurement, a cantilever connected to a piezoelectric position control

and holding a very sharp tip raster-scans physically over the surface and measures the height at every point on the sample. The cantilever and the tip are commonly micro-fabricated from Si or Si_3N_4. Dependent on the force between tip and surface, the cantilever is deflected to the surface or rather away from the surface. A detector converts the deflection and motion of the cantilever into an electric signal. It is possible to operate an AFM in a contact mode, a tapping mode, as well as in a non-contact mode, depending on the requirements of the sample and the desired imaging information.[2]

2.14 X-ray photoelectron spectroscopy

XPS is a surface-sensitive spectroscopic technique for identifying the elemental composition within a material or covering its surface. The chemical states of the elements, their electronic structure, as well as the densitiy of the electronic states can be analyzed. Notably, not only the presence of elements, but also their bonding to other elements can be determined. The technique is sensitive to the sample´s surface and to a depth of a few atomic layers, depending on the elements present.

Atoms in a sample absorb photons of a monochromatic X-ray beam, which causes secondary electrons with a kinetic energy E_s to be ejected from the sample. This excitation energy is the sum of the binding energy E_b needed to lift the excited electron to the Fermi level and the orientation-dependent work function ϕ, needed to move the electron from the Fermi level into the vacuum, which is located outside the surface. The following equation defines the binding energy of the photoelectron:

$$E_b = h\nu - (E_s + \phi) \qquad (14)$$

The emission of electrons from energy levels in the inner electron shells of the sample are shown as lines in the photoemission spectrum. Auger peaks from Auger electrons are also included in the spectrum, which are energy transitions within an atom, after excitation by an incident X-ray photon. Background signals in the spectrum arise from multiply scattered, secondary electrons, generated in the deeper, inner layers.[2]

2.15 References

(1) Meyer, A. Institute of Physical Chemistry, University of Hamburg. *http://www.gisaxs.de/theory.html.*

(2) *Microstructural Characterization of Materials;* Brandon, D.; Kaplan, W. D., Eds., second edition; John Wiley & Sons, 2008.

(3) *The Essential Physics of Medical Imaging;* Bushberg, J. T.; Seibert, J. A.; Leidholdt, E. M. J., Eds.; Lippincott Williams & Wilkins: Philadelphia, 2002.

(4) *30.06.2021*; https://www.nobelprize.org/prizes/physics/1915/summary/.

(5) Cohen, S. M. Postsynthetic methods for the Functionalization of Metal-Organic Frameworks. *Chem. Rev.* **2012**, *112*, 970–1000.

(6) *PhD-thesis;* Cohen, J.; Levine, J., Eds.; Northwestern University: United States, 1989.

(7) Schlipf, J.; Müller-Buschbaum, P. Structure of Organometal Halide Perovskite Films as Determined with Grazing-Incidence X-Ray Scattering Methods. *Adv. Energy Mater.* **2017**, *7*, 1700131.

(8) Sing, K. S.; Everett, D. H.; Haul, R. A. W.; Moscou, L.; Pierotti, R. A.; Rouquerol, J.; Siemieniewska. Reporting Physisorption Data for Gas/ Solid Systems with Special Reference to the Determination ofSurface Area and Porosity. *Pure Appl. Chem.* **1985**, *57*, 603.

(9) Thommes, M.; Kaneko, K.; Neimar K, A. V.; Olivier, J. P.; Rodriguez-Reinoso, F.; Rouquerol, J.; Sing, K. S. W. Physisorption of gases, with special reference to the evaluation of surface area and pore size distribution (IUPAC Technical Report). *Pure Appl. Chem.* **2015**, *87*, 1051–1069.

(10) Brunauer, S.; Emmett, P. H.; Teller, E. Adsorption of Gases in Multimolecular Layers. *J. Am. Chem. Soc.* **1938**, *60*, 309–319.

(11) Gabbott, P. *Principles and Applications ofThermal Analysis*; Blackwell Publishing: Oxford, 2008.

(12) Perkampus, H.-H. *UV-VIS Spectroscopy and Its Applications*; Springer: Berlin Heidelber, 2013.

(13) Trepakov, V.; Dejneka, A.; Jastrabik, L.; Lynnyk, A.; Chvostova, D.; Syrnikov, P.; Markovin, P. The negative thermo-optic effect in KTaO3: an ellipsometry study. *Phase Transitions* **2015**, *88*, 991-1000.

(14) Hecht, H. G. The interpretation of diffuse reflectance spectra. *J. Res. Natl. Bur. Stand. Sec. A* **1976**, *80A*, 567–583.

(15) Lakowicz, J. R. *Principles of Fluorescence Spectroscopy, Third Edition*; Springer US: Baltimore, 2007.

(16) van der Pauw, L.J. A method of measuring specific resistivity and hall effect of discs of arbitrary shape. *Philips Research Reports* **1958**, *13*, 1–9.

(17) Heinze, J. Cyclic Voltammetry—"Electrochemical Spectroscopy". *Angew. Chem. Int. Ed.* **1984**, *23*, 831–847.

(18) Nebraska Center for Materials and Nanoscience, Ed.; https://ncmn.unl.edu/enif/microscopy/TEM.shtml, Accessed: 2021.

3 Anthracene-based MOF-74

This chapter is reproduced from the following publication:

A highly crystalline anthracene-based MOF-74 series featuring electrical conductivity and luminescence

Patricia I. Scheurle[‡,a,b], Andre Mähringer[‡ a,b], Andreas C. Jakowetz [a,b], Pouya Hosseini[c], Alexander F. Richter[d], Gunther Wittstock[c], Dana D. Medina[* a,b] and Thomas Bein[* a,b] *Nanoscale* **2019**, *11*, 20949-20955.

[a]Department of Chemistry, Ludwig-Maximilians-Universität (LMU), Butenandtstr. 5-13 (E), 81377 Munich, Germany.

[b]Nanosystems Initiative Munich (NIM) and Center for NanoScience (CeNS), Schellingstr. 4, 80799 Munich, Germany.

[c]Institute of Chemistry, Carl von Ossietzky Universität Oldenburg, 26111 Oldenburg, Germany.

[d]Chair for Photonics and Optoelectronics, Nano-Institute Munich, Department of Physics, Ludwig-Maximilians-Universität (LMU), Königinstr. 10, 80539 Munich, Germany.

[‡]The authors contributed equally to this work

[*]Corresponding Author

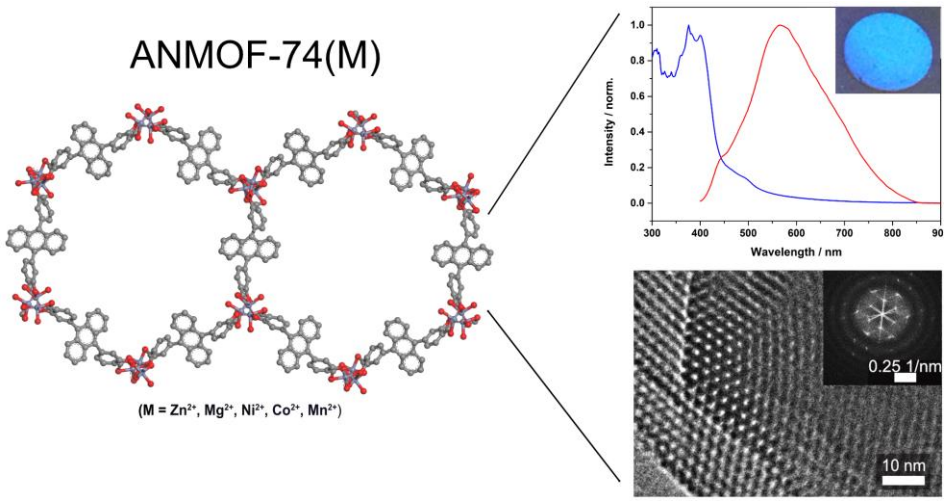

3.1 Abstract

Recently, a small group of metal-organic frameworks (MOFs) has been discovered featuring substantial charge transport properties and electrical conductivity, hence promising to broaden the scope of potential MOF applications in fields such as batteries, fuel cells and supercapacitors. In combination with light emission, electroactive MOFs are intriguing candidates for chemical sensing and optoelectronic applications. Here, we incorporated anthracene-based building blocks into the MOF-74 topology with five different divalent metal ions, that is, Zn^{2+}, Mg^{2+}, Ni^{2+}, Co^{2+} and Mn^{2+}, resulting in a series of highly crystalline MOFs, coined ANMOF-74(M). This series of MOFs features substantial photoluminescence, with ANMOF-74(Zn) emitting across the whole visible spectrum. The materials moreover combine this photoluminescence with high surface areas and electrical conductivity. Compared to the original MOF-74 materials constructed from 2,5-dihydroxy terephthalic acid and the same metal ions Zn^{2+}, Mg^{2+}, Ni^{2+}, Co^{2+} and Mn^{2+}, we observed a conductivity enhancement of up to six orders of magnitude. Our results point towards the importance of building block design and the careful choice of the embedded MOF topology for obtaining materials with desired properties such as photoluminescence and electrical conductivity.

3.2 Introduction

Metal-organic frameworks (MOFs) are composed of metal ions or clusters that are interconnected by rigid organic building blocks forming crystalline porous structures.[1] Based on their well-defined and tunable pore spaces and high surface areas, many MOFs are attractive candidates for gas separation and storage applications.[2,3] Depending on the organic building blocks and the respective metal species, MOFs can be synthesized with diverse chemical composition, connectivity and functionality. Therefore, a large variety of different chemical and physical properties can be attained[4-6] Recently, the intriguing property of electrical conductivity was added to this portfolio.[2,7–12] Hereby, an increasing number of MOFs were investigated with a view towards applications in the fields of charge storage, semiconductors, chemical sensing, energy conversion or electrocatalysis.[11,13–20]

To date, only few MOFs have been reported exhibiting the desired property of electrical conductivity in combination with ultrahigh surface area, which is viewed to be essential for sensing or charge storage applications.[21] Recently, structures based on the MOF-74 topology constructed with 2,5-dihydroxy terephthalic acid were introduced as electrically conductive platforms.[2,5,22,23]

MOF-74 isostructures connected through phenoxide-metal nodes showed low conductivity values, whereas structures containing sulfur ligating functionalities in the linking motif or mixed valance of the metal ions showed an increased electrical conductivity of up to 10^{-6} S cm^{-1}.[2,24]

Here, we present a series of MOF-74 analogs comprising an anthracene core in the linear organic linker. Anthracene and its derivatives are known for their high charge carrier mobility and electroluminescent properties.[10,21] We demonstrate that the incorporation of anthracene-containing building blocks can strongly enhance electrical conductivity in phenoxide-connected MOF-74 topology. Furthermore, we show that the anthracene core endows the MOFs with photoluminescent properties allowing for the realization of light emitting and electrically conducting MOFs. For constructing the framework, we first established the synthesis of an anthracene-based building block modified with *ortho*-hydroxy *para*-carboxylic functionalities enabling the required bonding to metal ions, namely 4,4´-(anthracene-9,10-diyl)bis(2-hydroxybenzoic acid), ABHB.

Using the anthracene building blocks and divalent metal ions, that is, Zn^{2+}, Mg^{2+}, Ni^{2+}, Co^{2+} and Mn^{2+}, five novel, highly crystalline and porous anthracene-based MOF-74-type (ANMOF-74) materials were synthesised under solvothermal conditions (Figure 3-1). The ANMOF-74 series features an enhancement of electrical conductivity by several orders of magnitude compared to the respective original MOF-74 isostructures. Furthermore, the photoluminescence life time and quantum yield were determined for the ANMOF-74 series.

3.3 Results and discussion

The employed ABHB linker was synthesized *via* a three-step reaction procedure (see Schemes 3-1 to 3-3).[25,26] In short, the reaction of methyl 4-iodosalicylate and bis(pinacolato)diboron afforded a boronated intermediate product, which was subsequently coupled in a Suzuki reaction with the brominated anthracene core to the methyl protected ABHB linking motif. After deprotection and purification, the final organic building block ABHB was obtained in a sufficient yield (*ca.* 70%) as a beige powder. For the MOF synthesis, the stoichiometric reaction of ABHB with the respective metal precursors (Zn^{2+}, Mg^{2+}, Ni^{2+}, Co^{2+} and Mn^{2+}) in different DMF/ MeOH/ EtOH/ BnOH/ H_2O mixtures at 120 °C for 2 days led to the precipitation of colored powders. Here, the color of the obtained powders was strongly dependent on the utilized metal ion precursor (for further information see SI). The obtained powders were washed with DMF and methanol and subsequent dried under dynamic vacuum.

Powder X-ray diffraction (PXRD) data of the dried powders are shown in Figure 3-2. All materials exhibit a high degree of crystallinity with pronounced reflections at 3.75°, 6.51°, 10.02°, 11.34°,

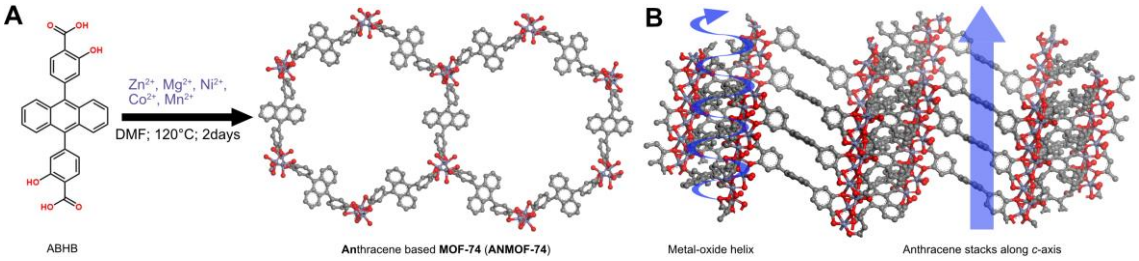

Figure 3-1: (A) Synthesis scheme of the anthracene-based MOF-74 (ANMOF-74). The organic building block ABHB forms porous hexagonal frameworks with the respective metal ions. (B) View on the helical metal-oxo chains of the ANMOF-74 structure *(left)* and the anthracene moieties *(right)* stacked along the crystallographic *c*-direction.

13.14° and 13.66° 2θ. Bragg reflections at up to 25° 2θ could be detected, underlining the high crystallinity of the obtained ANMOF-74 series. The collected diffractograms matched with the ones predicted from simulated model structures. The predicted model structures were obtained with *Accelrys Materials Studio 6.0* using the calculated MOF-74 crystal structure as a basis for the simulations.[2] After establishing the simulated unit cells, PXRD patterns were calculated, which were Rietveld-refined according to the respective experimental PXRD pattern (R_{wp} ranging from 3.94-6.96%). From the refinement, we conclude that the ANMOF-74 system crystallizes in the trigonal space group, *R*-3, with exemplary lattice constants of $a = b = 46.1$ Å, c = 5.8 Å, $\alpha = \beta = 90°$ and $\gamma = 120°$for the ANMOF-74(Zn), for further information see SI. These findings are in good agreement with simulations performed for related MOF-74 structures.[10,27] All ANMOF-74 materials exhibit one-dimensional hexagonal channels with pore apertures of 2 nm. These channels are formed by the ABHB units that are interconnected in the *c*-direction by infinite helical metal-oxo chains. Furthermore, ANMOF-74 include infinite stacks of the anthracene core arranged along the *c*-direction, with interlayer distance between adjacent anthracene cores estimated to be 5.7 Å (Figure 3-1B). For the ABHB unit, we determined a torsion angle of 60.7° between the para-positioned benzene rings and the anthracene core. Transmission electron microscopy (TEM) analysis of the ANMOF-74 series revealed highly crystalline materials (Figure 3-9). For ANMOF-74(Co), hexagonally shaped crystal facets and large cross-section domain sizes of about 120 nm illustrate the high degree of crystallinity (Figure 3-2F). The calculated diffraction pattern in the fast Fourier transform (FFT) of the TEM image shows angles of 120° in accordance with the proposed trigonal crystal system.

The synthesized powders were further investigated using X-ray photoelectron spectroscopy (XPS). As summarized in Figure 3-19 to Figure 3-23, XPS spectra of ANMOF-74(M) show the presence of the respective metal, C and O peaks attributed to the MOFs, as well as nitrogen, tentatively attributed to DMF residues coordinating to the metal ions in the structure. These findings are in accordance with the high-resolution analysis of the O 1s regions in the XPS spectra of

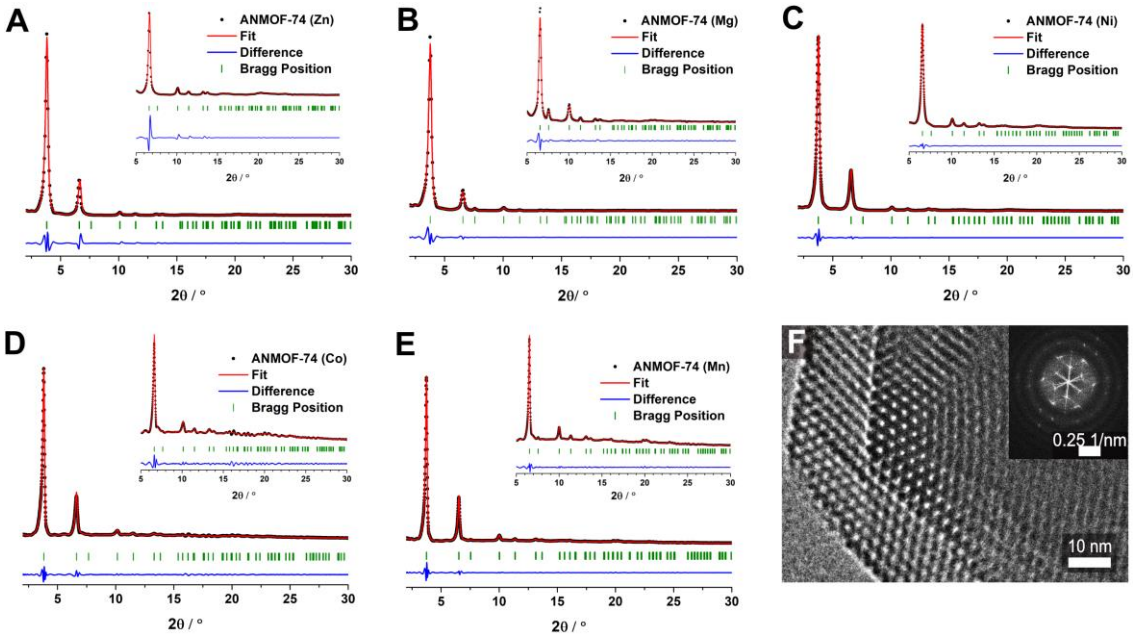

Figure 3-2: Experimental powder X-ray diffraction (PXRD) patterns of the ANMOF-74(M) series showing (A) Zn-, (B) Mg-, (C) Ni-, (D) Co- and (E) Mn-MOF derivatives, respectively (black). The simulated PXRD pattern were Rietveld-refined (red) according to the experimental data, whereby the difference plots are depicted in blue. The respective Bragg positions of the predicted hexagonal unit cell are shown as green bars. (F) A high resolution TEM image of an ANMOF-74 (Co) crystal oriented along the [001] axis with FFT of the entire image as inset.

all ANMOFs, indicating three types of oxygen atoms. The signals can be assigned to the functional groups (carboxy and hydroxy) of the ligating building block and to the oxygen related to DMF. Only ANMOF-74(Zn) has a second N 1s peak arising from residual NO_3^-, which apparently originates from the $Zn(NO_3)_2$ synthesis precursor. Importantly, Cl^- or additional N peaks related to impurities originating from the metal precursors were not observed for all other samples of the ANMOF-74 series. The purity of the obtained materials was further studied by energy dispersive X-ray spectroscopy (EDX) which showed no impurities arising from precursor anions (see Figure 3-17). Thermogravimetric analysis (TGA) revealed that the ANMOF-74(M) materials were stable below 300 °C under dynamic conditions (Figure 3-16).

The pore accessibility of the activated samples was investigated by nitrogen physisorption experiments. The nitrogen isotherms (77 K) of all ANMOF-74(M) powders (Figure 3-3) show IUPAC Type I(b)[29] sorption curves, indicating that the ANMOF-74(M) form micropores (< 2.5 nm). All examined MOFs show an initial uptake of about 200 cm^3g^{-1} at low pressures and a second uptake at 0.02-0.05 p/p_0 of about 100 cm^3g^{-1}. The adsorption branch and the desorption branch merge at low relative pressures illustrating a reversible process. The Brunauer-Emmett-Teller (BET) surface areas and total pore volumes for the ANMOF-74(M) bulk materials series were calculated to be 1124 $m^2\ g^{-1}$ and 0.49 $cm^3\ g^{-1}$ for Zn, 1137 $m^2\ g^{-1}$ and 0.48 $cm^3\ g^{-1}$ for Mg, 1352 $m^2\ g^{-1}$ and 0.56 $cm^{23}\ g^{-1}$ for Ni, 1213 $m^2\ g^{-1}$ and 0.53 $cm^3\ g^{-1}$ for Co, 1748 $m^2\ g^{-1}$ and 0.83 $cm^3\ g^{-1}$ for Mn, respectively. The pore size distributions were calculated using quenched solid density functional

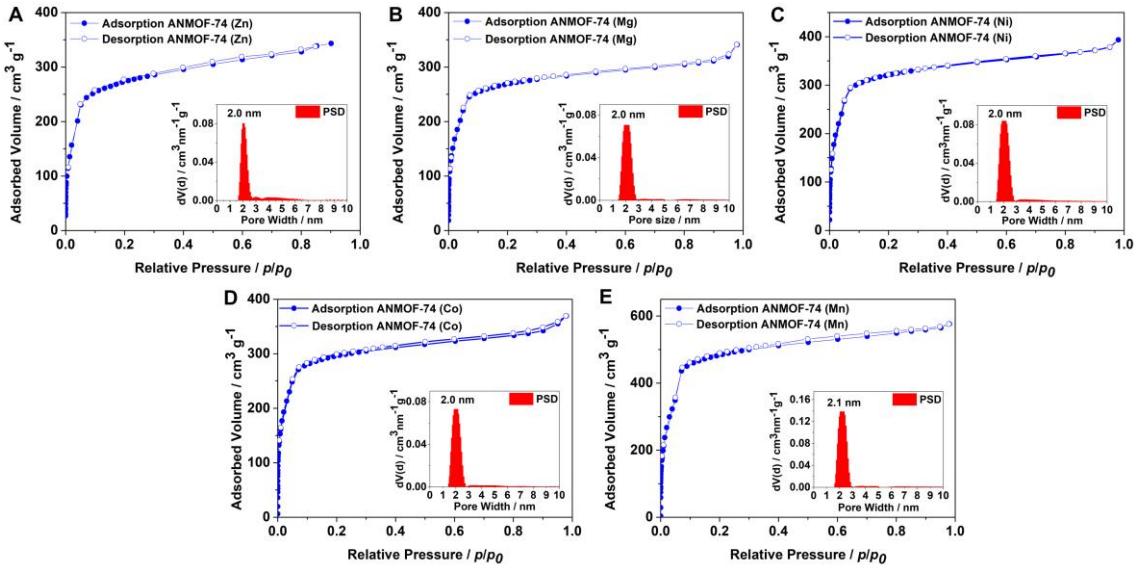

Figure 3-3: Nitrogen physisorption isotherms of (A) ANMOF-74(Zn), (B) ANMOF-74(Mg), (C) ANMOF-74(Ni), (D) ANMOF-74(Co) and (E) ANMOF-74(Mn) showing Type I(b) isotherm curves. The ad- and desorption branches are depicted as blue and white colored circles, respectively. Pore size distributions (PSD) are included as insets.

theory (QSDFT), revealing pore sizes of 2.1 nm in ANMOF- 74(Mn) and 2.0 nm in all other ANMOF-74(M) structures, which match the predicted value of 2.0 nm obtained by the simulated structure. Connolly surface area calculations with nitrogen as a probe molecule (2.6 Å) predict a theoretical surface area of 1757 m^2 g^{-1}, which matched best with the BET results obtained for the ANMOF-74(Mn) sample. Scanning electron microscopy (SEM) images of the ANMOF-74(M) powders showed needle-shaped crystallites forming spherical agglomerates (Figure 3-4 and Figure 3-8). In addition, high magnification SEM analysis revealed crystallites with a well-faceted hexagonal cross-section, further confirming the proposed trigonal crystal structures.

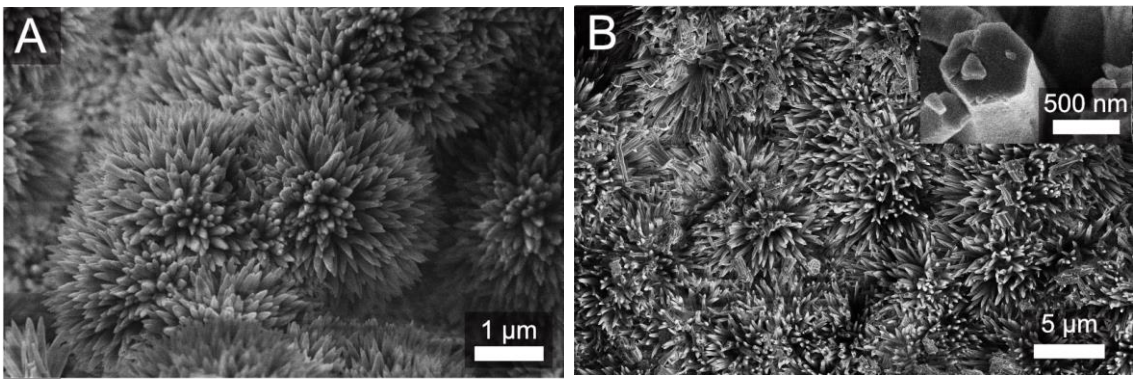

Figure 3-4: SEM images of the ANMOF-74 bulk materials (A) ANMOF-74(Ni) (B) ANMOF-74(Mn) with a high magnification of a hexagonally shaped crystal depicted as inset.

To elucidate the electrical properties of the ANMOF-74 series, we performed four-point probe van der Pauw measurements of crystalline and pelletized samples (for further details see SI). The obtained results are summarized in Table 3-1: Electrical conductivity values of ANMOF-74(M)

and MOF-74(M) samples obtained with pellets by using the four-point probe van der Pauw technique.

Table 3-1: Electrical conductivity values of ANMOF-74(M) and MOF-74(M) samples obtained with pellets by using the four-point probe van der Pauw technique.

ANMOF-74 (Zn)	**ANMOF-74 (Mg)**	**ANMOF-74 (Ni)**	**ANMOF-74 (Co)**	**ANMOF-74 (Mn)**
6×10^{-8} S cm^{-1}	5×10^{-9} S cm^{-1}	4×10^{-7} S cm^{-1}	4×10^{-8} S cm^{-1}	3×10^{-8} S cm^{-1}
MOF-74 (Zn)	**MOF-74 (Mg)**	**MOF-74 (Ni)**	**MOF-74 (Co)**	**MOF-74 (Mn)**
6×10^{-12} S cm^{-1}	6×10^{-13} S cm^{-1}	6×10^{-13} S cm^{-1}	6×10^{-13} S cm^{-1}	4×10^{-13} S cm^{-1}

The values obtained for ANMOF-74(M) range from 10^{-7} to 10^{-9} S cm^{-1}, corresponding to a striking increase of up to six orders of magnitude with regard to the values obtained (and reported)[2] for the respective MOF-74. To validate the impact of the anthracene core on the electrical conductivity, crystalline MOF-74 powders with the same set of metal ions were synthesized, activated (vacuum dried), compressed into pellets and their electrical conductivity was evaluated. The van der Pauw measurements of the MOF-74 pellets confirmed the ANMOF-74 series to be substantially more conductive than the MOF-74 isostructures. We attribute the enhanced electrical conductivity to the presence of the electron-rich anthracene core incorporated in the ANMOF-74 backbone, in contrast to the rather electron-poor 2,5-dihydroxy terephthalic acid building block embedded in the MOF-74. Here, our strategy of embedding the electron-rich anthracene-based linker resulted in a remarkable increase in relative conductivity, however, the measured values are still modest compared to other conducting MOF platforms.[29,30] Due to the fairly large stacking distance between adjacent anthracene units we postulate that charge transport still occurs mostly through the metal-oxo chains by charge carrier hopping between metal nodes.

To further elucidate the impact of the MOF-embedded anthracene moiety, we examined the optical properties of the ANMOF-74(M) bulk materials by using UV-Vis absorption and photoluminescence (PL) spectroscopy, summarized in Figure 3-8. The UV-Vis spectra were measured in diffusive reflectance geometry and obtained using the Kubelka-Munk equation. For all examined ANMOF-74 samples the absorption bands are located in the UV and blue spectral regions. ANMOF-74(Zn) has an absorption onset of around 528 nm and a second one at around 450 nm, and ANMOF-74(Mg; Ni; Co; Mn) at around 440 nm. Tauc plots were analyzed, assuming direct band gaps, yielding an optical band gap of 2.86 eV for ANMOF-74(Zn) and in case of ANMOF-74(Mg; Ni; Co; Mn) band gaps between 2.91 eV and 2.95 eV (Figure 3-11). These five MOFs have two sharp absorption maxima at 400 nm and 380 nm, which originate from the integrated ABHB building blocks (Figure 3-10A). Photoluminescence (PL) of the ANMOF- 74(M) bulk

materials was measured with a 378 nm excitation under argon atmosphere to protect the anthracene from degradation.

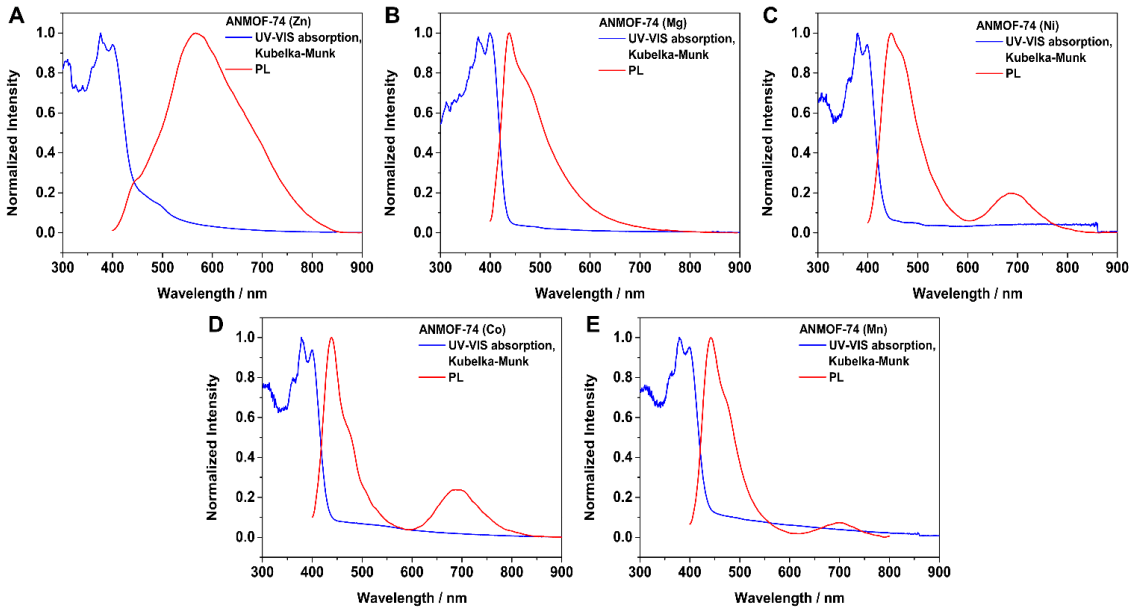

Figure 3-5: Diffusive reflectance UV-VIS absorption spectra of the ANMOF-74 powders (blue line) and the photoluminescence (PL) spectra of the pristine MOF bulk materials measured with 378 nm excitation (red line): (A) ANMOF-74(Zn), (B) ANMOF-74(Mg), (C) ANMOF-7(Ni), (D) ANMOF-74(Co) and (E) ANMOF-74(Mn).

The PL spectrum of ANMOF-74(Zn) shows a very broad emission band over the whole visible spectrum with a maximum at 570 nm and a large Stokes shift of 170 nm. ANMOF-74(Mg) and ANMOF-74(Co), as well as ANMOF-74(Ni) and ANMOF-74(Mn) have a narrow emission band with a small shoulder and an emission maximum between 438 nm and 444 nm, respectively. It is similar to the emission band at 441 nm of the ABHB linker monomer measured in solution (see Figure 3-10 B). These MOFs exhibit smaller Stokes shifts of 38 – 44 nm. ANMOF-74(Co) and ANMOF-74(Ni) also have a weaker emission band at 692 nm. ANMOF-74(Mn) has a weak emission band at 701 nm. Time-correlated single photon counting (TCSPC) traces of ANMOF-74(Zn) and ANMOF-74(Mg) were recorded at the respective emission maxima of 570 nm and 438 nm, shown in Figure 3-6. Both MOFs exhibit very similar relaxation behaviour, analyzed with a triexponential fit. Both exhibit fast decays of around τ_1 = 0.16 ns, which is near the instrumental response limit. However, the instrument response function was not included during the fitting procedure. The medium component has a lifetime τ_2 of 0.79 ns and 1.03 ns while the third component has a lifetime τ_3 of 3.44 ns and 4.90 ns for Zn and Mg, respectively. The main difference between the two materials is the fractional distribution of lifetimes. While the medium-lifetime decay channel is contributing almost 60% to the overall emission in the ANMOF-74(Zn) and only 50% in the ANMOF-74(Mg), this difference is balanced by the longer lifetime components, i.e. 18%

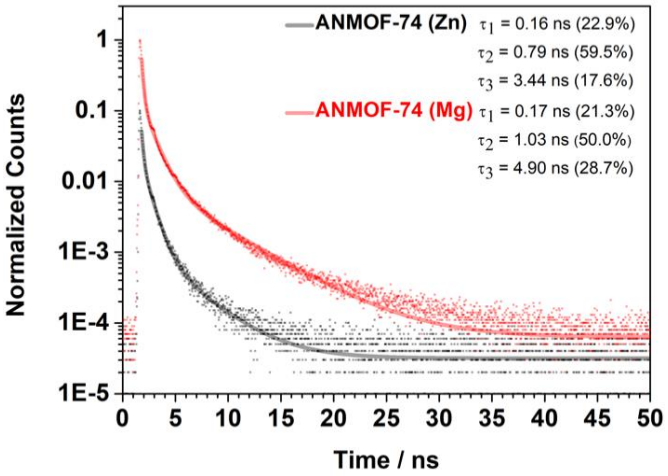

Figure 3-6: The time-correlated single photon counting (TCSPC) traces corresponding to the PL spectra of ANMOF-74(Zn) (black) and ANMOF-74(Mg) (red), which were recorded at the respective emission maximum of each MOF. The lifetimes were obtained from triexponential fits (solid lines) to the data (scatter). The fractions of emitted photons corresponding to the respective lifetimes are stated in brackets.

versus 29% in the Zn and Mg ANMOFs, respectively. This results in the faster overall decay of the ANMOF-74(Zn) as compared to the longer-lived ANMOF-7(Mg). Due to the bright emission and long lifetime of ANMOF-74(Mg), we also measured the photoluminescence quantum yield (PLQY), which reaches 2.5% (see Figure 3-13). The ABHB linker molecules (as solid powder) show PLQY values of up to 13%, which is reduced by one order of magnitude upon incorporation into the framework. However, the luminescence is still detectable with the naked eye by irradiating the ANMOF-74(Mg) sample with a UV lamp (see Figure 3-14 and Figure 3-15).

TCSPC traces of ANMOF-74(Ni), ANMOF-74(Co) and ANMOF-74(Mn) show similar lifetime components with τ_1 around 0.06 ns, τ_2 between 0.79 ns and 0.89 ns and τ_3 in the range of 5 – 7 ns (see Figure 3-12). The ABHB linker monomer has a monoexponential decay with a lifetime of 4.3 ns (see Figure 3-12). The long PL lifetime of ANMOF-74(Mg) in comparison to the other ANMOFs might be related to the different emission spectrum. ANMOF-74(Mg), similar to the ABHB linker, does not have a second emission band at around 700 nm. But the PL lifetime of ANMOF-74(Mg) and of the ABHB linker are much longer compared to the other ANMOFs. Thus, in the ANMOF-74(Mg), the linkers might be similarly electronically ´isolated` as the monomer in solution while the emission band at around 700 nm might be related to electronic interactions between linkers (and transition metal ions), effectively decreasing the PL lifetime.

3.4 Conclusion

In our study, we present the successful synthesis of a novel series of metal-organic frameworks showing MOF-74 topology, coined ANMOF-74. The frameworks are built from anthracene-based linking motifs (ABHB) connected *via* helical metal-oxo chains, whereby a range of different metal ions could be incorporated (Zn, Mg, Co, Ni and Mn) into the framework. All ANMOF-

74 materials feature a high degree of crystallinity and show BET surface areas exceeding 1000 m^2g^{-1}. Furthermore, all ANMOF-74 materials exhibit an enhancement of electrical conductivity of up to one-million fold compared to regular MOF-74. The ANMOF-74 materials feature direct optical band gaps of around 2.9 eV and most show photoluminescence in the blue spectral region. In contrast to the other derivatives, the ANMOF-74(Mg) shows a rather high quantum efficiency of 2.5%. Remarkably, ANMOF-74(Zn) emits photoluminescence across the entire visible spectrum. We believe that this promising combination of high crystallinity, defined porosity, luminescence as well as electrical conductivity embedded in a fixed MOF matrix will enable a range of possible applications such as sensing and charge storage. Our study highlights the great versatility of the MOF-74 topology, allowing for the integration of sterically demanding organic linker structures with interesting electrical and optical properties. In the future, we envision the integration of additional chromophores with interesting optoelectronic properties and a tunable degree of electronic coupling into this highly attractive MOF topology, to further broaden the field of MOF-74 based structures for optoelectronic applications.

3.5 References

(1) Yaghi, O. M.; Li, H. Hydrothermal Synthesis of a Metal-Organic Framework Containing Large Rectangular Channels. *J. Am. Chem. Soc.* **1995**, 10401–10402.

(2) Sun, L.; Hendon, C. H.; Minier, M. A.; Walsh, A.; Dincă, M. Million-Fold Electrical Conductivity Enhancement in Fe2(DEBDC) versus Mn2(DEBDC) (E = S, O). *J. Am. Chem. Soc.* **2015**, *137*, 6164–6167.

(3) Meek, S. T.; Greathouse, J. A.; Allendorf, M. D. Metal-organic frameworks: a rapidly growing class of versatile nanoporous materials. *Adv. Mater.* **2011**, *23*, 249–267.

(4) Rosi, N. L.; Kim, J.; Eddaoudi, M.; Chen, B.; O'Keeffe, M.; Yaghi, O. M. Rod packings and metal-organic frameworks constructed from rod-shaped secondary building units. *J. Am. Chem. Soc.* **2005**, *127*, 1504–1518.

(5) Dolgopolova, E. A.; Shustova, N. B. Metal–organic framework photophysics: Optoelectronic devices, photoswitches, sensors, and photocatalysts. *MRS Bull.* **2016**, *41*, 890–896.

(6) Kapelewski, M. T.; Geier, S. J.; Hudson, M. R.; Stück, D.; Mason, J. A.; Nelson, J. N.; Xiao, D. J.; Hulvey, Z.; Gilmour, E.; FitzGerald, S. A.; Head-Gordon, M.; Brown, C. M.; Long, J. R. M2(m-dobdc) (M = Mg, Mn, Fe, Co, Ni) metal-organic frameworks exhibiting increased charge density and enhanced H2 binding at the open metal sites. *J. Am. Chem. Soc.* **2014**, *136*, 12119–12129.

(7) Evans, J. D.; Garai, B.; Reinsch, H.; Li, W.; Dissegna, S.; Bon, V.; Senkovska, I.; Fischer, R. A.; Kaskel, S.; Janiak, C.; Stock, N.; Volkmer, D. Metal-Organic Frameworks in Germany: from Synthesis to Function. *Coord. Chem. Rev.* **2019**, *380*, 378–418.

(8) Kobayashi, Y.; Jacobs, B.; Allendorf, M. D.; Long, J. R. Conductivity, Doping, and Redox Chemistry of a Microporous Dithiolene-Based Metal−Organic Framework. *Chem. Mater.* **2010**, *22*, 4120–4122.

(9) Usman, M.; Mendiratta, S.; Lu, K.-L. Semiconductor Metal-Organic Frameworks: Future Low-Bandgap Materials. *Adv. Mater.* **2017**, *29*.

(10) Sun, L.; Campbell, M. G.; Dincă, M. Electrically Conductive Porous Metal-Organic Frameworks. *Angew. Chem.* **2016**, *55*, 3566–3579.

(11) Usman, M.; Mendiratta, S.; Batjargal, S.; H., G.; Haider, M.; Rao Gade, N.; Chen, J.-W.; Chen, Y.-F.; Lu, K.-L. Semiconductor Behavior of a Three-Dimensional Strontium-Based Metal-Organic Framework. *ACS Appl. Mater. Interfaces* **2015**, *7*, 22767–22774.

(12) Stavila, V.; Talin, A. A.; Allendorf, M. D. MOF-based electronic and opto-electronic devices. *Chem. Soc. Rev.* **2014**, *43*, 5994–6010.

(13) Gérard, F.; Millange, F.; Morcrette, M.; Serre, C.; Doublet, M.-L.; Grenèche, J.-M.; Tarascon, J.-M. Mixed-valence li/fe-based metal-organic frameworks with both reversible redox and sorption properties. *Angew. Chem.* **2007**, *46*, 3259–3263.

(14) Kim, H.; Rao, S. R.; Kapustin, E. A.; Zhao, L.; Yang, S.; Yaghi, O. M.; Wang, E. N. Adsorption-based atmospheric water harvesting device for arid climates. *Nat. Commun.* **2018**, *9*, 1191.

(15) Yi, F.-Y.; Chen, D.; Wu, M.-K.; Han, L.; Jiang, H.-L. Chemical Sensors Based on Metal-Organic Frameworks. *ChemPlusChem* **2016**, *81*, 675–690.

(16) Watanabe, Y.; Haraguchi, T.; Otsubo, K.; Sakata, O.; Fujiwara, A.; Kitagawa, H. A highly crystalline oriented metal-organic framework thin film with an inorganic pillar. *Chem. Commun.* **2017**, *53*, 10112–10115.

(17) Kreno, L. E.; Leong, K.; Farha, O. K.; Allendorf, M.; van Duyne, R. P.; Hupp, J. T. Metal-organic framework materials as chemical sensors. *Chem. Rev.* **2012**, *112*, 1105–1125.

(18) Campbell, M. G.; Dincă, M. Metal-Organic Frameworks as Active Materials in Electronic Sensor Devices. *Sensors* **2017**, *17*, 1108.

(19) Zhang, Z.; Yoshikawa, H.i.; Awaga, K. Monitoring the solid-state electrochemistry of Cu(2,7-AQDC) (AQDC = anthraquinone dicarboxylate) in a lithium battery: coexistence of metal and ligand redox activities in a metal-organic framework. *J. Am. Chem. Soc.* **2014**, *136*, 16112–16115.

(20) Campbell, M. G.; Sheberla, D.; Liu, S. F.; Swager, T. M.; Dincă, M. Cu_3(hexaiminotriphenylene)$_2$: an electrically conductive 2D metal-organic framework for chemiresistive sensing. *Angew. Chem.* **2015**, *54*, 4349–4352.

(21) Chen, D.; Xing, H.; Su, Z.; Wang, C. Electrical conductivity and electroluminescence of a new anthracene-based metal-organic framework with π-conjugated zigzag chains. *Chem. Commun.* **2016**, *52*, 2019–2022.

(22) Deng, H.; Grunder, S.; Cordova, K. E.; Valente, C.; Furukawa, H.; Hmadeh, M.; Gándara, F.; Whalley, A. C.; Liu, Z.; Asahina, S.; Kazumori, H.; O'Keeffe, M.; Terasaki, O.; Stoddart, J. F.; Yaghi, O. M. Large-pore apertures in a series of metal-organic frameworks. *Science* **2012**, *336*, 1018–1023.

(23) Cozzolino, A. F.; Brozek, C. K.; Palmer, R. D.; Yano, J.; Li, M.; Dincă, M. Ligand redox non-innocence in the stoichiometric oxidation of Mn2(2,5-dioxidoterephthalate) (Mn-MOF-74). *J. Am. Chem. Soc.* **2014**, *136*, 3334–3337.

(24) Sun, L.; Miyakai, T.; Seki, S.; Dincă, M. Mn2(2,5-disulfhydrylbenzene-1,4-dicarboxylate): a microporous metal-organic framework with infinite (-Mn-S-)∞ chains and high intrinsic charge mobility. *J Am Chem Soc* **2013**, *135*, 8185–8188.

(25) Fracaroli, A. M.; Furukawa, H.; Suzuki, M.; Dodd, M.; Okajima, S.; Gándara, F.; Reimer, J. A.; Yaghi, O. M. Metal-organic frameworks with precisely designed interior for carbon dioxide capture in the presence of water. *J. Am. Chem. Soc.* **2014**, *136*, 8863–8866.

(26) Hirofumi, M.; Akira, S.; Yusuke, M.; Yoshinori, I. Polycarboxylic acid containing condensed aromatic ring, crystalline network complex using same, and gas storage material. *WO 2017006638 A1* **2017**.

(27) Zheng, J.; Vemuri, R. S.; Estevez, L.; Koech, P. K.; Varga, T.; Camaioni, D. M.; Blake, T. A.; McGrail, B. P.; Motkuri, R. K. Pore-Engineered Metal-Organic Frameworks with Excellent Adsorption of Water and Fluorocarbon Refrigerant for Cooling Applications. *J. Am. Chem. Soc.* **2017**, *139*, 10601–10604.

(28) Thommes, M.; Kaneko, K.; Neimar K, A. V.; Olivier, J. P.; Rodriguez-Reinoso, F.; Rouquerol, J.; Sing, K. S. W. Physisorption of gases, with special reference to the evaluation of surface area and pore size distribution (IUPAC Technical Report). *Pure Appl. Chem.* **2015**, *87*, 1051–1069.

(29) Ko, M.; Mendecki, L.; Mirica, K. Conductive two-dimensional metal–organic frameworks as multifunctional materials. *Chem. Commun.* **2018**, *54*, 7873–7891.

(30) Mähringer, A.; Jakowetz, A. C.; Rotter, J. M.; Bohn, B. J.; Stolarczyk, J. K.; Feldmann, J.; Bein, T.; Medina, D. D. Oriented Thin Films of Electroactive Triphenylene Catecholate-Based Two-Dimensional Metal-Organic Frameworks. *ACS Nano* **2019**, *13*, 6711–6719.

3.6 Supporting information

3.6.1 Characterization methods

Nuclear magnetic resonance (NMR)

NMR spectra were recorded on *Bruker AV400* and *AV400 TR* spectrometers. The chemical shifts are expressed in parts per million and calibrated using residual (undeuterated) solvent peaks as an internal reference (^{1}H-NMR: DMSO-d_6: 2.50; ^{13}C-NMR: DMSO-d_6: 39.52). The data for ^{1}H-NMR spectra are written as follows: s = singlet, d = doublet, t = triplet, q = quartet, m = multiplet.

X-ray analysis

X-ray diffraction (XRD) analyzes were performed on a *Bruker D8* diffractometer in Bragg-Brentano geometry with Ni-filtered Cu K_α (λ = 1.54060 Å) radiation operating at 40 kV and 30 mA with a position-sensitive detector (*LynxEye*).

Scanning electron microscopy (SEM)

SEM images were recorded on a *FEI Helios NanoLab G3 UC* electron microscope with an acceleration voltage of 2 kV from a field emission gun. For the cross-section analysis substrates were partially cut and broken manually to reveal fresh cross-sections. Prior to SEM analysis the samples were coated with a thin carbon layer by carbon fiber flash evaporation in high vacuum.

Transmission electron microscopy (TEM)

TEM images were collected on an *FEI Titan Themis 60-300* microscope at an acceleration voltage of 300 kV. Powder samples were prepared by crushing the particles with a razor blade and subsequently depositing the powder onto a copper grid supporting a thin electron transparent carbon film.

Nitrogen sorption

Ad- and desorption measurements were performed on an *Autosorb 1* (*Quantachrome instruments, Florida, USA*) with nitrogen of 99.9999% purity at 77.3 K. The samples were activated (dried) under high vacuum at 120 °C for at least 12 h. Evaluation of ad- and desorption isotherms was carried out with the *AsiQwin v.3.01* (*Quantachrome instruments, Florida, USA*) software.

For BET calculations, pressure ranges of the nitrogen isotherms were chosen with the help of the BET assistant in the *AsiQwin* software. In accordance with the ISO recommendations, multipoint BET tags equal to or below the maximum in V x (1-p/p_0) were chosen.

Van der Pauw measurements

Van der Pauw measurements were conducted on a *ECOPIA Model HMS 3000* Hall measurement setup. The samples were fixed in an *SPCB-1* spring clip board without any additional contacts. Distances between the single probes were adjusted to be 5 mm.

Preparation of ANMOF-74 and MOF-74 pellets

ANMMOF-74 and MOF-74 pellets with 1 cm diameter (obtained from several described batches) for electrical conductivity measurements were fabricated with 100 mg of the respective MOF bulk material with a standard *Paul-Weber* KBr Press with 45 kg/ cm^2 pressure.

UV-Vis spectroscopy

UV-Vis spectra were recorded using a *PERKIN ELMER UV VIS/NIR Lambda 1050* spectrophotometer equipped with a 150 mm InGaAs integrating sphere. Diffuse reflectance spectra were collected with a Praying Mantis (Harrick) accessory and were referenced to barium sulphate powder as white standard.

Photoluminescence (PL) spectroscopy

PL measurements were performed on a *PicoQuant FluoTime 300* time-correlated single photon counting (TCSPC) setup. Steady-state spectra and time-resolved histograms were acquired using a 378 nm laser (*PicoQuant LDH-P-C-375*). Residual laser scattering was removed using a 400 nm dielectric long pass (*Thorlabs FELH0400*) in the beam path of the emitted light, which was detected under magic angle (54.7°) on a photomultiplying tube (*PicoQuant PMA 192*).

For measuring the absolute photoluminescence quantum yield and CIE-values, we used a *Horiba FluoroLog 3* in combination with an integrating sphere by *Horiba*. The sample was prepared as follows: a small amount of powder of the MOF was sandwiched between two glass coverslips and sealed using Parafilm at the edges. A reference structure without sample was prepared as well. By relating the signal area change between sample and reference at the luminescence region and at the Rayleigh peak the absolute radiative quantum yield was calculated.

Thermogravimetric analysis

Thermogravimetric analysis (TGA) measurements were performed on a *Netzsch Jupiter ST 449 C* instrument equipped with a *Netzsch TASC 414/4* controller. The samples were heated from room temperature to 800 °C under a synthetic air flow (25 mL min^{-1}) at a heating rate of 1 K min^{-1}.

X-ray photoelectron spectroscopy

XPS was performed using an ESCALAB 250 Xi instrument (Thermo Fisher, East Grinsted, UK) with monochromatized Al Kα (hν = 1486.6 eV) radiation focused to a spot of 500 micron diameter at the surface of samples. Spectra were measured with pass energies of 200 eV for survey scans and 10 eV for high-resolution regions. Charging was compensated by use of an internal electron flood gun. Peak fitting was performed by the software Avantage, version 5.9904 (Thermo Fisher) using a Shirley background ("Smart Shirley") and a convolution of Gaussian and Lorentzian functions for each signal component. All spectra were referenced to remaining adventitious carbon at 284.8 eV.

Elemental analysis

The analysis of carbon and hydrogen for ANMOF-74 (M) were taken on a vario MICRO cube (Elementar Analyzensysteme GmbH, Germany). The metal detection for all samples was carried out on a Varian Vista RL ICP-OES spectroscope. All materials were activated under dynamic vacuum prior to analysis.

3.6.2 Experimental

3.6.2.1 General

All materials were purchased from *Sigma Aldrich, Acros or TCI Europe* in the common purities *purum, puriss* or *reagent grade.* The materials were used as received without additional purification and handled in air unless otherwise noted.

The water utilized in the synthesis was subjected to a *Merck-Milipore Mili-Q* purification system prior to use.

3.6.2.2 Synthetic procedures

Methyl 2-hydroxy-4-(4,4,5,5-tetramethyl-1,3,2-dioxaborolan-2-yl)benzoate (compound 3) (adapted from Fracaroli, A. M.; Furukawat, H.; Suzuki, M.; Dodd, M.; Okajima, S.; Gandarat, F.; Reimer, J. A.; Yaghi, O. M. Metal-organic Frameworks with Preciseley Designed Interior for Carbon Dioxide Capture in the Presence of Water. *J. Am. Chem. Soc.* 2014, ***136***, 8863–8866.)

Scheme 3-1

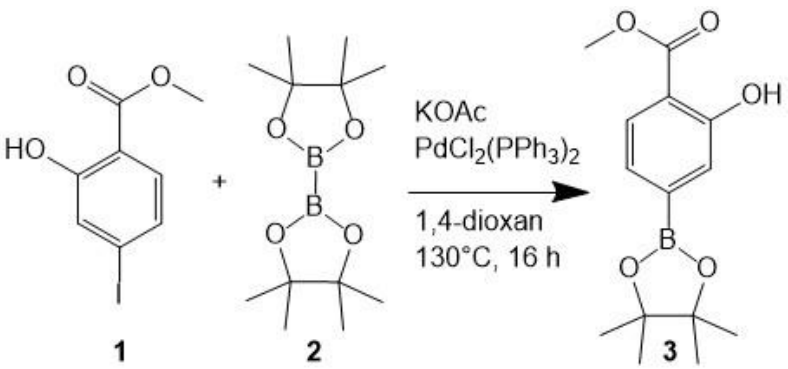

Methyl 4-iodosalicylate (compound **1**) (1.0 g, 3.6 mmol), bis(pinacolato)diboron (compound **2**) (1.01 g, 3.98 mmol), KOAc (1.1 g, 10.8 mmol), and $PdCl_2(PPh_3)_2$ (50.7 mg, 0.072 mmol) were dissolved in 18 mL anhydrous 1,4-dioxane in a 100 mL flask under nitrogen atmosphere. The resulting solution was heated to 130 °C for 13 h under stirring. The solution was allowed to cool to room temperature and filtered through celite. It was washed with 1,4-dioxane, toluene and ethyl acetate. The filtrate was concentrated in vacuo. The obtained yellow solid was dissolved in ethyl acetate. The white solid was filtered off. The filtrate was concentrated under vacuum. The obtained yellow needles were recrystallized in methanol (2 mL), giving colorless crystals with 71% yield. ^{1}H NMR (400 MHz, DMSO-d_6) δ (ppm): 10.35 (s, 1H), 7.75 (d, 1H) 7.20 (s, 1H), 7.17 (d, 1H), 3.87 (s, 3 H), 1.26 (s, 12H).

Dimethyl 4,4´-(anthracene-9,10-diyl)bis(2-hydroxybenzoate) (compound 5) (adapted from Hirofumi M., Akira S., Yusuke M., Yoshinori I. Polycarboxylic acid containing condensed aromatic ring, crystalline network complex using same, and gas storage material. 2017. WO 2017006638 A1.)

Scheme 3-2

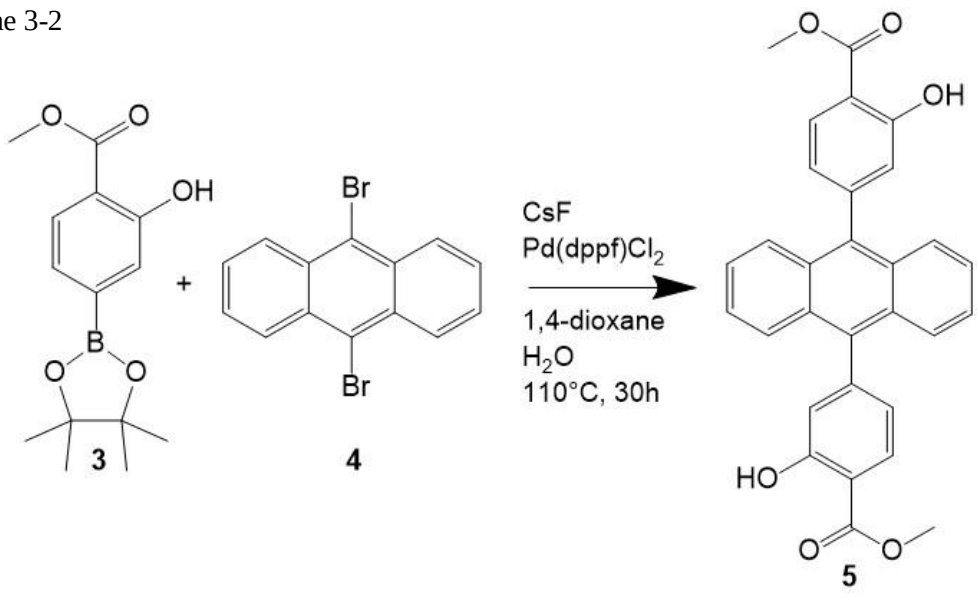

Methyl 2-hydroxy-4-(4,4,5,5-tetramethyl-1,3,2-dioxaborolan-2-yl)benzoate (compound 3) (700 mg, 2.5 mmol), 9,10-dibromoanthracene (compound 4) (369 mg, 1.099 mmol), CsF (1.0 g, 65.8 µmol), $Pd(dppf)Cl_2$ (44.85 mg, 613 µmol) were dissolved in 12.8 mL 1,4-dioxane and 1.8 mL water in a 100 mL flask under nitrogen atmosphere. The resulting solution was heated to 110 °C for 30 h. The solution was allowed to cool to room temperature and NH_4Cl (40 mL) and chloroform (40 mL) were added. It was filtered through celite and the residue was washed with chloroform (400 mL). The filtrate was separated and the aqueous layer was extracted with chloroform. The organic layer was washed with saturated sodium chloride solution (3 x 200 mL) and dried over $MgSO_4$. The filtrate was concentrated under vacuum, giving a brown powder with 72% yield. ^{1}H NMR (400 MHz, DMSO-d_6) δ (ppm): 8.04 (d, 2H), 7.64-7.59 (m, 4H), 7.49-7.45 (m, 4H), 7.09 (t, 2H), 7.06-7.03 (ddd, 2H), 3.99 (s, 6H).

4,4´-(anthracene-9,10-diyl)bis(2-hydroxybenzoic acid) (compound 6) ABHB linker, (adapted from Hirofumi M., Akira S., Yusuke M., Yoshinori I. (2017). WO 2017006638 A1.)

Scheme 3-3

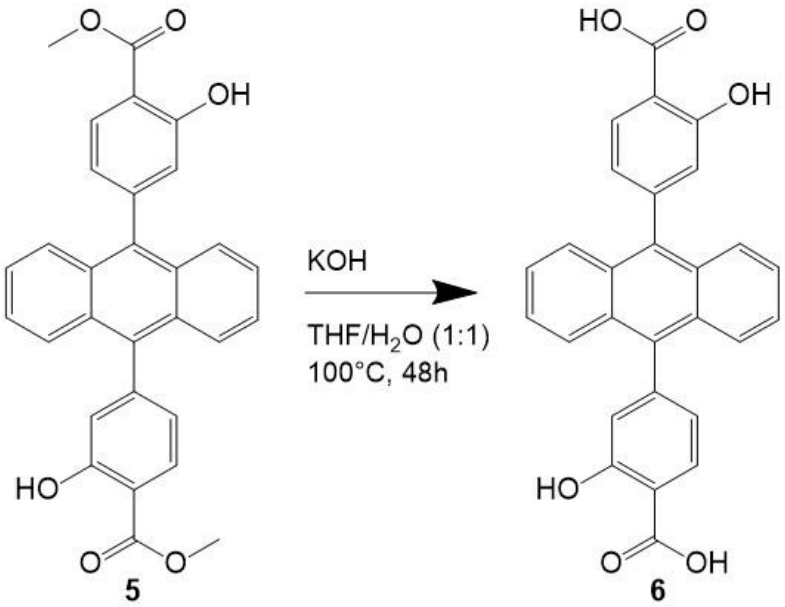

Dimethyl 4,4´-(anthracene-9,10-diyl)bis(2-hydroxybenzoate) (compound **5**) (300 mg, 0.63 mmol), potassium hydroxide (KOH) (500 mg, 8.9 mmol) and a mixture of THF/H_2O (1:1) (30 mL) were heated in a 100 mL flask under nitrogen atmosphere at 100 °C for 48 h. The resulting solution was allowed to cool to room temperature and poured into HCl (200 mL). The solid was filtered off, washed with acetic acid (30 mL), water (500 mL) and MeOH (30 mL) and dried under vacuum, giving a beige powder with 70% yield. ^{1}H NMR (400 MHz, DMSO-d_6) δ (ppm): 8.03 (d, 2H), 7.64-7.59 (m, 4H), 7.48-7.43 (m, 4H), 7.03 (s, 2H), 7.02-6.97 (m, 2H), 3.99 (s, 6H). ^{13}C NMR (400 MHz, DMSO-d_6) δ (ppm): 171.73 (2C), 161.07 (2C), 145.75 (2C), 135.59 (2C), 130.60 (3C), 128.51 (3C), 126.13 (6C), 125.92 (3C), 122.11 (4C).

3.6.2.3 Anthracene-based MOF-74 (ANMOF-74) synthesis

ANMOF-74(Zn)

4,4´-(anthracene-9,10-diyl)bis(2-hydroxybenzoic acid) (10.00 mg, 0.022 mmol), $Zn(NO_3)_2 \cdot 4H_2O$ (22.07 mg, 0.084 mmol) and benzoic acid (2.7 mg, 0.022 mmol) were suspended in DMF (1.5 mL). The resulting mixture was sonicated until complete dissolution of the educts was achieved and it was kept in a culture tube at 120 °C for 2 days. The resulting precipitate was washed with DMF (2 x 10 mL) and MeOH (1 x 10 mL) and activated at 120°C to remove the less volatile solvent to obtain a brownish crystalline powder. The PXRD pattern of the synthesized MOF matches the simulated ANMOF-74 PXRD pattern. Elemental Analysis (activated): Calculated for $Zn_{18}C_{252}H_{126}O_{63} \cdot$ DMF (%): Zn, 22.04; C, 56.70; H. 2.38; Found (%): Zn, 21.68; C, 56.81; H, 2.57, N, 0.71.

ANMOF-74(Mg)

4,4´-(anthracene-9,10-diyl)bis(2-hydroxybenzoic acid) (10.00 mg, 0.022 mmol) and $Mg(NO_3)_2 \cdot 6H_2O$ (21.60 mg, 0.084 mmol) were suspended in DMF (1.3 mL) and MeOH (0.2 mL). The resulting mixture was sonicated until complete dissolution of the educts was achieved and it was kept in a culture tube at 120°C for 2 days. The resulting precipitate was washed with DMF (2 x 10 mL) and MeOH (1 x 10 mL) and activated at 120 °C to remove the less volatile solvent to obtain a bright beige crystalline powder. The PXRD pattern of the synthesized MOF matches the simulated ANMOF-74 PXRD pattern. Elemental Analysis (activated): Calculated for $Mg_{18}C_{252}H_{126}O_{63} \cdot$ DMF (%): Mg, 9.51; C, 65.81; H, 2.76; Found (%): Mg, 9.12; C, 65.92; H, 2.97, N, 0.59.

ANMOF-74(Ni)

4,4´-(anthracene-9,10-diyl)bis(2-hydroxybenzoic acid) (10.00 mg, 0.022 mmol), $NiCl_2$ $6H_2O$ (10.80 mg, 0.084 mmol) and benzoic acid (2.7 mg, 0.022 mmol) were suspended in benzyl alcohol (0.7 mL) and EtOH (0.7 mL) The resulting mixture was sonicated until complete dissolution of the educts was achieved and it was kept in a culture tube at 120 C for 2 days. The resulting precipitate was washed with DMF (2 x 10 mL) and MeOH (1 x 10 mL) and activated at 120°C to remove the less volatile solvent to obtain a green crystalline powder. The PXRD pattern of the synthesized MOF matches the simulated ANMOF-74 PXRD pattern. Elemental Analysis (activated): Calculated for $Ni_{18}C_{252}H_{126}O_{63} \cdot$ DMF (%): Ni, 20.25; C, 58.00; H. 2.43; Found (%): Ni, 20.09; C, 58.84; H, 2.60, N 0.61.

ANMOF-74(Co)

4,4´-(anthracene-9,10-diyl)bis(2-hydroxybenzoic acid) (10.00 mg, 0.022 mmol), $Co(NO_3)_2 \cdot 6H_2O$ (24.30 mg, 0.084 mmol) and benzoic acid (2.7 mg, 0.022 mmol) were suspended in DMF (1.1 mL), EtOH (0.3 mL) and H_2O (1 mL). The resulting mixture was sonicated until complete dissolution of the educts was achieved and it was kept in a culture tube at 120 C for 2 days. The resulting precipitate was washed with DMF (2 x 10 mL) and MeOH (1 x 10 mL) and activated at 120 °C to remove the less volatile solvent to obtain a pink crystalline powder. The PXRD pattern of the synthesized MOF matches the simulated ANMOF-74 PXRD pattern. Elemental Analysis (activated): Calculated for $Co_{18}C_{252}H_{126}O_{63} \cdot$ DMF (%): Co, 20.31; C, 57.96; H. 2.43; Found (%): Co, 20.11; C, 58.16; H, 2.79, N, 0.65.

ANMOF-74(Mn)

4,4´-(anthracene-9,10-diyl)bis(2-hydroxybenzoic acid) (10.00 mg, 0.022 mmol) and $MnCl_2 \cdot 4H_2O$ (22.60 mg, 0.084 mmol) were suspended in DMF (1.5 mL). The resulting mixture was sonicated until complete dissolution of the educts was achieved and it was kept in a culture tube at 120°C for 2 days. The resulting precipitate was washed with DMF (2 x 10 mL) and MeOH (1 x 10 mL) and activated at 120 °C to remove the less volatile solvent to obtain a light beige crystalline powder. The PXRD pattern of the synthesized MOF matches the simulated ANMOF-74 PXRD pattern. Elemental Analysis (activated): Calculated for $Mn_{18}C_{252}H_{126}O_{63} \cdot$ DMF (%): Mn, 19.20; C, 58.77; H. 2.47; Found (%): Mn, 18.07; C, 58.44, H, 2.67, N, 0.56.

3.6.2.4 MOF-74 synthesis

MOF-74(Zn)

The synthesis was adapted from: Rosi, N. L.; Kim, J.; Eddaoudi, M.; Chen, B.; O´Keeffe, M.; Yaghi, O. M. Rod Packings and metal-Organic Frameworks Constructed from Rod-Shaped Secondary Building Units. *J. Am. Chem. Soc.* **2005**, *127*, 1504-1518.

2,5-dihydroxy-1,4-benzenedicarboxylic acid (0.019 g, 0.096 mmol) and zinc nitrate tetrahydrate, $Zn(NO_3)_2 \cdot 4H_2O$ (0.053 mg, 0.203 mmol) were dissolved in DMF (2 mL), 2-propanol (0.1 mL) and water (0.1 mL). The resulting mixture was sonicated until complete dissolution of the educts was achieved and it was kept in a culture tube at 105°C for 1 day. The resulting precipitate was washed with DMF (2 x 10 mL) and ethanol (1 x 10 mL) and dried under reduced pressure.

MOF-74(Mg)

The synthesis was adapted from: Caskey, S. R.; Wong-Foy, A. G.; Matzger, A. J. Dramatic Tuning of Carbon Dioxide Uptake via Metal Substitution in a Coordination Polymer with Cylindrical Pores. *J. Am. Chem. Soc.* **2008**, *130*, 18070-18071.

2,5-dihydroxy-1,4-benzenedicarboxylic acid (0.111 g, 0.559 mmol) and magnesia nitrate hexahydrate, Mg(NO3)2·6H2O (0.475 mg, 1.85 mmol) were dissolved in a 15:1:1 mixture of DMF-ethanol-water (50 mL). The resulting mixture was sonicated until complete dissolution of the educts was achieved and it was kept in a Teflon sealed 100 mL Schott Duran glass bottle at 125°C for 1 day. The resulting precipitate was washed with DMF (2 x 10 mL) and methanol (1 x 10 mL) and dried under reduced pressure.

MOF-74(Ni)

The synthesis was adapted from: Caskey, S. R.; Wong-Foy, A. G.; Matzger, A. J. Dramatic Tuning of Carbon Dioxide Uptake via Metal Substitution in a Coordination Polymer with Cylindrical Pores. *J. Am. Chem. Soc.* **2008**, *130*, 18070-18071.

2,5-dihydroxy-1,4-benzenedicarboxylic acid (0.478 g, 2.41 mmol) and nickel nitrate hexahydrate, $Ni(NO_3)_2 \cdot 6H_2O$ (2.378 mg, 8.178 mmol) were dissolved in a 1:1:1 mixture of DMF-ethanol-water (200 mL). The resulting mixture was sonicated until complete dissolution of the educts was achieved and it was kept in three Teflon sealed 100 mL Schott Duran glass bottles at 100°C for 1 day. The resulting precipitate was washed with DMF (2 x 10 mL) and methanol (1 x 10 mL) and dried under reduced pressure.

MOF-74(Co)

The synthesis was adapted from: Caskey, S. R.; Wong-Foy, A. G.; Matzger, A. J. Dramatic Tuning of Carbon Dioxide Uptake via Metal Substitution in a Coordination Polymer with Cylindrical Pores. *J. Am. Chem. Soc.* **2008**, *130*, 18070-18071.

2,5-dihydroxy-1,4-benzenedicarboxylic acid (0.482 g, 2.43 mmol) and cobalt nitrate hexahydrate, $Co(NO_3)_2 \cdot 6H_2O$ (2.377 g, 8.67 mmol) were dissolved in a 1:1:1 mixture of DMF-ethanol-water (200 mL). The resulting mixture was sonicated until complete dissolution of the educts was achieved and it was kept in three Teflon sealed 100 mL Schott Duran glass bottles at 100°C for 1 day. The resulting precipitate was washed with DMF (2 x 10 mL) and methanol (1 x 10 mL) and dried under reduced pressure.

MOF-74(Mn)

The synthesis was adapted from: Cozzolino, A. F.; Brozek, A. K., Palmer, R. D.; Yano, J.; Li, Minyuan; Dinca, M. Ligand Redox Non-Innocence in the Stoichiometric Oxidation of Mn_2(2,5-dioxidoterephtalate) (Mn-MOF-74). *J. Am. Chem. Soc.* **2014**, *136*, 3334-3337.

2,5-dihydroxy-1,4-benzenedicarboxylic acid (0.27 g, 1.3 mmol) and $MnCl_2 \cdot 4H_2O$ (1.07 g, 5.41 mmol) were dissolved in a 15:1 mixture of DMF-ethanol (32 mL) under argon atmosphere. The resulting mixture was sonicated until complete dissolution of the educts was achieved and it was kept in a Teflon sealed 100 mL Schott Duran glass bottle at 135°C for 3 day. The resulting precipitate was washed with DMF (2 x 10 mL) and methanol (1 x 10 mL) and dried under reduced pressure.

3.6.3 Characterization

3.6.3.1 Powder X-ray diffraction

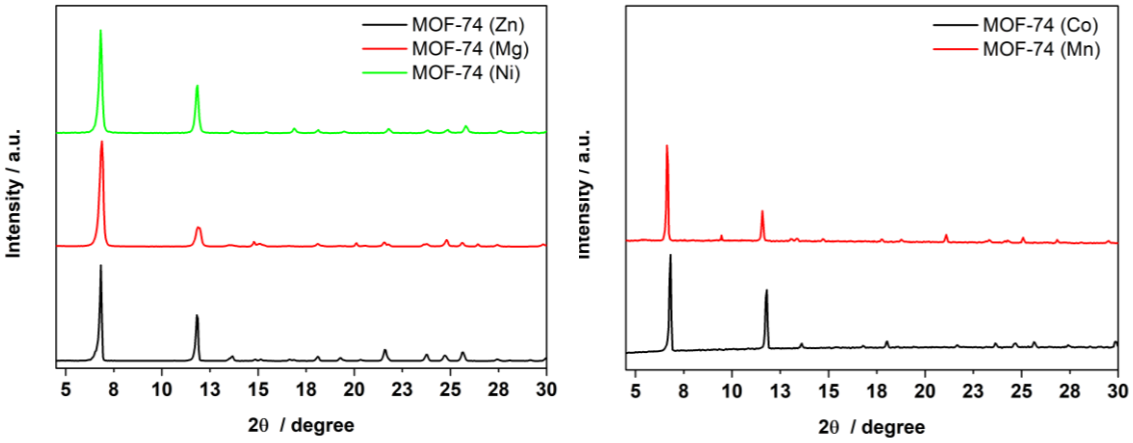

Figure 3-7: PXRD patterns of the MOF-74(M) bulk materials.

3.6.3.2 Scanning-electron microscopy

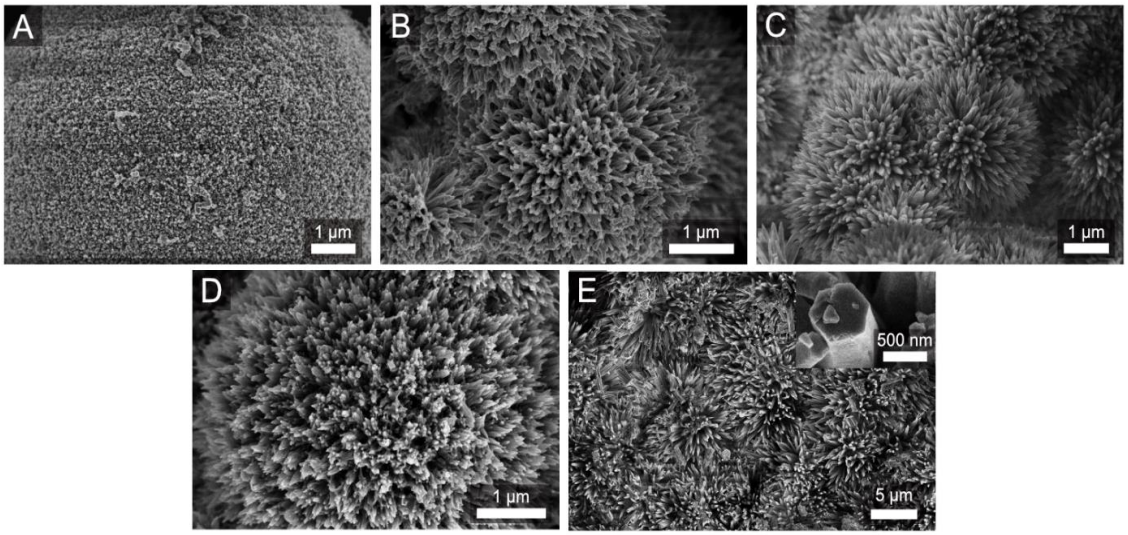

Figure 3-8: SEM images of the ANMOF-74 bulk materials (A) ANMOF-74(Zn), (B) ANMOF-74(Mg), (C) ANMOF-74(Ni), (D) ANMOF-74(Co), (E) ANMOF-74(Mn) and a close-up of a hexagonally shaped monolith depicted as inset.

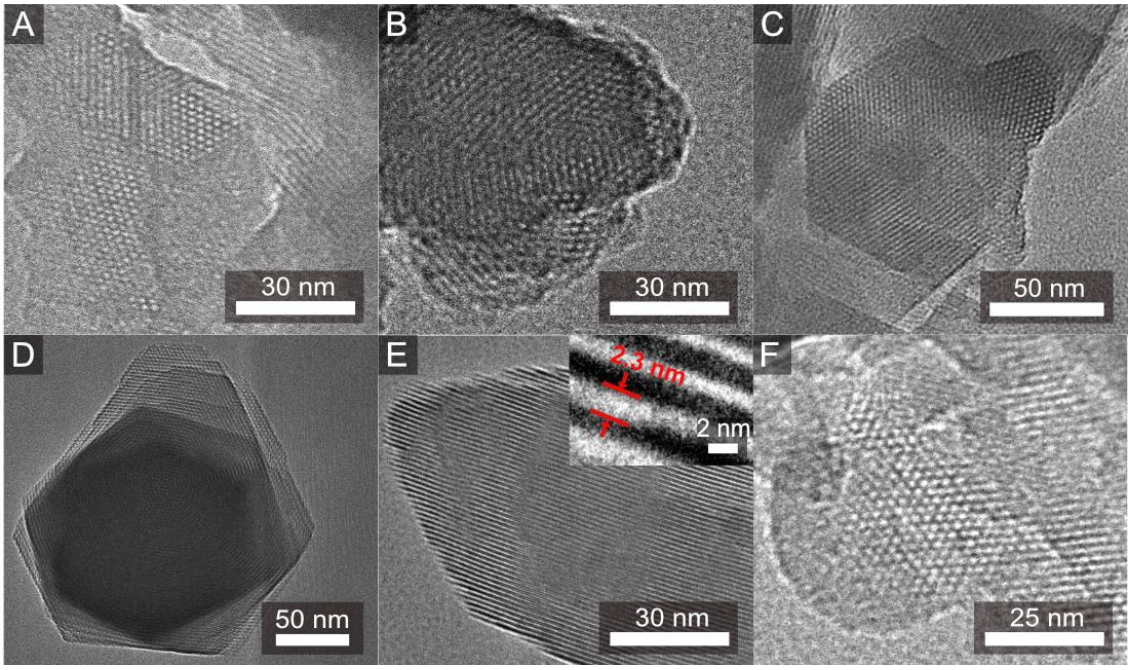

Figure 3-9: High resolution TEM images of the ANMOF-74(M) series in [001] orientation showing (A) the Zn-, (B) Mg-, (C) Ni-, (D) Co-, (F) Mn-ANMOF-74 materials, respectively. (E) High resolution TEM image of ANMOF-74(Co) in side view showing a close-up of the lattice planes as inset.

3.6.3.3 UV-Vis spectroscopy and photoluminescence of the ABHB linker

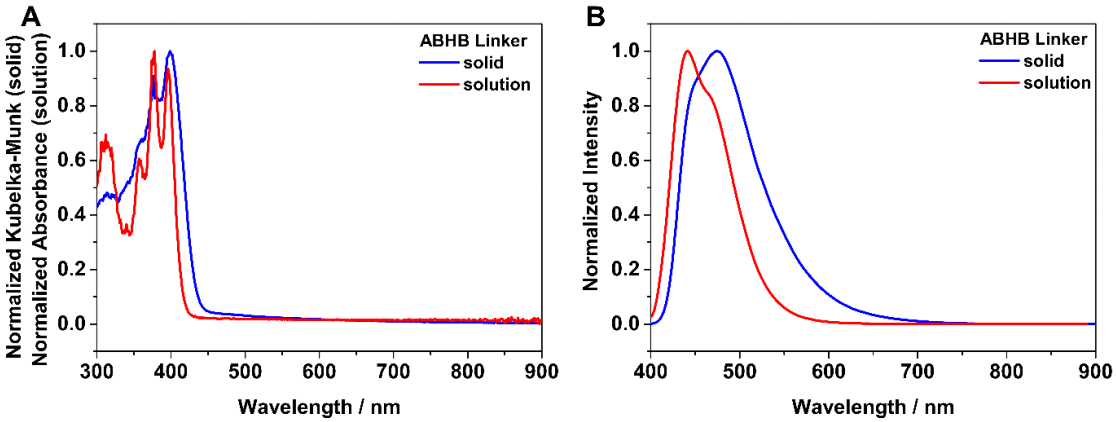

Figure 3-10: (A) Comparison of the absorption and diffuse reflectance spectra of the ABHB linker in $CHCl_3$ solution (red) and as solid dispersed in $BaSO_4$ (blue). (B) PL spectra of the ABHB linker measured with pulsed 378 nm excitation in $CHCl_3$ solution (red) and as solid (blue).

3.6.3.4 Tauc plots of the ANMOF-74 series

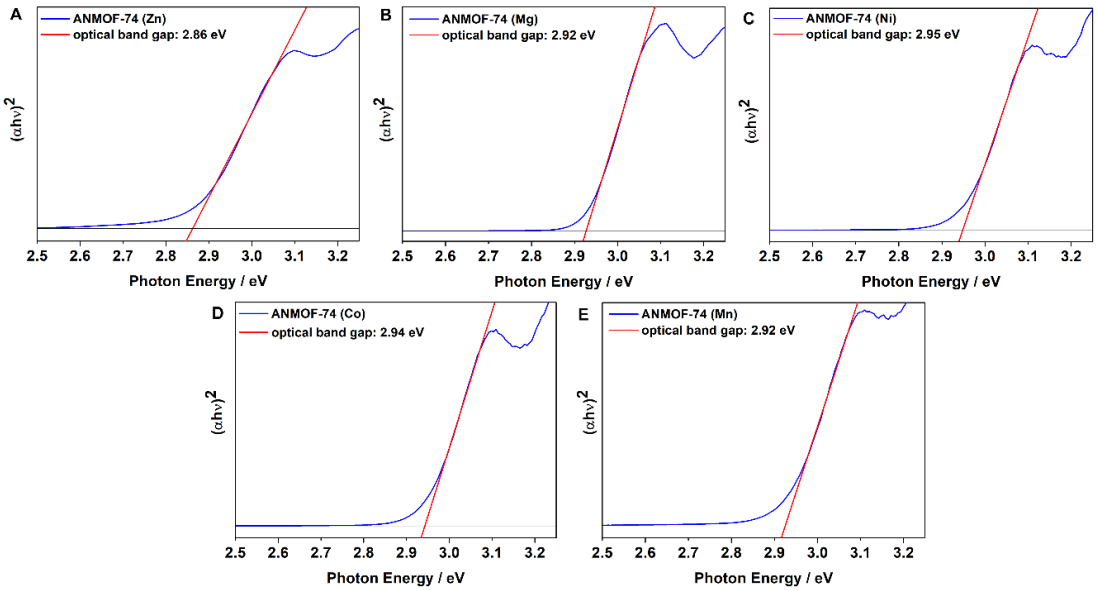

Figure 3-11: Tauc plots of ANMOF-74(Zn) (A), ANMOF-7(Mg) (B), ANMOF-74 (Ni) (C), ANMOF-74(Co) (D) and ANMOF-74(Mn) (E), suggesting the presence of direct band gaps.

3.6.3.5 Time-correlated single photon counting (TCSPC) traces

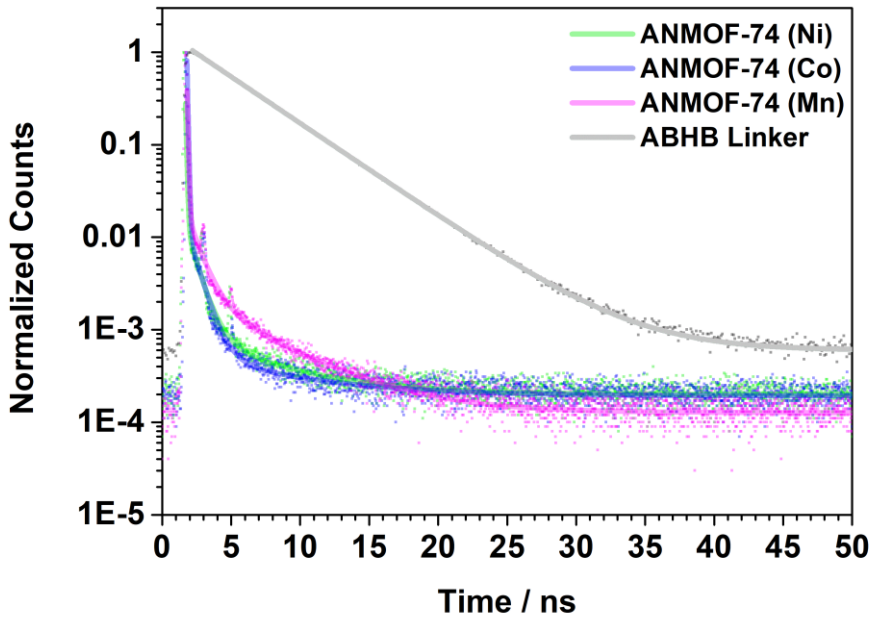

Figure 3-12: The time-correlated single photon counting (TCSPC) traces corresponding to the PL spectra of ANMOF-74(Ni), ANMOF-74(Co) and ANMOF-74(Mn) as solids and of the ABHB linker in solution which were recorded at the respective emission maximum of each material. The solid lines represent the exponential fits.

.

Table 3-2: The PL lifetimes (τ) of the ANMOF-74(M) series and of the ABHB linker, obtained from triexponential fits (see Figure S5 and 6) the TCSPC traces of the MOFs and from a monoexpontial fit of the TCSPC trace of the ABHB linker, as well as the error and the fractional intensities in percentages, which are the fractions of emitted photons corresponding to the respective lifetimes. We note that the stated error is the fitting error and that it does not necessarily reflect the actual resolution of the setup of around 100 ps.

sample		**τ / ns**	**error / ns**	**fractional intensity / %**
ANMOF-74 (Zn)	τ_1	0.162	±0.012	22.9
	τ_2	0.79	±0.03	59.5
	τ_3	3.4	±0.2	17.6
ANMOF-74 (Mg)	τ_1	0.169	±0.006	28.7
	τ_2	1.03	±0.02	50.0
	τ_3	4.90	±0.12	21.3
ANMOF-74 (Ni)	τ_1	0.065	±0.004	55.3
	τ_2	0.80	±0.06	31.9
	τ_3	5.6	±1.0	12.8
ANMOF-74 (Co)	τ_1	0.064	±0.002	80.5
	τ_2	0.79	±0.06	15.5
	τ_3	7	±2	4.0
ANMOF-74 (Mn)	τ_1	0.065	±0.003	48.3
	τ_2	0.89	±0.06	28.8
	τ_3	5.1	±0.4	22.9
Anthracene (Monomer)	τ	4.32	±0.011	100

3.6.3.6 Photoluminescence quantum yield (PLQY) and CIE color space

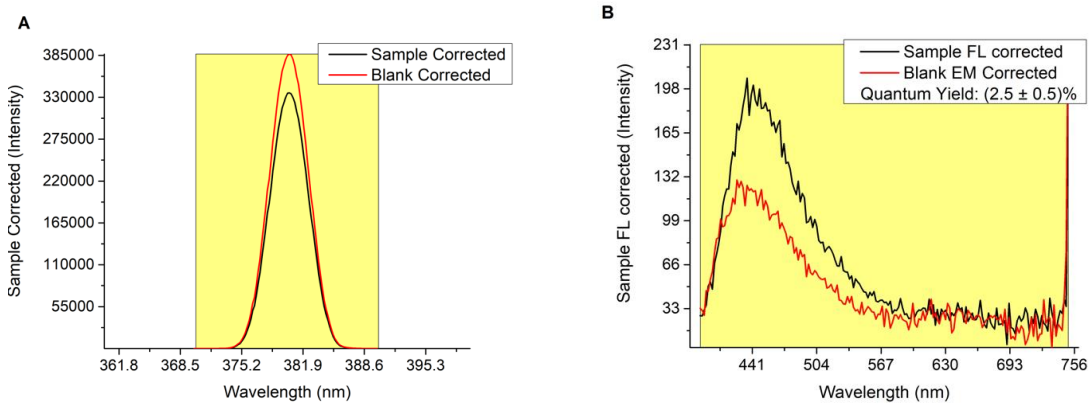

Figure 3-13: Photoluminescence quantum yield (PLQY) measurement of ANMOF-74(Mg). Rayleigh peak (A) and emission (B) data with integration boundaries.

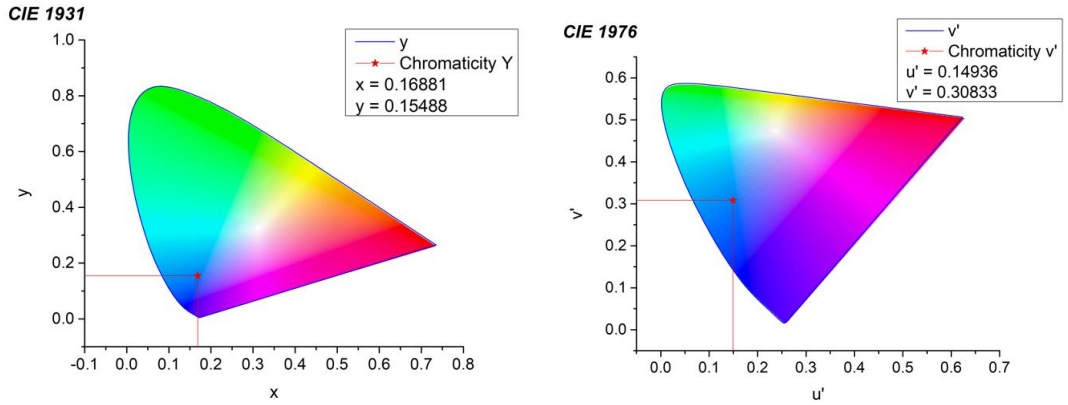

Figure 3-14: CIE 1931 and CIE 1976 color spaces with the ANMOF-74(Mg) emission and the respective coordinates.

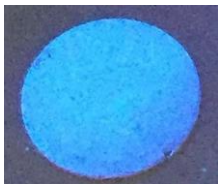

Figure 3-15: Photo image of an ANMOF-74(Mg) pellet during irradiation with a 365 nm wavelength.

3.6.3.7 Thermogravimetric analysis (TGA) of the ANMOF-74 series

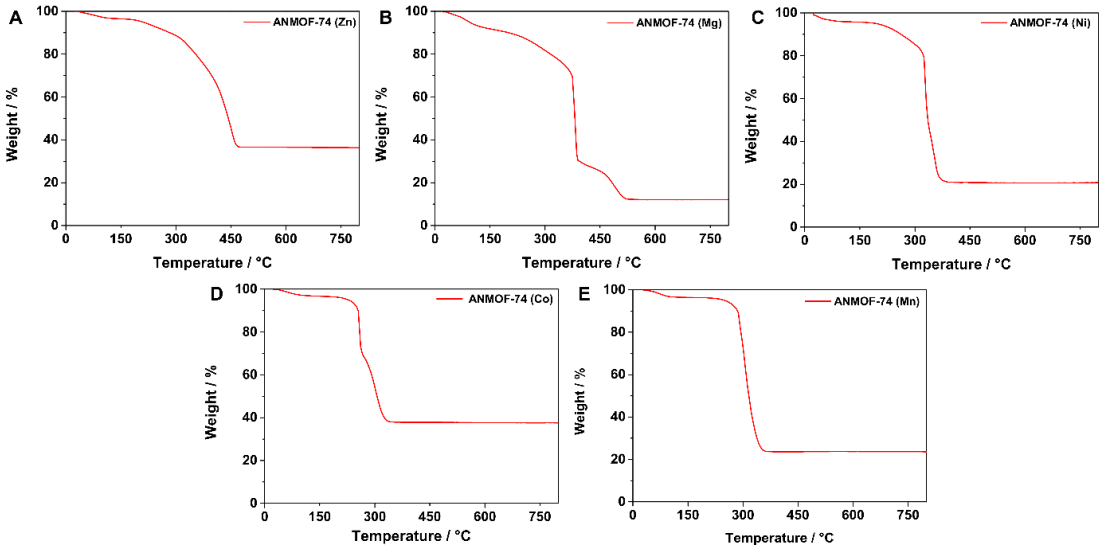

Figure 3-16: Thermogravimetric Analysis (TGA) of (A) ANMOF-74(Zn), (B) ANMOF-74(Mg), (C), ANMOF-74(Ni), (D) ANMOF-74(Co) and (E) ANMOF-74(Mn) measured as bulk materials (20 mg).

3.6.3.8 Energy dispersive X-ray (EDX) spectra of ANMOF-74 (M)

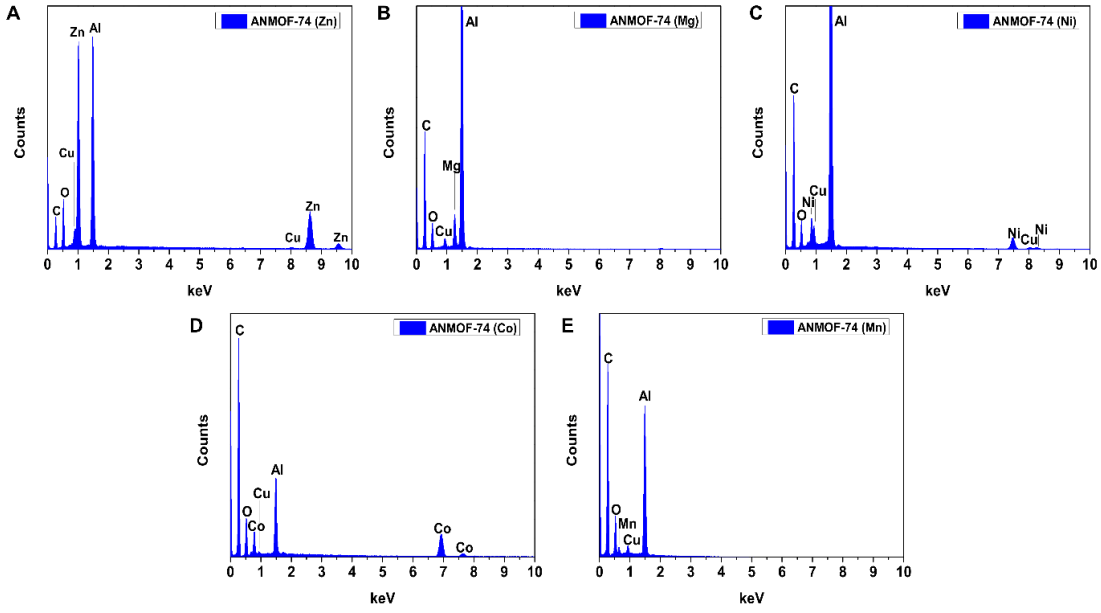

Figure 3-17: Energy dispersive X-ray (EDX) spectra of (A) ANMOF-74(Zn), (B) ANMOF-74(Mg), (C), ANMOF-74(Ni), (D) ANMOF-74(Co) and (E) ANMOF-74(Mn), measured as bulk materials on an SEM sample holder.

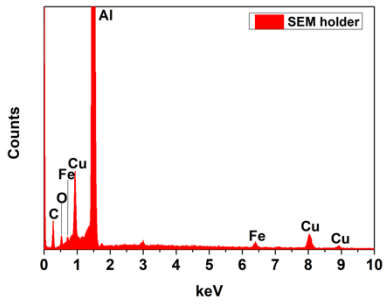

Figure 3-18: Energy dispersive X-ray (EDX) spectrum of the SEM sample holder.

3.6.3.9 X-ray photoelectron spectroscopy (XPS) of the ANMOF-74 series

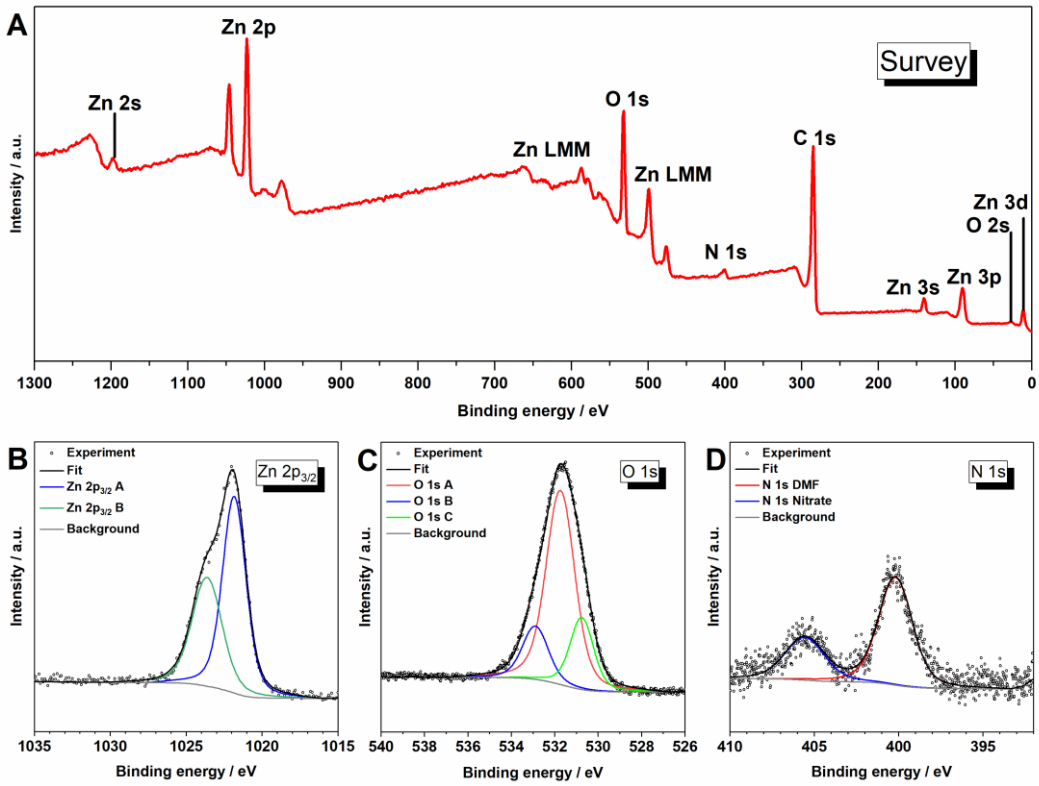

Figure 3-19: XPS spectra of ANMOF-74(Zn) powder: (A) survey scan, (B) Zn 2p spectrum, (C) O 1s spectrum and (D) N 1s spectrum.

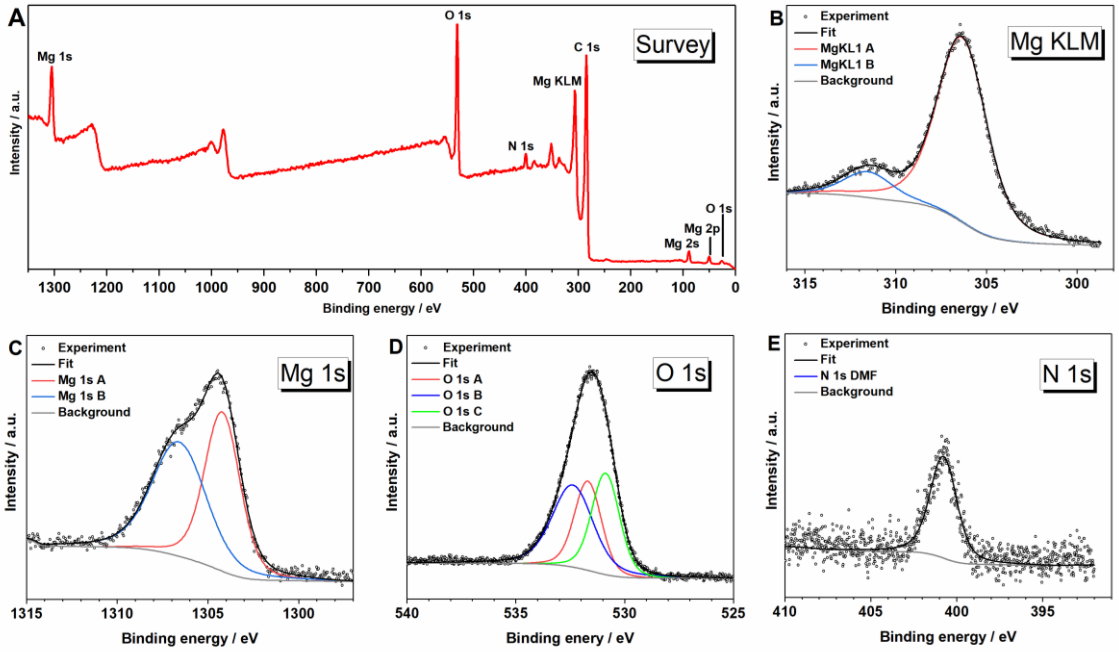

Figure 3-20: XPS spectra of ANMOF-74(Mg) powder: (A) survey scan, (B) Mg KLM spectrum, (C) Mg 1s spectrum, (D) O 1s spectrum and (E) N 1s spectrum.

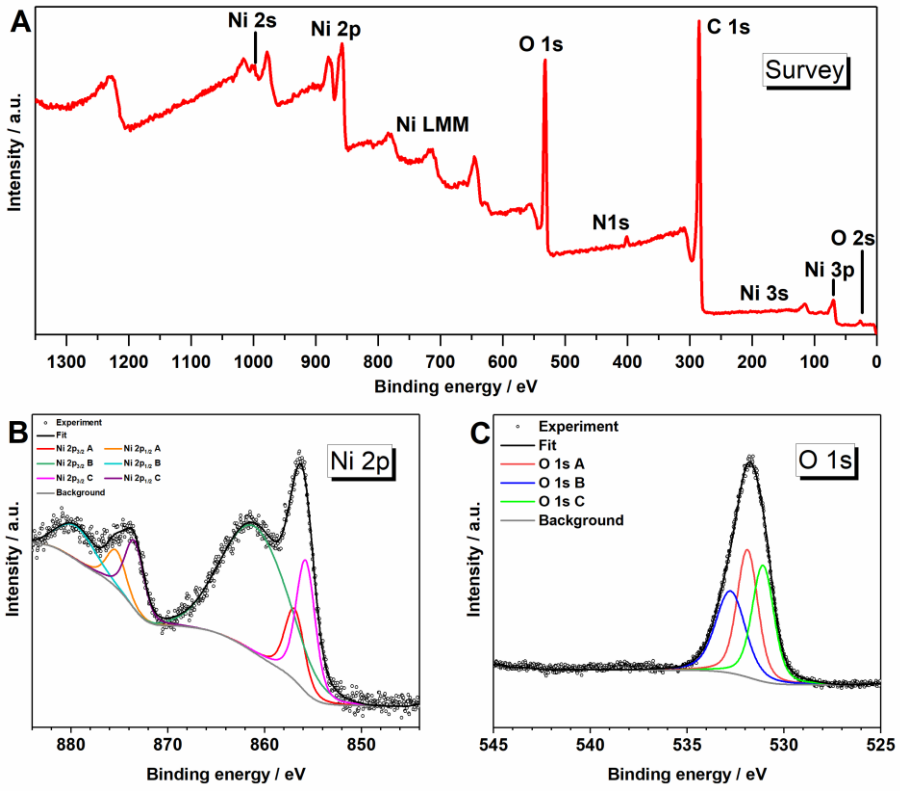

Figure 3-21: XPS spectra of ANMOF-74(Ni) powder: (A) survey scan, (B) Ni 2p spectrum and (C) O 1s spectrum.

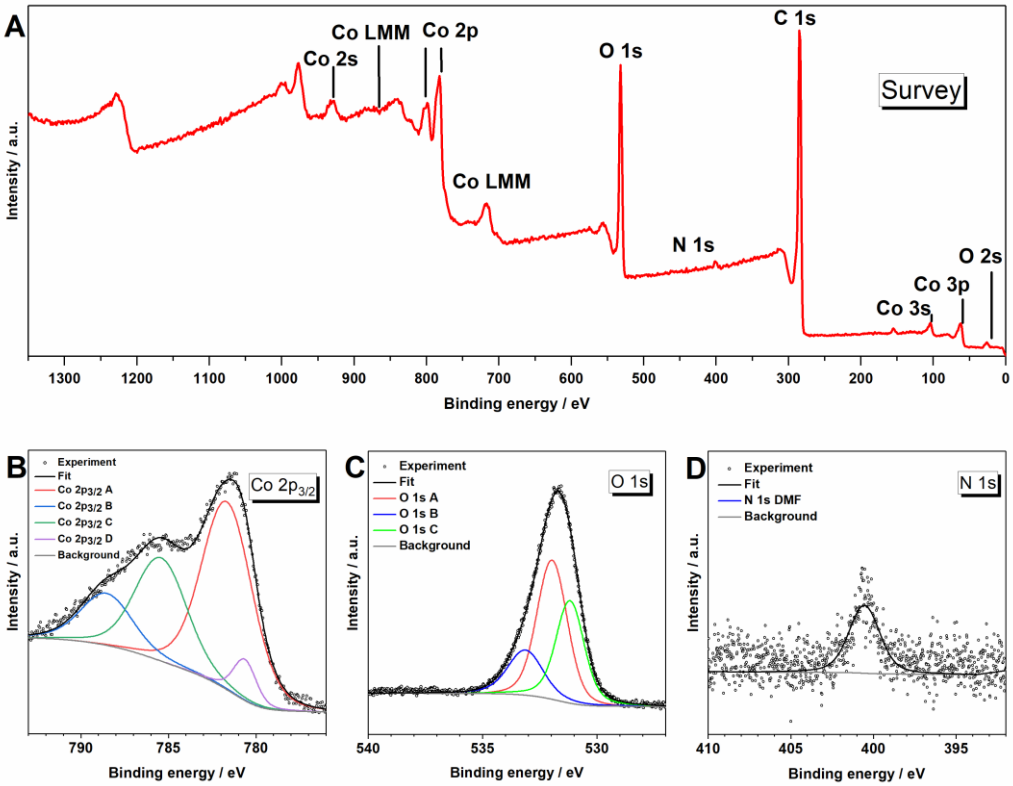

Figure 3-22: XPS spectra of ANMOF-74(Co) powder: (A) survey scan, (B) Co 2p spectrum, (C) O 1s spectrum and (D) N 1s spectrum.

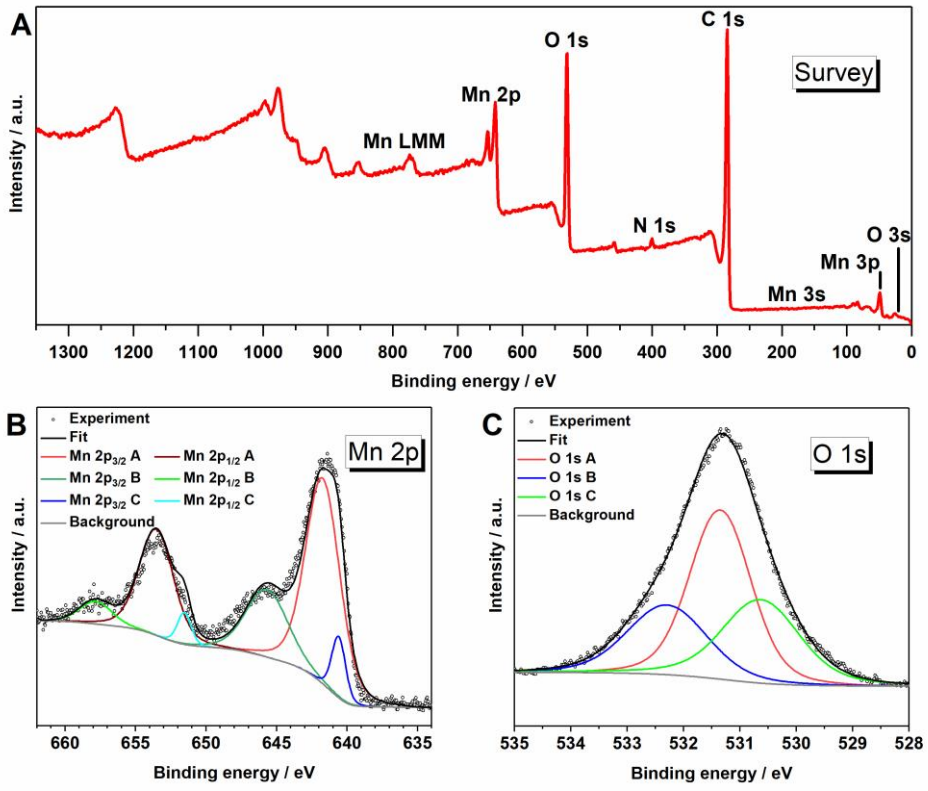

Figure 3-23: XPS spectra of ANMOF-74(Mn) powder: (A) survey scan, (B) Mn 2p spectrum and (C) O 1s spectrum.

3.6.3.10 Unit cell parameters and atomic coordinates

ANMOF-74(Zn)

R_{wp} = 6.74%, R_p = 4.99%

R*3* (146) - trigonal
a = b = 46.06 Å, c = 5.78 Å
α = β = 90°, γ = 120°

Atom	x/a	y/b	z/c
O1	0.6592	0.6089	0.8710
O2	0.6262	0.6377	0.0040
O3	0.6388	0.6434	0.4834
O4	0.4006	0.3608	0.6904
O5	0.3647	0.3616	0.9242
O6	0.3149	0.3512	0.6837
Zn7	0.6622	0.6539	0.8175
O8	0.3548	0.2984	0.2372
Zn9	0.3595	0.3454	0.6430
C10	0.6163	0.6077	0.4376
C11	0.5890	0.5870	0.5889
C12	0.5687	0.5518	0.5495
C13	0.5772	0.5377	0.3678
C14	0.6015	0.5577	0.2096
C15	0.4166	0.4155	0.8479
C16	0.3885	0.3933	0.9881
C17	0.4061	0.4486	0.2674
C18	0.4324	0.4707	0.1253
C19	0.4385	0.4493	0.9190
C20	0.4709	0.4741	0.8078
C21	0.5002	0.4726	0.8493
C22	0.5323	0.4991	0.7803
C23	0.5361	0.5282	0.6700
C24	0.5068	0.5299	0.6302
C25	0.4747	0.5033	0.6996
C26	0.4464	0.5063	0.6562
C27	0.4493	0.5342	0.5447
C28	0.4804	0.5598	0.4744
C29	0.5088	0.5576	0.5165
C30	0.5605	0.4961	0.8249
C31	0.5577	0.4681	0.9369
C32	0.5333	0.4483	0.0118
C33	0.4981	0.4448	0.9632
C34	0.6286	0.6102	0.0372
C35	0.6180	0.5924	0.2302

C36	0.3719	0.3873	0.3652
C37	0.3904	0.4106	0.2009

ANMOF-74(Mg)

R_{wp} = 6.96%, R_p = 5.16%

R*3* (146) - trigonal
a = b = 46.36 Å, c = 6.05 Å
α = β = 90°, γ = 120°

Atom	**x/a**	**y/b**	**z/c**
O1	0.6592	0.6089	0.8710
O2	0.6262	0.6377	0.0040
O3	0.6388	0.6434	0.4834
O4	0.4006	0.3608	0.6904
O5	0.3647	0.3616	0.9242
O6	0.3149	0.3512	0.6837
Mg7	0.6622	0.6539	0.8175
O8	0.3548	0.2984	0.2372
Mg9	0.3595	0.3454	0.6430
C10	0.6163	0.6077	0.4376
C11	0.5890	0.5870	0.5889
C12	0.5687	0.5518	0.5495
C13	0.5772	0.5377	0.3678
C14	0.6015	0.5577	0.2096
C15	0.4166	0.4155	0.8479
C16	0.3885	0.3933	0.9881
C17	0.4061	0.4486	0.2674
C18	0.4324	0.4707	0.1253
C19	0.4385	0.4493	0.9190
C20	0.4709	0.4741	0.8078
C21	0.5002	0.4726	0.8493
C22	0.5323	0.4991	0.7803
C23	0.5361	0.5282	0.6700
C24	0.5068	0.5299	0.6302
C25	0.4747	0.5033	0.6996
C26	0.4464	0.5063	0.6562
C27	0.4493	0.5342	0.5447
C28	0.4804	0.5598	0.4744
C29	0.5088	0.5576	0.5165
C30	0.5605	0.4961	0.8249
C31	0.5577	0.4681	0.9369
C32	0.5333	0.4483	0.0118
C33	0.4981	0.4448	0.9632

C34	0.6286	0.6102	0.0372
C35	0.6180	0.5924	0.2302
C36	0.3719	0.3873	0.3652
C37	0.3904	0.4106	0.2009

ANMOF-74(Ni)

R_{wp} = 3.94%, R_p = 3.15%

R*3* (146) - trigonal
a = b = 46.21 Å, c = 5.76 Å
α = β = 90°, γ = 120°

Atom	**x/a**	**y/b**	**z/c**
O1	0.6592	0.6089	0.8710
O2	0.6262	0.6377	0.0040
O3	0.6388	0.6434	0.4834
O4	0.4006	0.3608	0.6904
O5	0.3647	0.3616	0.9242
O6	0.3149	0.3512	0.6837
Ni7	0.6622	0.6539	0.8175
O8	0.3548	0.2984	0.2372
Ni9	0.3595	0.3454	0.6430
C10	0.6163	0.6077	0.4376
C11	0.5890	0.5870	0.5889
C12	0.5687	0.5518	0.5495
C13	0.5772	0.5377	0.3678
C14	0.6015	0.5577	0.2096
C15	0.4166	0.4155	0.8479
C16	0.3885	0.3933	0.9881
C17	0.4061	0.4486	0.2674
C18	0.4324	0.4707	0.1253
C19	0.4385	0.4493	0.9190
C20	0.4709	0.4741	0.8078
C21	0.5002	0.4726	0.8493
C22	0.5323	0.4991	0.7803
C23	0.5361	0.5282	0.6700
C24	0.5068	0.5299	0.6302
C25	0.4747	0.5033	0.6996
C26	0.4464	0.5063	0.6562
C27	0.4493	0.5342	0.5447
C28	0.4804	0.5598	0.4744
C29	0.5088	0.5576	0.5165
C30	0.5605	0.4961	0.8249
C31	0.5577	0.4681	0.9369

C32	0.5333	0.4483	0.0118
C33	0.4981	0.4448	0.9632
C34	0.6286	0.6102	0.0372
C35	0.6180	0.5924	0.2302
C36	0.3719	0.3873	0.3652
C37	0.3904	0.4106	0.2009

ANMOF-74(Co)

R_{wp} = 4.18%, R_p = 2.55%

R*3* (146) - trigonal
a = b = 46.11 Å, c = 5.92 Å
α = β = 90°, γ = 120°

Atom	**x/a**	**y/b**	**z/c**
O1	0.6592	0.6089	0.8710
O2	0.6262	0.6377	0.0040
O3	0.6388	0.6434	0.4834
O4	0.4006	0.3608	0.6904
O5	0.3647	0.3616	0.9242
O6	0.3149	0.3512	0.6837
Co7	0.6622	0.6539	0.8175
O8	0.3548	0.2984	0.2372
Co9	0.3595	0.3454	0.6430
C10	0.6163	0.6077	0.4376
C11	0.5890	0.5870	0.5889
C12	0.5687	0.5518	0.5495
C13	0.5772	0.5377	0.3678
C14	0.6015	0.5577	0.2096
C15	0.4166	0.4155	0.8479
C16	0.3885	0.3933	0.9881
C17	0.4061	0.4486	0.2674
C18	0.4324	0.4707	0.1253
C19	0.4385	0.4493	0.9190
C20	0.4709	0.4741	0.8078
C21	0.5002	0.4726	0.8493
C22	0.5323	0.4991	0.7803
C23	0.5361	0.5282	0.6700
C24	0.5068	0.5299	0.6302
C25	0.4747	0.5033	0.6996
C26	0.4464	0.5063	0.6562
C27	0.4493	0.5342	0.5447
C28	0.4804	0.5598	0.4744
C29	0.5088	0.5576	0.5165

C30	0.5605	0.4961	0.8249
C31	0.5577	0.4681	0.9369
C32	0.5333	0.4483	0.0118
C33	0.4981	0.4448	0.9632
C34	0.6286	0.6102	0.0372
C35	0.6180	0.5924	0.2302
C36	0.3719	0.3873	0.3652
C37	0.3904	0.4106	0.2009

ANMOF-74(Mn)

R_{wp} = 4.38%, R_p = 2.80%

R*3* (146) - trigonal
a = b = 46.21 Å, c = 5.69 Å
α = β = 90°, γ = 120°

Atom	**x/a**	**y/b**	**z/c**
O1	0.6592	0.6089	0.8710
O2	0.6262	0.6377	0.0040
O3	0.6388	0.6434	0.4834
O4	0.4006	0.3608	0.6904
O5	0.3647	0.3616	0.9242
O6	0.3149	0.3512	0.6837
Mn7	0.6622	0.6539	0.8175
O8	0.3548	0.2984	0.2372
Mn9	0.3595	0.3454	0.6430
C10	0.6163	0.6077	0.4376
C11	0.5890	0.5870	0.5889
C12	0.5687	0.5518	0.5495
C13	0.5772	0.5377	0.3678
C14	0.6015	0.5577	0.2096
C15	0.4166	0.4155	0.8479
C16	0.3885	0.3933	0.9881
C17	0.4061	0.4486	0.2674
C18	0.4324	0.4707	0.1253
C19	0.4385	0.4493	0.9190
C20	0.4709	0.4741	0.8078
C21	0.5002	0.4726	0.8493
C22	0.5323	0.4991	0.7803
C23	0.5361	0.5282	0.6700
C24	0.5068	0.5299	0.6302
C25	0.4747	0.5033	0.6996
C26	0.4464	0.5063	0.6562
C27	0.4493	0.5342	0.5447

C28	0.4804	0.5598	0.4744
C29	0.5088	0.5576	0.5165
C30	0.5605	0.4961	0.8249
C31	0.5577	0.4681	0.9369
C32	0.5333	0.4483	0.0118
C33	0.4981	0.4448	0.9632
C34	0.6286	0.6102	0.0372
C35	0.6180	0.5924	0.2302
C36	0.3719	0.3873	0.3652
C37	0.3904	0.4106	0.2009

3.7 On-surface growth of ANMOF-74(Zn) films *via* vapor-assisted conversion

ANMOF-74(Zn) bulk material showed intriguing photoluminescence properties (Figure 3-5 A). Due to its broad emission over the whole visible spectrum, it is a possible candidate for LED-technology. For applications of MOFs in (opto)electronic devices, the controlled on-surface growth of thin films is neccessary. It requires a film with high crystallinity as well as a homogeneous surface coverage, ideally with small thicknesses in the nm range.

The vapor-assisted conversion (VAC) method was utilized for the growth of ANMOF-74(Zn) on the substrates glass, gold and a 100 nm atomic-layer-deposition (ALD) ZnO seed layer on glass (1.0 cm x 1.2 cm). The reaction parameters for the ANMOF-74(Zn) bulk material synthesis were slightly modified for the film growth. For the precursor solution, the ligand 4,4´-(anthracene-9,10-diyl)bis(2-hydroxybenzoic acid) (ABHB) and a potential crystallization modulator such as benzoic acid or acetic acid were dissolved in different amounts of DMF. Afterwards, $Zn(NO_3)_2 \cdot 4H_2O$ (2 eq.) was added to the solution and the reaction mixture was sonicated until the metal salt was dissolved. The vapor source DMF was filled into a glass vessel. Afterwards, the substrate was placed upon a glass platform and 50 µL – 100 µL of the precursor solution were dropcasted on the substrate. The sealed vessel was put in a preheated oven at 100 °C – 120°C for 18 h. After removal from the oven and cooling down to room temperature, the substrates were taken out and dried under reduced pressure, resulting in a yellowish film on top of the substrates.

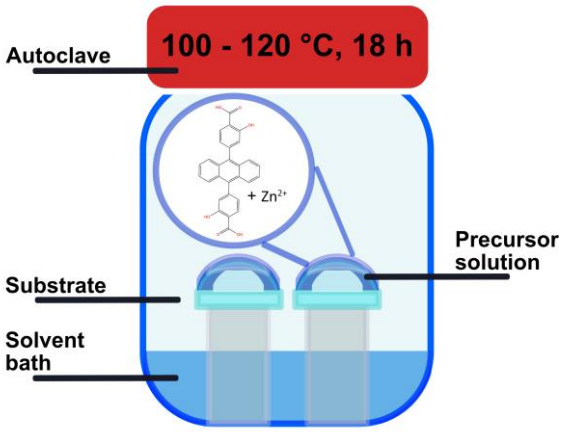

Figure 3-24: Schematic setup of the film synthesis *via* the vapor-assisted conversion (VAC).

3.7.1 ANMOF-74(Zn) film synthesis on glass

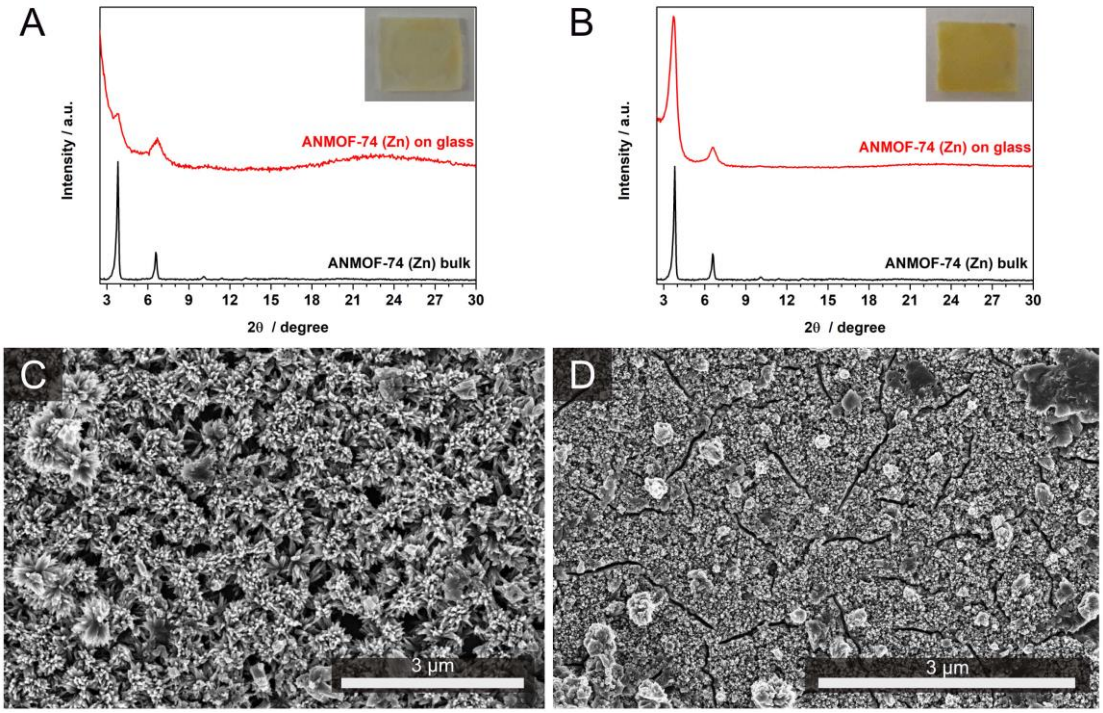

Figure 3-25: (A + B) XRD patterns of ANMOF-74(Zn) bulk material (black) and of ANMOF-74(Zn) grown on glass (red) with precursor concentrations of (A) 2.2 mmol/L, (B) 4.4 mmol/L, with a photo image as inset. (C+D) SEM top-view micrographs of ANMOF-74(Zn) grown on glass with precursor concentrations of (C) 2.2 mmol/L, (D) 4.4 mmol/L.

For the synthesis of ANMOF-74(Zn) thin films on glass we used two different precursor concentrations, 2.2 mmol/L and 4.4 mmol/L. This led to the formation of phase-pure ANMOF-74(Zn) films grown on glass in both cases. The reflections in the XRD patterns of the ANMOF-74(Zn) films nicely agree with the ones of the ANMOF-74(Zn) bulk material (see Figure 3-25). However, the more concentrated precursor concentration resulted in films with enhanced crystallinity. Also, the top-view SEM images show a dense film of intergrown rod-shaped crystallites with a diameter of about 35 nm and good continuous substrate coverage (see Figure 3-23 Figure 3-25D). However, the film is broken by cracks due to a large film thickness. Furthermore, additional bulk material is visible on top of the film. The top-view SEM images of the MOF film with the lower concentration (2.2 mmol/L) show needle-shaped crystallites forming spherical agglomerates, with 500 nm – 1 µm diameter, laying in layers on top of the substrate, forming no homogeneous film (see Figure 3-25 C). The screening of different reaction parameters like precursor concentration, temperature, reaction time, dropcast volume and the addition of the modulators acetic acid, benzoic acid and salicylic acid did not lead to the formation of homogeneous, crystalline and crack-free ANMOF-74(Zn) films on glass.

3.7.2 ANMOF-74(Zn) film synthesis on gold

The best ANMOF-74(Zn) film on gold was obtained with a precursor concentration of 2.2 mmol/L and with benzoic acid as modulator. The synthesised film reveals high degree of crystallinity with distinct Bragg reflections at 3.75° and 6.51° 2Θ (see Figure 3-26 A (red)). SEM top-view and cross-section images show a homogeneous long-range coverage with MOF crystallites over the substrate (see Figure 3-26 B – D). The morphology is composed of needle-shaped crystallites, with a length of about 1.7 µm and a width of 75 nm, forming hemispherical agglomerates. The agglomerates have a diameter of about 3 µm, and are individually growing out of single spots on top of the gold substrate. Furthermore, the films are crack-free and without any additional surface deposits. Cross-section SEM images indicate film thicknesses of about 1.7 µm (see Figure 3-26 C).

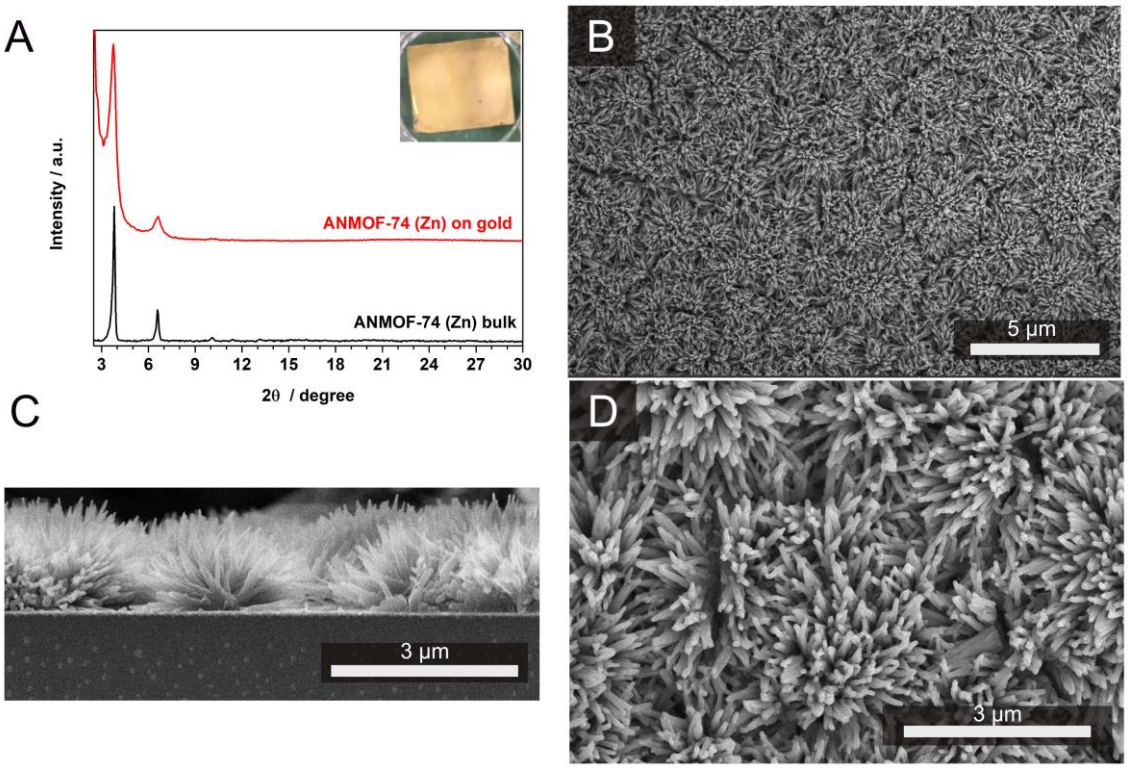

Figure 3-26: (A) XRD patterns of ANMOF-74(Zn) bulk material (black) and of ANMOF-74(Zn) grown on gold (red) with a precursor concentration of 2.2 mmol/L, with a photo image as inset. SEM top-view (B+D) and SEM cross-section (C) micrographs of ANMOF-74(Zn) grown on gold.

3.7.3 ANMOF-74(Zn) film synthesis on glass substrates with 100 nm ALD ZnO layer

The successful growth of ANMOF-74(Zn) was also carried out on glass substrates covered with a 100 nm ZnO ALD layer, which was confirmed by XRD (see Figure 3-27 A (red)). The ZnO layer served as seed layer for the crystal growth, to enable a more favorable growth on glass

substrates. For the film synthesis a precursor concentration of 2.2 mmol/L and acetic acid as modulator were used. In contrast to the film growth on plain glass substrates, highly crystalline ANMOF-74(Zn) films were obtained. Furthermore, SEM top-view images reveal homogeneous long-range surface coverage with MOF crystallites, with a few cracks visible, but without any additional surface deposits (impurities) (see Figure 3-27 B). Similar to the ANMOF-74(Zn) film on gold, needle-shaped MOF crystallites with a length of at least 500 nm and a width of 50 nm are connected to the substrate surface, apparently originating from common nucleation points on the substrate (see Figure 3-27 C).

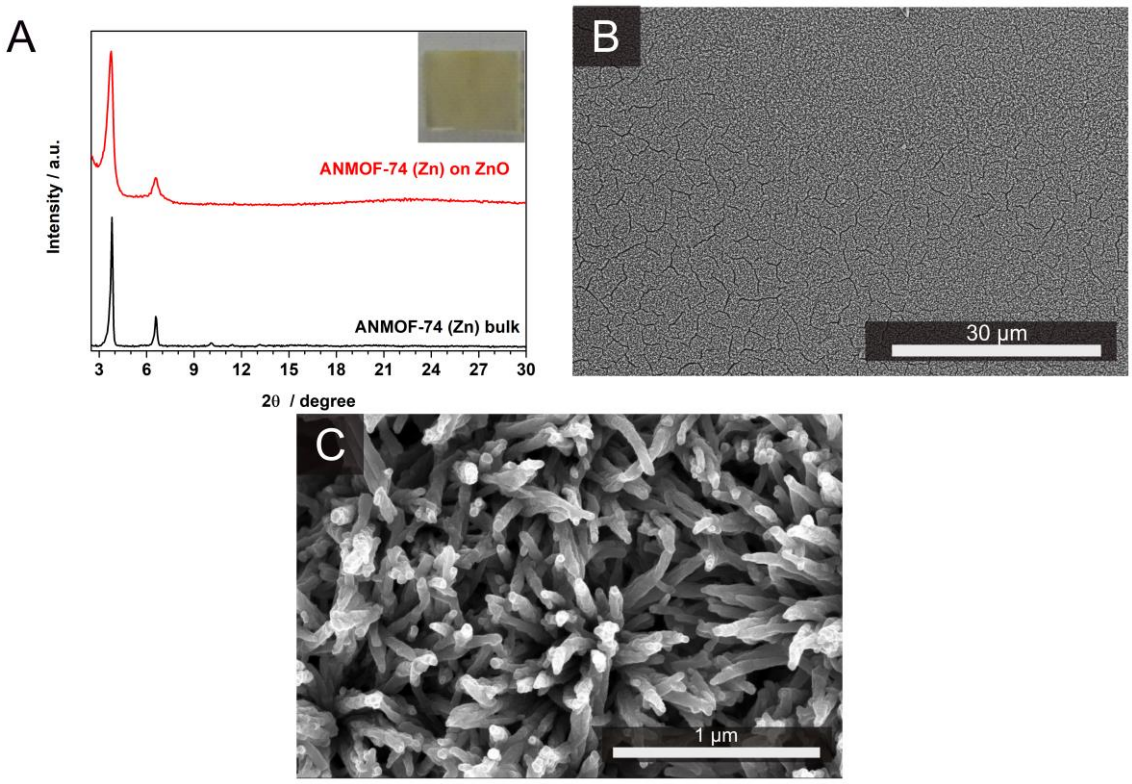

Figure 3-27: XRD patterns of ANMOF-74(Zn) bulk material (black) and of ANMOF-74(Zn) grown on a 100 nm ZnO ALD layer (red) with a precursor concentration of 2.2 mmol/L, with a photo image as inset. (B, C) SEM top-view micrographs of the respective ANMOF-74(Zn) film.

To minimize the ZnO layer thickness between the glass substrate and the MOF layer, a reduced amount of metal precursor (0.5 eq.) was used. In this case, the ZnO layer served as seed layer, as well as metal source. For the synthesis, a precursor concentration of 4.4 mmol/L was used. XRD analysis confirms high crystallinity of the film (see Figure 3-28 A). SEM images reveal a homogenous film growth, without any impurities on top of the film. Individual needle-shaped MOF crystallites, with a length of about 2.6 µm and a width of 150 nm, are growing out of the ZnO layer (see Figure 3-28 B – D). The increased film thickness is caused by the higher precursor concentration. In contrast to the other obtained films, here the individual MOF crystallites are not

agglomerated or growing out of from common spots on the substrate. Furthermore, a ZnO layer of about 50 nm is left on the substrate.

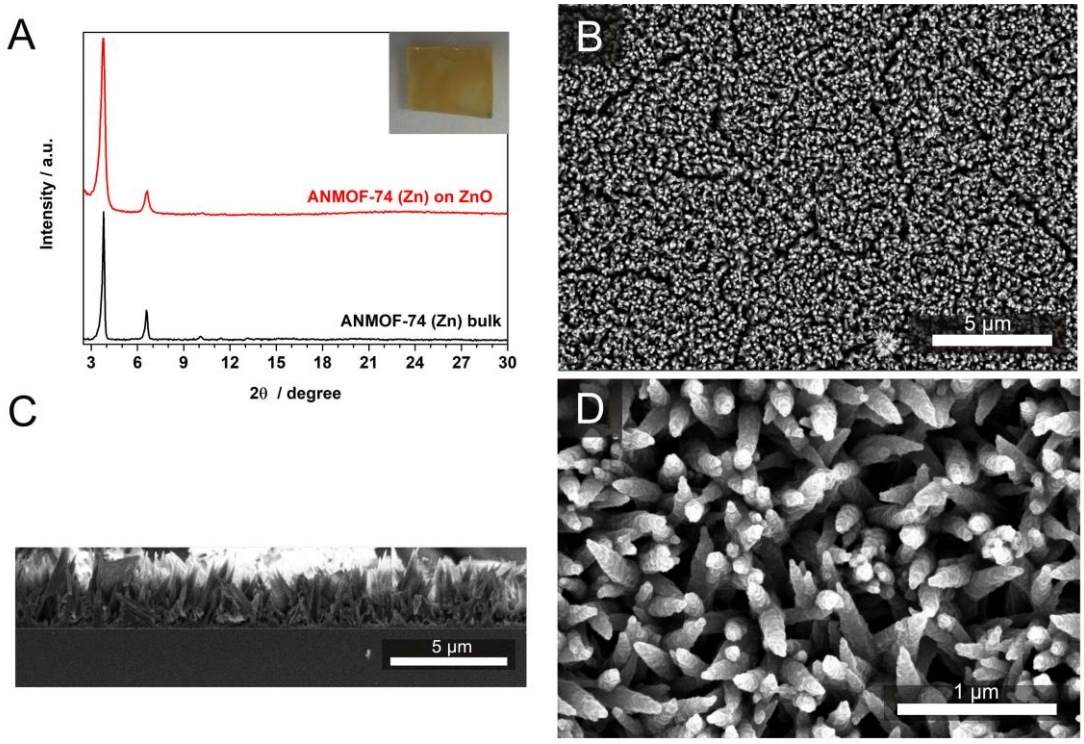

Figure 3-28: (A) XRD patterns of ANMOF-74(Zn) bulk material (black) and of ANMOF-74(Zn) grown on a 100 nm ALD ZnO layer (red) with a precursor concentration of 4.4 mmol/L, with a photo image as inset. SEM top-view (B+D) and SEM cross-section (C) micrographs of ANMOF-74(Zn) of the respective film.

Benzoic acid was added as modulator to slow down the crystal growth, aimed at achieving an even more defined crystallization of individual and oriented MOF crystallites on the substrate. However, SEM images reveal the formation of dense films, with a thickness of 2.1 µm, consisting of intergrown MOF crystallites (see Figure 3-29 B – D). Furthermore, the crystallinity of the films is much lower (see Figure 3-29 A), in comparison to the previously obtained film without modulator.

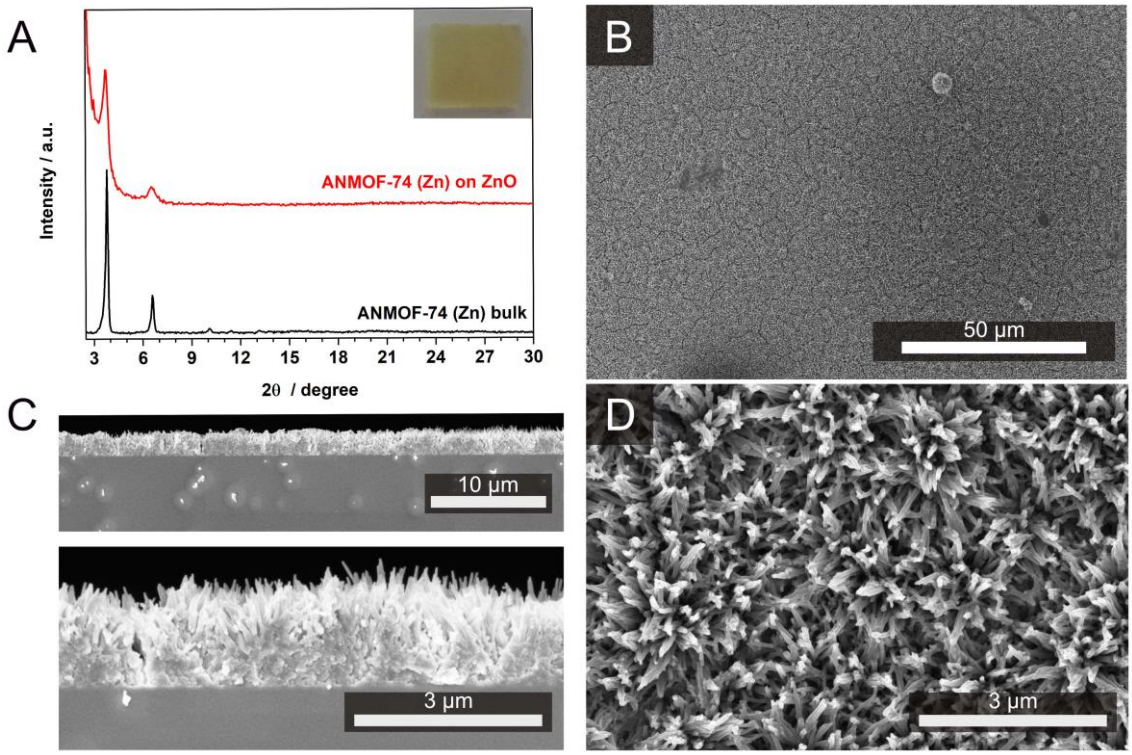

Figure 3-29: (A) XRD patterns of ANMOF-74 (Zn) bulk material (black) and of ANMOF-74(Zn) grown on a 100 nm ALD ZnO layer (red) with a precursor concentrtion of 4.4 mmol/L and benzoic acid as modulator, with a photo image as inset. SEM top-view (B+D) and SEM cross-section (C) micrographs of ANMOF-74(Zn) of the respective film.

3.7.4 Experimental

3.7.4.1 General

All materials were purchased from *Sigma Aldrich, Acros or TCI Europe* in the common purities *purum, puriss* or *reagent grade.* The materials were used as received without additional purification and handled in air unless otherwise noted. The water utilized in the synthesis was subjected to a *Merck-Milipore Mili-Q* purification system prior to use.

3.7.4.2 Substrates

The preparation of the gold-substrates is based on the procedure described by Hinterholzinger *et al.*. Seven microscope glass slides (Menzel, 76 mm x 26 mm) were washed with a 1:100 mixture of Hellmanex III and water, water and finally ethanol. Oxygen plasma cleaning (Diener electronic, Plasma-Surface-Technology) for 30 min was conducted, prior to the mounting of the glass slides in a vacuum deposition unit installed in a glove box (MBraun Labmaster Pro SP) equipped with an Inficon SQC-310C deposition controller. A layer of 10 nm titanium and then a layer of

40 nm gold were thermally deposited under high vacuum onto the microscope glass slides. Afterwards, the microscope slides were cut into 1.2 cm x 1 cm pieces. These substrates were directly used for the MOF film preparation.

The glass substrates were prepared by cutting microscope glass slides (Menzel, 76 mm x 26 mm) into 1.2 cm x 1.0 cm pieces. Afterwards they were washed with a 1:100 mixture of Hellmanex III and water, rinsed with water and finally ethanol and dried in a nitrogen flow.

Thermal atomic layer deposition of ZnO thin films was carried out in a *Picosun R-200 Advanced Reactor* at 250 °C and approximately 6 hPa. The carrier/purge gas was nitrogen (air Liquide, 99.999%). Microscope slides were used as substrates (Menzel, 76 mm x 26 mm. The precursors diethyl zinc (DEZ, Strem, 95%) and water (Millipore, *Q-grade*) were held in stainless steel cylinders at 18 °C during the process. One ALD cycle consisted of a 0.1 s DEZ pulse, 6 s purge, 0.1 s water pulse and 8 s purge. The gas flow in both precursor lines was constant at 100 sccm each. For 73 nm thick films a growth rate of 0.098 nm/ cycle with a non-uniformity of 1.1% across a 20 cm wafer was determined by spectroscopic ellipsometry (*J. A. Woollam M-2000*) on Si(100) witness substrates with native oxide. The ZnO layer was represented by a Cauchy model layer.

3.7.4.3 ANMOF-74(Zn) film synthesis via vapor-assisted conversion

For the film formation using VAC, a glass bottle (Schott Duran, borosilicate 3.3, ISO4796, 100 mL) with a PBT cap equipped with a Teflon seal was used. The bottom part of the bottle was filled with 14 Raschig-rings (10 mm x 10 mm, soda-lime glass) to obtain an elevated flat platform for the substrate. DMF was filled into the bottle (5 ml). Afterwards, a substrate (1.2 cm x 1 cm) was placed on top of the Raschig-rings and fully coated with a specific volume of freshly prepared MOF precursor solution (see Table 3-3 for specific conditions). The bottle was closed and was transferred into a preheated oven where it was kept for the specified time. Afterwards the bottle was removed from the oven and was allowed to cool down to room temperature before the substrate was removed and dried under reduced pressure.

For the precursor solution, ABHB was dissolved in DMF by ultrasonic treatment. If desired, benzoic acid or acetic acid was added to this solution. The metal precursor was added to the solution and dissolved by applying ultrasonic treatment.

Table 3-3: Synthesis conditions of the ANMOF-74(Zn) films via VAC.

	Precursor solution				Droplet Volume	Sub-strate	Temp-erature	Reaction time	Vapor source
Concen-tration	ABHB	$Zn(NO_3)_2$ $4H_2O$	modulator	DMF					DMF
4.4 mmol/L	2.19 mg 4.86 µmol 1 eq	2.51 mg 9.6 µmol 2 eq		1.1 mL	100 µL	glass	120°C	18 h	5 mL
2.2 mmol/L	1.09 mg 2.42 µmol 1 eq	1.26 mg 4.82 µmol 2 eq		1.1 mL	100 µL	glass	100 °C	18 h	5 mL
2.2 mmol/L	1.09 mg 2.42 µmol 1 eq	1.26 mg 4.82 µmol 2 eq	b.a* 25 µL 16 eq	1.1 mL	100 µL	gold	120°C	18 h	5 mL
2.2 mmol/L	1.09 mg 2.42 µmol 1 eq	1.26 mg 4.82 µmol 2 eq	a.a. 11 µL 79 eq	1.1 mL	100 µL	100 nm ALD ZnO on glass	120°C	18 h	5 mL
2.2 mmol/L	2.19 mg 4.86 µmol 1 eq	0.63 mg 2.41 µmol 0.5 eq		1.1 mL	100 µL	100 nm ALD ZnO on glass	120°C	18 h	5 mL
4.4 mmol/L	2.19 mg 4.86 µmol 1 eq	0.63 mg 2.41 µmol 0.5 eq	b.a.* 250 µL 80 eq	1.1 mL	100 µL	100 nm ALD ZnO on glass	120°C	18 h	5 mL

*Benzoic acid (3.07 mmol, 375.15 mg) was dissolved in 2 mL DMF (c = 1.536 mol/L)

4 Anthracene-ethyne MOF-74

This chapter is based on the following article:

A helical anthracene-ethyne-based MOF-74 analog

Patricia I. Scheurle[a,b], Andre Mähringer[a,b], Tabea Haug[a,b], Alexander Biewald[a,b], Daniel Axthammer[a,b], Achim Hartschuh[a,b], Dana D. Medina*[a,b] and Thomas Bein*[,a,b] *Under Revision*.

[a]Department of Chemistry, Ludwig-Maximilians-Universität (LMU), Butenandtstr. 5-13 (E), 81377 Munich, Germany.

[b]Center for NanoScience (CeNS), Schellingstr. 4, 80799 Munich, Germany.

*Corresponding Author

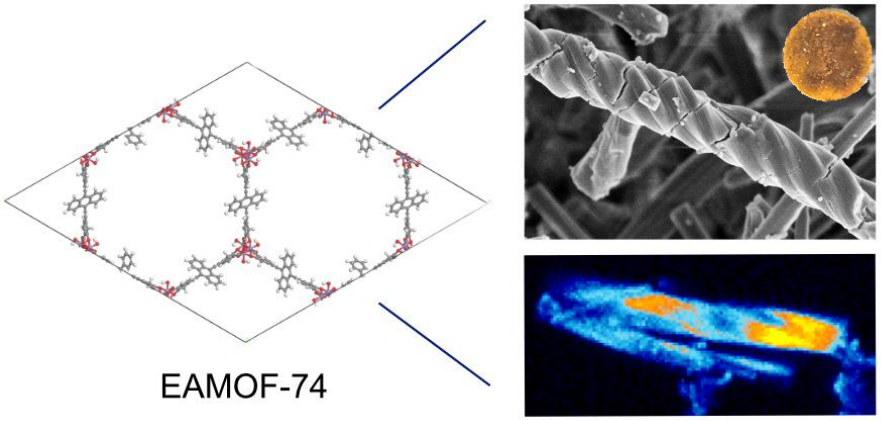

4.1 Abstract

A flexible, electron-rich building block was integrated into the backbone of a metal-organic framework with MOF-74 topology. The building block comprises a central anthracene core connected to acetylene groups. Solvothermal synthesis with Mn^{2+} yields a highly crystalline anthracene-ethyne based MOF-74 structure. It shows an unusual helical rod-like morphology, exhibiting visible light absorption, and photoluminescence.

4.2 Introduction

Metal-organic frameworks (MOFs) are highly crystalline and porous materials composed of metal nodes interconnected by rigid organic ligands, forming network structures.[1] Due to their well-defined pore structures in combination with high surface areas, MOFs are prominent candidates for applications such as gas storage or separation.[2–4] Especially crystalline materials based on the MOF-74 topology have attracted much interest in recent years, due to its robust architecture, permanent porosity in combination with high surface areas and good thermal stability.[5–7] In the prototype MOF-74, linear 2,5-dihydroxyterephthalic acid ligands and 3*d* transition metals form a trigonal crystal structure with hexagonal pore aperture.[7] It comprises an ideal platform for modifications in the linear backbone, by incorporating elongated ligands and dye molecules, while maintaining its topology, which is formed by the terminal hydroxy- and carboxyl- functional groups. By elongating the ligand with phenyl groups, the pores can be expanded, forming an isoreticular MOF-74 series.[7] Anthracene and its derivatives are fluorescence dyes with interesting optical properties.[8] Recently, we reported about a new MOF-74 reticular series, by incorporating phenoxide anthracene-based building blocks combined with several transition metal ions in the MOF-74 backbone.[9] Here, we introduce a novel elongated electron-rich building block for the construction of frameworks with MOF-74 topology: two acetylene groups were installed adjacent to a central anthracene core terminated by phenyl groups decorated with ortho-hydroxy para-carboxylic functionalities, namely, 4,4'-(anthracene-9,10-diylbis(ethyne-2,1-diyl))bis(2-hydroxybenzoic acid), abbreviated AEHA. The solvothermal reaction of AEHA and Mn^{2+} precursor ions led to a highly crystalline ethyne-anthracene based MOF-74 (EAMOF-74) being isoreticular to previous MOF-74 structures, as well as to the previous reported ANMOF-74 series.[9] Scanning electron microscopy (SEM) revealed an unusual bulk morphology of helical rod-like crystallites (Figure 4-3). Furthermore detailed optical and electrical analysis shed light on the photophysical properties. The ethyne-anthracene-based ligand AEHA) was synthesized in a four-step reaction, including a Sonogashira cross-coupling (for more details see SI). Briefly, for the MOF synthesis, the AEHA ligand was reacted stoichiometrically with $MnCl_2 \cdot 4H_2O$ in a 1:1 DMF/ BnOH solvent

mixture at 120 °C for 2 days, giving a yellow colored powder (Figure 4-1 A). The precipitate was collected by centrifugation and washed three times with dimethylformamide (DMF). Subsequently, the obtained powder was dried under dynamic vacuum for 2 h prior to characterization (for more details see SI).

4.3 Results and discussions

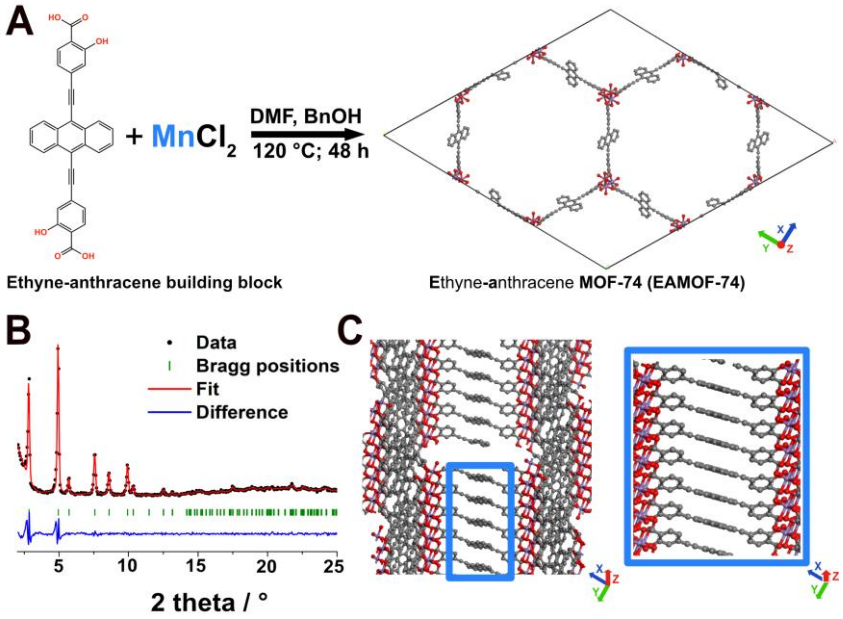

Figure 4-1: (A) Synthesis scheme of the ethyne-anthracene building block and manganese dichloride under solvothermal conditions in DMF/ BnOH for 48 h giving EAMOF-74. View along the crystallographic c-direction of the hexagonal EAMOF-74 lattice. (B) PXRD pattern of EAMOF-74(Mn) and corresponding Pawley fit. (C) Perspective view along the hexagonal channels of the structure. Highlighted in blue are the stacked anthracene cores in c-direction. The shortest interlayer distance was measured to be 0.51 nm between an anthracene core and an opposite ethyne group.

Powder X-ray diffraction (PXRD) analysis of the obtained EAMOF-74(Mn) reveals a high degree of crystallinity indicated by the pronounced reflection intensities at 2.8°, 4,9°, 5.6°, 7.6°, 8.5°, 9.9°, 10.3°, 12.5°, 13.0°, 17.5° and 21.8° 2Θ (Figure 4-1 B). Next, the recorded PXRD pattern was compared to one obtained from a simulated model structure (Figure 4-6). The predicted model structure was constructed with Accelrys Materials Studio 2017 using the calculated MOF-74 structure as a starting model.[2] A PXRD pattern was calculated from the simulated cell, which was subsequently refined by Pawley refinement using the experimental EAMOF-74(Mn) PXRD pattern (Cu $K_{\alpha 1}$-radiation, R_{wp} = 6.6 %). According to the model, the material crystallizes in the triganol space group R3 with lattice parameters of $a = b$ = 6.14 nm, c = 0.66 nm, $\alpha = \beta$ = 90° and γ = 120°. The obtained structure is analogous to those of related MOF-74-based frameworks.[7,9] The structure is composed of infinite hexagonal channels along the crystallographic c-direction, exhibiting pore apertures of 3.1 nm to 3.6 nm (Figure 4-1 C, Figure 4-5). These channels are constructed from helical Mn-oxo chains that are bridged by the AEHA building blocks (close-up

in Figure 4-1 C). The anthracenes in successive layers are oriented parallel to each other in a regular stack, with the shortest interlayer distance of 0.51 nm. Transmission electron microscopy (TEM) analysis shows large, helical rod-like crystals, with a width of about 400 nm and a length of about 6 µm, in side-view. A close-up of the lattice fringes shows a distance of 3.2 nm (Figure 4-7). The purity of the obtained EAMOF-74(Mn) bulk material was further verified by energy dispersive X-ray spectroscopy (EDX), showing no Cl^- anions or other relevant impurities arising from non-reacted precursors (Figure 4-8). Thermogravimetric analysis shows a thermal stability up to 100 °C (Figure 4-9). Interestingly, nitrogen sorption measurements of the activated sample (50 °C, 18 h, vacuum) display limited gas uptake, exhibiting a BET surface area of 110.5 $m^2 g^{-1}$ (Figure 4-10). Analysis of the sorption data with quenched solid density functional theory (QSDFT) gives a pore size of 3.1 nm, which fits well with the simulated model (Figure 4-12). However, the desorption isotherm is not reversible with respect to the adsorption isotherm, indicating a structural degradation and/or pore plugging with residual oligomers during the sorption process. The PXRD pattern of the activated sample after the sorption measurement indeed displays a drastic structural change related to amorphization of the sample, attributed to the removal of coordinating solvent molecules during the activation process (Figure 4-11). We attribute the poor stability of EAMOF-74(Mn) to the less rigid nature of the long AEHA building block. However, pore accessibility and structural integrity were successfully validated by dye adsorption experiments (Figure 4-13). EAMOF-74 exhibited encapsulation of methyl red (MR), methyl orange (MO), as well as of methylene blue (MB) molecules at room temperature. The morphology of EAMOF-74(Mn) bulk material was further characterized by light microscopy (see Figure 4-2 A-D). Thin rods with a wide size distribution showing an average length of 5 µm, up to 50 µm and 500 nm to 3 µm width were observed (Figure 4-2 A, B). Notably, by employing different illumination techniques (e.g., Figure 4-2 B - illumination-bright field, Figure 4-2 C-D - transmission dark-field using polarized light), the helical structure of the rods could be effectively visualized. Specifically, polarized light attenuated distinct areas of the crystallites to highlight the helical morphology of EAMOF-74(Mn) (Figure 4-2 B).

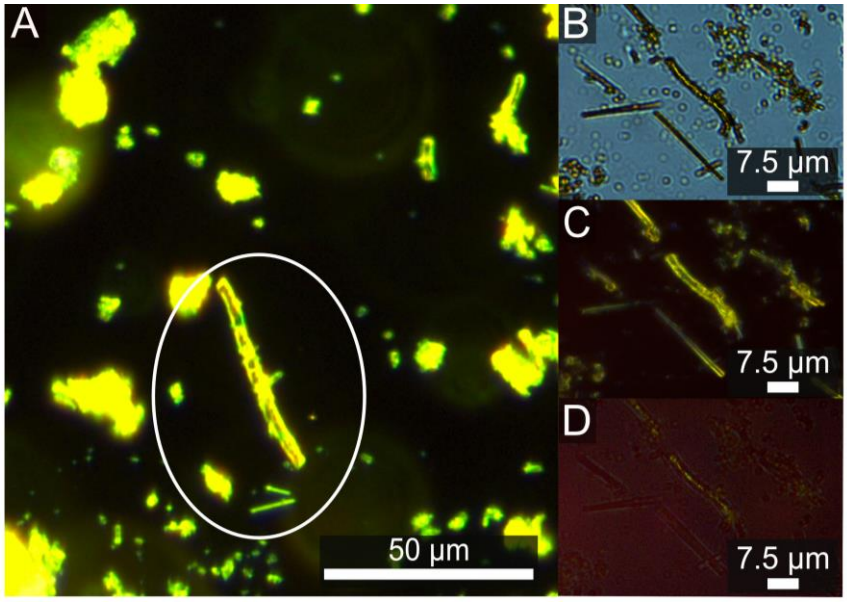

Figure 4-2: (A) Light microscope image of EAMOF-74(Mn) crystallites recorded in transmission dark-field mode showing the helical structure of EAMOF-74. (B) Illumination bright-field, transmission dark-field employing (C-D) polarized light.

SEM images of EAMOF-74(Mn) powder confirm the morphology of helical rods with an average width of 600 nm and a length between 4.5 µm and 6.5 µm with a variety of single helix turns (pitch) (Figure 4-3). Furthermore, the rotation of the crystals ends in a well-faceted hexagonal cross-section (Figure 4-3A inset). This finding corresponds well to the proposed trigonal crystal structure. We also analyzed the ratio between the left- and right twisted crystallites. The different twist rotations of the MOF crystallites are illustrated by the blue and red dots in the SEM image (Figure 4-3 B). We postulate that EAMOF-74(Mn) crystallizes as racemate, including an equal number of twisted rods with left- and right rotations, as demonstrated by the statistics in Figure 4-3.

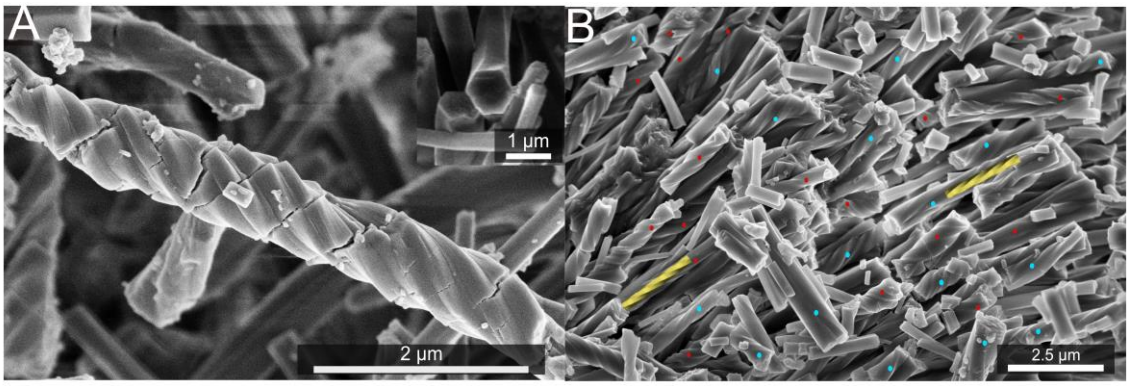

Figure 4-3: (A) SEM micrograph showing a screw-like needle of EAMOF-74. (B) Larger view on the bulk material showing a racemate of MOF crystallite screws. The ratio of EAMOF-74(Mn) crystallite screws showing left rotation (blue dots, 25 pieces) and showing right rotation (red dots, 24 pieces) is close to 1:1.

In the literature, helical MOF-74 structures were observed only once in Zn-MOF-74-II, consisting of the 3,3´-dihydroxy-[1,1´-biphenyl]-4,4´-dicarboxylic acid ligand.[10] In that report, mild solvothermal conditions yielded a helical MOF-74-II superstructure, assembled from multiple flexible MOF-74-II single rods, while higher temperatures caused an oriented evolution of rigid non-twisted tubular rods to multichannel superstructures. Evidently, the helical morphology is a rarely observed and poorly understood phenomenon in the family of MOF-74 derived frameworks, and shedding light on the parameters that govern this process is expected to result in design principles towards specific morphologies. The evolution of chiral shapes from non-chiral building blocks was also reported in the case of tellurium nanocrystals. [11] In this case, no chiral crystal structure or chiral ligands led to the formation of the shape chirality. Instead, a screw dislocation-mediated growth was postulated as reason for this phenomen, which was analyzed by TEM. A screw dislocation- mediated growth could also be a rather likely explanation for the present helical EAMOF-74 morphology, formed from achiral ligands. However, TEM analysis could not give evidence, due to the low stability of the MOF during the measurement.[11]

Next, the electrical properties of EAMOF-74(Mn) were examined by means of two-point probe measurements of crystalline pressed pellets of the bulk material (see Figure 4-6 and Figure 4-14), showing an ohmic resistance and an average electrical conductivity value of 1 x 10^{-10} S/cm. Strikingly, EAMOF-74(Mn) shows an enhancement in electrical conductivity compared to the isoreticular MOF-74(Mn) framework based on the same Mn(II) metal ions, with 2,5-dihydroxyterephthalic acid serving as the organic ligand, showing a van der Pauw conductivity value of 4 x 10^{-13} S/cm.[9] We assume that the main charge transport path is through-bond, where metal-oxo chains provide a continuous electron conductance path, similar to the ANMOF-74(M) derivatives.[12] For the photophysical characterization of the EAMOF-74(Mn) bulk material, we performed UV-Vis absorption and photoluminescence (PL) spectroscopy (Figure 4-4). EAMOF-74(Mn) exhibits an absorption onset at around 530 nm. Assuming a direct band gap, an optical band gap of 2.49 eV was examined by TAUC plot (Figure 4-15). In addition, EAMOF-74(Mn) shows a broad absorption band with two absorption maxima at 488 nm and 460 nm, originating from the integrated EAHA building blocks (Figure 4-16). Confocal photoluminescence mapping was performed on single EAMOF-74(Mn) crystallites, showing a homogenous emission (Figure 4-4 A and Figure 4-17), the steady-state PL measurement shows narrow green emission with a maximum at 541 nm (Figure 4-4 B). Only a small Stokes shift of about 38 nm is observed, as well as an additional weaker emission band at 687 nm. At the emission maximum of 541 nm, a time-correlated single photon counting (TCSPC) trace of EAMOF-74(Mn) was measured (Figure 4-18). The decay of the PL lifetime was evaluated by a stretched exponential fit indicating a

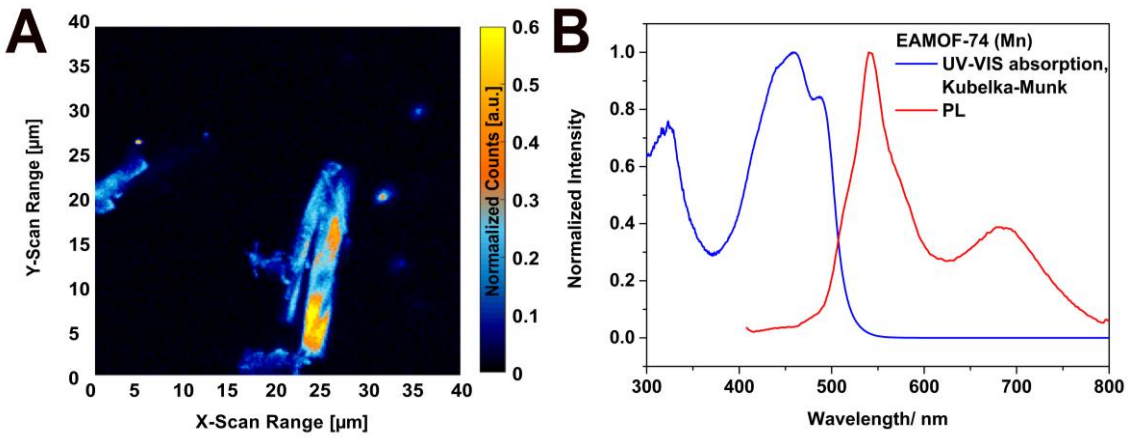

Figure 4-4: (A) Confocal photoluminescence mapping of a single EAMOF-74(Mn) crystallite. (B) UV-Vis absorption measured in diffusive reflectance of the MOF powder dispersed with $BaSO_4$ (blue line) and the photoluminescence (PL) spectrum of the neat MOF bulk material measured with 378 nm excitation (red line).

fast decay process, with an average lifetime of τ_1 = 375 ps. The weaker emission band at 687 nm could be induced by energy transfers between ligands and the manganese ions, causing a decrease of the PL of the emission at 541 nm. A similar effect was already observed in the ANMOF-74(M) series, with M = Ni, Co, Mn.[9]

4.4 Conclusion

Concluding, we have demonstrated the successful synthesis of a novel anthracene-containing MOF with MOF-74 topology, coined EAMOF-74(Mn). Both light and scanning electron microscopy reveal an unusual helical rod-like morphology showing the presence of a racemic mixture. Notably, photoluminescence analysis reveals emission in the green spectral region, which is rare for MOF-74 topologies. Based on this work, we envision to develop further luminescent MOF-74 structures by the integration of even more complex and electron-rich building blocks to enrich the field of isoreticular MOF-74 structures

4.5 References

(1) Yaghi, O. M.; Li, H. Hydrothermal Synthesis of a Metal-Organic Framework Containing Large Rectangular Channels. *J. Am. Chem. Soc.* **1995**, 117, 10401–10402.

(2) Sun, L.; Hendon, C. H.; Minier, M. A.; Walsh, A.; Dincă, M. Million-Fold Electrical Conductivity Enhancement in Fe2(DEBDC) versus Mn2(DEBDC) (E = S, O). *J. Am. Chem. Soc.* **2015**, 137, 6164–6167.

(3) Dolgopolova, E. A.; Shustova, N. B. Metal–organic framework photophysics: Optoelectronic devices, photoswitches, sensors, and photocatalysts. *MRS Bull.* **2016**, 41, 890–896.

(4) Sun, C.-Y.; Qin, C.; Wang, X.-L.; Su, Z.-M. Metal-organic frameworks as potential drug delivery systems. *Expert Opin Drug Deliv* **2013**, 10, 89–101.

(5) Wang, L. J.; Deng, H.; Furukawa, H.; Gándara, F.; Cordova, K. E.; Peri, D.; Yaghi, O. M. Synthesis and characterization of metal-organic framework-74 containing 2, 4, 6, 8, and 10 different metals. *Inorganic chemistry* **2014**, 53, 5881–5883.

(6) Rosi, N. L.; Kim, J.; Eddaoudi, M.; Chen, B.; O'Keeffe, M.; Yaghi, O. M. Rod packings and metal-organic frameworks constructed from rod-shaped secondary building units. *Journal of the American Chemical Society* **2005**, 127, 1504–1518.

(7) Deng, H.; Grunder, S.; Cordova, K. E.; Valente, C.; Furukawa, H.; Hmadeh, M.; Gándara, F.; Whalley, A. C.; Liu, Z.; Asahina, S.; Kazumori, H.; O'Keeffe, M.; Terasaki, O.; Stoddart, J. F.; Yaghi, O. M. Large-pore apertures in a series of metal-organic frameworks. *Science* **2012**, 336, 1018–1023.

(8) Chen, D.; Xing, H.; Su, Z.; Wang, C. Electrical conductivity and electroluminescence of a new anthracene-based metal-organic framework with π-conjugated zigzag chains. *Chem. Commun.* **2016**, 52, 2019–2022.

(9) Scheurle, P. I.; Mähringer, A.; Jakowetz, A. C.; Hosseini, P.; Richter, A. F.; Wittstock, G.; Medina, D. D.; Bein, T. A highly crystalline anthracene-based MOF-74 series featuring electrical conductivity and luminescence. *Nanoscale* **2019**, 11, 20949–20955.

(10) Feng, L.; Li, J.-L.; Day, G. S.; Lv, X.-L.; Zhou, H.-C. Temperature-Controlled Evolution of Nanoporous MOF Crystallites into Hierarchically Porous Superstructures. *Chem* **2019**, 5, 1265–1274.

(11) Ben-Moshe, A.; da Silva, A.; Müller, A.; Abu-Odeh, A.; Harrison, P.; Waelder, J.; Niroui, F.; Ophus, C.; Minor, A. M.; Asta, M.; Theis, W.; Ercius, P.; Alivisatos, A. P. The chain of chirality transfer in tellurium nanocrystals. *Science* **2021**, 372, 729–733.

(12) Kriebel, M.; Hennemann, M.; Beierlein, F. R.; Medina, D. D.; Bein, T.; Clark, T. Propagation of Holes and Electrons in Metal-Organic Frameworks. *J. Chem. Inf. Model.* **2019**, 59, 5057–5064.

4.6 Supporting information

4.6.1 Characterization methods

Nuclear magnetic resonance (NMR)

NMR spectra were recorded on *Bruker AV400* and *AV400 TR* spectrometers. The chemical shifts are expressed in parts per million and calibrated using residual (undeuterated) solvent peaks as an internal reference (^{1}H-NMR: DMSO-d_6: 2.50; ^{13}C-NMR: DMSO-d_6: 39.52). The data for ^{1}H-NMR spectra are written as follows: s = singlet, d = doublet, t = triplet, q = quartet, m = multiplet.

X-ray analysis

X-ray diffraction (XRD) analyzes were performed on a *Bruker D8* diffractometer in Bragg-Brentano geometry with Ni-filtered Cu K_α (λ = 1.54060 Å) radiation operating at 40 kV and 30 mA with a position-sensitive detector (*LynxEye*).

Scanning electron microscopy (SEM)

SEM images were recorded on a *FEI Helios NanoLab G3 UC* electron microscope with an acceleration voltage of 2 kV from a field emission gun. Prior to SEM analysis the samples were coated with a thin carbon layer by carbon fiber flash evaporation in high vacuum.

Transmission electron microscopy (TEM)

TEM images were collected on an FEI Titan Themis 60-300 microscope at an acceleration voltage of 300 kV. Powder samples were prepared by crushing the particles with a razor blade and subsequently depositing the powder onto a copper grid supporting a thin electron transparent carbon film.

Nitrogen sorption

Ad- and desorption measurements were performed on an *Autosorb 1* (*Quantachrome instruments, Florida, USA*) with nitrogen of 99.9999% purity at 77.3 K. The samples were activated (dried) under high vacuum at 120 °C for at least 12 h. Evaluation of ad- and desorption isotherms was carried out with the *AsiQwin v.3.01* (*Quantachrome instruments, Florida, USA*) software.

For BET calculations, pressure ranges of the nitrogen isotherms were chosen with the help of the BET assistant in the *AsiQwin* software. In accordance with the ISO recommendations, multipoint BET tags equal to or below the maximum in V x (1-p/p_0) were chosen.

Electrical conductivity measurements

Two-point probe measurements of crystalline pellets were carried out with a Metrohm Autolab PGStat302N. an in house constructed dc-conductivity measurements cell by recording *I–V* curves between -5 to +5 V by an AUTOLAB 302N. The distance between the elctrodes is equivalent to the thickness of the pellet, which was measured to be 800 µm.

Preparation of EAMOF-74 pellets

EAMOF-74 pellets with 1 cm diameter (obtained from several repeated batch syntheses) for electrical conductivity measurements were fabricated with 100 mg of the respective MOF bulk material with a standard *Paul-Weber* KBr Press with 45 kg/ cm^2 pressure.

UV-Vis spectroscopy

UV-Vis spectra were recorded using a *Perkin-Elmer UV VIS/NIR Lambda 1050* spectrophotometer equipped with an InGaAs detector. Diffuse reflectance spectra were collected with a Praying Mantis (Harrick) accessory and were referenced to barium sulphate powder as white standard.

Photoluminescence (PL) spectroscopy

PL measurements were performed on a *PicoQuant FluoTime 300* time-correlated single photon counting (TCSPC) setup. Steady-state spectra and time-resolved histograms were acquired using a 378 nm excitation laser (*PicoQuant LDH-P-C-375*). Residual laser scattering was removed using a 400 nm dielectric long pass filter (*Thorlabs FELH0400*) in the beam path of the emitted light, which was detected under magic angle (54.7°) on a photomultiplying tube (*PicoQuant PMA 192*). The microscopic emission images were taken with a self-modified Nikon Microscope and a Nikon objective with a numerical aperture of 0.95. As excitation laser source a 405 nm pulsed PicoQuant diode was used and in the detection beam path a 490 nm long pass filter (FEL 490 Thorlabs) was installed to suppress residual laser light. For the detection an avalanche photo diode (Laser Components) was used.

Thermogravimetric analysis

Thermogravimetric analysis (TGA) measurements were performed on a *Netzsch Jupiter ST 449 C* instrument equipped with a *Netzsch TASC 414/4* controller. The samples were heated from room temperature to 800 °C under a synthetic air flow (25 mL min^{-1}) at a heating rate of 1 K min^{-1}.

Dye Adsorption

For the dye adsorption, freshly prepared and still wet EAMOF-74(Mn) bulk material (of two batches, about 10 mg) was soaked for 1 day at room temperature in air, in 25 mL solutions of methyl orange, methyl red and methylene blue, respectively, with dye concentrations of 240 mg/ L. Afterwards, the solution was removed by centrifugation and the MOF was washed with DMF (1 x 20 mL) to remove residual dye molecules, followed by drying under reduced pressure.

4.6.2 Experimental

4.6.2.1 General

All materials were purchased from *Sigma Aldrich, Acros or TCI Europe* in the common purities *purum, puriss* or *reagent grade.* The materials were used as received without additional purification and handled in air unless otherwise noted.

The water utilized in the synthesis was subjected to a *Merck-Milipore Mili-Q* purification system prior to use.

4.6.2.2 Synthetic procedures

4.6.2.3 EAHA Linker synthesis

The synthesis was adapted and modified from D. Chen, H. Xing, Z. Su, Ac. Wang, *Chem. Commun.*, 2016,52, 2019-2022.

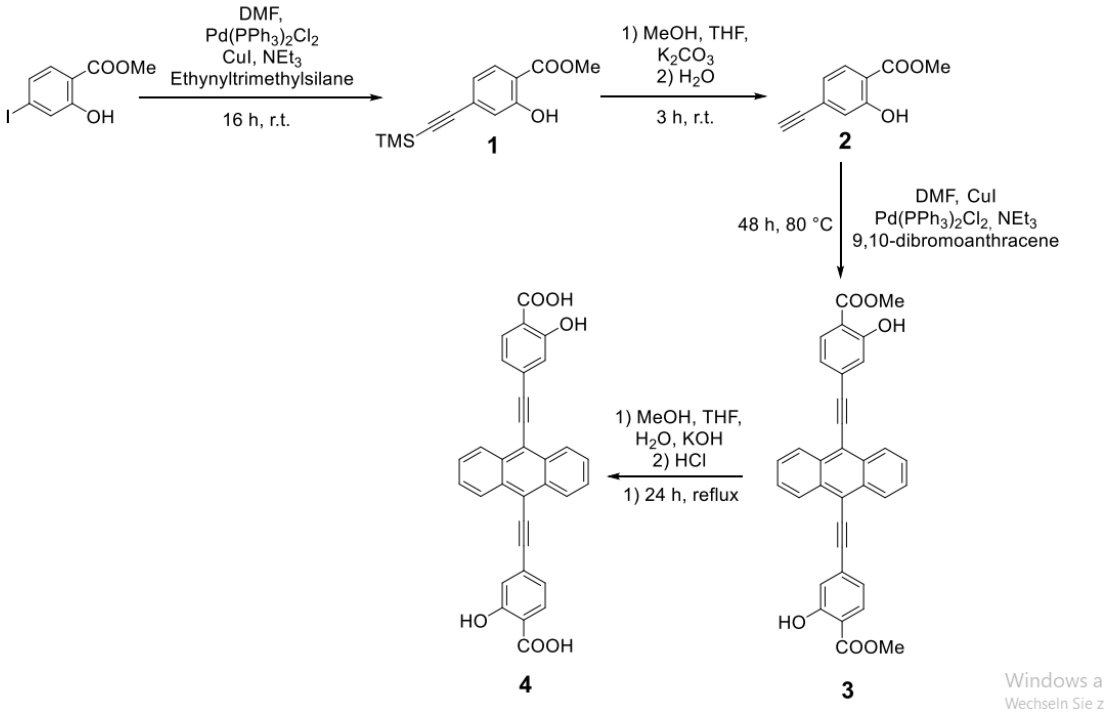

Compound 1

Methyl-2-hydroxy-4-iodobenzoate (5.0 g, 18.0 mmol, 1 eq) was dissolved in 50 mL DMF in a 100 mL Schlenk flask under argon atmosphere. Bis(triphenylphosphine) palladium(II) dichloride (250 mg, 0.35 mmol), copper(I) iodide (135 mg, 0.70 mmol), triethylamine (2.65 g, 27 mmol, 1.5 eq) and ethynyltrimethylsilane (2.65 g, 27 mmol, 1.5 eq) were added to the reaction mixture and the resulting reaction mixture was stirred at room temperature for 18 h. Water was added to the reaction mixture, it was extracted with ethyl acetate (3 x 200 mL) and the organic phase was dried over $MgSO_4$. The solvent was removed under reduced pressure and the obtained crude product was purified by common silica column chromatography over *n*-hexane and diethyl ether (9:1 *v*:*v*). After removing the solvent under reduced pressure, the desired Compound **1**, methyl-2-hydroxy-4-(trimethylsilyl)ethynylbenzoate, (3.91 g, 15.8 mmol, 88 %) was obtained as a red oily liquid.

^{1}H NMR ($CDCl_3$, 400 MHz, ppm) δ = 10.53 (s, 1H) 7.54 (d, J = 8.2 Hz, 1H), 6.87 (d, *J* = 1.4 Hz, 1H), 6.75 (dd, *J* = 8.2, 1.5 Hz, 1H), 3.75 (s, 3H), 0.07 (s, 9H).

Compound 2

Compound 1 (3.91 g, 15.8 mmol, 1 eq) was dissolved in 25 mL THF and H_2O (1:1) in a 100 mL Schlenk flask under argon atmosphere and potassium carbonate (2.20 g, 15.8 mmol, 1 eq) was added. It was stirred for 3 hours at room temperature and quenched with H_2O. The reaction mixture was extracted with ethyl acetate (3 x 200 mL) and the organic layers were washed with saturated ammonium chloride solution (3 x 100 mL). It was dried over $MgSO_4$ and the solvent was removed under reduced pressure. Column purification using *n*-hexane and diethyl ether (9:1 *v*:*v*) gave the desired Compound **2**, methyl-4-ethynyl-2-hydroxybenzoate, (1.92 g, 10.8 mmol, 69 %) as a pale-yellow solid, after removing the solvent under reduced pressure.

^{1}H NMR (d_6-DMSO, 400 MHz, ppm) δ = 10.67 (s, 1H), 7.72 (d, *J* = 8.1 Hz, 1H), 7.04 (d, *J* =1.5 Hz, 1H), 6.93 (dd, *J* = 8.1, 1.6 Hz, 1H), 3.89 (s, 1H), 3.14 (s, 3H).

Compound 3

Compound **2** (500 mg, 2.81 mmol, 1 eq) was dissolved in 5.6 mL DMF in a 25 mL Schlenk flask under argon atmosphere and 9,10-dibromoanthracene (429 mg, 1.28 mmol, 0.45 eq) was added. Copper(I) iodide (11.3 mg, 0.06 mmol), triethylamine (5.6 mL) and bis(triphenylphosphine)palladium(II) dichloride (22.6 mg, 0.03 mmol) were added and the resulting reaction mixture was stirred at 80 °C for 48 h under argon atmosphere. The reaction mixture was allowed to cool to room temperature and was quenched with H_2O extracted with chloroform $CHCl_3$ (3 x 300 mL)

and the obtained organic layers were washed with saturated sodium chloride solution (3 x 200 mL). The organic solution was dried over $MgSO_4$ and the solvent was removed under reduced pressure. Recrystallization in $CHCl_3$ (10 mL) gave Compound **3** (95.2 mg, 0.18 mmol, 15 %) as dark orange powder.

^{1}H NMR ($CDCl_3$, 400 MHz, ppm) δ = 10.79 (s, 2H), 8.60 (d, *J* = 9.9 Hz, 4H), 7.86 (d, *J* = 11.6 Hz, 2H), 7.61 (d, *J* = 9.1 Hz, 4H), 7.33 (s, 2H), 7.19 (s, 2H), 3.94 (s, 6H).

Compound 4

Compound **3** (95.2 mg, 0.18 mmol, 1 eq) was dissolved in 6.3 mL of a mixed solution of THF, MeOH and H_2O (1:1:1 *v*:*v*:*v*) in a 250 mL Schlenk flask under nitrogen atmosphere, and potassium hydroxide (234 mg, 0.42 mmol, 2.3 eq) was added. The reaction mixture was refluxed with stirring for 48 hours. After cooling down to room temperature, it was acidified with 2M aqueous hydrochloric acid (200 mL) and the desired Compound **4** (4,4'-(anthracene-9,10-diylbis(ethyne-2,1-diyl))bis (2-hydroxybenzoic acid) (76.4 mg, 0.15 mmol, 83 %) was obtained by filtration as bright orange powder, and washed with water (200 mL) and MeOH (20 mL). **^{1}H NMR** (d_6-DMSO, 400 MHz, ppm) δ = 8.74 (dd, *J* = 6.6, 3.3 Hz, 4H), 7.94 (d, *J* = 8.1 Hz, 2H), 7.87 (dt, *J* = 6.7, 3.0 Hz, 4H), 7.51 (d, *J* = 1.5 Hz, 2H), 7.45 7.43 (m, 2H).

4.6.2.4 MOF synthesis

EAMOF-74(Mn)

Compound **4** (4,4'-(anthracene-9,10-diylbis(ethyne-2,1-diyl))bis(2-hydroxybenzoic acid)) (10.00 mg, 0.022 mmol) and $MnCl_2 \cdot 4H_2O$ (13.85 mg, 0.070 mmol) were suspended in DMF (0.75 mL) and benzyl alcohol (0.75 mL) under argon atmosphere in a 5 mL DURAN culture tube. The resulting mixture was sonicated at room temperature until complete dissolution of the reactants was achieved and it was kept in a closed culture tube (Schott duran) at 120 °C for 48 h. The resulting precipitate was washed with DMF (3x 10 mL) and dried under reduced pressure for 2 h.

4.6.3 Characterization

4.6.3.1 Unit cell parameters and atomic coordinates

EAMOF-74(Mn)

R_{wp} = 6.60 %, R_p = 4.44 %

R-*3* (148) - trigonal
a = b = 61.40 Å, c = 6.64 Å
α = β = 90°, γ = 120°

Atom	**x/a**	**y/b**	**z/c**
C1	0.365310	0.362700	0.702780
C2	0.384600	0.381440	0.849340
C3	0.383650	0.377830	0.06390
Mn4	0.340080	0.351640	0.329330
O5	0.36273	0.37549	0.53305
O6	0.34247	0.34912	0.80665
O7	0.36754	0.35472	0.16049
O8	0.34005	0.37947	0.18906
C9	0.403087	0.398343	0.190373
C10	0.421897	0.420233	0.0987133
C11	0.33658	0.24108	0.43827
C12	0.33789	0.26129	0.31636
C13	0.520640	0.520970	0.594880
C14	0.475660	0.489210	0.584970
C15	0.496300	0.510120	0.680170
C16	0.441320	0.440300	0.216400
C17	0.458300	0.457700	0.305910
C18	0.451580	0.478890	0.672200
C19	0.447840	0.488800	0.850750

C20	0.468110	0.509230	0.944900
C21	0.492140	0.519820	0.860200

4.6.3.2 Image of the simulated model structure of EAMOF-74(Mn)

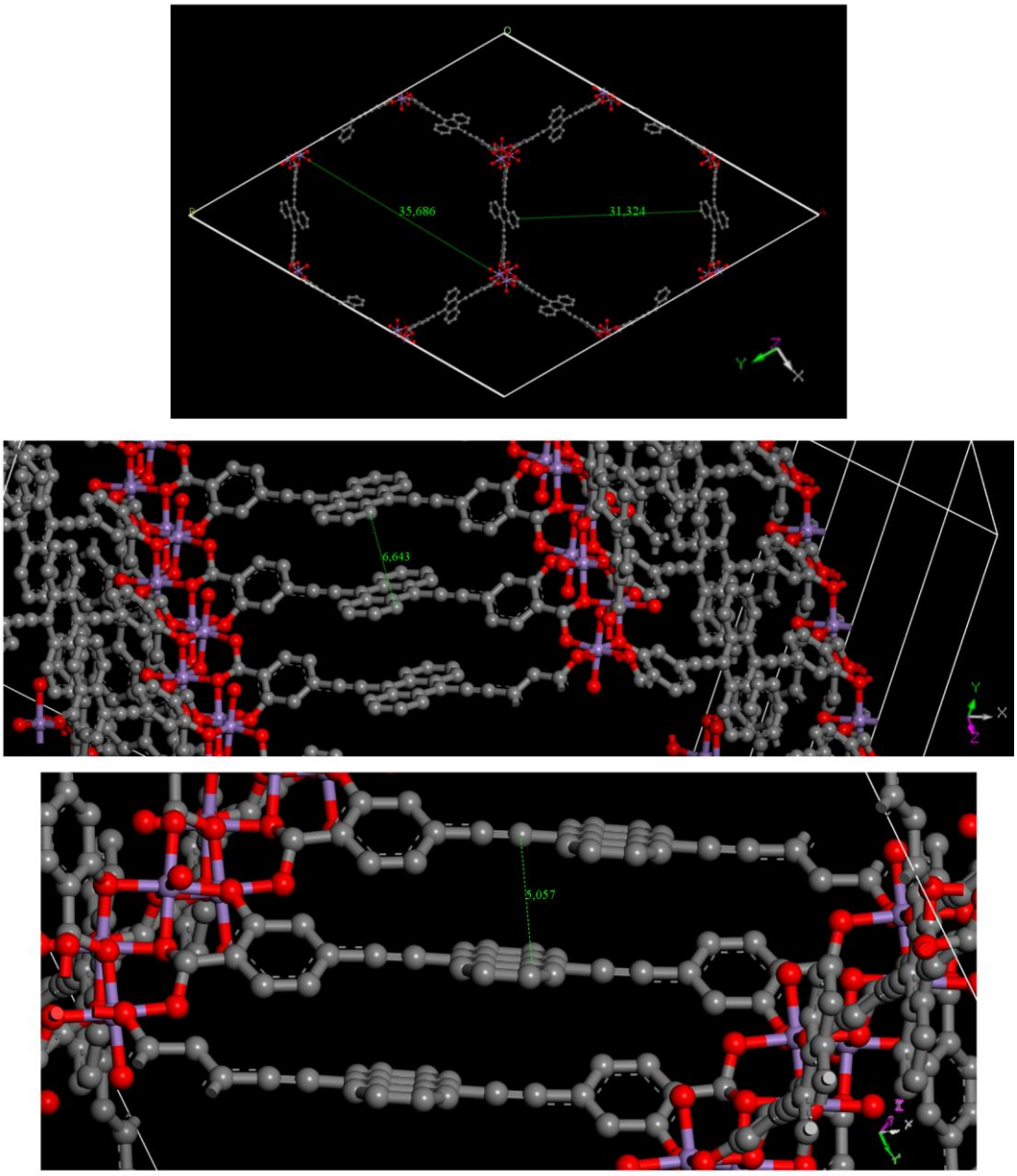

Figure 4-5: View along the crystallographic *c*-direction of the hexagonal lattice (top) and of the stacking distance between adjacent anthracene cores (middle). The shortest interlayer distance of 0.51 nm can be measured between an anthracene core and an opposite ethyne group (bottom).

4.6.3.3 Powder X-ray diffraction pattern

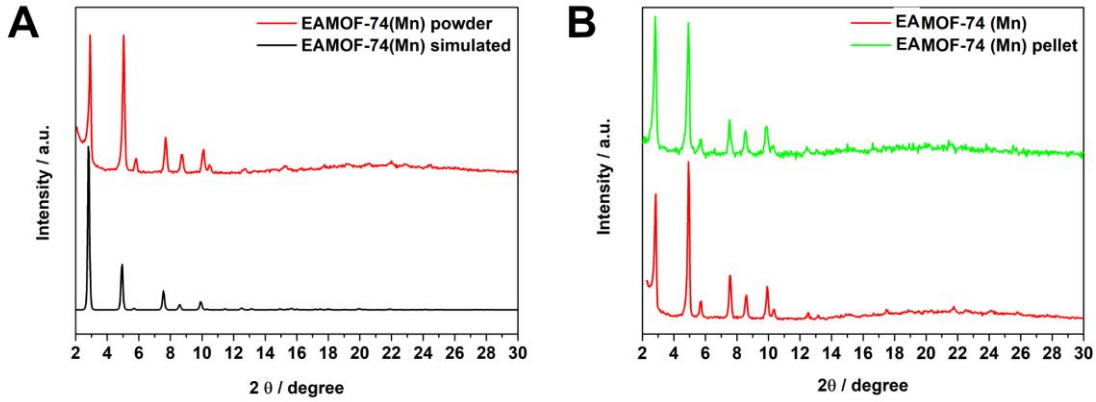

Figure 4-6: Powder X-ray diffraction (PXRD) patterns of EAMOF-74 (Mn) bulk material (red), of the simulated EAMOF-74(Mn) pattern (black) and of the pressed pellet (green).

4.6.3.4 Transmission electron microscopy

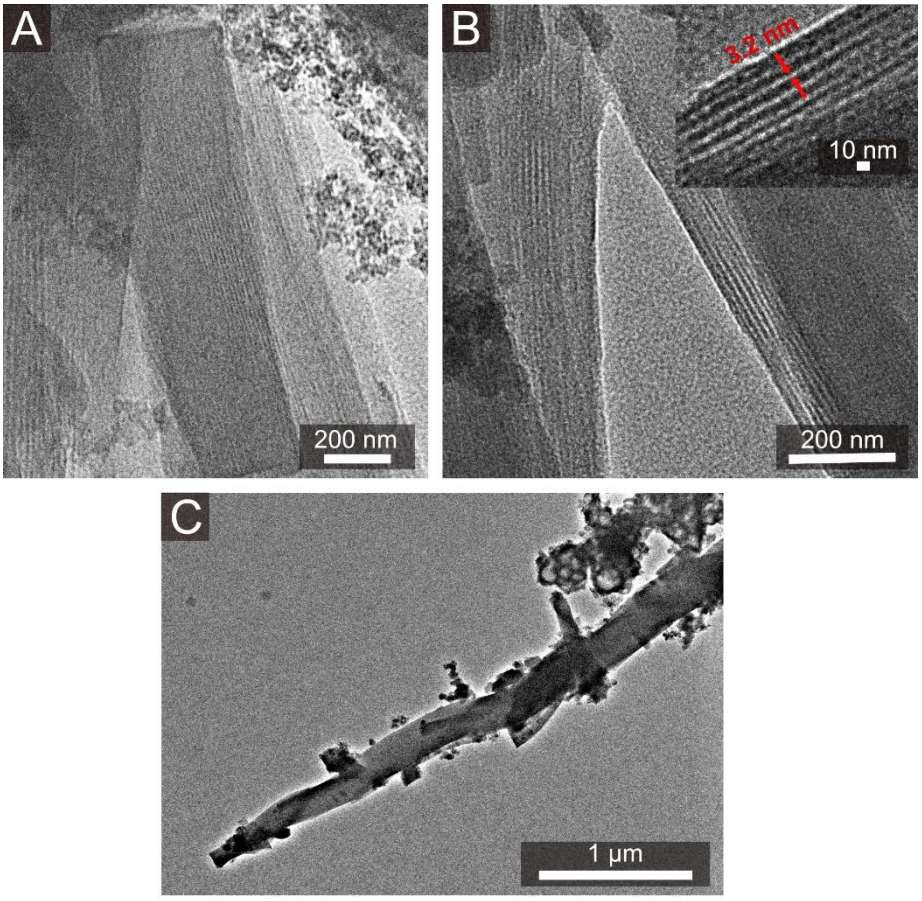

Figure 4-7: Transmission electron microscopy image (TEM) of EAMOF-74(Mn) crystals in side view, with a close-up of the lattice planes as inset in (B).

4.6.3.5 Energy dispersive X-ray (EDX) spectra

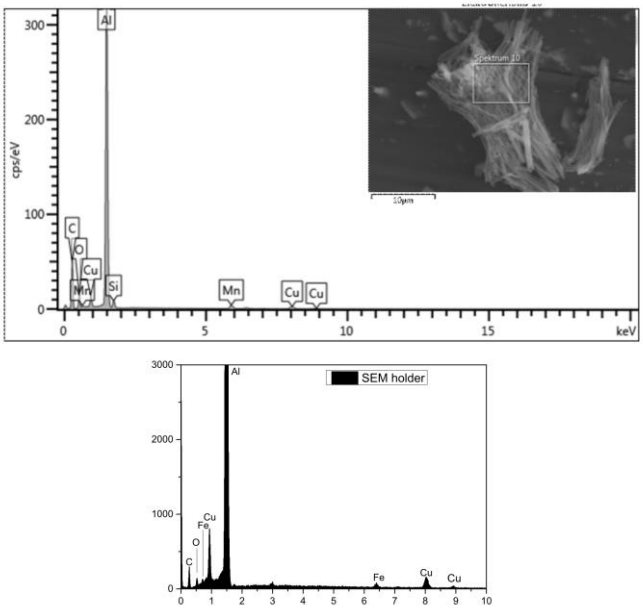

Figure 4-8: Energy dispersive X-ray (EDX) spectrum of EAMOF-74(Mn) bulk material (upper image) and of the SEM sample holder (lower image).

4.6.3.6 Thermogravimetric analysis

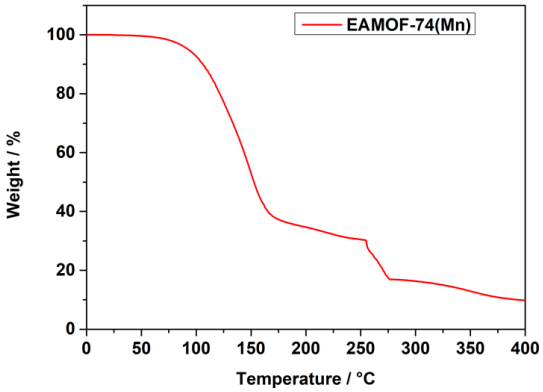

Figure 4-9: Thermogravimetric analysis of EAMOF-74(Mn), measured as bulk material.

4.6.3.7 Nitrogen sorption analysis

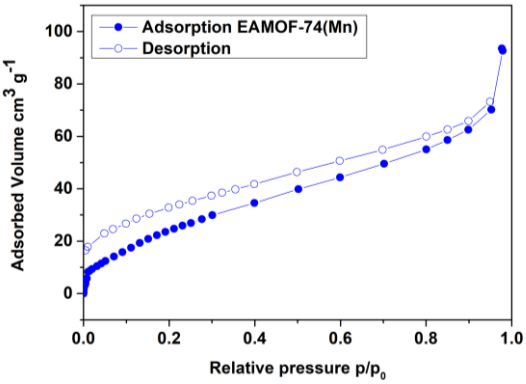

Figure 4-10: Nitrogen sorption analysis of EAMOF-74(Mn) bulk material after activation at 50 °C.

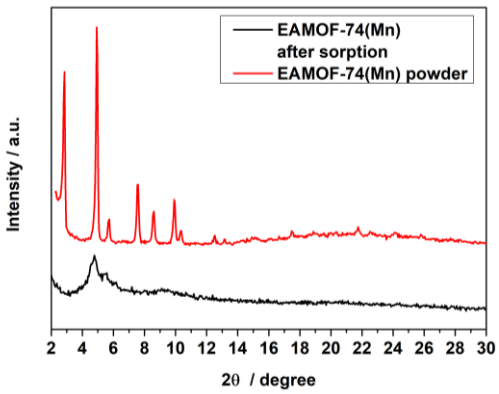

Figure 4-11: PXRD pattern of EAMOF-74 (Mn) as bulk material and after sorption analysis, including activation at 50 °C for 12 h, showing the loss of crystallinity.

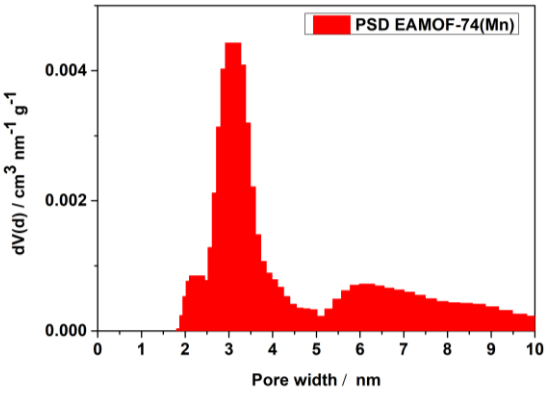

Figure 4-12: Quenched solid density functional theory (QSDFT) gives a pore size of 3.1 nm.

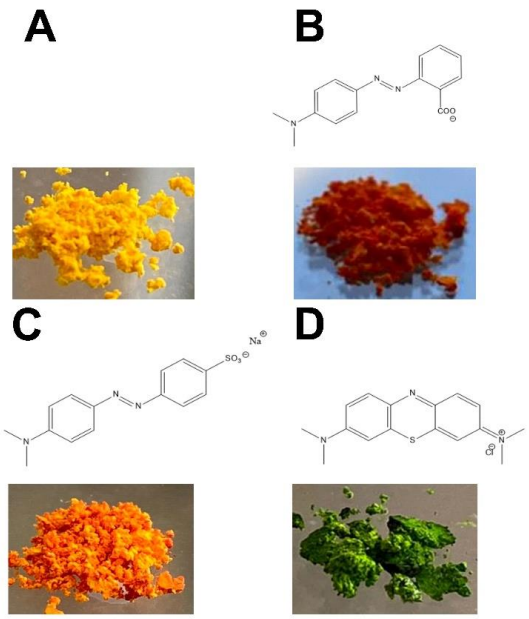

Figure 4-13: (A) Optical image of as-synthesized EAMOF-74 (Mn), (B) structural formula of methyl red and optical image of methyl red loaded EAMOF-74 (Mn), (C) structural formula of methyl orange and optical image of methyl orange loaded EAMOF-74 (Mn), (D) structural formula of methylene blue and optical image of methylene blue loaded EAMOF-74 (Mn).

4.6.3.8 Electrical conductivity measurement

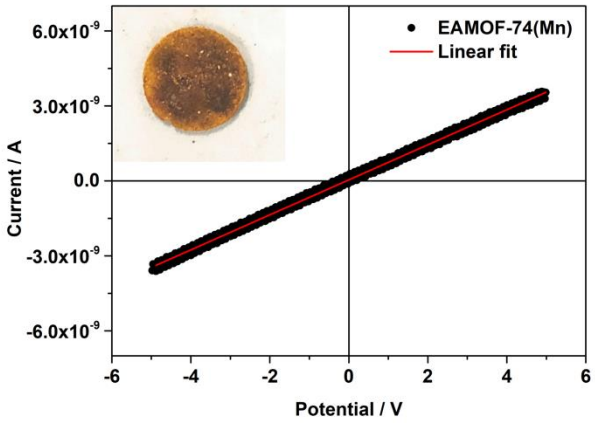

Figure 4-14: *I-V* curve of a pelletized EAMOF-74(Mn) sample measured via two-point probe showing an ohmic resistance. Photographic image of a pressed pellet of EAMOF-74 (Mn) is shown as inset.

4.6.3.9 Optical measurements

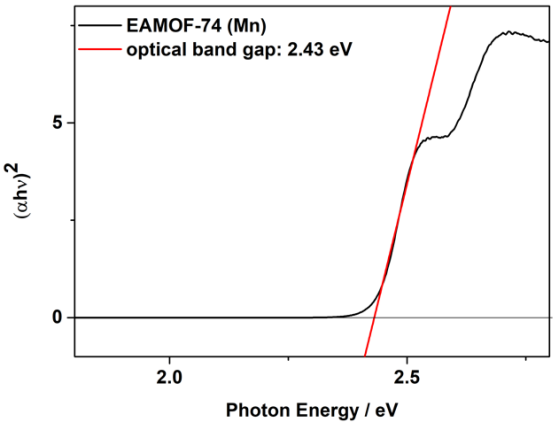

Figure 4-15: Tauc plot analysis assuming a direct band gap of EAMOF-74(Mn). The absorption of EAMOF-74(Mn) is dominated by the EAHA ligand. The ligand absorption in EAMOF-74(Mn) is shifted to higher energies with a bandgap of EAMOF-74(Mn) of 2.43 eV in comparison to the EAHA ligand (2.25 eV see below Fig. 4-20). This shift could be caused by intermolecular couplings between EAHA linker molecules and different twist angles in the EAHA ligand.

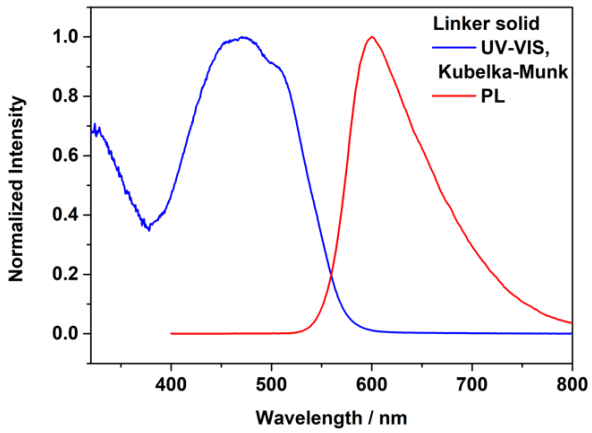

Figure 4-16: UV-Vis and photoluminescence (PL) spectra of the EAHA linker as solid.

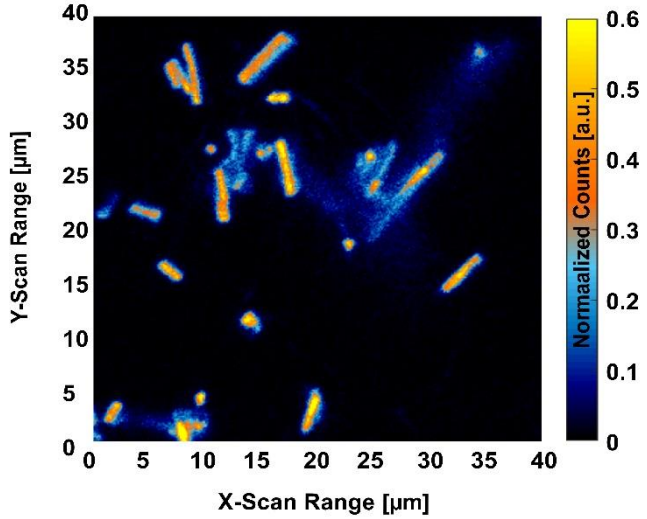

Figure 4-17: Confocal PL mapping of single EAMOF-74(Mn) crystallites in the bulk material with 405 nm exciation.

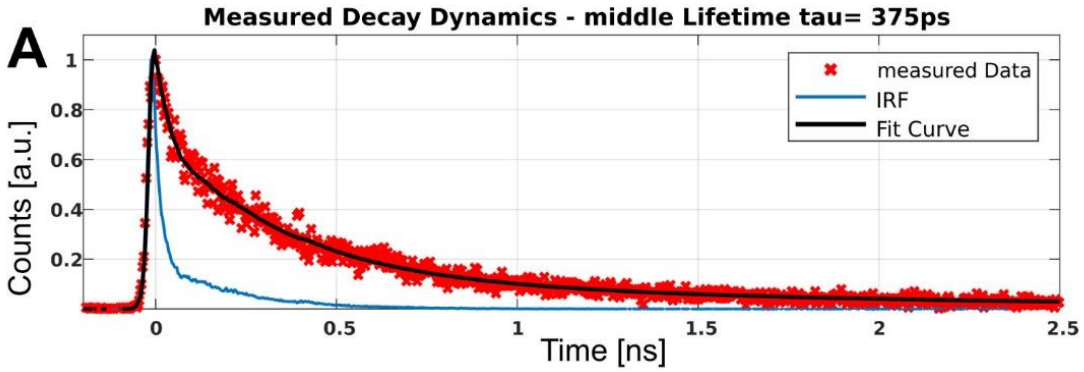

Figure 4-18: The time-correlated single photon counting (TCSPC) trace corresponding to the PL spectra of EAMOF-74(Mn) measured as solid (red data points). The average lifetime, of 375 ps, was obtained by a stretched exponential function convoluted with the instrument response function (IRF).

Figure 4-19: Photo images of the EAHA linker as bulk material (left) and dissolved in $CHCl_3$ (right).

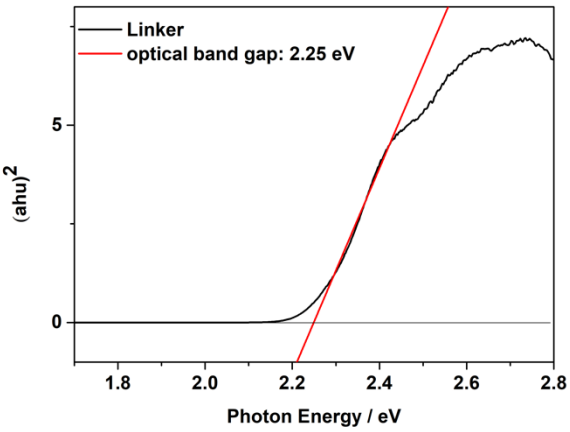

Figure 4-20: Tauc plot of the EAHA linker as solid, suggesting the presence of a direct band gap.

5 Perylene diimide MOF-74 analog

This chapter is based on the following manuscript:

A novel electrically conductive perylene diimide-based MOF-74 series featuring luminescence and redox activity

Patricia I. Scheurle[a,b], Alexander Biewald[a,b], Andre Mähringer[a,b], Julian Rotter[a,b], Achim Hartschuh[a,b], Dana D. Medina[*,a,b] and Thomas Bein[*,a,b] *Submitted.*

[a]Department of Chemistry, Ludwig-Maximilians-Universität (LMU), Butenandtstr. 5-13 (E), 81377 Munich, Germany.

[b]Center for NanoScience (CeNS), Schellingstr. 4, 80799 Munich, Germany.

[*]Corresponding Author

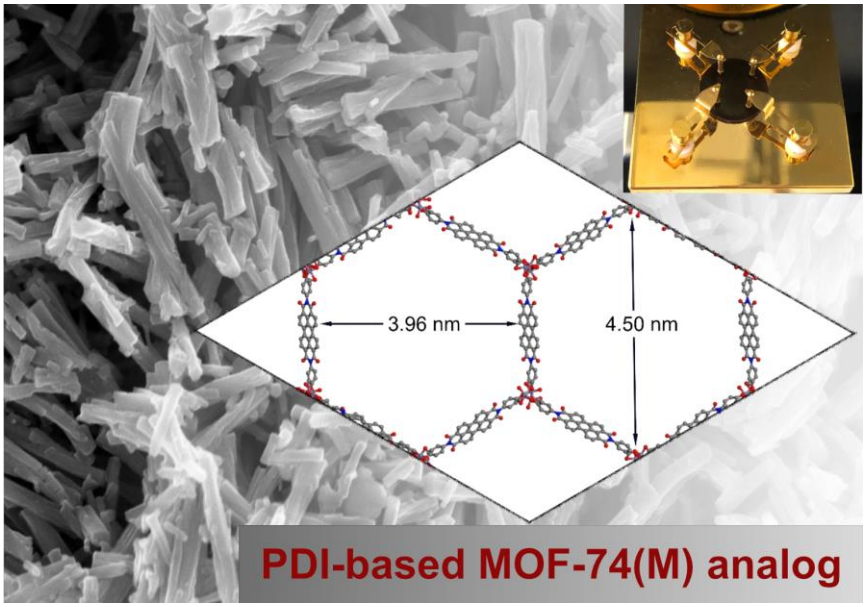

5.1 Abstract

Metal-organic frameworks (MOFs) featuring significant electrical conductivity constitute a growing class of materials, with intriguing possible applications as porous semiconductors or supercapacitors. If such features are combined with photoluminescence, additional functionalities such as selective chemical sensing become accessible. Here, we incorporated perylene diimide (PDI) based linear building blocks into the MOF-74 topology with the three metal ions Zn^{II}, Mg^{II} and Ni^{II}, resulting in a new series of MOFs, namely PDI-MOF-74(M). PDI derivatives are dye molecules exhibiting remarkable optical properties, high electron mobilities, as well as interesting redox behavior. However, PDI-based 3D MOFs are very rare and to date were only reported once. The frameworks of the PDI-MOF-74(M) series exhibit high crystallinity, electrical conductivity and show well-defined redox activity. In addition, the frameworks of the series feature photoluminescence in the orange and red spectral regions. With this work we expand the series of electroactive MOF-74 topologies as well as the group of 3D PDI-based MOFs, hence opening up the development of novel MOFs with promising optoelectronic properties comprising PDI building blocks.

5.2 Introduction

Metal-organic frameworks (MOFs) are crystalline and porous materials that are composed of inorganic nodes interconnected by rigid organic ligands.[1] Typical applications include gas separation and gas storage, due to their well-defined pore apertures in combination with high surface areas.[2,3] The chemical and physical properties of MOFs can be tuned via the nature of the incorporated organic ligands and the metal species defining structural nodes, utilizing different chemical compositions, connectivities and functionalities.[4–6] Recently, this even enabled the construction of MOFs featuring the desired ability of electrical conductivity,[2,7–12] hence opening the way towards new applications in the fields of electrochemical energy storage,[13] semiconductors and electrocatalysis.[14, 9] If combined with photoluminescence, electroactive MOFs become interesting for applications in chemical sensors and optoelectronic uses.[15–18] In the last few years, an increasing number of electrically conductive MOFs based on the MOF-74 topology have been reported.[2,5,11,19,20] The original MOF-74 structure is constructed of 2,5-dihydroxyterephthalic acid ligands and divalent metal ions, forming a three-dimensional honeycomb-like structure.[12] While MOF-74 isoreticular structures based on phenoxide-metal nodes showed rather low conductivity values, MOF-74 isostructures with sulfur-containing functionalities in the organic ligand in combination with mixed valance of the metal ion iron, showed an increased electrical conductivity of up to 10^{-6} S/cm.[2,21] Recently our group introduced a series of MOF-74 analogs comprising an anthracene core in the linear organic building block and the metal ions Zn^{II}, Mg^{II}, Ni^{II}, Co^{II} or

Mn^{II}.[11] An electrical conductivity enhancement of up to six orders of magnitude, compared to the respective regular MOF-74, could be achieved by the incorporation of the electron-rich anthracene core.

Perylene diimide and its derivatives are electron-acceptor molecules and a well-known class of extremely stable organic dye molecules and pigments, for example used for automotive coatings.[22–25] They feature high thermal, chemical and photo-stability, in combination with well-defined redox behavior.[26–28] Perylene diimide derivatives can form delocalized radical anions, which motivated investigations towards further applications ranging from photocatalysis[29] to *n*-channel transistors[30] and in organic field-effect transistors [24,38], to photoconduction.[31] Such applications are based on their high electron mobilities[32] and their *n*-type semiconducting properties.[33,34] In addition, PDI derivatives show notable optical properties like electroluminescence and high photoluminescence quantum yields.[28,35] Therefore, they are used in dye lasers[26,36], solar collectors[37] and organic photovoltaics[30].

Incorporating a perylene diimide core into the fixed matrix of a porous and highly ordered 3D MOF scaffold is highly desirable due to the diverse optical and electrical properties of perylene diimide derivatives. However, PDIs tend to form π-π-stacks, leading to one- and two-dimensional (metal-)organic assemblies, or rather one-/two-dimensional polymers.[23,39–42] Therefore, PDI-based 3D-MOFs are a rare class of materials and were only reported once in a Zr-PDI based MOF, which crystallized in the tetragonal space group.[43]

Here we present a new series of perylene diimide based MOFs, crystallizing in the MOF-74 topology. The incorporation of a linear PDI-based organic ligand (acting as linker) strongly enhances the electrical conductivity in phenoxide-connected MOF-74 structures containing the metal ions Zn^{II}, Mg^{II} and Ni^{II}. Furthermore, the PDI core endows the MOF with photoluminescent properties and with redox activity, yielding a series of light-emitting, redox active and electrically conducting MOFs.

First, we established the synthesis of a perylene diimide based building block, containing terminal phenyl groups with para-hydroxy, ortho-carboxylic functionalities for the bonding to the metal ions, namely 5,5´-(1,3,8,10-tetraoxo-1,3,8,10-tetrahydroanthra[2,1,9-*def*:6,5,10-*d´e´f´*]diisoquinoline-2,9-diyl)bi(2-hydroxybenzoic acid), short PDI-based ligand. The two functional groups are inverted in comparison to the original MOF-74 structure. Similarly, Dinca *et. al* reported an NDI-MOF-74 analog, which also exhibited inverted functional groups, forming a MOF with the MOF-74 topology.[44] Under solvothermal conditions, three novel perylene diimide based MOF-74 structures (PDI-MOF-74), were synthesized using the PDI building block and the divalent metal ions Zn^{II}, Mg^{II} and Ni^{II} (Figure 5-1).

5.3 Results and discussion

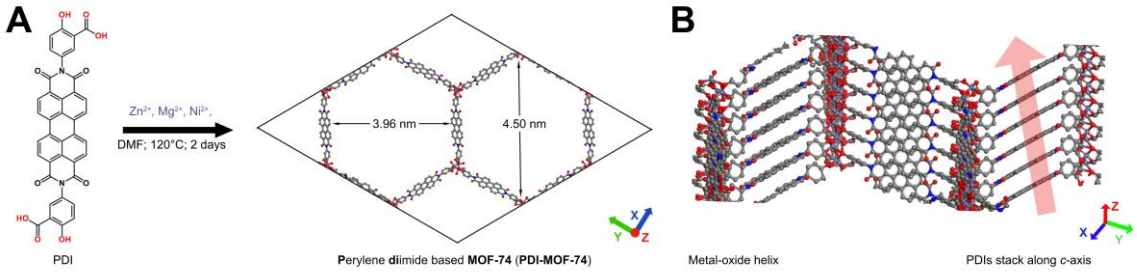

Figure 5-1: (A) Synthesis scheme of the PDI-based MOF-74(M) series. The organic building block (linker) forms porous, hexagonal frameworks with the respective metal ions. (B) Adjacent PDI cores stack along the *c*-axis.

The PDI-based linker was synthesized in a one-step reaction procedure (see SI). The condensation reaction of perylene-3,4,9,10-tetracarboxylic dianhydride with 5-amino-2-hydroxy benzoic acid in a melt afforded, after purification, the final organic building block in sufficient yield (65%) as a red powder. For the MOF synthesis, the stoichiometric reaction of the PDI-based ligand with the respective metal precursor, namely $Zn(NO_3)_2 \cdot 4H_2O$, $Mg(NO_3)_2 \cdot 6H_2O$, $NiCl_2 \cdot 6H_2O$, in DMF, MeOH, BnOH mixtures at 120°C for two days led to the precipitation of dark red powders. The powders were washed with DMF, methanol and THF and dried under dynamic vacuum (see Figure 5-1 A, for more details see SI). Powder X-ray diffraction (PXRD) data of the dried MOFs are shown in Figure 5-2, confirming a high degree of crystallinity for all three samples. The PXRD patterns of the three analogs are slightly different at higher angles with pronounced reflections of PDI-MOF-74(Zn) at 2.45°, 3.97°, 8.10°, 10.52°, 12.01°2θ, of PDI-MOF-74(Mg) at 2.45°, 3.97°, 4.76°, 6.31°, 8.18°, 10.66° 2θ and 11.97°, and for PDI-MOF-74(Ni) at 2.45°, 3.97°, 6.31°, 8.04°/ 8.48°,10.35°/ 10.88° and 11.70° 2θ. The collected diffractograms matched with the ones predicted from simulated model structures (see Figure 5-10). The predicted model structures were obtained with Accelrys Materials Studio 7.0 using the calculated MOF-74 structure as a starting model. A simulated unit cell was established and a PXRD was calculated, which was Pawley-refined according to the respective experimental PXRD patterns (R_{wp} ranging from 2.4 – 4.0 %). The best refinements could be achieved with a slightly distorted unit cell in the y-direction, crystallizing in the triclinic space group P1. PDI-MOF-74(Zn, Mg) have the resulting lattice paramters a = 72.63 Å, b = 74.56 Å, c = 5.59 Å, $\alpha = \beta = 90°$ and $\gamma = 120°$ and PDI-MOF-74(Ni) a = 72.28 Å, b = 75.67 Å, c = 5.55 Å, $\alpha = \beta = 90°$ and $\gamma = 120°$.

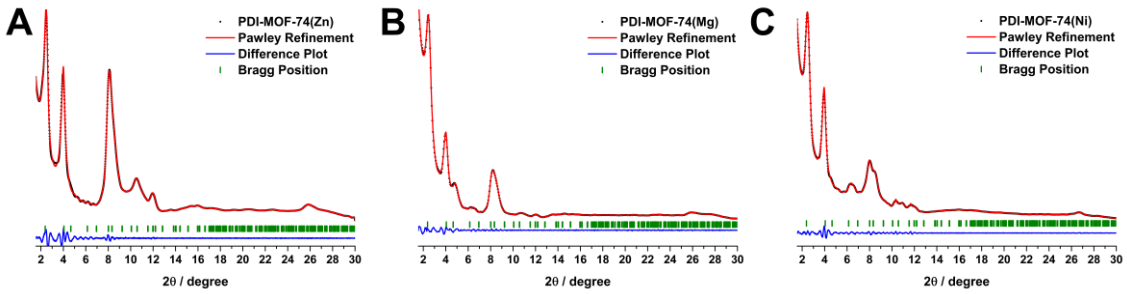

Figure 5-2: Experimental powder X-ray diffraction (PXRD) of the PDI-MOF-74(M) series showing (A) the Zn-, (B) Mg- and (C) Ni-MOF derivatives, respectively (black). The simulated PXRD pattern was Pawley-refined (red) according to the experimental data, the difference plot is shown in blue. The respective Bragg positions of the predicted unit cell are presented as green bars.

All three PDI-MOF-74 materials exhibit one-dimensional hexagonal channels with pore apertures of 3.96 to 4.5 nm (see Figure 5-1 A, Figure 5-7). The PDI units are bridged by phenyl groups and interconnected by infinite helical metal-oxo chains in the *c*-direction, forming the pore channels. For the PDI unit, we determined a torsion angle of 71.1° between the benzene rings and the PDI core. Adjacent planar PDI cores are offset-stacked along the *c*-direction with the shortest stacking distance of 3.54 Å, estimated from the simulated model structure (see Figure 5-1 B, Figure 5-8, Figure 5-9). This is in good accordance with the distance calculated from the π-π-stacking reflection in the PXRD patterns. In PDI-MOF-74(Zn) and PDI-MOF-74(Mg), the reflections are at 25.8° and 25.9° 2 θ, respectively, revealing a distance of 3.44 Å between adjacent PDI cores. For PDI-MOF-74(Ni), the reflection occurs at 26.6 2θ in the PXRD pattern, indicating a π-π-stacking distance of 3.34 Å between adjacent PDI cores. The unit cell of PDI-MOF-74(Ni) is slightly more distorted than that of the Zn and Mg analogs; we attribute this observation to the ionic radius of nickel being slightly smaller, resulting in a smaller stacking distance.

We were also able to grow PDI-MOF-74(Zn) as thin films on glass substrates *via* vapor-assisted conversion.[45–50] For the precursor solution, the PDI-based ligand, $Zn(NO_3)_2 \cdot 6H_2O$ and salicylic acid as modulator were dissolved in DMF. The precursor solution was dropcasted on glass substrates in a glass bottle and heated at 120 °C for 48 h (for more details see SI). Grazing-incidence wide-angle scattering (GIWAXS) and XRD patterns (Figure 5-34) confirm the formation of crystalline films. SEM top-view and cross-section images show a homogeneous surface coverage and a film thickness of 17 µm (Figure 5-35).

Transmission electron microscopy (TEM) analysis of the PDI-MOF-74 series in powder form confirmed the formation of highly crystalline materials (Figure 5-3A, Figure 5-11 - Figure 5-15). In the TEM micrographs, parallel-aligned pores are visible. For PDI-MOF-74(Mg), large domain sizes of 400 nm – 530 nm in length and about 40 nm to 90 nm in width illustrate the high degree of crystallinity (Figure 5-3A, Figure 5-11, Figure 5-12). Furthermore, a close-up of the lattice

planes, as well as the calculated diffraction pattern in the fast Fourier transform (FFT) of the TEM image (Figure 5-3 A), show distances of 3.5 nm, which are in good accordance with the first reflection in the PXRD pattern at 2.45° (Figure 5-2).

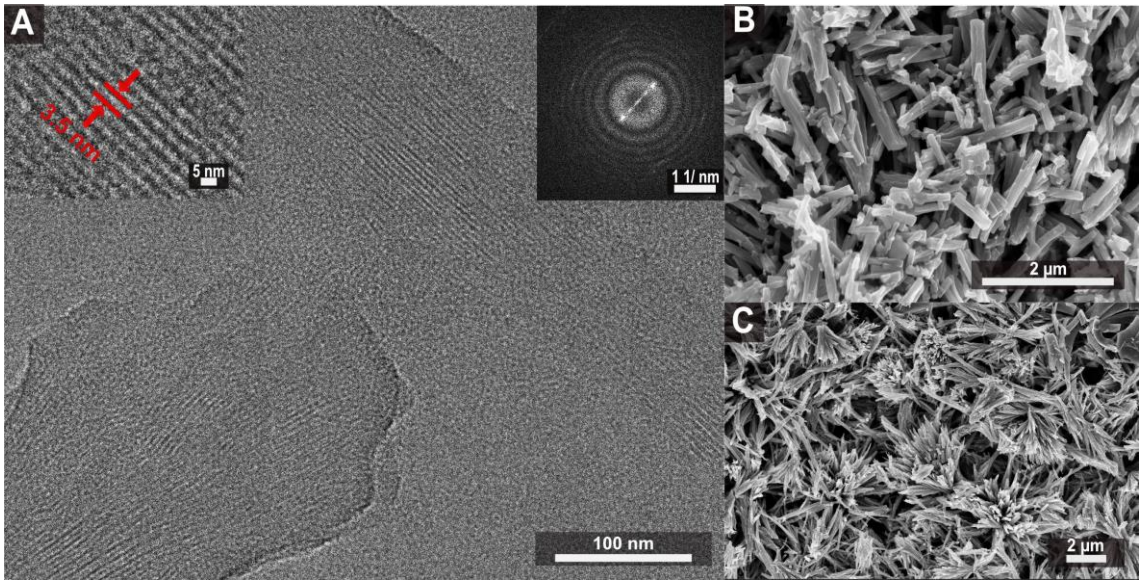

Figure 5-3: (A) TEM image of a PDI-MOF-74(Mg) crystal in side view, with a close-up of the lattice plane (left corner inset) and with FFT of the entire image (right corner inset), showing distances of 3.5 nm. (B) SEM image of PDI-MOF-74(Mg) crystallites. (C) SEM image of PDI-MOF-74(Zn) crystallites.

Scanning electron microscopy (SEM) images of the PDI-MOF-74(M) powders show needle-shaped crystallites (Figure 5-3, Figure 5-16, Figure 5-17). In case of PDI-MOF-74(Zn), bunches of needle-shaped crystallites, with a length of 1 – 3 µm and a width of 100 - 300 nm, form agglomerates (Figure 5-3 C). The sizes of the PDI-MOF-74(Mg) crystallites are smaller, with a length of 400 - 900 nm and a width of 80 – 100 nm (Figure 5-3 B, Figure 5-16). The biggest crystallites were observed for PDI-MOF-74(Ni), with a length of 2.5 – 5 µm and a width of 500 nm - 1.2 µm (Figure 5-17). Notably, hints for secondary nucleation can be observed, where small needle-shaped crystallites with a length of 100 -200 nm are growing on top of the big crystallites. The purity of the obtained samples was studied by energy dispersive X-ray spectroscopy (EDX) and elemental analysis. Elemental analysis indicates a small excess of H and N atoms in all samples, tentatively attributed to the presence of residual DMF and water molecules, coordinating to the metal ions in the structure. Furthermore, EDX analysis shows a small amount of chloride in PDI-MOF-74(Ni), which apparently originates from the $NiCl_2 \cdot 6H_2O$ synthesis precursor. (Figure 5-18 - Figure 5-20). Thermogravimetric analysis (TGA) indicates a high thermal stability of the PDI-MOF-74 series, which do not degrade below 300 °C under dynamic conditions (Figure 5-21). Furthermore, the first weight loss of about 5% in the TGA curve, also points to the presence of residual solvents inside the pores.

The pore accessibility of the activated (degassed) MOF samples was investigated by nitrogen physisorption experiments. The nitrogen isotherms (77 K) of PDI-MOF-74 (Zn, Mg, Ni) show IUPAC *Type IV(a)*[51] sorption behaviour, which is typical for wider mesoporous materials (Figure 5-23 A-C). However, PDI-MOF-74(Zn, Mg) show a steep initial uptake of about 175 $cm^3\ g^{-1}$ and 210 $cm^3\ g^{-1}$ at low pressures and a second uptake at 0.01-0.05 p/p_0 of about 20 $cm^3\ g^{-1}$ and 70 $cm^3\ g^{-1}$, respectively, attributed to initial monolayer-multilayer adsorption. The maximum uptake at 0.98 p/p_0 is about 515 $cm^3\ g^{-1}$ for the zinc MOF and 540 $cm^3\ g^{-1}$ for the magnesium MOF. PDI-MOF-74(Ni) shows a steep initial uptake of about 130 $cm^3\ g^{-1}$ at low pressures and a second uptake at 0.01-0.05 p/p_0 of about 50 $cm^3\ g^{-1}$. At low relative pressures the ad- and desorption branches merge, confirming a reversible process. The Brunauer-Emmett-Teller (BET) surface areas for PDI-MOF-74(M) were calculated to be 730 $m^2\ g^{-2}$, 1222 $m^2\ g^{-2}$ and 897 $m^2\ g^{-2}$ for PDI-MOF-74(Zn, Mg, Ni), respectively. The calculation of the pore size distribution, using quenched solid density functional theory (QSDFT), gave pore sizes of 1.9 nm for PDI-MOF-74(Zn, Mg) and 2.5 nm for PDI-MOF-74(Ni) (Figure 5-23 D-F). In addition, the crystal structure stays intact during the sorption analysis, which can be confirmed by the PXRD pattern of the MOF powder after sorption (Figure 5-22). The pore sizes determined here are much smaller than the value of about 4 nm predicted for the simulated structures, which could be caused by residual, coordinating DMF and water molecules blocking parts of the pores, which were already detected in the elemental analysis and in the infrared spectrum (Figure 5-24), als well as in the TGA curve (Figure 5-21).

To determine the electrical conductivity of the PDI-MOF-74(M) series, two-point-probe measurements with crystalline and pelleted samples were performed. SEM micrographs and PXRD patterns of the MOF pellet samples confirm that the rod-like crystallite morphology of the bulk material as well as the crystallinity are preserved after compression (see Figure 5-26, Figure 5-27). The thickness of the pellets was measured by a slide gauge to be 500 µm**.** For the two-point-probe measurements, voltage was applied in the range of -7 V to 7 V to perform linear sweep *I-V* scans (Figure 5-4, Figure 5-25). The scans result in linear ohmic resistance curves with electrical currents in the nanoampere range (see table 5-1). The curves were fitted by a linear regression and the slope of the linear fit curves yielded average electrical conductivity values of 3.0 x 10^{-7} S/cm**,** 2.1 x 10^{-7} S/cm and 4.6 x 10^{-7} S/cm for PDI-MOF-74(Zn, Mg, Ni), respectively. We note that the measurements of the pellets were conducted without applied pressure, hence, the current percolation pathways could be strongly limited by the grain-to-grain resistances. Strikingly, even under these conditions the electrical conductivity values of the PDI-MOF-74(M) series are up to six orders of magnitude higher in comparison to the respective prototype MOF-74(M) with the 2,5-dihydroxytherephthalic acid ligand, showing electrical conductivity values in the range of 10^{-12}

to 10^{-13} S/cm (measured *via* the van der Pauw technique).[11] We attribute the enormous enhancement of electrical conductivity to the smaller distance between adjacent PDI cores, enabling π-π-stacking. As a consequence, the charge transfer can very likely occur "through-space", in addition to the "through-bond" charge transfer *via* the metal-oxo backbone by charge carrier hopping between metal nodes.

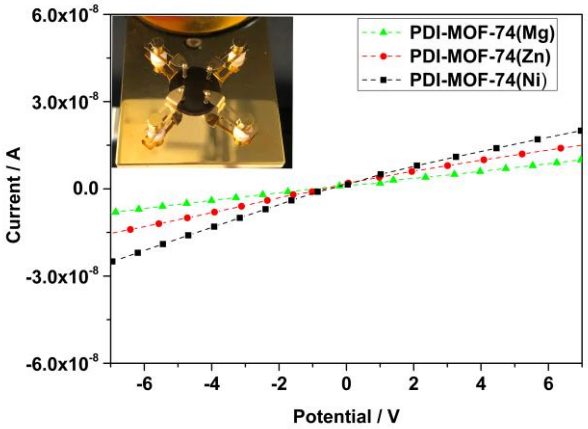

Figure 5-4: Electrical conductivity measurements of PDI-MOF-74(Mg, Zn, Ni) samples, obtained with pellets by using the two-point probe technique. Photo image of a PDI-MOF-74(Zn) pellet in the sample holder as inset.

To analyze the impact of the PDI core on the optical properties of the PDI-MOF-74(M) bulk materials, we performed UV-Vis absorption and photoluminescence (PL) spectroscopy measurements, summarized in Figure 5-5. The UV-Vis spectra were detected in diffuse reflectance geometry and transformed using the Kubelka-Munk equation (Figure 5-5 A). For the whole PDI-MOF-74(M) series, the absorption bands are located in the blue and green spectral region. The absorption onsets are located at around 622 – 627 nm, with two well-defined absorption maxima at about 498 nm and 545 nm, which originate from the integrated PDI building blocks (Figure 5-28). Notably, Tauc plots assuming direct band gaps yield optical band gaps of about 2.1 eV for the whole PDI-MOF-74(M) series (Figure 5-29). This corresponds to a band gap reduction of up to 0.7 eV in comparison to the prototype MOF-74(M) series (with 2,5-dihydroxyterephthalic acid ligands).[47] PL measurements were performed on PDI-MOF-74(M) bulk materials with excitation at 405 nm. All samples display a broad emission band with onsets at about 560 nm and 600 nm, as well as maxima at 640 nm and 660 nm in the spectra for PDI-MOF-74(Ni) and PDI-MOF-74(Mg, Zn), respectively (see Figure 5-5 B). The MOFs exhibit large Stoke shifts of 95 nm for PDI-MOF-74(Ni) and 115 nm for PDI-MOF-74(Zn, Mg). The broad emission band is similar to the emission band at 660 nm of the PDI-based linker monomer (see Figure 5-30). Time-correlated single photon counting (TCSPC) traces of all three MOFs were recorded at the respective emission maxima of 520 nm and 530 nm with 476 nm excitation, shown in Figure 5-5 D-F. The PL transients of the PDI-MOF-74(M) were analyzed with a stretched exponential fit. PDI-MOF-74(Mg) exhibits the slowest decay with a medium PL lifetime of 430 ps, followed by PDI-MOF-74(Zn) revealing a

PL lifetime of 160 ps. PDI-MOF-74(Ni) displays the fastest overall decay with a medium lifetime of 60 ps. Comparison with the PL transient of the PDI-linker molecule, which features a medium lifetime of 172 ps (Figure 5-31), suggests that the incorporation into the MOF does not lead to significant new loss channels.

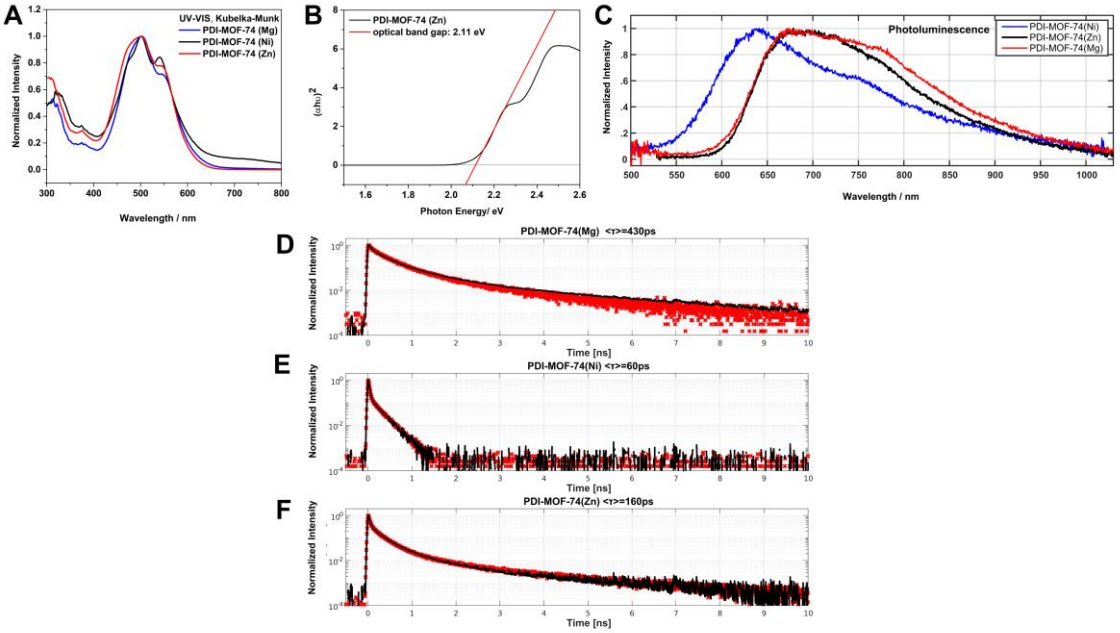

Figure 5-5: (A) UV-Vis absorption measured in diffuse reflectance of the PDI-MOF-74(M) powders dispersed with $BaSO_4$ and (B) Tauc plot of PDI-MOF-74(Zn), assuming a direct band gap. (C) Photoluminescence of the neat MOF bulk materials measured with 405 nm excitation, showing the Mg MOF in blue, the Ni MOF in black and the Zn MOF in red. (D-F) The time-correlated single photon counting (TCSPC) traces corresponding to the PL spectra of the MOFs, which were recorded at the respective emission maximum of each MOF, (D) of the Mg MOF, (E) of the Ni MOF and (F) of the Zn MOF. The lifetimes were obtained from stretched exponential fits (black) to the data (red).

Perylene diimide and its derivatives are known as electron acceptor materials and for their redox activity. We performed cyclic voltammetry (CV) to determine the reduction potentials of the PDI-MOF-74(M) series electrochemically (Figure 5-6). For this purpose, we pressed a mixture of MOF bulk material with active carbon into a stainless steel mesh. The CV measurements were subsequently carried out in a typical three-electrode setup using tetraethylammonium tetrafluoroborate as the electrolyte in argon-purged anhydrous *N*-dimethylformamide. The PDI-MOF-74(M) series shows an electrochemical reduction behavior that is stable during several cycles (see Figure 5-32). Two quasi-reversible redox couples are visible in the CV curve, with the first one having an onset at -0.2 V and the second at -0.5 V vs. Ag/Ag^+ (Figure 5-5, Figure 5-33 C). We attribute the first reduction peak to the formation of the $[PDI]^{\cdot-}$ radical anion state and the second reduction peak to the dianion state $[PDI]^{2-}$ of the integrated PDI-based ligands.

With the CV data in hand, the reduction onset potential against the HOMO energy of ferrocene can be used for the calculation of the absolute energy of the conduction band edge against the

vacuum scale (Figure 5-33 B). The energy of the valence band edge can then be determined by subtracting the optical band gap energy from the absolute energy of the conduction band. The absolute conduction band energy is determined by using the first reduction onset potential of the MOF and correlating this to the vacuum energy of the ferrocene HOMO energy of 4.8 eV and to the oxidation onset of ferrocene under the used measurement conditions. Conduction band energies of -4.0 eV and valence band energies of -6.1 eV were calculated for the PDI-MOF-74(M) series (Table S 5-2). This is in good accordance with other reported HOMO/ LUMO energies of perylene diimide based materials.[52,53]

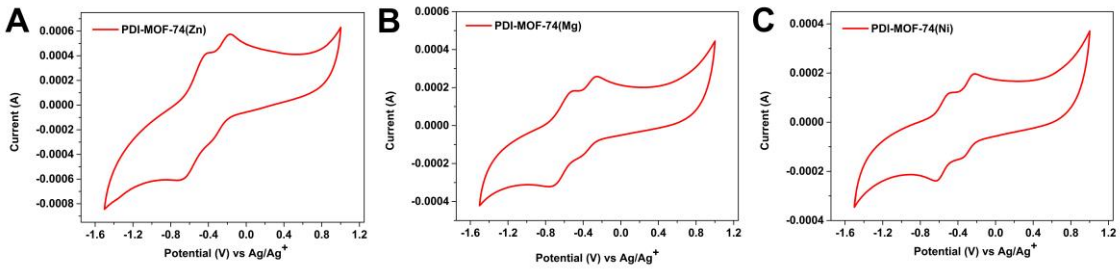

Figure 5-6: Voltammograms of the PDI-MOF-74(M) series as bulk material, pressed in a stainless stell mesh, showing (A)-Zn, (B)- Mg and (C)-Ni MOF derivatives, respectively. It was measured in a solution of 0.1 M tetrabutylammonium hexafluorophosphate ($TBAPF_6$) in DMF versus Ag/Ag^+ (in V) with scan rate 0.1 V/ s under argon atmosphere.

5.4 Conclusion

We present the successful synthesis of a novel perylene diimide based MOF series crystallizing in the MOF-74 topology, coined PDI-MOF-74(M). The series is constructed of linear perylene diimide based linking motifs, interconnected by helical metal-oxo secondary building units comprising the metal ions Zn^{II}, Mg^{II} and Ni^{II}. TEM and PXRD analyzes reveal the formation of highly crystalline materials. Notably, all PDI-MOF-74(M) materials display ohmic behavior and feature electrical conductivity values in the range of 10^{-7} S/cm. Furthermore, the reduction potentials of the whole series could be analyzed by means of CV measurements. Together with the optical band gaps of around 2.1 eV determined with Tauc plots, we obtained HOMO/LUMO levels of -6.1 eV and -4.0 eV against vacuum, respectively. In addition, the PDI-MOF-74 series exhibits photoluminescence in the orange and red spectral region with PL lifetimes of up to 430 ps. We suggest that this promising combination of high crystallinity, luminescence, as well as high electrical conductivity embedded in a fixed MOF matrix will enable a range of possible functionalities like chemical sensing or optoelectronic devices such as photodetectors. With this new series in the family of MOF-74 topologies, we enrich the field of electroactive 3D MOFs as well as the small group of PDI-based 3D MOFs. This work also illustrates the enormous flexibility of the

MOF-74 topology with respect to modifying the nature and functionality of the linear building blocks connecting the structure.

5.5 References

(1) Yaghi, O. M.; Li, H. Hydrothermal Synthesis of a Metal-Organic Framework Containing Large Rectangular Channels. *J. Am. Chem. Soc.* **1995**, *117*, 10401–10402.

(2) Sun, L.; Hendon, C. H.; Minier, M. A.; Walsh, A.; Dincă, M. Million-Fold Electrical Conductivity Enhancement in Fe2(DEBDC) versus Mn2(DEBDC) (E = S, O). *J. Am. Chem. Soc.* **2015**, *137*, 6164–6167.

(3) Meek, S. T.; Greathouse, J. A.; Allendorf, M. D. Metal-organic frameworks: a rapidly growing class of versatile nanoporous materials. *Adv. Mater.* **2011**, *23*, 249–267.

(4) Wang, L. J.; Deng, H.; Furukawa, H.; Gándara, F.; Cordova, K. E.; Peri, D.; Yaghi, O. M. Synthesis and characterization of metal-organic framework-74 containing 2, 4, 6, 8, and 10 different metals. *Inorg Chem* **2014**, *53*, 5881–5883.

(5) Kapelewski, M. T.; Geier, S. J.; Hudson, M. R.; Stück, D.; Mason, J. A.; Nelson, J. N.; Xiao, D. J.; Hulvey, Z.; Gilmour, E.; FitzGerald, S. A.; Head-Gordon, M.; Brown, C. M.; Long, J. R. M2(m-dobdc) (M = Mg, Mn, Fe, Co, Ni) metal-organic frameworks exhibiting increased charge density and enhanced H2 binding at the open metal sites. *J. Am. Chem. Soc.* **2014**, *136*, 12119–12129.

(6) Rosi, N. L.; Kim, J.; Eddaoudi, M.; Chen, B.; O'Keeffe, M.; Yaghi, O. M. Rod packings and metal-organic frameworks constructed from rod-shaped secondary building units. *J. Am. Chem. Soc.* **2005**, *127*, 1504–1518.

(7) Usman, M.; Mendiratta, S.; Batjargal, S.; Haider, G.; Hayashi, M.; Gade, N. R.; Chen, J.-W.; Chen, Y.-F.; Lu, K.-L. Semiconductor Behavior of a Three-Dimensional Strontium-Based Metal-Organic Framework. *ACS Appl. Mater. Interfaces* **2015**, *7*, 22767–22774.

(8) Kobayashi, Y.; Jacobs, B.; Allendorf, M. D.; Long, J. R. Conductivity, Doping, and Redox Chemistry of a Microporous Dithiolene-Based Metal−Organic Framework. *Chem. Mater.* **2010**, *22*, 4120–4122.

(9) Guo, Z.; Panda, D. K.; Gordillo, M. A.; Khatun, A.; Wu, H.; Zhou, W.; Saha, S. Lowering Band Gap of an Electroactive Metal-Organic Framework via Complementary Guest Intercalation. *ACS Appl. Mater. Interfaces* **2017**, *9*, 32413–32417.

(10) Stavila, V.; Talin, A. A.; Allendorf, M. D. MOF-based electronic and opto-electronic devices. *Chem. Soc. Rev.* **2014**, *43*, 5994–6010.

(11) Scheurle, P. I.; Mähringer, A.; Jakowetz, A. C.; Hosseini, P.; Richter, A. F.; Wittstock, G.; Medina, D. D.; Bein, T. A highly crystalline anthracene-based MOF-74 series featuring electrical conductivity and luminescence. *Nanoscale* **2019**, *11*, 20949–20955.

(12) Mähringer, A.; Döblinger, M.; Hennemann, M.; Gruber, C.; Fehn, D.; Scheurle, P. I.; Hosseini, P.; Santourian, I.; Schirmacher, A.; Rotter, J. M.; Wittstock, G.; Meyer, K.; Clark, T.; Bein, T.; Medina, D. D. An electrically conducting three-dimensional iron-catecholate porous framework. *Angew. Chem.* **2021**, *133*, 18213–18220.

(13) Bi., S.; Banda, H.; Chen, M.; Niu, L.; Chen; Wu, T.; Wang, J.; Wang, R.; Feng, J.; Chen, T.; Dinca, M.; Kornyshev, A. A.; Feng, G. Molecular understanding of charge storage and charging dynamics in supercapacitors with MOF electrodes and ionic liquid electrolytes. *Nat. Mater.* **2020**, *19*, 552–558.

(14) Zhang, Z.; Yoshikawa, H. I.; Awaga, K. Monitoring the solid-state electrochemistry of Cu(2,7-AQDC) (AQDC = anthraquinone dicarboxylate) in a lithium battery: coexistence of metal and ligand redox activities in a metal-organic framework. *J. Am. Chem. Soc.* **2014**, *136*, 16112–16115.

(15) Campbell, M. G.; Sheberla, D.; Liu, S. F.; Swager, T. M.; Dincă, M. Cu_3(hexaiminotriphenylene)$_2$: an electrically conductive 2D metal-organic framework for chemiresistive sensing. *Angew. Chem.* **2015**, *54*, 4349–4352.

(16) Campbell, M. G.; Dincă, M. Metal-Organic Frameworks as Active Materials in Electronic Sensor Devices. *Sensors* **2017**, *17*, 1108.

(17) Kreno, L. E.; Leong, K.; Farha, O. K.; Allendorf, M.; van Duyne, R. P.; Hupp, J. T. Metal-organic framework materials as chemical sensors. *Chem. Rev.* **2012**, *112*, 1105–1125.

(18) Yi, F.-Y.; Chen, D.; Wu, M.-K.; Han, L.; Jiang, H.-L. Chemical Sensors Based on Metal-Organic Frameworks. *ChemPlusChem* **2016**, *81*, 675–690.

(19) Deng, H.; Grunder, S.; Cordova, K. E.; Valente, C.; Furukawa, H.; Hmadeh, M.; Gándara, F.; Whalley, A. C.; Liu, Z.; Asahina, S.; Kazumori, H.; O'Keeffe, M.; Terasaki, O.; Stoddart, J. F.; Yaghi, O. M. Large-pore apertures in a series of metal-organic frameworks. *Science* **2012**, *336*, 1018–1023.

(20) Cozzolino, A. F.; Brozek, C. K.; Palmer, R. D.; Yano, J.; Li, M.; Dincă, M. Ligand redox non-innocence in the stoichiometric oxidation of Mn2(2,5-dioxidoterephthalate) (Mn-MOF-74). *J. Am. Chem. Soc.* **2014**, *136*, 3334–3337.

(21) Sun, L.; Miyakai, T.; Seki, S.; Dincă, M. Mn2(2,5-disulfhydrylbenzene-1,4-dicarboxylate): a microporous metal-organic framework with infinite (-Mn-S-)∞ chains and high intrinsic charge mobility. *J. Am. Chem. Soc.* **2013**, *135*, 8185–8188.

(22) Würthner, F.; Saha-Möller, C. R.; Fimmel, B.; Ogi, S.; Leowanawat; Schmidt, D. Perylene Bisimide Dye Assemblies as Archetype Functional Supramolecular Materials **2016**, *115*, 962–1052.

(23) Chen, S.; Slattum, P.; Wang, C.; Zang, L. Self-Assembly of Perylene Imide Molecules into 1D Nanostructures: Methods, Morphologies, and Applications. *Chem. Rev.* **2015**, *115*, 11967–11998.

(24) Struijk, C. W.; Sieval, A. B.; Dakhorst, J. E. J.; van Dijk, M.; Kimkes, P.; Koehorst, R. B. M.; Donker, H.; Schaafsma, T. J.; Picken, S. J.; van de Craats, A. M.; Warman, J. M.; Zuilhof, H.; Sudhölter, E. J. R. Liquid Crystalline Perylene Diimides: Architecture and Charge Carrier Mobilities. *J. Am. Chem. Soc.* **2000**, *122*, 11057–11066.

(25) *Color Chemistry, 3rd Edn.;* Zollinger, H., Ed.; Wiley-VCH: Weinheim, 2003.

(26) Würthner, F. Perylene bisimide dyes as versatile building blocks for functional supramolecular architectures. *Chem. Commun.* **2004**, 1564–1579.

(27) Chen, G.; Gee, L. B.; Xu, W.; Zhu, Y.; Lezama-Pacheco, J. S.; Huang, Z.; Li, Z.; Babicz, J. T.; Choudhury, S.; Chang, T.-H.; Reed, E.; Solomon, E. I.; Bao, Z. Valence-Dependent Electrical Conductivity in a 3D Tetrahydroxyquinone-Based Metal–Organic Framework. *J. Am. Chem. Soc.* **2020**, *142*, 21243–21248.

(28) Huang, C.; Barlow, S. Marder, S. A. Perylene-3,4,9,10-tetracarboxylic Acid Diimides: Synthesis, Physical Properties, and Use in Organic Electronics. *J. Org. Chem.* **2011**, *76*, 2386–2407.

(29) Ghosh, I.; Ghosh, T.; Bardagi, J. I.; König, B. Reduction of aryl halides by consecutive visible light-induced electron transfer processes. *Science* **2014**, *346*, 725–728.

(30) Würthner, F. Plastic Transistors Reach Maturity for Mass Applications in Microelectronics. *Angew. Chem. Int. Ed.* **2001**, *40*, 1037–1039.

(31) Che, Y.; Datar, A.; Yang, X.; Naddo, T.; Zhao, J.; Zang, L. Enhancing one-dimensional charge transport through intermolecular pi-electron delocalization: conductivity improvement for organic nanobelts. *J. Am. Chem. Soc.* **2007**, *129*, 6354–6355.

(32) Shirman, E.; Ustinov, A.; Ben-Shihit, N.; Weissman, H.; Iron, M. A.; Cohen, R.; Rybttchinski, B. Stable Aromatic Dianion in Water. *J. Phys. Chem. B* **2008**, *112*, 8855–8858.

(33) Newmann, C. D.; Friesbe, C. D.; Silva-Filho, D. A.; Bredas, J. L.; Ewbank, P. C.; Mann, K. R. Introduction to Organic Thin Film Transistors and Design of n-Channel Organic Semiconductors. *Chem. Mater.* **2004**, *16*, 4436–4451.

(34) Dimitrakopoulos, C. D.; Malefant, P. R. L. Organic Thin Film Transistors for Large Area Electronics. *Adv. Mater.* **2002**, *14*, 99–117.

(35) Gregg, B. A.; Cormier, V. Doping Molecular Semiconductors: n-Type Doping of a Liquid Crystal Perylene Diimide. *J. Am. Chem. Soc.* **2001**, *123*, 7959–7960.

(36) Sadrai, M.; Bird, G. R. *Opt. Commun* **1984**, *51*, 62–64.

(37) Gvishi, R.; Reisfeld, R.; Burshtein, Z. *Chem. Phys. Lett.* **1993**, *213*, 338–344.

(38) Zhan, X.; Facchetti, A.; Barlow, S.; Marks, T. J.; Ratner, M. A.; Wasielewski, M. R.; Marder, S. R. Rylene and Related Diimides for Organic Electronics. *Adv. Mater.* **2011**, *23*, 268–284.

(39) Zeng, L.; Liu, T.; He, C.; Shi, D.; Zhang, F.; Duan, C. Organized Aggregation Makes Insoluble Perylene Diimide Efficient for the Reduction of Aryl Halides via Consecutive Visible Light-Induced Electron-Transfer Processes. *J. Am. Chem. Soc.* **2016**, *138*, 3958–3961.

(40) Nelson, A. P.; Farha, O. K.; Mulfort, K. L.; Hupp, J. T. Supercritical processing as a route to high internal surface areas and permanent microporosity in metal-organic framework materials. *J. Am. Chem. Soc.* **2009**, *131*, 458–460.

(41) Boer, S. A.; Nolvachai, Y.; Kulsing, C.; McCormick, L. J.; Hawes, C. S.; Marriott, P. J.; Turner, D. R. Liquid-phase enantioselective chromatographic resolution using interpenetrated, homochiral framework materials. *Chemistry* **2014**, *20*, 11308–11312.

(42) Bellitto, C.; Righini, G.; Gómez-García, C. J.; Caminiti, R.; Carbone, M.; Matassa, R.; Bauer, E. M. Nickel(II) 3,4;9,10-perylenediimide bis-phosphonate pentahydrate: a metal-organic ferromagnetic dye. *Inorg. Chem.* **2012**, *51*, 7332–7339.

(43) Lü, B.; Chen, Y.; Li, P.; Wang, B.; Müllen, K.; Yin, M. Stable radical anions generated from a porous perylenediimide metal-organic framework for boosting near-infrared photothermal conversion. *Nat. Commun.* **2019**, *10*, 767.

(44) Transparent-to-Dark Electrochromic Behavior in Naphthalene-Diimide-Based Mesoporous MOF-74 Analogs.

(45) Mähringer, A.; Jakowetz, A. C.; Rotter, J. M.; Bohn, B. J.; Stolarczyk, J. K.; Feldmann, J.; Bein, T.; Medina, D. D. Oriented Thin Films of Electroactive Triphenylene Catecholate-Based Two-Dimensional Metal-Organic Frameworks. *ACS Nano* **2019**, *13*, 6711–6719.

(46) Virmani, E.; Rotter, J. M.; Mähringer, A.; Zons, T. von; Godt, A.; Bein, T.; Wuttke, S.; Medina, D. D. On-Surface Synthesis of Highly Oriented Thin Metal-Organic Framework Films through Vapor-Assisted Conversion. *J. Am. Chem. Soc.* **2018**, *140*, 4812–4819.

(47) Mähringer, A.; Rotter, J. M.; Medina, D. D. Nanostructured and oriented metal-organic framework films enabling extreme surface wetting properties. *Beilstein J. Nanotechnol.* **2019**, *10*, 1994–2003.

(48) Scheurle, P. I.; Mähringer, A.; Biewald, A.; Hartschuh, A.; Bein, T.; Medina, D. D. MOF-74(M) Films Obtained through Vapor-Assisted Conversion—Impact on Crystal Orientation and Optical Properties. *Chem. Mater.* **2021**, *33*, 5896–5904.

(49) Mähringer, A.; Hennemann, M.; Clark, T.; Bein, T.; Medina, D. D. Energy Efficient Ultrahigh Flux Separation of Oily Pollutants from Water with Superhydrophilic Nanoscale Metal-Organic Framework Architectures. *Angew. Chem.* **2021**, *60*, 5519–5526.

(50) Medina, D. D.; Rotter, J. M.; Hu, Y.; Dogru, M.; Werner, V.; Auras, F.; Markiewicz, J. T.; Knochel, P.; Bein, T. Room temperature synthesis of covalent-organic framework films through vapor-assisted conversion. *J. Am. Chem. Soc.* **2015**, *137*, 1016–1019.

(51) Thommes, M.; Kaneko, K.; Neimar K, A. V.; Olivier, J. P.; Rodriguez-Reinoso, F.; Rouquerol, J.; Sing, K. S. W. Physisorption of gases, with special reference to the evaluation of surface area and pore size distribution (IUPAC Technical Report). *Pure Appl. Chem.* **2015**, *87*, 1051–1069.

(52) Ramanan, C.; Smeigh, A. L.; Anthony, J. E.; Marks, T. J.; Wasielewski, M. R. Competition between singlet fission and charge separation in solution-processed blend films of 6,13-bis(triisopropylsilylethynyl)pentacene with sterically-encumbered perylene-3,4:9,10-bis(dicarboximide)s. *J. Am. Chem. Soc.* **2012**, *134*, 386–397.

(53) Sato, R.; Yoo, D.; Mori; T. 1 : 2 charge-transfer complexes of perylene and coronene with perylene diimide, and the ambipolar transistors. *CrystEngComm* **2019**, *21*, 3218–3222.

5.6 Supporting information

5.6.1 Characterization methods

Nuclear magnetic resonance (NMR)

NMR spectra were recorded on *Bruker AV400* and *AV400 TR* spectrometers. The chemical shifts are expressed in parts per million and calibrated using residual (undeuterated) solvent peaks as an internal reference (^{1}H-NMR: DMSO-d_6: 2.50; ^{13}C-NMR: DMSO-d_6: 39.52). The data for ^{1}H-NMR spectra are written as follows: s = singlet, d = doublet, t = triplet, q = quartet, m = multiplet.

X-ray diffraction

X-ray diffraction (XRD) analyzes were performed on a *Bruker D8* diffractometer in Bragg-Brentano geometry with Ni-filtered Cu K_α (λ = 1.54060 Å) radiation operating at 40 kV and 30 mA with a position-sensitive detector (*LynxEye*).

Scanning electron microscopy (SEM)

SEM images were recorded on an *FEI Helios NanoLab G3 UC* electron microscope with an acceleration voltage of 2 kV from a field emission gun. For the cross-section analysis substrates were partially cut and broken manually to reveal fresh cross-sections. Prior to SEM analysis the samples were coated with a thin carbon layer by carbon fiber flash evaporation in high vacuum.

Transmission electron microscopy (TEM)

TEM images were collected on an *FEI Titan Themis 60-300* microscope at an acceleration voltage of 300 kV. Powder samples were prepared by crushing the particles with a razor blade and subsequently depositing the powder onto a copper grid supporting a thin electron transparent carbon film.

Nitrogen sorption

Ad- and desorption measurements were performed on an *Autosorb 1* (*Quantachrome instruments, Florida, USA*) with nitrogen of 99.9999% purity at 77.3 K. The samples were activated (dried) under high vacuum at 120 °C for at least 12 h. Evaluation of ad- and desorption isotherms was carried out with the *AsiQwin v.3.01* (*Quantachrome instruments, Florida, USA*) software.

For BET calculations, pressure ranges of the nitrogen isotherms were chosen with the help of the BET assistant in the *AsiQwin* software. In accordance with the ISO recommendations, multipoint BET tags equal to or below the maximum in V x (1-p/p_0) were chosen.

Electrical conductivity measurements

I-V curves to determine the electrical conductivity were collected with an HMS-5000/ AMP55 Ecopia Hall Effect Measurement System. Gold contact electrodes were placed in a square geometry with distances of about 5.2 mm. Pellet thicknesses were measured to be about 500 µm and the probe contacts have a size of 45 µm in diameter. Electrical conductivity measurements were carried out under ambient conditions at room temperature and in the dark.

Preparation of PDI-MOF-74(M) pellets

MOF pellets with 1 cm diameter (obtained from several described batches) for electrical conductivity measurements were fabricated with 80 mg of the respective MOF bulk material with a standard *Paul-Weber* KBr Press with 45 kg/ cm^2 pressure.

Electrochemical measurements

Electrochemical measurements were performed on a Metrohm µAutolabIII/FRA2 instrument using a three-electrode setup with a Pt-wire counter-electrode and a silverwire as a pseudo reference electrode under argon atmosphere. Measurements were carried out in dry DMF with tetrabutylammonium hexafluorophosphate (TBAPF6) (0.1 M) as the electrolyte at a scan rate of 0.1 V/ s. The MOF bulk material was pressed into a stainless steel mesh.

After recording CV data, the measurement was repeated after a small amount of ferrocene was added to the sample. The position of the redox couple from Fc/Fc^+ was then used as the reference system.

UV-Vis spectroscopy

UV-Vis spectra were recorded using a *PERKIN ELMER UV VIS/NIR Lambda 1050* spectrophotometer equipped with a 150 mm InGaAs integrating sphere. Diffuse reflectance spectra were collected with a Praying Mantis (Harrick) accessory and were referenced to barium sulphate powder as white standard.

Photoluminescence (PL) spectroscopy

Photoluminescence spectra were measured with a self-built confocal microscope system. A NIKON 60x APO-Chromat oil-objective is used with a numerical aperture of 1.4. The sample is placed on a holder of a x,y,z-piezo scanning stage (Physik Instrumente). A tunable subpicosecond pulsed laser source (TOPTICA ichrome), exciting the sample, is implemented with a repetition rate of 40 MHz. In these measurements a wavelength of 405 nm was used with a 473/10 band

pass filter (Chroma) as a laser-line filter combined with a 490 long pass filter (Chroma) in the detection branch. In the detection path, an Avalanche Photo Diode (APD, model MPD PDM, 50µm detector size) is inserted for confocal images and is combined with a Time Correlated Single Photon Counting (TCSPC)-Card (BECKER & HICKEL) measuring time dependent PL-decays. In addition, a second optical path is implemented with an ANDOR SHAMROCK spectrometer SR303i combined with a charged coupled device (CCD) camera (ANDOR NEWTON DU920 open electrode) to record spectra.

Thermogravimetric analysis

Thermogravimetric analysis (TGA) measurements were performed on a *Netzsch Jupiter ST 449 C* instrument equipped with a *Netzsch TASC 414/4* controller. The samples were heated from room temperature to 800 °C under a synthetic air flow (25 mL min^{-1}) at a heating rate of 1 K min^{-1}.

Elemental Analysis

The elemental analysis for carbon and hydrogen for PDI-MOF-74(M) was performed on a Vario MICRO cube instrument (Elementar Analyzensysteme GmbH, Germany). The metal detection for all samples was carried out on a Varian Vista RL ICP-OES spectrometer. All materials were treated under dynamic vacuum prior to analysis.

5.6.2 Experimental

5.6.2.1 General

All materials were purchased from *Sigma Aldrich, Acros or TCI Europe* in the common purities *purum, puriss* or *reagent grade.* The materials were used as received without additional purification and handled in air unless otherwise noted.

The water utilized in the synthesis was subjected to a *Merck-Milipore Mili-Q* purification system prior to use.

5.6.2.2 Film formation via vapor-assisted conversion (VAC)

For the film formation using VAC, a glass bottle (Schott Duran, borosilicate 3.3, ISO4796, 100 mL) with a PBT cap equipped with a Teflon seal was used. The bottom part of the bottle was filled with 14 Raschig-rings (10 mm x 10 mm, soda-lime glass) to obtain an elevated flat platform for the substrate. DMF was filled into the bottle (5 ml). Afterwards, a substrate (1.2 cm x 1 cm) was placed on top of the Raschig-rings and fully coated with a drop of freshly prepared MOF precursor solution. The bottle was closed and was transferred into a preheated oven where it was kept for 48 h at 120 °C. Afterwards the bottle was removed from the oven and was allowed to cool down to room temperature before the substrate was removed and dried under reduced pressure.

The glass substrates were prepared by cutting microscope glass slides (Menzel, 76 mm x 26 mm) into 1.2 cm x 1.0 cm pieces. Afterwards they were washed with a 1:100 mixture of Hellmanex III and water, rinsed with water and finally ethanol and dried in a nitrogen flow.

5.6.2.3 Synthetic procedures

5.6.2.4 PDI-based ligand

Synthesis of 5,5´-(1,3,8,10-tetraoxo-1,3,8,10-tetrahydroanthra[2,1,9-*def*:6,5,10-*d´e´f´*]diisoquinoline-2,9-diyl)bi(2-hydroxybenzoic acid) **(**modified from the procedure by M. E. Bhosale, K. Krishnamoorthy, *Chem. Mater*. 2015, 27, 6, 2121–2126.

A mixture of perylene-3,4,9,10-tetracarboxylic dianhydride (500 mg, 1.27 mmol, 1 eq), 5-amino-2-hydroxy benzoic acid (487 mg, 3.18 mmol, 2.5 eq), imidazole (20 g, 293.8 mmol, 231 eq) and $Zn(OAc)_2$ (100 mg, 0.456 mmol, 0.36 eq) was heated in a 250 mL Schlenk flask under nitrogen atmosphere at 100 °C for 2 h and at 140°C for 20 h under stirring. The solution was allowed to cool to room temperature and 100 mL of 2 M hydrochloric acid was added. The precipitate was filtered and washed with 2 M hydrochloric acid (600 mL), with hot water (800 mL) and methanol

(50 mL). The precipiate was dried under reduced pressure to yield a dark red solid with 65% yield (545 mg, 0.823 mmol). **^{1}H NMR** (*D_2SO_4*, 400 MHz, ppm) δ = 8.53 - 8.55 (m, 8H), 7.79 (s, 2H), 7.44 (d, 2H), 7.09 (d, 2H).

Elemental Analysis (vacuum treated): Calculated for $C_{38}H_{18}N_2O_{10}$ (%): C, 69.89; H, 2.74; N, 4.23; Found in analysis (%): C, 68.21; H, 3.04; N, 4.37.

Scheme 5-1

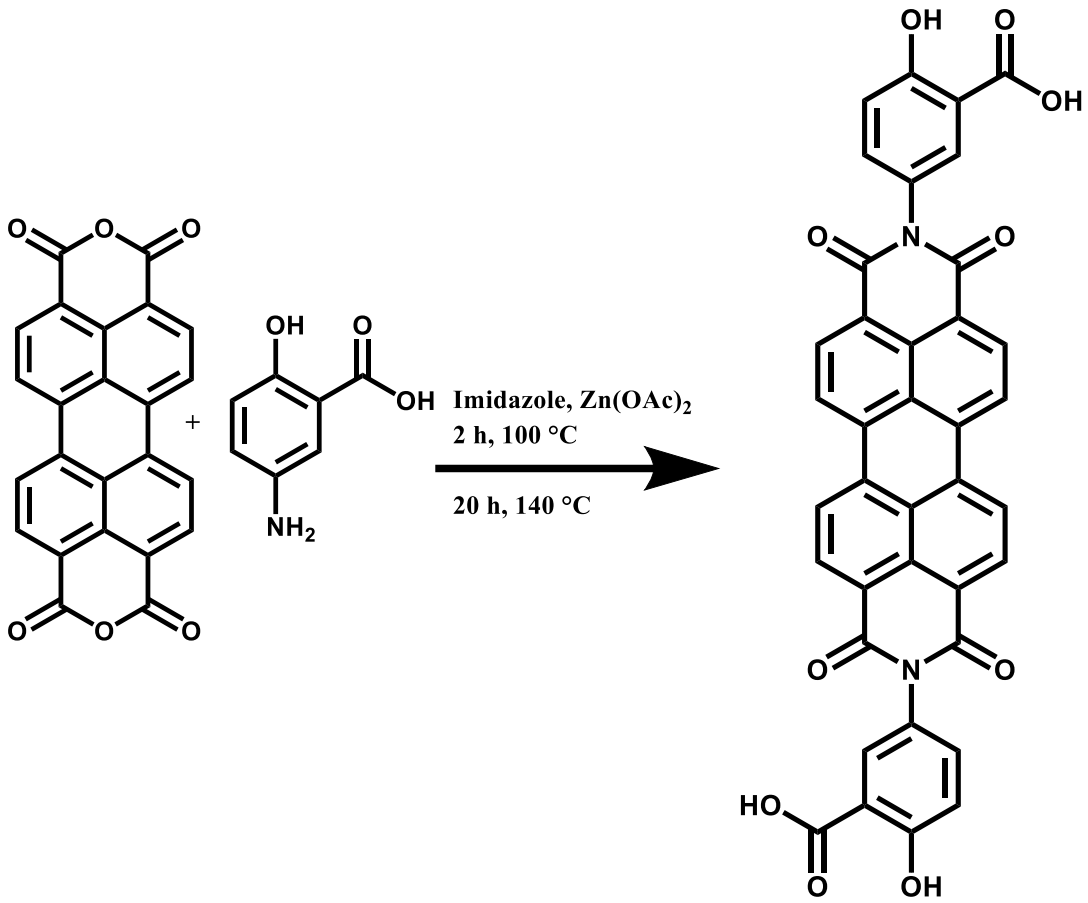

5.6.2.5 PDI-MOF-74(M) synthesis

PDI-MOF-74(Zn)

5,5´-(1,3,8,10-tetraoxo-1,3,8,10-tetrahydroanthra[2,1,9-*def*:6,5,10-*d´e´f´*]diisoquinoline-2,9-diyl)bi(2-hydroxybenzoic acid) (38.7 mg, 0.06 mmol, 1 eq), $Zn(NO_3)_2{\cdot}4H_2O$ (58.17 mg, 0.22 mmol, 3.7 eq) were suspended in DMF (18 mL). Acetic acid (12 µL, 0.21 mmol, 10.5 eq) was added to the precursor mixture. The resulting mixture was sonicated for 1 h and it was kept in a 50 mL Schott Duran vial at 120 °C for 2 days. The resulting precipitate was washed with DMF (4 x 30 mL). Afterwards, the precipitate was soaked in MeOH (1 x 30 mL) for 1 h and then in THF (1 x 30 mL) for 1 h. The precipitate was filtered and evacuated at 120°C to remove the

less volatile solvents to obtain a dark red crystalline powder. The PXRD pattern of the synthesized MOF matches the simulated PDI-MOF-74 PXRD pattern. Elemental Analysis (vacuum treated): Calculated for $Zn_{18}C_{342}N_{18}H_{126}O_{99}$ 2 DMF 2 H_2O (Mass %): C, 56.26; N, 3.77; H. 1.95; Found (%):C, 56.05; N, 4.23; H, 2.72. (Sum formula calculated with JASPER v2.0 – JavaScript Percentage Elemental Results Calculator).

PDI-MOF-74(Mg)

5,5´-(1,3,8,10-tetraoxo-1,3,8,10-tetrahydroanthra[2,1,9-*def*:6,5,10-*d´e´f´*]diisoquinoline-2,9-diyl)bi(2-hydroxybenzoic acid) (12.9 mg, 0.02 mmol, 1 eq), $Mg(NO_3)_2{\cdot}6H_2O$ (21.68 mg, 0.08 mmol, 4 eq) were suspended in DMF (10 mL) and MeOH (4 mL). Acetic acid (10 µL, 0.17 mmol, 8.7 eq) was added to the precursor mixture. The resulting mixture was sonicated for 1 h and was kept in a 25 mL Schott Duran vial at 120 °C for 2 days. The resulting precipitate was washed with DMF (4 x 30 mL). Afterwards, the precipitate was soaked in MeOH (1 x 30 mL) for 1 h and then in THF (1 x 30 mL) for 1 h. The precipitate was filtered and evacuated at 120°C to remove the less volatile solvents to obtain a dark red crystalline powder. The PXRD pattern of the synthesized MOF matches the simulated PDI-MOF-74 PXRD pattern. Elemental Analysis (vacuum treated): Calculated for $Mg_{18}C_{342}N_{18}H_{126}O_{99}$ 2 DMF 2 H_2O (Mass %): C, 62.47; N, 4.19; H. 2.17; Found (Mass %): C, 60.98, N; 3.79 H; 3.49. (Sum formula calculated with JASPER v2.0 – JavaScript Percentage Elemental Results Calculator).

PDI-MOF-74(Ni)

5,5´-(1,3,8,10-tetraoxo-1,3,8,10-tetrahydroanthra[2,1,9-def:6,5,10-d´e´f´]diisoquinoline-2,9-diyl)bi(2-hydroxybenzoic acid) (10.37 mg, 0.016 mmol, 1 eq), NiCl2·6H2O (14.30 mg, 0.07 mmol, 4.4 eq) were suspended in DMF (2 mL) and BnOH (2 mL). The resulting mixture was sonicated for 1 h and it was kept in a culture tube at 120 °C for 2 days. The resulting precipitate was washed with DMF (4 x 30 mL). Afterwards, the precipitate was soaked in MeOH (1 x 30 mL) for 1 h and then in THF (1 x 30 mL) for 1 h. The precipitate was filtered and evacuated at 120°C to remove the less volatile solvents to obtain a dark red crystalline powder. The PXRD pattern of the synthesized MOF matches the simulated PDI-MOF-74 PXRD pattern. Elemental Analysis (vacuum treated): Calculated for Ni18C342N18H126O99 2 DMF 2 H2O (Mass %): C, 57.63; N, 3.54; H. 1.78; Found (%): C, 45.51; N, 3.29; H, 2.42. (Sum formula calculated with JASPER v2.0 – JavaScript Percentage Elemental Results Calculator).

PDI-MOF-74(Zn) films

For the precursor solution, 5,5´-(1,3,8,10-tetraoxo-1,3,8,10-tetrahydroanthra[2,1,9-*def*:6,5,10-*d´e´f´*]diisoquinoline-2,9-diyl)bi(2-hydroxybenzoic acid) (3.17 mg, 4.9 mmol, 1 eq.) was suspended in 1.1 mL DMF, salicylic acid (25 µL from a solution of 424 mg salicylic acid in 2 mL DMF) was added and the whole mixture was sonicated for 1 h. Afterwards, $Zn(NO_3)_2 \cdot 6H_2O$ (2.60 mg, 9.8 mmol, 2 eq) was added to the suspension and shortly sonicated. A droplet of the MOF precursor solution (100 µL) was dropcasted on top of the glass substrate. The glass bottle was heated in a preheated oven at 120 °C for 48 h. Afterwards the bottle was removed from the oven and allowed to cool down to room temperature before the substrate was removed and dried under reduced pressure.

5.6.3 Characterization

5.6.3.1 Unit cell parameters and atomic coordinates

Pawley refinement in the trigonal space group:

R*3* (146) - trigonal
a = b = 77.83, c = 5.53 Å
α = β = 90°, γ = 120°

PDI-MOF-74(Zn): R_{wp} = 8.95%, R_p = 6.42%

PDI-MOF-74(Mg): R_{wp} = 8.02%, R_p = 5.19%

PDI-MOF-74(Ni): R_{wp} = 8.51%, R_p = 6.47%

Pawley refinement in the triclinic space group:

PDI-MOF-74(Zn)

R_{wp} = 2.38%, R_p = 1.56%

P*1* (1) - triclinic
a = 72.6294, b = 74.5613, c = 5.5891 Å
α = β = 90°, γ = 120°

Atom	a/x	b/y	c/z
O1	0.99737	0.29192	0.36763
O2	0.99073	0.31639	0.48362
O3	0.99994	0.31953	0.97645
O4	0.70848	0.98745	0.19742
O5	0.66498	0.00799	0.78751

O6	0.69622	0.00783	0.89113	**C29**	0.35501	0.10505	0.70627
Zn7	0.01166	0.32000	0.30840	**C30**	0.36595	0.13858	0.49759
O8	0.70318	0.03374	0.09547	**C31**	0.36500	0.15668	0.47019
Zn9	0.69012	0.00537	0.17497	**C32**	0.35245	0.16110	0.62336
C10	0.30413	0.96144	0.60849	**C33**	0.34084	0.14700	0.80881
C11	0.28720	0.95579	0.76792	**C34**	0.32801	0.15101	0.96551
C12	0.26807	0.93700	0.75138	**C35**	0.31673	0.13674	0.14196
C13	0.26488	0.92294	0.56908	**C36**	0.31800	0.11879	0.16938
C14	0.28042	0.92835	0.39414	**C37**	0.32663	0.16906	0.93524
C15	0.05733	0.69612	0.03087	**C38**	0.33815	0.18310	0.74901
C16	0.03920	0.68840	0.17583	**C39**	0.35111	0.17917	0.59356
C17	0.05946	0.71988	0.43894	**C40**	0.36234	0.19337	0.41024
C18	0.07643	0.72725	0.27772	**C41**	0.36074	0.21110	0.37940
C19	0.07553	0.71509	0.08145	**C42**	0.34787	0.21506	0.53132
C20	0.64815	0.62832	0.85731	**C43**	0.33662	0.20116	0.71719
C21	0.63888	0.61856	0.07235	**C44**	0.32380	0.20517	0.87067
C22	0.36659	0.35719	0.23735	**C45**	0.31246	0.19120	0.04821
C23	0.37973	0.36922	0.06067	**C46**	0.31386	0.17337	0.08009
N24	0.34367	0.09127	0.88702	**C47**	0.32226	0.22405	0.83434
C25	0.33181	0.09551	0.04025	**N48**	0.33323	0.23753	0.64972
C26	0.33058	0.11465	0.01461	**C49**	0.34584	0.23368	0.49758
C27	0.34198	0.12870	0.83665	**O50**	0.36568	0.10133	0.56741
C28	0.35442	0.12448	0.67928	**O51**	0.32201	0.08337	0.20144

O52	0.35550	0.24565	0.33455	**C75**	0.02774	0.68727	0.57273
O53	0.31102	0.22746	0.96727	**C76**	0.04087	0.69930	0.39605
O54	0.65851	0.62199	0.70301	**N77**	0.00482	0.42134	0.21626
O55	0.65188	0.64646	0.81900	**C78**	0.0095	0.42558	0.37562
O56	0.66109	0.64961	0.30569	**C79**	0.00828	0.44472	0.34999
O57	0.36963	0.32730	0.53280	**C80**	0.00313	0.45877	0.16590
O58	0.32613	0.33806	0.11676	**C81**	0.01557	0.45455	0.00853
O59	0.35737	0.33791	0.22037	**C82**	0.01616	0.43513	0.03551
Zn60	0.67283	0.65007	0.64378	**C83**	0.02710	0.46866	0.83297
O61	0.36432	0.36381	0.43085	**C84**	0.02614	0.48676	0.80557
Zn62	0.35127	0.33544	0.51035	**C85**	0.01360	0.49117	0.95874
C63	0.98184	0.30129	0.94387	**C86**	0.00199	0.47707	0.13806
C64	0.96491	0.29564	0.09717	**C87**	0.01572	0.48108	0.29475
C65	0.94577	0.27685	0.08063	**C88**	0.99444	0.46681	0.47733
C66	0.94258	0.26279	0.90446	**C89**	0.99571	0.44886	0.50476
C67	0.95813	0.26820	0.72952	**C90**	0.00434	0.49913	0.26449
C68	0.73504	0.03597	0.36625	**C91**	0.011586	0.51318	0.07825
C69	0.71691	0.02825	0.51121	**C92**	0.01226	0.50924	0.92894
C70	0.73717	0.05973	0.77432	**C93**	0.02349	0.52344	0.74562
C71	0.75413	0.06710	0.61310	**C94**	0.02188	0.54117	0.71478
C72	0.75324	0.05494	0.41683	**C95**	0.00901	0.54513	0.86670
C73	0.30930	0.95839	0.18655	**C96**	0.01433	0.53124	0.04644
C74	0.30002	0.94864	0.40773	**C97**	0.00150	0.53525	0.19991

C98	0.99017	0.52128	0.38359	**C121**	0.39619	0.36604	0.70163
C99	0.99157	0.50344	0.41547	**C122**	0.37805	0.35833	0.84659
C100	0.99997	0.55412	0.16358	**C123**	0.39831	0.38981	0.10356
N101	0.01094	0.56761	0.98510	**C124**	0.41528	0.39717	0.94848
C102	0.00699	0.56376	0.83296	**C125**	0.41438	0.38501	0.75220
O103	0.02682	0.43140	0.90279	**C126**	0.98700	0.29824	0.52193
O104	0.99971	0.41344	0.53682	**C127**	0.97773	0.28849	0.74311
O105	0.01665	0.57573	0.66993	**C128**	0.70545	0.02712	0.90811
O106	0.98872	0.55754	0.29651	**C129**	0.71858	0.03915	0.73143
O107	0.31966	0.95206	0.03225	**N130**	0.68252	0.75142	0.55164
O108	0.31302	0.97653	0.14824	**C131**	0.67066	0.75565	0.71100
O109	0.32223	0.97968	0.64107	**C132**	0.66943	0.77480	0.68537
O110	0.03077	0.65737	0.86818	**C133**	0.68084	0.78885	0.50127
O111	0.00384	0.66814	0.45213	**C134**	0.69328	0.78463	0.34390
O112	0.01851	0.66798	0.55575	**C135**	0.69387	0.76520	0.37089
Zn113	0.33397	0.98015	0.97916	**C136**	0.70481	0.79873	0.16222
O114	0.02547	0.69388	0.76623	**C137**	0.70385	0.81683	0.13481
Zn115	0.01242	0.66551	0.84572	**C138**	0.69131	0.82125	0.28798
C116	0.64299	0.63136	0.27311	**C139**	0.67970	0.80715	0.47343
C117	0.62605	0.62572	0.43254	**C140**	0.66687	0.81116	0.63013
C118	0.60692	0.60692	0.41600	**C141**	0.65558	0.79689	0.81271
C119	0.60373	0.59286	0.23370	**C142**	0.65685	0.77893	0.84014
C120	0.61927	0.59828	0.05877	**C143**	0.66549	0.82921	0.59987

C144	0.67700	0.84325	0.41363	**O167**	0.98193	0.65122	0.09547
C145	0.68996	0.83932	0.25818	**Zn168**	0.01105	0.66687	0.17497
C146	0.70120	0.85352	0.07486	**C169**	0.02955	0.32504	0.60849
C147	0.69959	0.87124	0.04403	**C170**	0.03535	0.31419	0.76792
C148	0.68672	0.87520	0.19594	**C171**	0.05464	0.31435	0.75138
C149	0.67548	0.86131	0.38182	**C172**	0.06908	0.32530	0.56908
C150	0.66265	0.86532	0.53529	**C173**	0.06351	0.33502	0.39414
C151	0.65131	0.85135	0.71897	**C174**	0.30193	0.34995	0.03087
C152	0.65272	0.83352	0.75085	**C175**	0.30985	0.34000	0.17583
C153	0.66111	0.88419	0.49896	**C176**	0.27753	0.32826	0.43894
N154	0.67208	0.89768	0.31434	**C177**	0.26997	0.33742	0.27772
C155	0.68470	0.89383	0.16221	**C178**	0.28245	0.34871	0.08145
O156	0.70453	0.76148	0.23203	**C179**	0.37153	0.00304	0.85731
O157	0.66086	0.74351	0.87220	**C180**	0.38155	0.00376	0.07235
O158	0.69436	0.90580	0.005310	**C181**	0.64987	0.99012	0.23735
O159	0.64987	0.88761	0.63189	**C182**	0.63752	0.00066	0.06067
O160	0.71688	0.67961	0.36763	**N183**	0.92286	0.24350	0.88702
O161	0.69176	0.64867	0.48362	**C184**	0.91851	0.22770	0.04025
O162	0.68853	0.65450	0.97645	**C185**	0.89886	0.20736	0.01461
O163	0.00285	0.69290	0.19742	**C186**	0.88444	0.20442	0.83665
O164	0.00836	0.63976	0.78751	**C187**	0.88877	0.22076	0.67928
O165	0.00852	0.67035	0.89113	**C188**	0.90871	0.24076	0.70627
Zn166	0.68805	0.66547	0.30840	**C189**	0.87429	0.21789	0.49759

C190	0.85571	0.19886	0.47019	**O213**	0.37803	0.01946	0.70301
C191	0.85118	0.18222	0.62336	**O214**	0.35291	0.97875	0.81900
C192	0.86565	0.18501	0.80881	**O215**	0.34967	0.98457	0.30569
C193	0.86154	0.16851	0.96551	**O216**	0.68055	0.03275	0.53280
C194	0.87618	0.17178	0.14196	**O217**	0.66950	0.96984	0.11676
C195	0.89461	0.19097	0.16938	**O218**	0.66967	0.01020	0.22037
C196	0.84300	0.14911	0.93524	**Zn219**	0.34920	0.00532	0.64378
C197	0.82859	0.14629	0.74901	**O220**	0.64307	0.98129	0.43085
C198	0.83262	0.16284	0.59356	**Zn221**	0.67220	0.00673	0.51035
C199	0.81805	0.15958	0.41024	**C222**	0.70726	0.65511	0.94387
C200	0.79985	0.14029	0.37940	**C223**	0.71305	0.64426	0.09717
C201	0.79578	0.12380	0.53132	**C224**	0.73235	0.64442	0.08063
C202	0.81005	0.12674	0.71719	**C225**	0.74678	0.65537	0.90446
C203	0.80593	0.11023	0.87067	**C226**	0.74122	0.66510	0.72952
C204	0.82027	0.11316	0.04821	**C227**	0.97964	0.68003	0.36625
C205	0.83858	0.13236	0.08009	**C228**	0.98756	0.67008	0.51121
C206	0.78655	0.08986	0.83434	**C229**	0.95524	0.65833	0.77432
N207	0.77271	0.08706	0.64972	**C230**	0.94768	0.66749	0.61310
C208	0.77666	0.10320	0.49758	**C231**	0.96016	0.67878	0.41683
O209	0.91254	0.25487	0.56741	**C232**	0.03268	0.33311	0.18655
O210	0.93098	0.23030	0.20144	**C233**	0.04269	0.33384	0.40773
O211	0.76437	0.10064	0.33455	**C234**	0.31101	0.32997	0.57273
O212	0.78305	0.07549	0.96727	**C235**	0.29866	0.33074	0.39605

N236	0.58401	0.57357	0.21626	**C259**	0.44770	0.41994	0.16358
C237	0.57966	0.55778	0.37562	**N260**	0.43385	0.41713	0.98510
C238	0.56001	0.53744	0.34999	**C261**	0.43781	0.43327	0.83296
C239	0.54559	0.53449	0.16590	**O262**	0.57368	0.58495	0.90279
C240	0.54992	0.55083	0.00853	**O263**	0.59212	0.56037	0.53682
C241	0.56986	0.57084	0.03551	**O264**	0.42552	0.43071	0.66993
C242	0.53544	0.54796	0.83297	**O265**	0.44419	0.40557	0.29651
C243	0.51686	0.52893	0.80557	**O266**	0.03917	0.34953	0.03225
C244	0.51232	0.51229	0.95874	**O267**	0.01405	0.31860	0.14824
C245	0.52680	0.51509	0.13806	**O268**	0.01082	0.32442	0.64107
C246	0.52268	0.49858	0.29475	**O269**	0.34170	0.36282	0.86818
C247	0.53733	0.50186	0.47733	**O270**	0.33065	0.30969	0.45213
C248	0.55576	0.52105	0.50476	**O271**	0.33081	0.34028	0.55575
C249	0.50415	0.47918	0.26449	**Zn272**	0.01034	0.33539	0.97916
C250	0.48974	0.47636	0.07825	**O273**	0.30422	0.32115	0.76623
C251	0.49377	0.49292	0.92894	**Zn274**	0.33334	0.33680	0.84572
C252	0.47919	0.48966	0.74562	**C275**	0.36841	0.98519	0.27311
C253	0.46100	0.47037	0.71478	**C276**	0.37420	0.97433	0.43254
C254	0.45693	0.45387	0.86670	**C277**	0.39349	0.97449	0.41600
C255	0.47119	0.45681	0.04644	**C278**	0.40793	0.98544	0.23370
C256	0.46708	0.44031	0.19991	**C279**	0.40237	0.00495	0.05877
C257	0.48142	0.44324	0.38359	**C280**	0.64078	0.01988	0.70163
C258	0.49973	0.46244	0.41547	**C281**	0.64870	0.00993	0.84659

C282	0.61639	0.98841	0.10356	**C305**	0.14034	0.81973	0.07486
C283	0.60882	0.00734	0.94848	**C306**	0.12214	0.80044	0.04403
C284	0.62131	0.01863	0.75220	**C307**	0.11808	0.78394	0.19594
C285	0.71039	0.66319	0.52193	**C308**	0.13234	0.78689	0.38182
C286	0.72040	0.66391	0.74311	**C309**	0.12822	0.77038	0.53529
C287	0.98872	0.66005	0.90811	**C310**	0.14257	0.77331	0.71897
C288	0.97637	0.66081	0.73143	**C311**	0.16087	0.79251	0.75085
N289	0.24516	0.90364	0.55164	**C312**	0.10885	0.75001	0.49896
C290	0.24081	0.88785	0.71100	**N313**	0.09500	0.74721	0.31434
C291	0.22116	0.86751	0.68537	**C314**	0.09896	0.76335	0.16221
C292	0.20673	0.86457	0.50127	**O315**	0.23483	0.91502	0.23203
C293	0.21106	0.88091	0.34390	**O316**	0.25327	0.89044	0.87220
C294	0.23101	0.90091	0.37089	**O317**	0.08667	0.76078	0.00531
C295	0.19659	0.87804	0.16222	**O318**	0.10534	0.73564	0.63189
C296	0.17800	0.85900	0.13481	**O319**	0.31887	0.01870	0.36763
C297	0.17347	0.84237	0.28798	**O320**	0.35063	0.02516	0.48362
C298	0.18795	0.84516	0.47343	**O321**	0.34465	0.01619	0.97645
C299	0.18383	0.82865	0.63013	**O322**	0.30523	0.30010	0.19742
C300	0.19848	0.83193	0.81271	**O323**	0.35978	0.34247	0.78751
C301	0.21691	0.85112	0.84014	**O324**	0.32838	0.31204	0.89113
C302	0.16530	0.80925	0.59987	**Zn325**	0.33339	0.00475	0.30840
C303	0.15088	0.80643	0.41363	**O326**	0.34802	0.30527	0.09547
C304	0.15492	0.82299	0.25818	**Zn327**	0.33195	0.31798	0.17497

C351	0.82663	0.65821	0.80881	**O374**	0.00580	0.34626	0.30569
C352	0.84357	0.67071	0.96551	**O375**	0.98294	0.63017	0.53280
C353	0.84021	0.68170	0.14196	**O376**	0.02093	0.67254	0.11676
C354	0.82051	0.68046	0.16938	**O377**	0.00609	0.64211	0.22037
C355	0.86349	0.67205	0.93524	**Zn378**	0.01110	0.33483	0.64378
C356	0.86638	0.66083	0.74901	**O379**	0.00917	0.63534	0.43085
C357	0.84939	0.64821	0.59356	**Zn380**	0.00966	0.64805	0.51035
C358	0.85273	0.63727	0.41024	**C381**	0.34402	0.03382	0.94387
C359	0.87253	0.63883	0.37940	**C382**	0.35516	0.05032	0.09717
C360	0.88947	0.65137	0.53132	**C383**	0.35500	0.06895	0.08063
C361	0.88645	0.66232	0.71719	**C384**	0.34376	0.07206	0.90446
C362	0.90340	0.67482	0.87067	**C385**	0.33377	0.05692	0.72952
C363	0.90039	0.68586	0.04821	**C386**	0.31844	0.27423	0.36625
C364	0.88068	0.68449	0.08009	**C387**	0.32866	0.29189	0.51121
C365	0.92431	0.67631	0.83434	**C388**	0.34072	0.27216	0.77432
N366	0.92719	0.66563	0.64972	**C389**	0.33131	0.25563	0.61310
C367	0.91062	0.65334	0.49758	**C390**	0.31973	0.25650	0.41683
O368	0.75491	0.63402	0.56741	**C391**	0.67459	0.68894	0.18655
O369	0.78014	0.67656	0.20144	**C392**	0.67384	0.69797	0.40773
O370	0.91325	0.64393	0.33455	**C393**	0.67781	0.96320	0.57273
O371	0.93906	0.68726	0.96727	**C394**	0.67703	0.95041	0.39605
O372	0.99658	0.34877	0.70301	**N395**	0.42774	0.98553	0.21626
O373	0.01178	0.35524	0.81900	**C396**	0.44395	0.00687	0.37562

C397	0.46483	0.00806	0.34999	**C420**	0.57176	0.98341	0.83296
C398	0.46785	0.98717	0.16590	**O421**	0.41605	0.96409	0.90279
C399	0.45108	0.97505	0.00853	**O422**	0.44129	0.01641	0.53682
C400	0.43054	0.97448	0.03551	**O423**	0.57439	0.97400	0.66993
C401	0.45402	0.96383	0.83297	**O424**	0.60020	0.02712	0.29651
C402	0.47356	0.96476	0.80557	**O425**	0.65773	0.67884	0.03225
C403	0.49064	0.97698	0.95874	**O426**	0.68949	0.68531	0.14824
C404	0.48777	0.98828	0.13806	**O427**	0.68351	0.67634	0.64107
C405	0.50472	0.01056	0.29475	**O428**	0.64409	0.96024	0.86818
C406	0.50135	0.02155	0.47733	**O429**	0.69864	0.01239	0.45213
C407	0.48165	0.02031	0.50476	**O430**	0.66723	0.97219	0.55575
C408	0.52463	0.01191	0.26449	**Zn431**	0.67225	0.66490	0.97916
C409	0.52753	0.00069	0.07825	**O432**	0.68687	0.96541	0.76623
C410	0.51053	0.97828	0.92894	**Zn433**	0.67080	0.97813	0.84572
C411	0.51388	0.96734	0.74562	**C434**	0.00517	0.36389	0.27311
C412	0.53368	0.96890	0.71478	**C435**	0.01631	0.38039	0.43254
C413	0.55062	0.98144	0.86670	**C436**	0.01615	0.39903	0.41600
C414	0.54760	0.00217	0.04644	**C437**	0.00490	0.40214	0.23370
C415	0.56454	0.01467	0.19991	**C438**	0.01148	0.38699	0.05877
C416	0.56153	0.02571	0.38359	**C439**	0.99615	0.60430	0.70163
C417	0.54182	0.02434	0.41547	**C440**	0.00637	0.62196	0.84659
C418	0.58545	0.01616	0.16358	**C441**	0.00186	0.60223	0.10356
N419	0.58833	0.00548	0.98510	**C442**	0.00902	0.58570	0.94848

C443	0.99743	0.58657	0.75220	**C466**	0.21176	0.32129	0.19594
C444	0.33573	0.02879	0.52193	**C467**	0.20874	0.33225	0.38182
C445	0.33499	0.03782	0.74311	**C468**	0.22569	0.34474	0.53529
C446	0.33896	0.30305	0.90811	**C469**	0.22268	0.35578	0.71897
C447	0.33817	0.29026	0.73143	**C470**	0.20297	0.35442	0.75085
N448	0.08888	0.32538	0.55164	**C471**	0.24660	0.34624	0.49896
C449	0.10510	0.33694	0.71100	**N472**	0.24948	0.33555	0.31434
C450	0.12598	0.33814	0.68537	**C473**	0.23291	0.32326	0.16221
C451	0.12899	0.32703	0.50127	**O474**	0.07720	0.30395	0.23203
C452	0.11222	0.31491	0.34390	**O475**	0.10243	0.34648	0.87220
C453	0.09169	0.31433	0.37089	**O476**	0.23554	0.31386	0.00531
C454	0.11517	0.30368	0.16222	**O477**	0.26135	0.35719	0.63189
C455	0.13471	0.30461	0.13481				
C456	0.15179	0.31683	0.28798				
C457	0.14892	0.32814	0.47343				
C458	0.16587	0.34063	0.63013				
C459	0.16250	0.35162	0.81271				
C460	0.14280	0.35039	0.84014				
C461	0.18578	0.34198	0.59987				
C462	0.18868	0.33076	0.41363				
C463	0.17168	0.31813	0.25818				
C464	0.17502	0.30719	0.07486				
C465	0.19483	0.30876	0.04403				

PDI-MOF-74(Mg)

R_{wp} = 3.23%, R_p = 2.29%

P*1* (1) - triclinic
a = 72.6294, b = 74.5613, c = 5.5891 Å
α = β = 90°, γ = 120°

PDI-MOF-74(Ni)

R_{wp} = 3.96%, R_p = 2.75%

P*1* (1) - triclinic
a = 72.2829, b = 75.6727, c = 5.5574 Å
α = β = 90°, γ = 120°

5.6.3.2 Images of the simulated model structure of PDI-MOF-74(M)

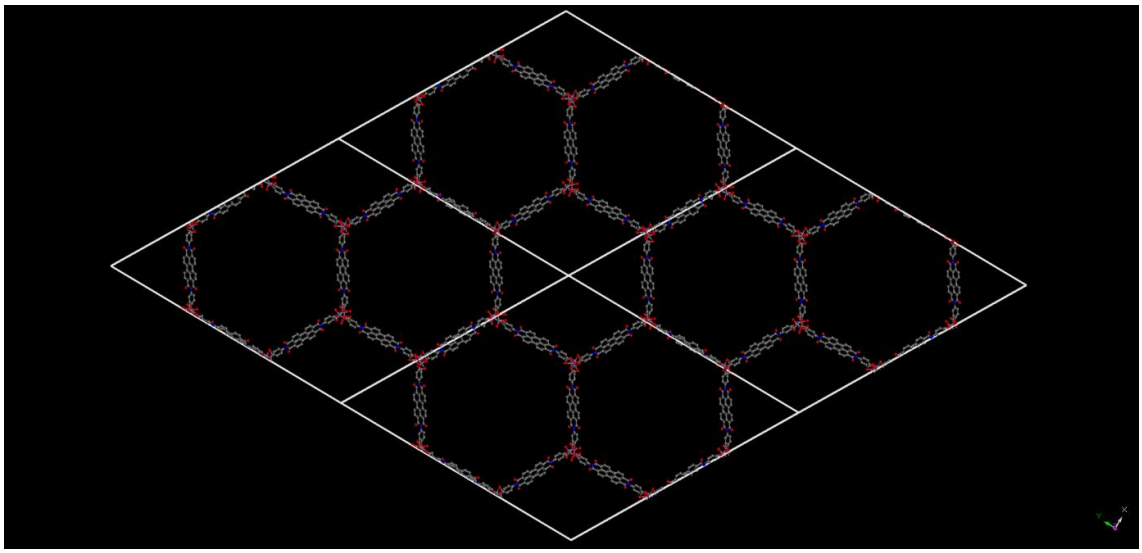

Figure 5-7: Simulated model structure of the PDI-MOF-74(M), in the triclinic space group, with view along the crystallographic *c*-direction of the lattice.

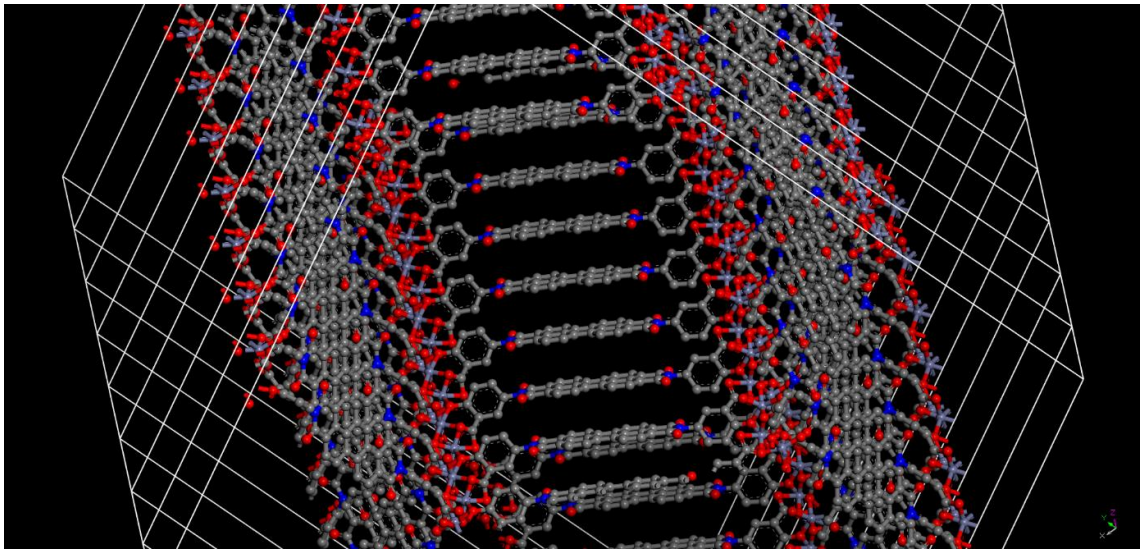

Figure 5-8: Simulated model structure of the PDI-MOF-74(M), in the triclinic space group, with perspective view along the channels of the structure, visible with the stacked PDI cores in *c*-direction.

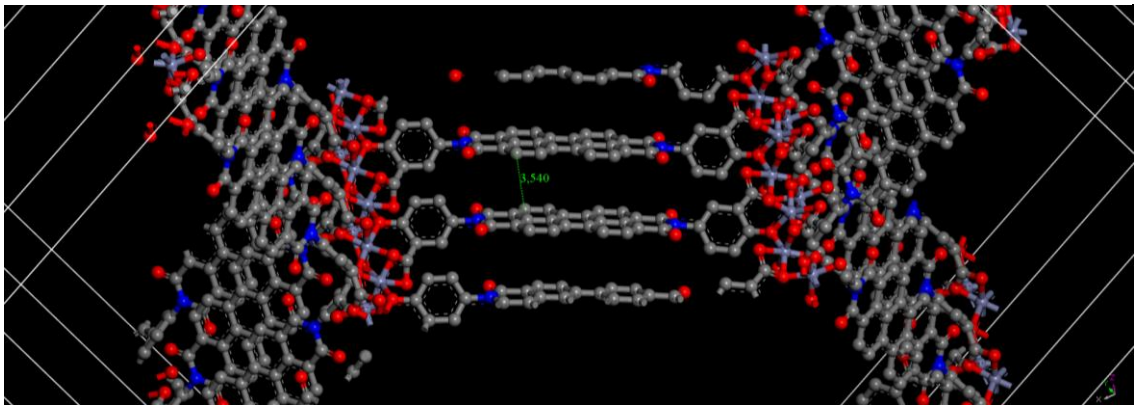

Figure 5-9: The interatomic distance between stacked PDI cores in PDI-MOF-74(Zn, Mg) in *c*-direction was measured to be 3.5 Å.

5.6.3.3 Powder X-ray Diffraction

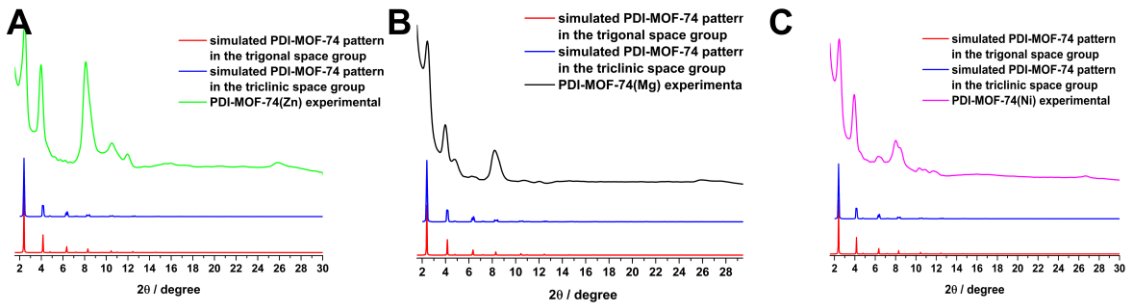

Figure 5-10: PXRD patterns of the PDI-MOF-74(M) bulk materials with (A) the Zn MOF, (B) Mg MOF and (C) the Ni MOF. The simulated PXRD pattern of the MOF in the trigonal space group is added in red and the simulated PXRD pattern of the MOF in the triclinic space group, with which the experimental PXRD patterns were refined, is added in blue.

5.6.3.4 Transmission electron microscopy

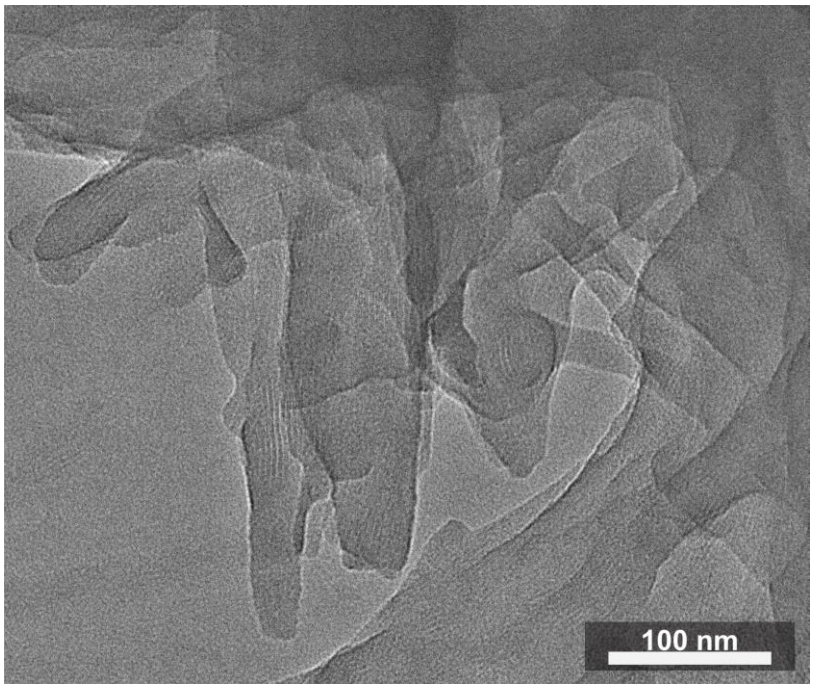

Figure 5-11: TEM image of the PDI-MOF-74(Mg) bulk material.

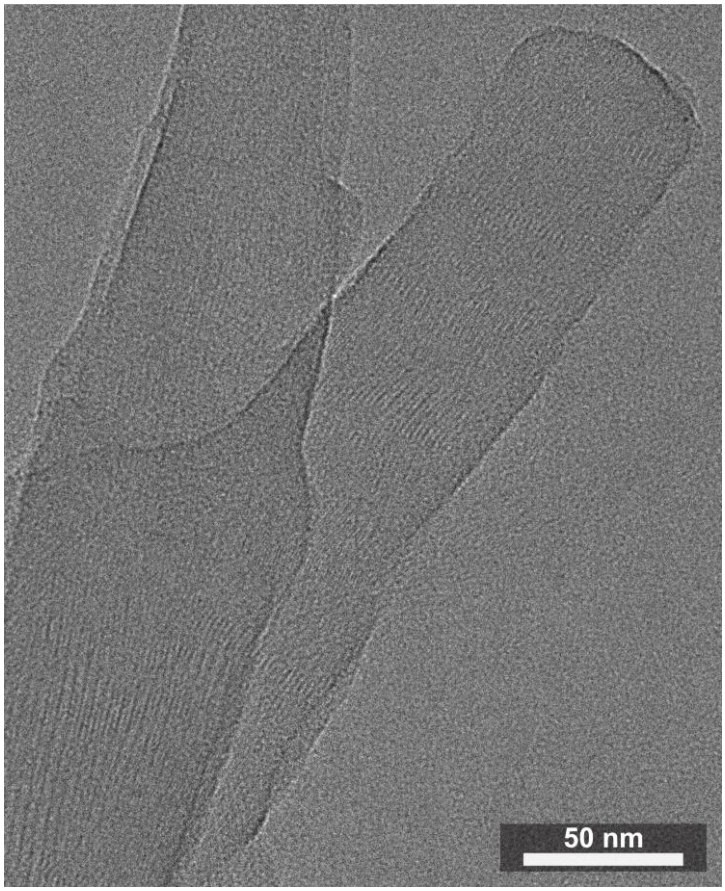

Figure 5-12: TEM image of PDI-MOF-74(Mg) crystallites in side view.

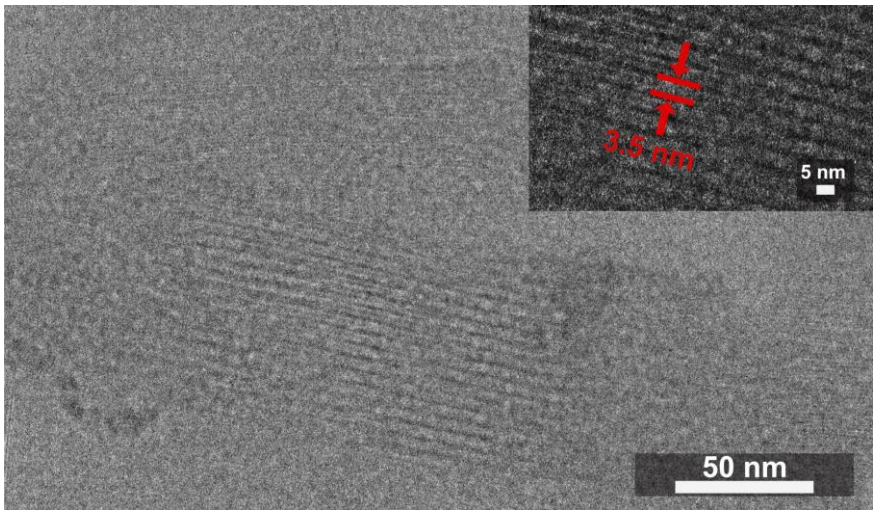

Figure 5-13: High resolution TEM image of PDI-MOF-74(Zn) in side view, showing a close-up of the lattice planes as inset.

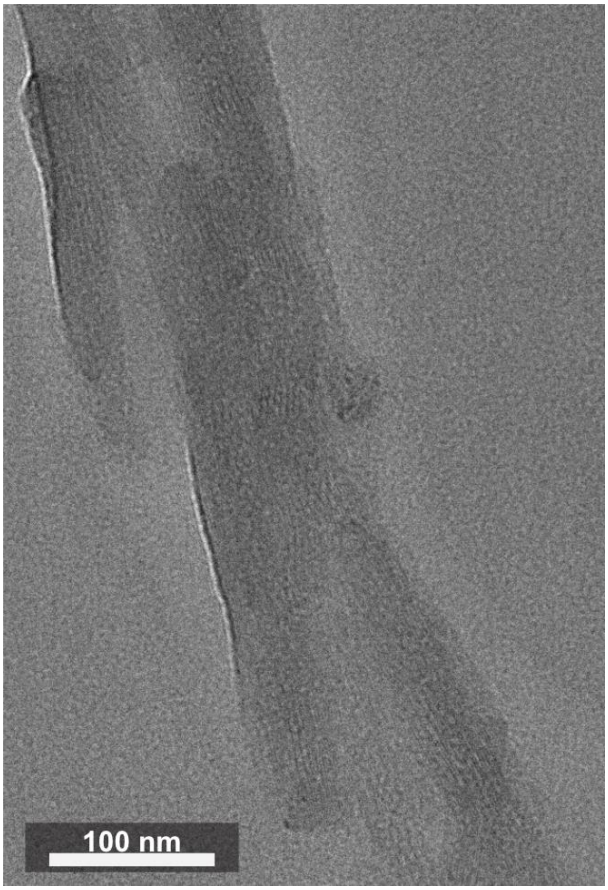

Figure 5-14: TEM image of PDI-MOF-74(Zn) in side view.

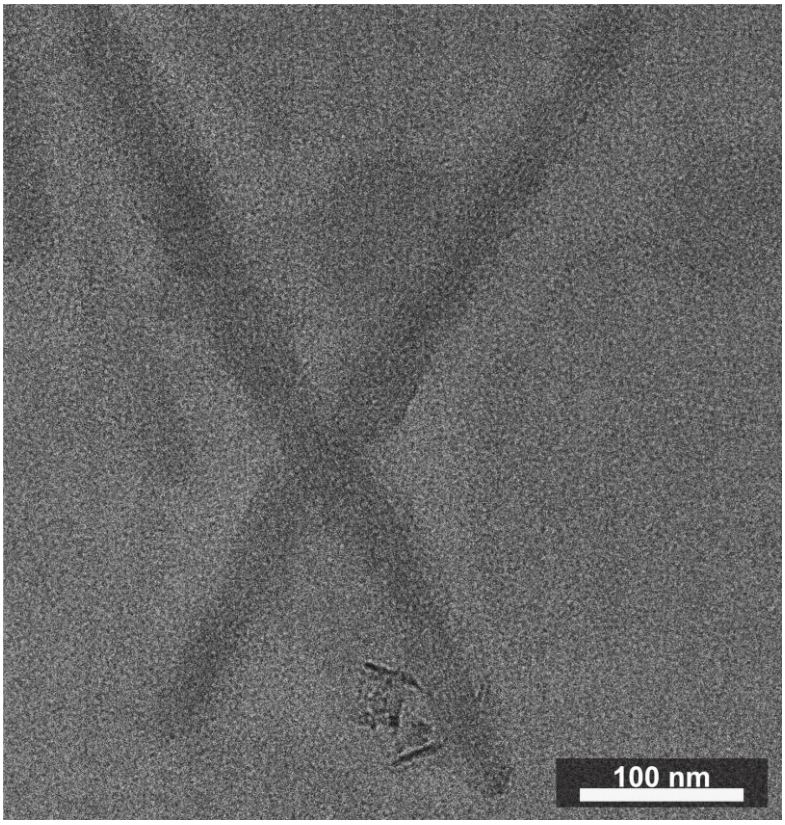

Figure 5-15: TEM image of PDI-MOF-74(Zn) in side view.

5.6.3.5 Scanning electron microscopy

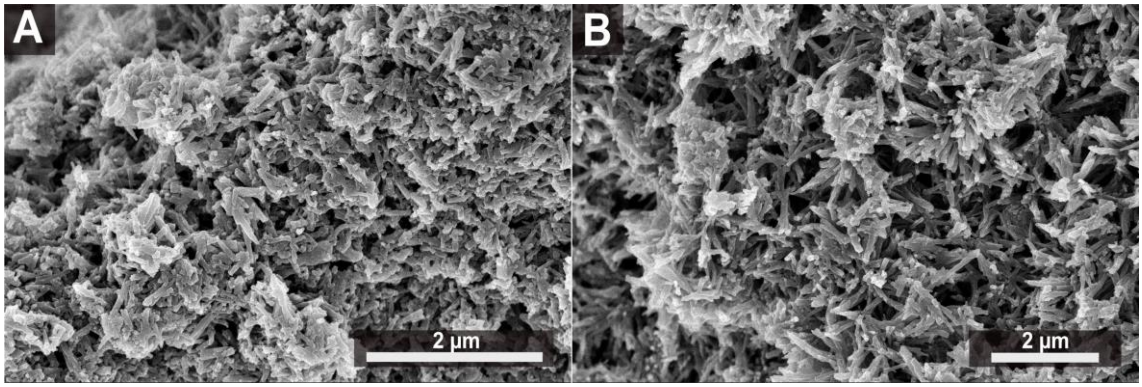

Figure 5-16: SEM images of the PDI-MOF-74(Mg) bulk material at different magnifications (A, B).

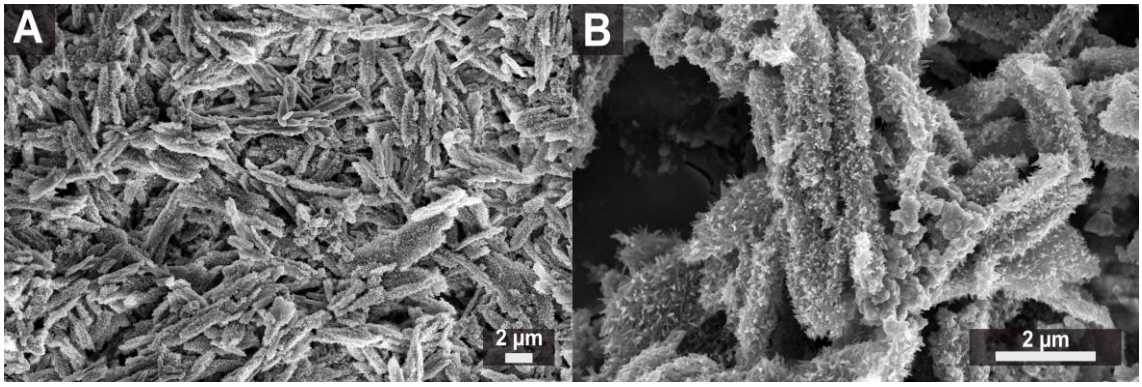

Figure 5-17: SEM images of the PDI-MOF-74(Ni) bulk material at different magnifications (A, B).

5.6.3.6 Energy dispersive X-ray (EDX) spectra of PDI-MOF-74(M)

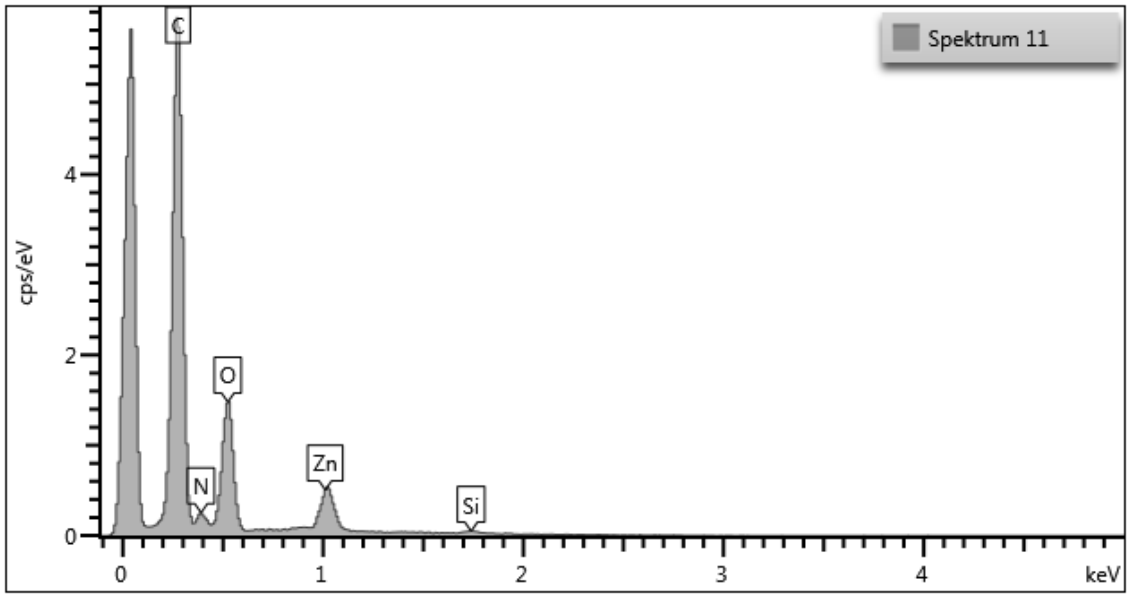

Figure 5-18: EDX analysis of PDI-MOF-74(Zn) confirming the presence of only the elements C, N, O, Zn.

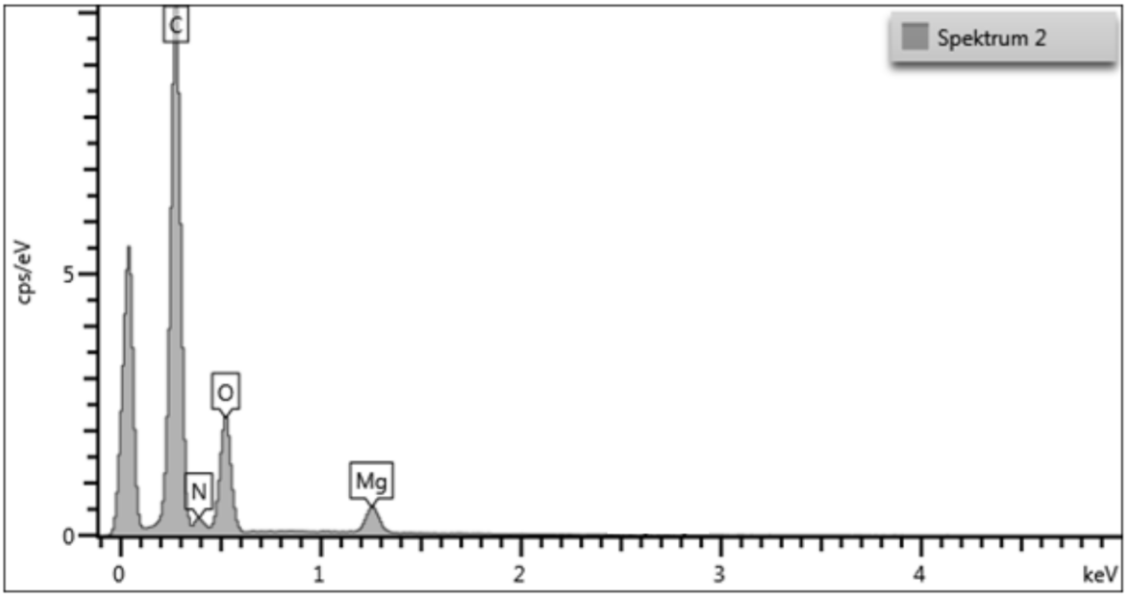

Figure 5-19: EDX analysis of PDI-MOF-74(Mg) confirming only the presence of the elements C, N, O, Mg.

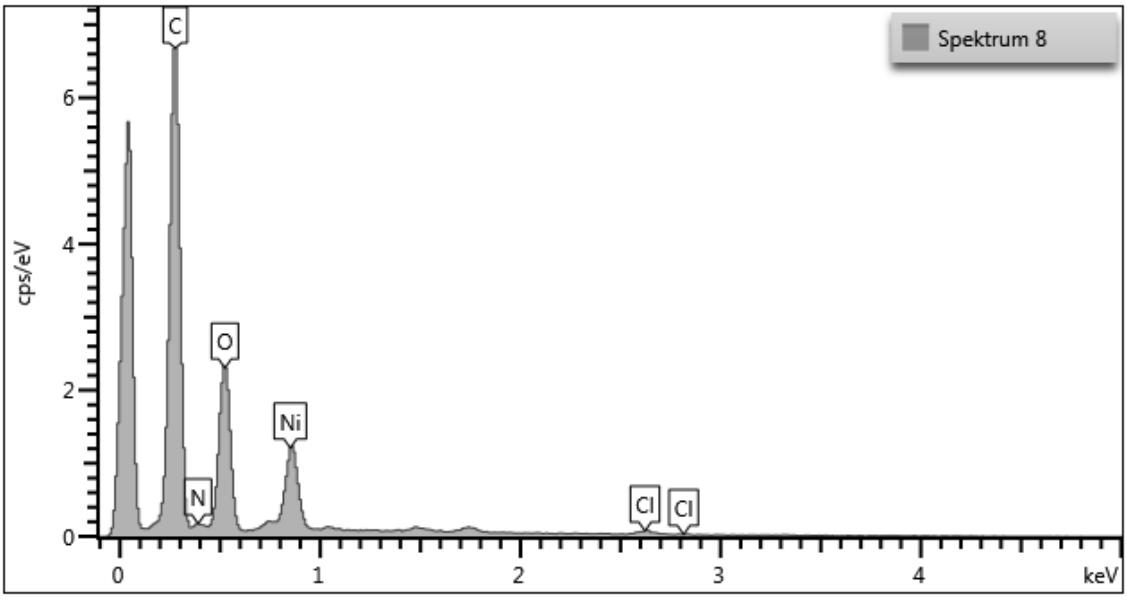

Figure 5-20: EDX analysis of PDI-MOF-74(Ni) confirming the presence of C, N, O, Ni and a small impurity of the $NiCl_2$ precursor.

5.6.3.7 Thermogravimetric analysis

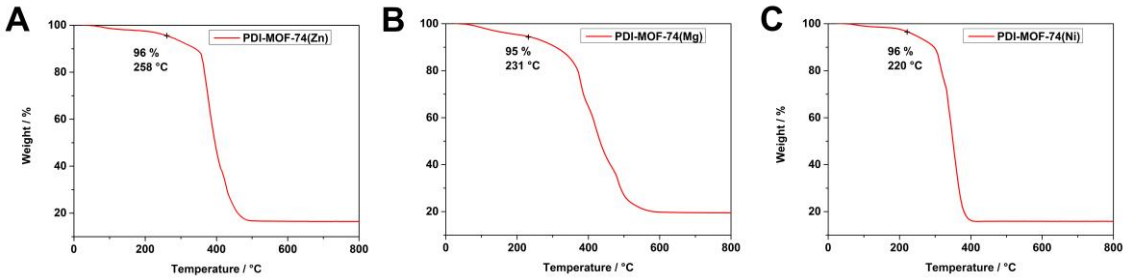

Figure 5-21: Thermogravimetric analysis (TGA) of (A) PDI-MOF-74(Zn), (B) PDI-MOF-74(Mg) and (C) PDI-MOF-74(Ni), measured as bulk material (20 mg each).

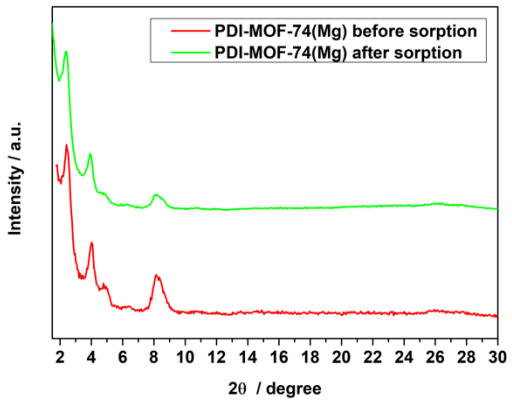

Figure 5-22: PXRD pattern of pelletized PDI-MOF-74(M) bulk material.

5.6.3.8 Nitrogen sorption analysis

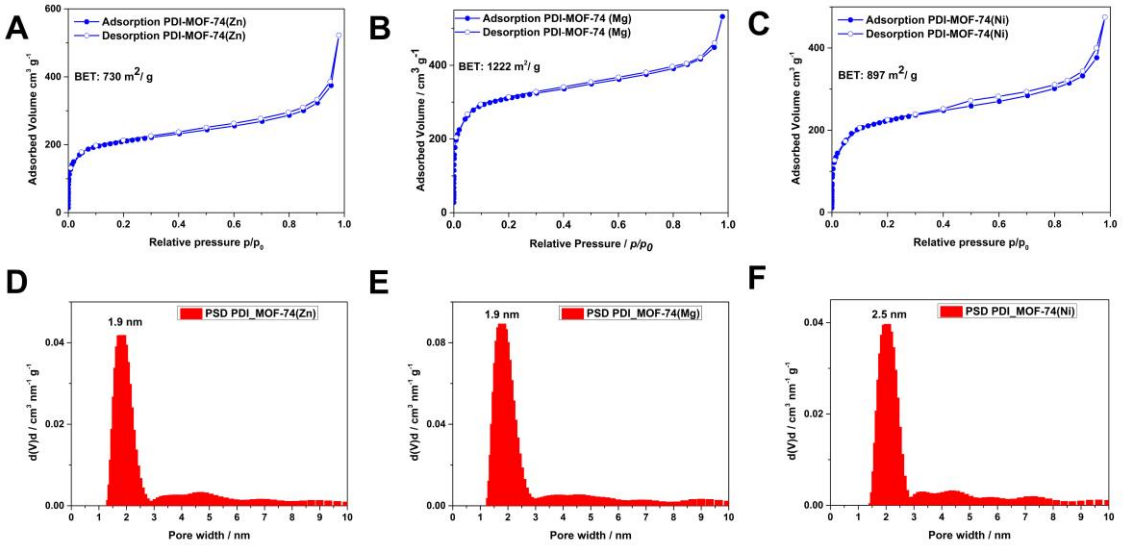

Figure 5-23: Nitrogen physisorption isotherms of (A) PDI-MOF-74 (Zn), (B) PDI-MOF-74 (Mg) and (C) PDI-MOF-74(Ni). The adsorption branches are depicted as blue coloured circles and the desorption branches as white coloured circles. Pore size distributions (PSD) are shown in D-F.

5.6.3.9 Infrared spectroscopy

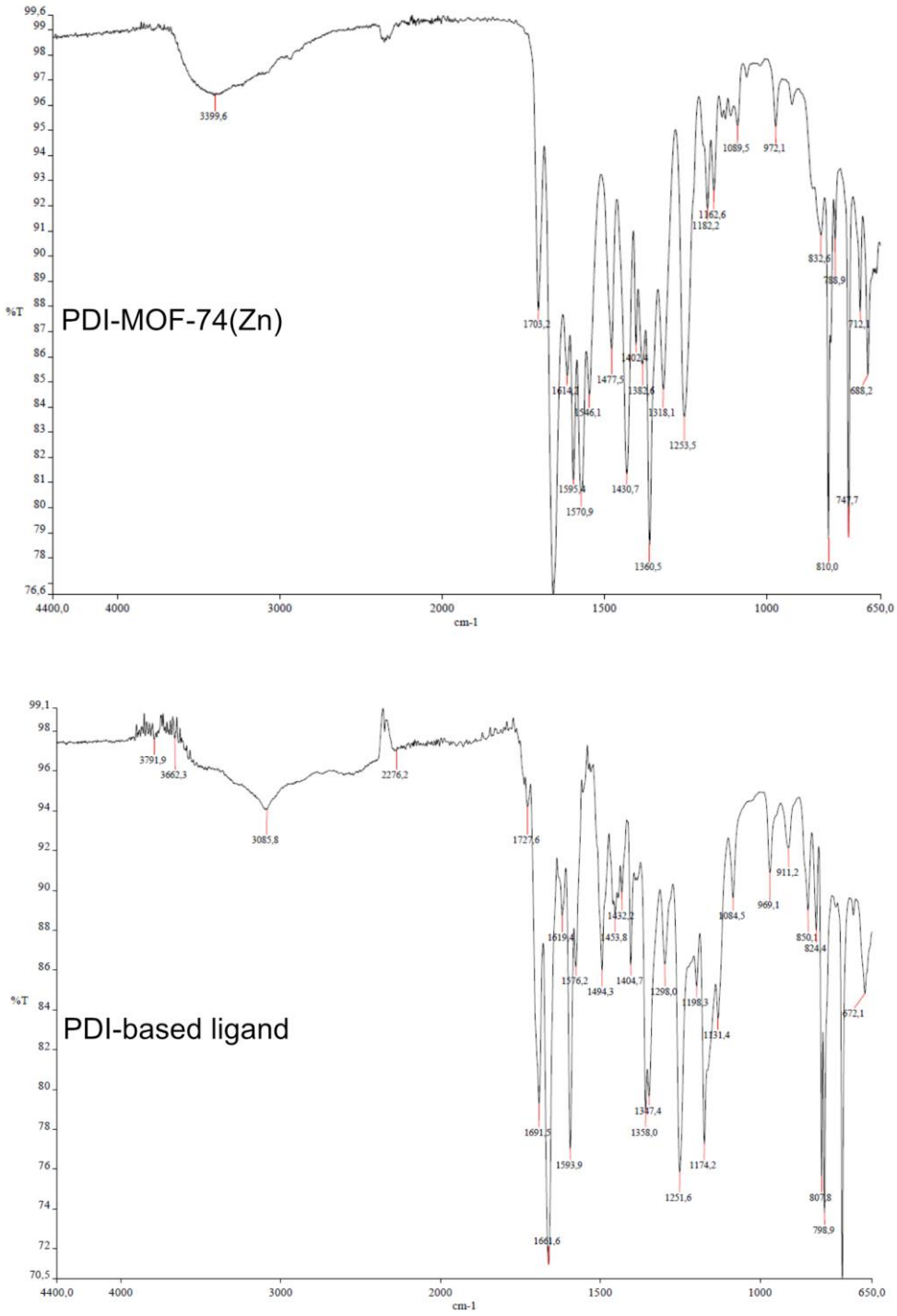

Figure 5-24: Infrared spectra of PDI-MOF-74(Zn) (top) and of the PDI-based ligand (bottom). The signal at 3399 cm^{-1} (top) indicates the presence of water and the signal at 1703 cm^{-1} the presence of DMF in the PDI-MOF-74 sample.

5.6.3.10 Electrical conductivity measurements

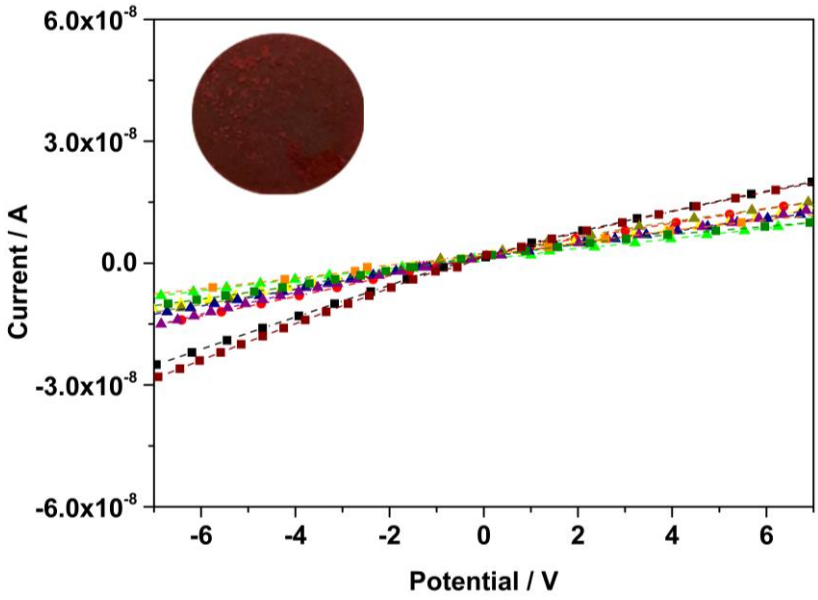

Figure 5-25: *I-V* curves of pelletized PDI-MOF-74(Ni, Zn, Mg) samples measured *via* two-point-probe showing an ohmic resistance. The curves were fitted by a linear regresssion and the slope of the linear fit curves yielded electrical conductivity values for PDI-MOF-74(Ni, Zn, Mg), respectively (see table S 1). A photo image of a PDI-MOF-74(Zn) pellet is shown as inset.

Table 5-1: Electrical conductivity values of 2-point probe *I-V* measurements of pressed pellets (see Figure 5-25).

MOF	**Pellet**	**Electrical conductivity (S cm^{-1})**
PDI-MOF-74(Zn)	1	2.8 x 10^{-7}
PDI-MOF-74(Zn)	2	2.8 x 10^{-7}
PDI-MOF-74(Zn)	3	3.1 x 10^{-7}
PDI-MOF-74(Zn)	4	3.4 x 10^{-7}
PDI-MOF-74(Mg)	1	2.0 x 10^{-7}
PDI-MOF-74(Mg)	2	2.1 x 10^{-7}
PDI-MOF-74(Mg)	3	2.3 x 10^{-7}
PDI-MOF-74(Ni)	1	5.1 x 10^{-7}
PDI-MOF-74(Ni)	2	5.4 x 10^{-7}
PDI-MOF-74(Ni)	3	3.2 x 10^{-7}

5.6.3.11 MOF pellets

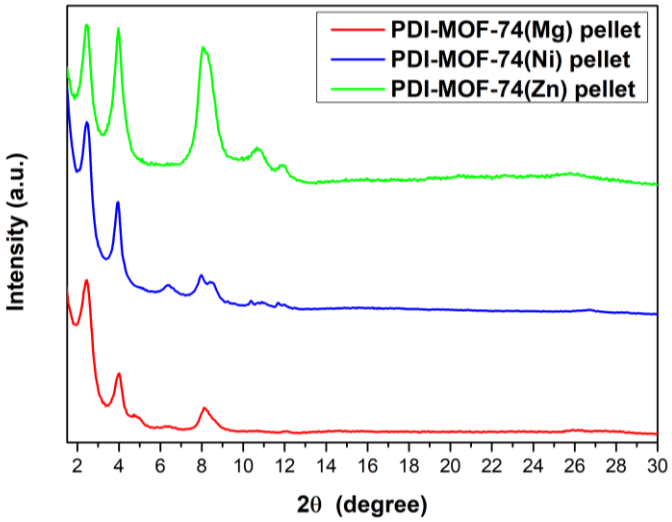

Figure 5-26: PXRD pattern of pelletized PDI-MOF-74(M) bulk material.

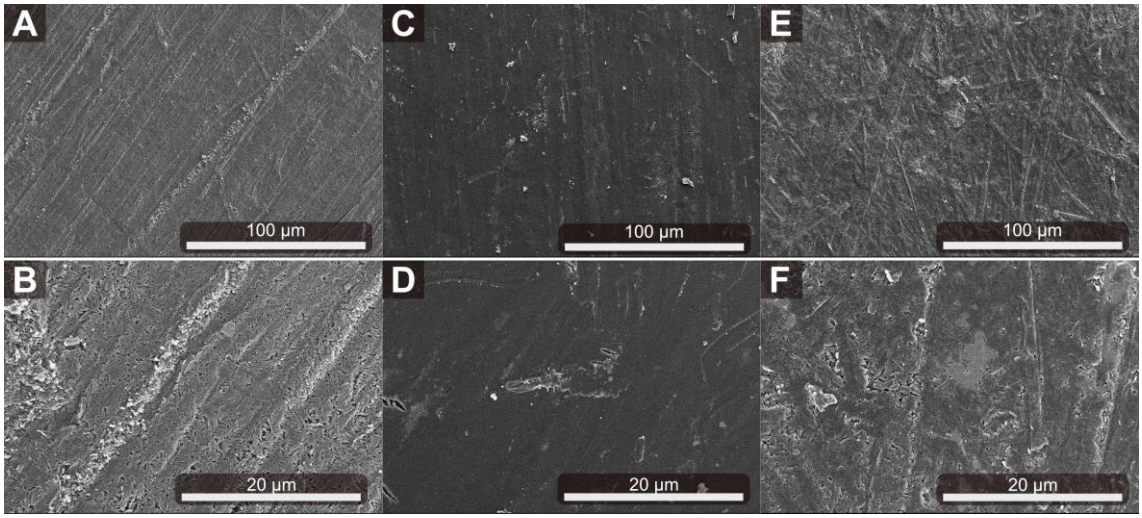

Figure 5-27: SEM images of pelletized PDI-MOF-74 (M), (A, B) –Zn, (C, D) –Mg, (E, F), –Ni.

5.6.3.12 UV-Vis spectroscopy and photoluminescence

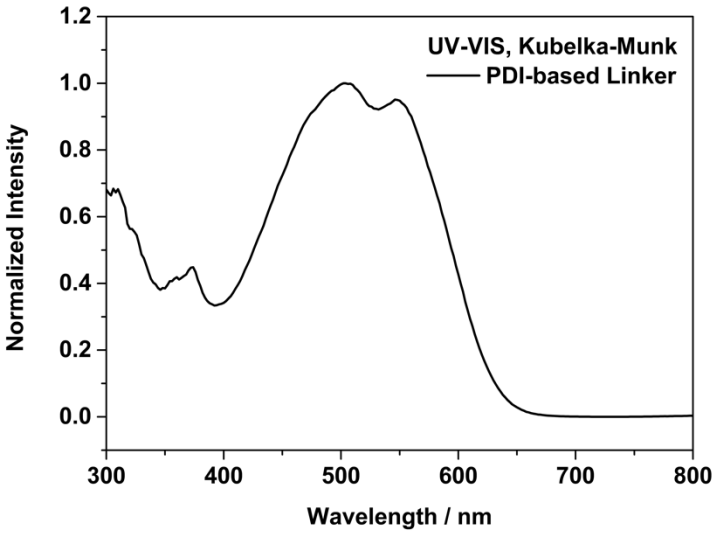

Figure 5-28: UV-Vis absorption measured in diffuse reflectance of the PDI-based ligand as powder dispersed with $BaSO_4$.

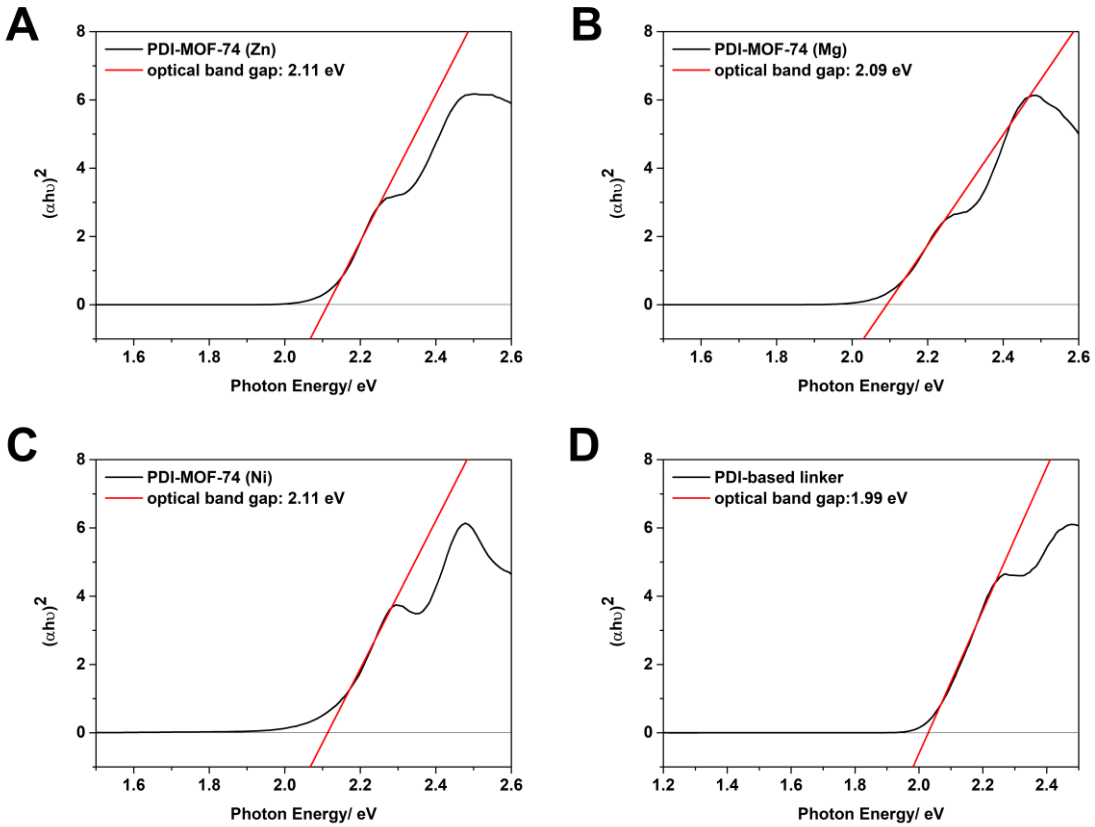

Figure 5-29: Tauc plots of (A) PDI-MOF-74(Zn), (B) PDI-MOF-74(Mg), (C) PDI-MOF-74(Ni) and (D) of the PDI based ligand, suggesting the presence of direct band gaps.

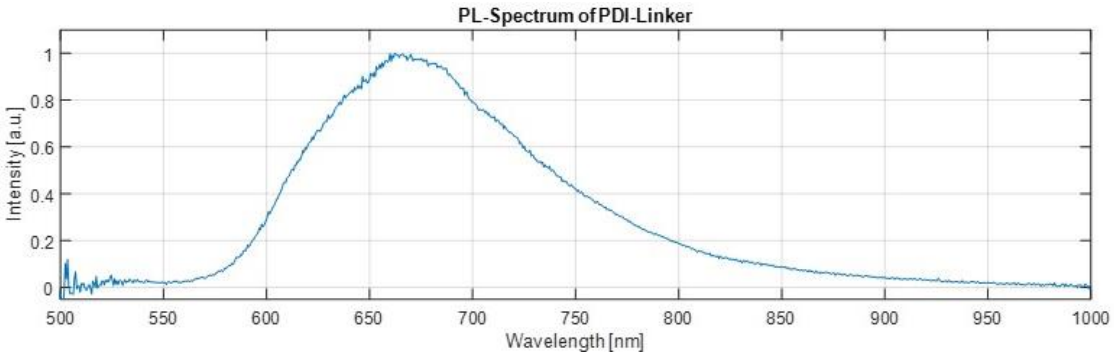

Figure 5-30: Photoluminescence of the PDI-based ligand as bulk material with 476 nm excitation.

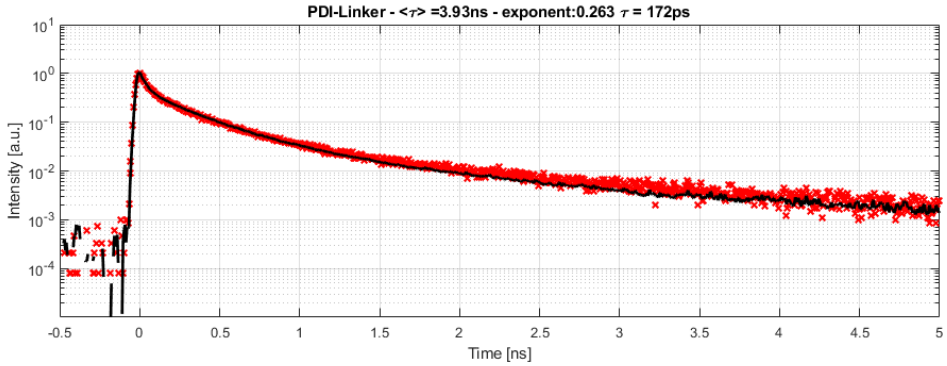

Figure 5-31: Time-correlated single photon counting (TCSPC) trace of the PL spectrum of the PDI based ligand.

5.6.3.13 Cyclic voltammetry

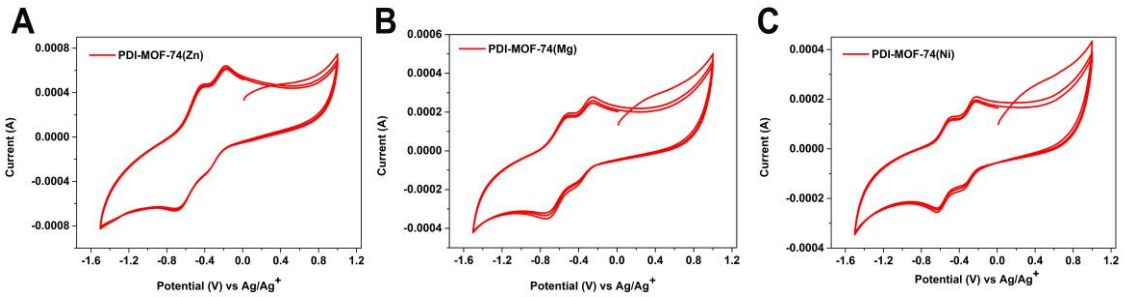

Figure 5-32: Voltammograms with three cycles of the PDI-MOF-74(M) series as bulk material, pressed in a stainless stell mesh, showing (A) Zn MOF, (B) Mg MOF and (C) Ni MOF, respectively. It was measured in a solution of 0.1 M tetrabutylammonium hexafluorophosphate ($TBAPF_6$) in DMF versus Ag/Ag^+ (in V) with scan rate 0.1 V/ s under argon atmosphere.

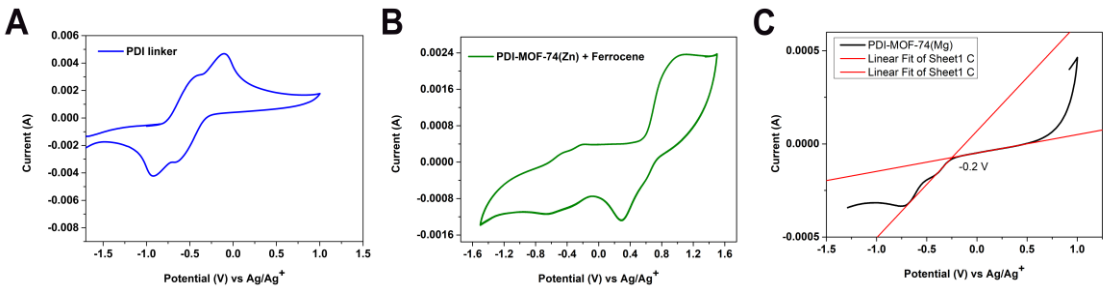

Figure 5-33: (A) Cyclic voltammogram of the PDI-based ligand. (B) Voltammogram of PDI-MOF-74(Zn) with the addition of ferrocene. (C) Linear Fit of the voltammogram of PDI-MOF-74(Mg) for the determination of the reduction onset.

Table 5-2: Positions of the reduction onsets in V, the HOMO/LUMO level and of the optical band gap of the PDI-MOF-74(M) series and of the PDI based ligand.

MOF	E_{red1}^{onset} (V)	HOMO (eV)	LUMO (eV)	Optical Eg (eV)
PDI-MOF-74(Zn)	-0.2	-6.1	-4.0	2.1
PDI-MOF-74(Mg)	-0.2	-6.1	-4.0	2.1
PDI-MOF-74(Ni)	-0.2	-6.1	-4.0	2.1
PDI Linker	-0.3	-5.9	-3.9	2.0

Calculated from: $E_{LUMO} = -(E_{red1}^{onset} + 4.8 - E_{Fc/Fc+})$, $E_{HOMO} = E_{LUMO} - E_g$

5.6.3.14 PDI-MOF-74(Zn) films

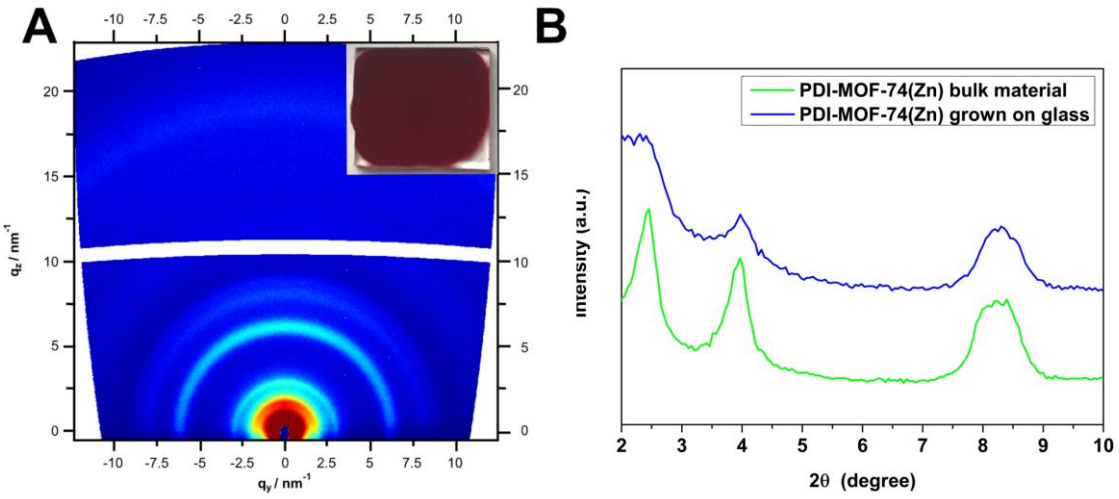

Figure 5-34: (A) Grazing-incidence small-angle X-ray scattering (GISAXS) data of PDI-MOF-74(Zn) films grown on glass *via* vapor-assisted conversion (VAC). A photo image of the PDI-MOF-74(Zn) films is shown as inset. (B) XRD data of the PDI-MOF-74(Zn) sample as bulk material and grown on glass.

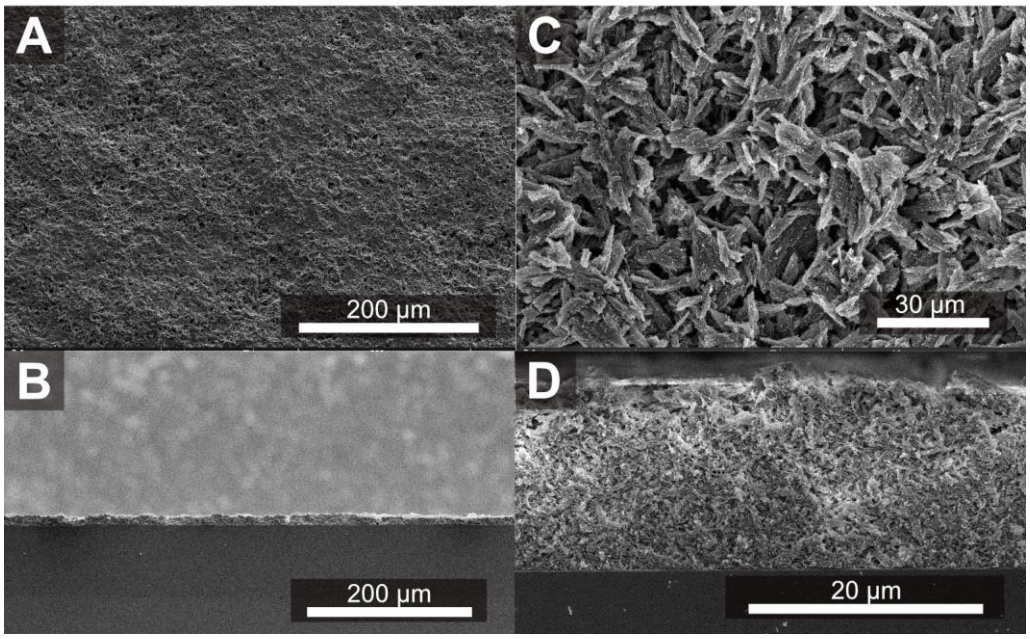

Figure 5-35: SEM images of the PDI-MOF-74(Zn) film grown on glass *via* VAC in top view (A, C) and side view (B, D), showing a film thickness of around 17 µm.

6 MOF-74 film synthesis

This chapter is based on the following publication:

MOF-74(M) films obtained through vapor-assisted conversion – impact on crystal orientation and optical properties

Patricia I. Scheurle[a, b], Andre Mähringer[a, b], Alexander Biewald[a, b], Achim Hartschuh[a, b], Thomas Bein[*,a, b] and Dana D. Medina[*,a, b]

[a]Department of Chemistry, Ludwig-Maximilians-Universität (LMU), Butenandtstr. 5-13 (E), 81377 Munich, Germany.

[b]Center for NanoScience (CeNS), Schellingstr. 4, 80799 Munich, Germany.

[*]Corresponding Author

6.1 Abstract

In recent years, metal-organic frameworks (MOFs) with the structure MOF-74 have attracted much interest owing to their tunable pore aperture, high surface area and electrical conductivity. The synthesis of well-defined, highly crystalline thin films of MOF-74 is of paramount importance for their implementation into device-based applications such as in chemical sensing, optoelectronics, gas storage and separations. Here, we present the synthesis of highly crystalline MOF-74(M = Zn^{2+}, Mg^{2+}, Ni^{2+}, Co^{2+}) films by vapor-assisted conversion (VAC). MOF-74(M) thin films were grown on bare glass, quartz, gold and silicon surfaces, featuring high crystallinity, crystal orientation, and average thicknesses of 500 nm. By including a benzoic acid modulator, oriented MOF-74(Zn) films, with the crystallographic *c*-axis of the MOF crystallites oriented horizontally to the surface, were obtained on all substrates. In addition, highly crystalline MOF-74(Mg) was grown on glass and gold substrates with the crystallographic *c*-axis aligned orthogonally to the surface. Moreover, randomly oriented highly crystalline MOF-74(Co) and MOF-74(Ni) films were synthesized on glass, quartz, gold and silicon. The pore accessibility of the obtained films was examined by means of krypton sorption measurements, revealing permanent and accessible porosity, reaching a BET surface area of 975 cm^2/cm^2 for MOF-74(Mg). Steady-state and time-resolved photoluminescence studies show emission in the blue spectral region of MOF-74(Zn, Mg) on quartz with a biexponential decay. In addition, confocal photoluminescence mapping confirmed a homogeneous MOF film surface with a similar emission profile over the whole examined area of 70 μm x 70 μm.

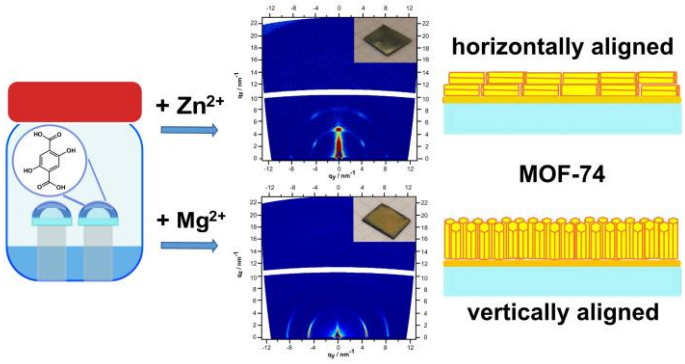

6.2 Introduction

Metal-organic frameworks (MOFs) are highly crystalline and porous materials formed by the attachment of organic linkers to metal-containing sub building units.[2] Their crystalline nature is reflected in the formation of well-defined cavities with atomically precise positioning of chemical groups.[23,32–34] The pore size and chemical environment can be tailored towards a defined functionality by the choice of the building blocks and their connectivity.[27,33,35] Based on these design principles, MOFs are being studied for numerous applications requiring defined host-guest interactions such as gas storage or separations, catalysis and drug delivery.[26,28,36–44]

The porous and crystalline materials based on the MOF-74 structure have attracted great attention, attributed to the MOF-74 robust and defined architecture[45], high surface area, adjustable pore apertures ranging from 1.4 to 9.8 nm and the capability of selectively adsorbing CO_2 with high capacity[36,41,46,47]. The MOF-74 series consists of 2,5-dihydroxyterephthalic acid ligands and divalent metal ions (M=Zn, Mg, Ni, Co, Mn, Fe, and Cu) forming a honeycomb-like structure of infinite metal-oxo (-M-O-) columns, which can also serve as a path for charge carrier transport.[16,33,48]

For the development of device-type technologies based on MOFs, their synthesis as thin and homogeneous films on various substrate types is of paramount importance.[16,19,49,50] Controlled MOF film growth, yielding a continuous film with a tunable morphology, thickness and crystallite orientation enables the fabrication of defined architectures corresponding with the desired functionality, charge transport between electrodes and/or host-guest interactions.[22,24,5] The on-surface-growth of vertically aligned MOF-74 crystallites is especially interesting, enabling an optimal architecture for guest molecules penetrating into the pores. Furthermore, the synthesis of MOF-74(M) on transparent substrates such as quartz and glass permits detailed optical characterization, which in turn allows for the design of novel functionalities including gas sensing.[19,5]

To date, there are only a limited number of reports describing the on-surface synthesis of MOF-74(M) films (see Table 6-1).[51–61] Important challenges include developing synthesis approaches that can be applied to different metal ion precursors, as well as growth on different nonmodified substrates such as glass, quartz, silicon and gold. Furthermore, controlling the film thickness and crystal orientation are additional key aspects in the synthesis of MOF-74 thin films that have not been addressed yet.

Recently, we have introduced the direct, on-surface vapor-assisted conversion (VAC) for the synthesis of thin films of molecular framework materials. In VAC, a deposited precursor solution layer is exposed to a vapor source in a closed vessel at a suitable temperature, thereby enabling

controlled precursor reactions resulting in thin films and coatings at high yields (see Figure S6-7Figure 6-1). So far, the synthesis of porphyrin-based MOFs, MIL-53, as well as highly oriented boronate-ester covalent organic frameworks, zirconium-based cubic MOFs such as UiOs and a PIZOF and layered anisotropic MOF structures such as M-CAT-1 thin films have been reported, establishing VAC as a powerful synthesis approach for thin films of a variety of framework materials.[30,62–66] The feasibility of varying many synthesis parameters and conditions such as solvents, potential modulators, temperature and substrates makes VAC a particularly flexible and attractive thin film deposition method.

Here, we present the direct on-surface synthesis of highly crystalline and porous MOF-74 (M = Zn, Mg, Ni, and Co) thin films on various surfaces including glass, quartz, gold and silicon. We studied the growth of MOF-74(M) thin films with particular attention to the crystal orientation on different substrates. The successfully synthesized MOF-74(M) thin films show an average thickness of 500 nm. Furthermore, the MOF-74(M) films feature varied rodlike morphologies with different degrees of surface coverage, ranging from dense in case of MOF-74(Zn and Ni) to loosely packed films in case of MOF-74(Mg and Co). The resulting MOF-74 crystallite orientations were identified by 2D grazing-incidence wide-angle X-ray scattering (2D GIWAXS) analysis. Furthermore, MOF-74(Zn) thin films were also obtained by the conversion of an atomic layer deposition (ALD)-deposited thin ZnO layer, serving as the metal precursor in the crystallization process on a glass substrate. Krypton sorption was employed to determine the pore accessibility of the synthesized MOF-74(M) films, with surface areas reaching 975 cm^2/cm^2. Water contact angle measurements demonstrate a hydrophilic surface of all MOF-74(M) films. Atomic force microscopy (AFM) measurements afforded the surface topography of the films, with MOF-74(Zn) films exhibiting the smallest Root Mean Square (RMS) roughness of 5 nm. Moreover, the photophysical properties of MOF-74(M) thin films grown on quartz substrates were investigated by means of UV-Vis and photoluminescence (PL) spectroscopy and imaging, showing a homogeneous blue emission over the whole examined film area.

6.3 Experimental section

Thin film syntheses of MOF-74(M = Zn, Mg, Ni, and Co), were carried out by employing a VAC procedure. The ligand, 2,5-dihydroxyterephthalic acid (DOT), the respective metal ion precursors, and in some cases the modulator benzoic acid were dissolved in different DMF/ EtOH/ H_2O solvent mixtures, providing the precursor solution. For the conversion of a precursor ZnO film, DOT was dissolved in a mixture of THF and H_2O (1:1 *v/v*). In the next step, a solvent mixture of DMF/ EtOH/ H_2O, providing the vapor source, was filled in a glass vessel and a substrate (gold, glass, quartz, silicon, or a 70 nm ZnO seed layer deposited by ALD; 1 cm x 1.2 cm) was placed

on an elevated glass platform above the vapor source. Subsequently, 50 -100 μL of the precursor solution was equally spread on the respective substrate. After sealing, the reaction vessel was placed into a preheated oven at 100 °C for 18 h. Afterwards, the vessel was removed from the oven and allowed to cool down to room temperature. The substrates were taken out of the vessel and dried under reduced pressure, revealing a yellowish film on top of the substrate (see Figure 6-1, for details see the Supporting Information).

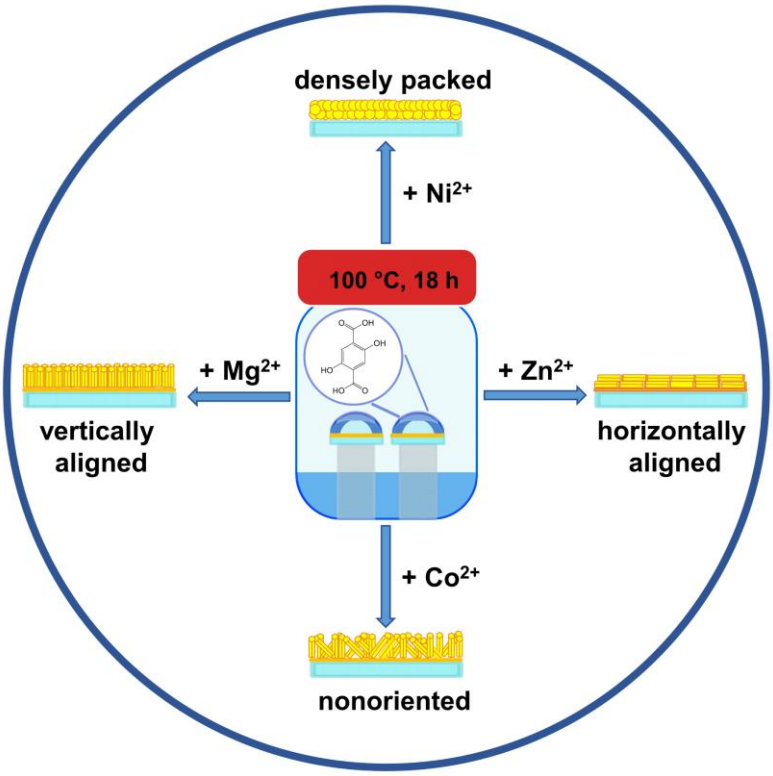

Figure 6-1: Scheme of the VAC reaction vessel in which the substrates are placed on top of the glass spacers above the solvent bath. The precursor solution, containing metal ions, the organic linker acid (DOT) and a modulator, is deposited onto the substrates. Keeping the closed vessel at elevated temperature for a suitable reaction time yields a MOF-74(M) thin film on the selected substrate. MOF-74(Zn) crystallizes with the crystallographic *c*-axis preferentially horizontally aligned with respect to the substrate, whereas MOF-74(Mg) crystallites are preferentially vertically aligned to the substrate. MOF-74(Ni and Co) films are formed without preferential orientation.

6.4 Results and discussion

6.4.1 Highly crystalline and oriented MOF-74(Zn) films

X-ray diffraction (XRD) analysis of the obtained coated substrates revealed the successful synthesis of a highly crystalline MOF-74(Zn) film on gold, glass, and silicon, where the obtained diffraction patterns are in excellent agreement with the PXRD pattern of the MOF-74(Zn) bulk material regarding reflection positions (Figure 6-8). However, the diffraction patterns of the MOF-74(Zn) films show different reflection intensity ratios attributed to the crystal planes, namely, (110) and (300), compared to the bulk material (Figure 6-8). Such a change in the reflection intensity ratios indicates a degree of ordering of crystals in the film compared to randomly distributed crystals in a bulk sample. To further study the degree of MOF crystallite orientation across the substrate, we performed 2D GIWAXS of the MOF-74(Zn) films. The patterns were indexed by using the software GIXSGUI[67]. The MOF-74 space group, *R*-3, was detected as the only symmetry for all MOF-74(Zn) films, with the 110 set of planes being preferentially oriented normal to the substrate. The intensity maxima of the reflections in the diffraction pattern are marked with circles and indexed (Figure 6-2). The displayed reflection at out-of-plane direction at q_y = 0 nm^{-1}, q_z = 4.8 nm^{-1} corresponds to the (110) plane. This reflection is distinct in the GIWAXS patterns of all three MOF-74(Zn) films, with the highest intensity detected for films grown a gold substrate. The reflection at q_y = 4.2 nm^{-1}, q_z = 2.3 nm^{-1}, corresponds to the (-120) / (2-10)

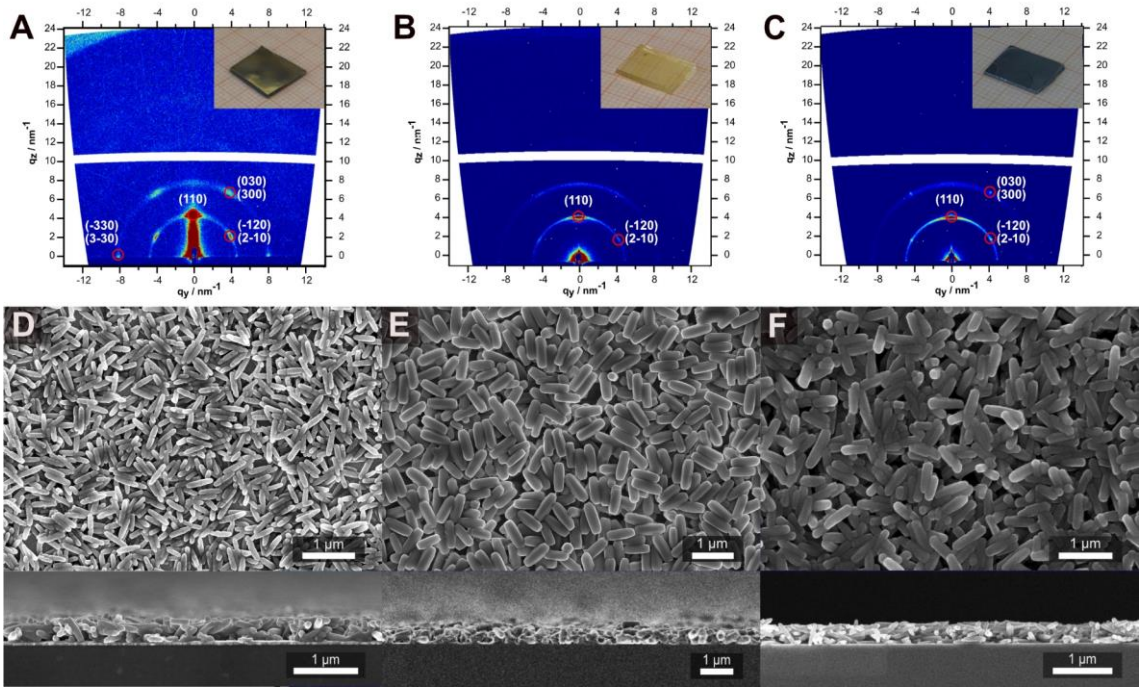

Figure 6-2: 2D GIWAXS patterns of MOF-74(Zn) thin films obtained by VAC, grown on (A) gold, (B) glass and (C) silicon (Miller indices are given in white). Macroscopic images of the samples are shown as insets. SEM top-view and cross-section (bottom) images of MOF-74(Zn) thin films grown on (D) gold, (E) glass, and (F) silicon.

plane, which is distinct in the GIWAXS patterns of the MOF-74(Zn) films, especially on gold and silicon. The reflection at q_y = 4.1 nm^{-1}, q_z = 7.1 nm^{-1} refers to the (030) / (300) plane and that at q_y = 8.3 nm^{-1}, q_z = 0 nm^{-1} to the (-330) / (3-30) plane, with the highest intensity in the GIWAXS patterns of the MOF-74(Zn) films on a gold substrate. The separated, distinct reflections in the GIWAXS patterns confirm the preferred crystallite orientation of the MOF crystals on the substrates, where the *c*-axis is aligned horizontally to the substrate, with the highest degree of order observed for the MOF-74(Zn) film on a gold substrate (see Figure 6-2 A-C).

Top-view SEM images of the MOF-74(Zn) films on gold, glass and silicon reveal a homogeneous long-range surface coverage with densely packed MOF crystallites on the examined substrates (see Figure 6-2 D-F, Figure 6-9). The MOF-74(Zn) films comprise single, rod-shaped crystallites with an average width of 150 nm and a length of 700 nm. Notably, the MOF-74(Zn) crystallites on glass have a very narrow size distribution with a defined width of 200 nm and a length ranging between 650 nm and 700 nm, indicating well-controlled crystal growth under the employed VAC conditions. The rod-shaped crystallite morphology is in good agreement with the morphology of the MOF-74(Zn) bulk material synthesized in our lab (see Figure 6-10) and with reports in the literature.[23] Furthermore, the films are crack-free and appear smooth without any undesired deposits (see Figure 6-9). Notably, while the SEM top-view images indicate the presence of a few non-horizontally oriented crystals, the statistically relevant GIWAXS patterns strongly indicate the formation of a well-oriented film. To study the crystal distribution in the film in greater detail, we performed several GIWAXS measurements across the substrate, which indicate an oriented film at all positions and homogeneous MOF crystallite growth (Figure 6-11). Cross-section SEM analysis shows densely-packed, continuous MOF films with thicknesses ranging from 350 to 650 nm for the employed substrates. Furthermore, in all the examined films, the MOF crystallites are mostly oriented horizontally to the surface (Figure 6-2 D-F (bottom), Figure 6-11). The surface roughness of the oriented MOF-74(Zn) films was examined by AFM surface scans in a tapping mode on film areas of 5 µm x 5 µm (see Figure 6-12 to Figure 6-14). RMS roughnesses of 11 and 33 nm were obtained for MOF-74(Zn) films grown on gold and on glass or silicon, respectively, indicating a uniform surface topography. The water contact angle (WCA) evaluation of the MOF-74(Zn) thin films indicates hydrophilic surfaces (see Figure 6-15). In addition to molecular precursors, we also explored the use of an immobilizedsolid metal precursor for the synthesis of MOF-74(Zn) thin films. To this end, we used a 70 nm ZnO layer obtained by ALD on a glass substrate. For the MOF-74(Zn) thin film synthesis, a DOT precursor solution was spread over the ZnO-supported glass substrates and the synthesis was carried out under VAC conditions similar to those used for a metal-organic precursor solution (for more details see Supporting Information Table). The successful conversion of the ZnO layer was confirmed by XRD

analysis revealing prominent reflections assigned to the MOF-74 structure (see Figure 6-16). However, in comparison to the densely packed and horizontally oriented MOF-74(Zn) crystallites on gold, glass, and silicon using zinc precursor solution, with the ZnO precursor layer, tilted needle-like MOF crystallites grow on the surface, resulting in a highly textured and rough film (see Figure 6-17).

6.4.2 Highly crystalline and oriented MOF-74(Mg) films

Next, we turned our attention to the synthesis of MOF-74(Mg) films on gold, glass, and silicon using the same VAC procedure as for the synthesis of MOF-74(Zn) employing reactive precursor solutions. The formation of phase-pure and crystalline MOF-74(Mg) films on the employed substrates was confirmed by XRD analysis, providing XRD patterns in agreement with the diffraction pattern of the MOF-74(Mg) bulk material (see Figure 6-18 and Figure 6-19). In the case of MOF-74(Mg) film grown on glass, by employing a mixture of DMF and benzoic acid modulator, individual, rod-shaped MOF-74(Mg) crystallites about 170 nm wide and 800 nm long, preferentially oriented orthogonally to the surface, are visible in the SEM-cross section images (see Figure 6-3 and

Figure 6-20). Distinct reflections at q_y = 4.8 nm^{-1} and q_y = 8.4 nm^{-1} near q_z = 0 nm^{-1} in the 2D GIWAXS analysis corresponding to the (110) and (300) planes of MOF-74(Mg) also confirm the preferential orientation of the MOF crystallites with the *c*-axis oriented orthogonally to the surface (see Figure 6-3B). For the MOF-74(Mg) film grown on gold, employing a DMF/ EtOH solvent mixture leads to intergrown rod-shaped crystallites with a film thickness of about 350 nm (see Figure 6-21). In agreement with the observed film morphology, 2D GIWAXS analysis of the MOF-74(Mg) film grown on gold under these conditions suggests random crystallite orientation in the films, where the reflections at q_y = 4.8 nm^{-1} and q_y = 8.4 nm^{-1} appear as a diffuse arc (see Figure 6-22). In our previous reports on VAC film synthesis, we demonstrated that thin film morphology can be tuned by altering the VAC synthesis conditions in terms of the precursor compounds and concentration.[30,62,63] Following this approach, extensive VAC reaction condition screening efforts were carried out for the growth of MOF-74(Mg) on gold substrate. Here, we found that the addition of water and modulator benzoic acid to the DMF/ EtOH mixture, in combination with an increase of the concentration of the precursor solution, results in the formation of a crystalline and highly oriented MOF-74(Mg) film on gold. The 2D GIWAXS analysis shows that the distinct reflections at q_y = 4.8 nm^{-1} and q_y = 8.4 nm^{-1} corresponding to the (110) and (300) planes are located at about q_z = 0 nm^{-1}, confirming the formation of a highly oriented and crystalline MOF-74(Mg) film (see Figure 6-3 A). This illustrates the important role of the substrate

surface in the VAC process, which must be considered together with the choice of the solvent mixture and modulators for achieving a successful film synthesis.

In contrast to the growth of MOF-74(Zn) on gold, the MOF-74(Mg) films are oriented such that the *c*-crystallographic axis is aligned nearly orthogonally to the substrate with a free rotation around this axis (see Figure 6-3 A). XRD analysis of the oriented MOF-74(Mg) film on gold, as well as transmission electron microscopy (TEM) images of scratched off film powder, revealed a highly crystalline material (see Figure 6-19 and Figure 6-23). In addition, a high-magnification TEM image shows lattice fringes with a distance of 1.3 nm, corresponding to the interplanar spacings of (110) planes. SEM top-view and cross-section micrographs show a long-range coverage of rod-shaped MOF-74(Mg) crystallite bundles with an average width of about 400 nm and a length of 3 μm, preferentially oriented nearly orthogonally to the substrate (see Figure 6-3 C and Figure 6-24). The films have a thickness of about 3 μm and are crack-free and homogeneous without undesired sediments of impurities on top of the MOF film, indicating an exclusively on-surface nucleation and growth rather than (additional) homogeneous nucleation in solution. AFM scans of the MOF-74(Mg) film on gold reveal a rough surface topography with a RMS roughness

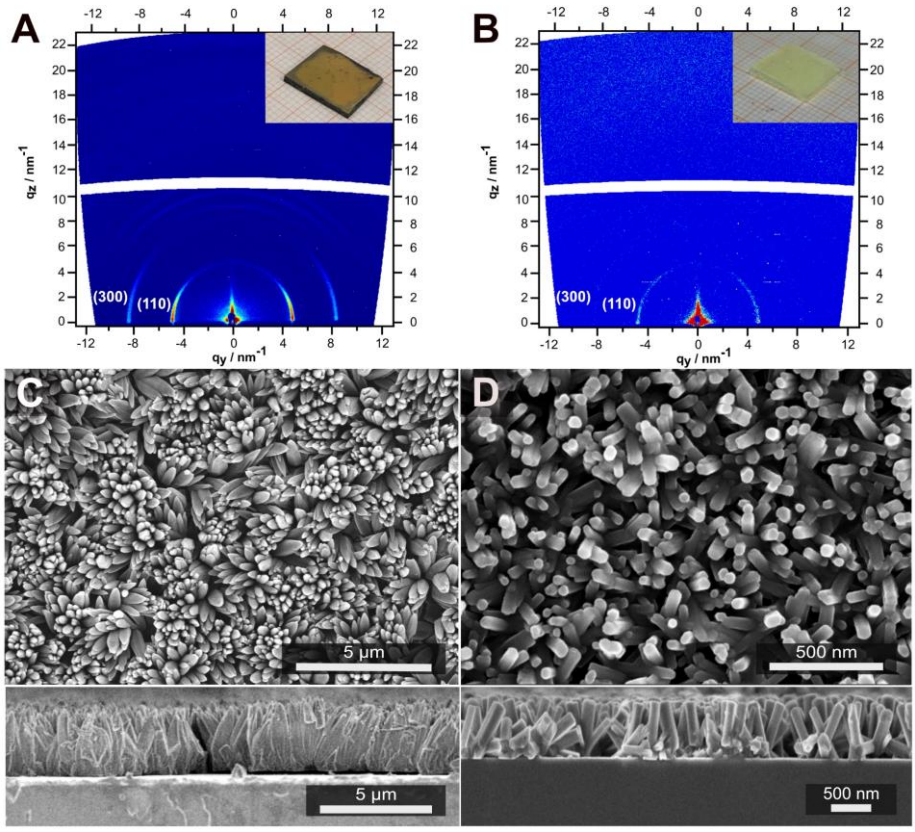

Figure 6-3: 2D GIWAXS patterns of MOF-74(Mg) thin films grown on (A) gold and (B) glass, obtained by VAC, with the Miller indices shown in white. Photo images of the thin films are shown as insets. SEM top-view and SEM cross-section micrographs (bottom) of MOF-74(Mg) grown on (C) gold (oriented) and (D) on glass (oriented).

of 52 nm (see Figure 6-25), and WCA measurements indicate the formation of superhydrophilic surfaces (seeFigure 6-26).

To gain further insights into the film formation and the evolution of crystal orientation in the two distinct cases of Mg- and Zn-MOF-74 films on a gold substrate, we tracked the film crystallization process by interrupting the synthesis at different time points and analyzing the obtained coatings on the surface. A series of XRD diffraction patterns and SEM images were collected for the different film formation stages and synthesis times of the respective MOFs (see Figure 6-27 and Figure 6-28). Briefly, MOF-74(Zn) films are formed through rapid layer solidification, yielding initially an amorphous interconnected network showing needle-like morphology already preferentially aligned parallel to the substrate (Figure 6-27). With time, nucleation and growth proceed in the formed layer to give the final crystalline phase attributed to dissolution and crystallization processes extending the crystalline domains under the mild specific conditions of VAC, where the crystallization process lasts about 18 h. In the case of MOF-74(Mg) films, the process takes longer and involves the nucleation of islands of nonoriented crystalline phase on the gold substrate in the shape of fans (Figure 6-28). With progressing reaction time, the number of islands increases at the surface limiting the arc shape of the crystallites and yielding well-aligned crystals perpendicular to the substrate. We therefore postulate that in the case of MOF-74(Zn), the selected surface plays a minor role for controlling orientation compared to MOF-74(Mg). In the context of crystallite orientation, we note that on gold, MOF-74(Mg) is formed as a nonoriented film with DMF/ EtOH as a solvent mixture, and that it grows oriented only after the addition of H_2O and benzoic acid serving as modulators potentially controlling nucleation and growth. As already demonstrated in previous reports dealing with bulk MOFs, the addition of a crystallization competitor or 'modulator' can strongly influence the nucleation and crystal growth.[68,69]

6.4.3 Highly crystalline MOF-74(Co) and MOF-74(Ni) films

Above, we have demonstrated that by employing VAC, MOF-74(Zn and Mg) films can by synthesized in two distinctly different crystallite orientations on the substrate, respectively. The synthesis of MOF-74(Co) thin films by VAC utilizing the developed protocols for the MOF-74(Zn) derivative resulted in phase-pure crystalline MOF films, as indicated by the XRD analysis. The XRD patterns of the obtained films agree well with the PXRD data of the MOF-74(Co) bulk material (see Figure 6-4 A and Figure 6-30). Here, 2D GIWAXS analysis reveals that MOF-74(Co) crystallites are randomly distributed (see Figure 6-31). Screening efforts regarding solvent compositions and modulator mixtures, as well as different metal salt precursors and temperatures for the respective substrates, yielded crystalline, phase-pure and nonoriented MOF-74(Co) films on gold (see Figure 6-4 A, Figure 6-31), glass and silicon (see Figure 6-30). Similar to the growth

of MOF-74(Mg), we observed a strong impact of the employed surface, metal precursor, and solvent mixtures on the final film morphology (see Figure 6-4 C, Figure 6-32, and Figure 6-33). For example, employing a $CoCl_2 \cdot 6H_2O$ metal precursor in a DMF and H_2O (22:1 *v/v*) mixture on gold allowed for the formation of MOF films consisting of individual, rod-shaped MOF-74(Co) crystallites of an average 130 nm width and an average 380 nm length, with a defined hexagonally shaped cross-section (see Figure 6-4 C). In contrast, employing a $Co(OAc)_2$ metal precursor and a pure DMF solution on glass, as well as a DMF/EtOH/H2O (1:1:1 *v/v*) solvent mixture on silicon, rather spherical, intergrown MOF crystallites were formed (see Figure 6-33).

The film fabrication of MOF-74(Ni) on gold was carried out in DMF as a solvent in the presence of benzoic acid as modulator. For the film synthesis on glass and silicon, different solvent mixtures, namely DMF/EtOH/H_2O mixtures (22:1:1 *v/v*) and (1:1:1 *v/v*), respectively, were employed. Similar to the MOF-74(Co) film growth, MOF-74(Ni) film syntheses on gold, glass and silicon afforded crystalline MOF films with random crystallite orientation, despite extensive screening effort (see Figure 6-4 B, Figure 6-35). Top-view SEM images of MOF-74(Ni) thin films reveal spherically shaped small MOF crystallites having a diameter of around 50 nm (see Figure 6-4 D, Figure 6-36 and Figure 6-37). Interestingly, cross-section SEM images show the formation of a dense and continuous film of about 250 nm thickness on glass (see Figure 6-4 D). AFM scans

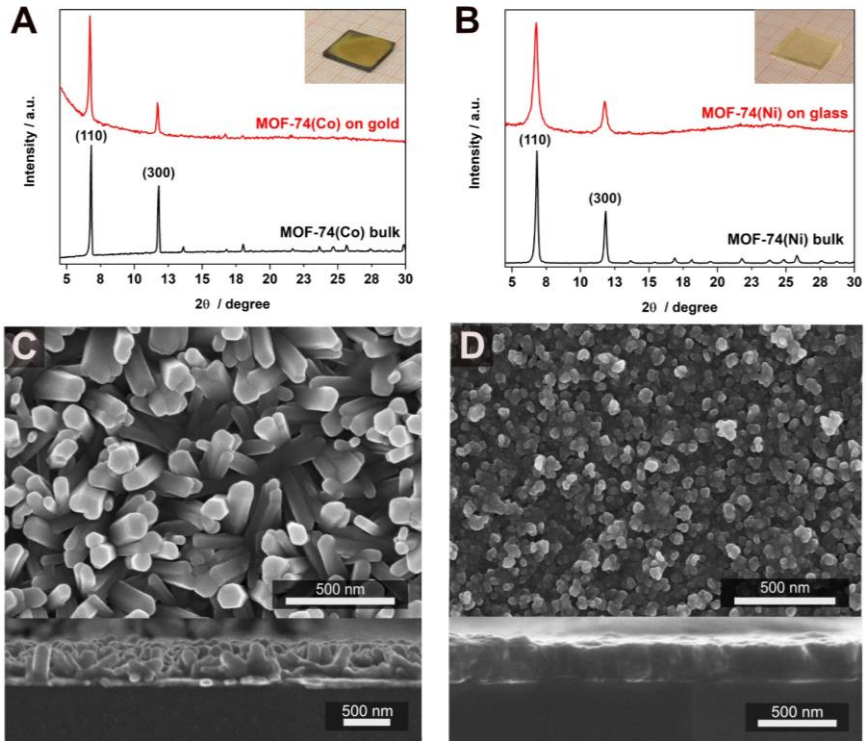

Figure 6-4: (A) XRD patterns of MOF-74(Co) bulk material and of MOF-74(Co) grown on gold, with a macroscopic image as the inset. (B) XRD patterns of MOF-74(Ni) bulk material and of MOF-74(Ni) grown on glass. (C) SEM top-view (top) and cross-section micrographs (bottom) of MOF-74(Co) on gold. (D) SEM top-view (top) and cross-section micrographs (bottom) of MOF-74(Ni) on glass.

of the MOF-74(Ni) film on glass show a smooth surface topography with a RMS roughness of 10 nm (see Figure 6-38). For further characterization, WCA measurements were performed of a MOF-74(Co) thin film on gold and of a MOF-74(Ni) thin film on glass, revealing hydrophilic surfaces (see Figure 6-39).

6.4.4 Accessible pores of the MOF films

On-surface permanent porosity as well as pore accessibility are important features for the realization of MOF films as porous hosts in surface-based technologies such as sieving and sensing. To demonstrate porosity, the framework must be free of impurities such as starting materials or undesired entrapped solvents. The porosity of the MOF-74(M) activated films (heating at 120 °C for 12 h) was investigated by means of krypton sorption analysis at 77 K. To examine the porosity of the films, we choose oriented MOF-74(Zn and Mg), nonoriented MOF-74(Co) grown on gold, and nonoriented MOF-74(Ni) grown on glass as representative crystalline models of the VAC-derived films. The examined MOF films show microporous-type IUPAC[29] Type I(b) isotherms (see Figure 6-5) characterized by a steep krypton uptake at very low relative pressures (p/p_0 = 0-0.03), which indicates a narrow pore size distribution and a defined microporous structure. Normalizing to the geometric surface area, the Brunauer-Emmett-Teller (BET) surface area is calculated to be as high as 127 cm^2/cm^2 for MOF-74(Zn) (p/p_0 = 0.009 – 0.08 of the adsorption branch), 975 cm^2/cm^2 for MOF-74(Mg) (p/p_0 = 0.002 – 0.08 of the adsorption branch), 365 cm^2/cm^2 for MOF-74(Ni) (p/p_0 = 0.008 – 0.08 of the adsorption branch) and 50.3 cm^2/cm^2 for MOF-74(Co) (p/p_0 = 0.005 – 0.07 at the adsorption branch). Notably, oriented MOF-74(Mg) films on gold show a very high BET surface area, attributed to the thickness of the film being in the range of about 3 µm. Moreover, the isotherm resulting from krypton sorption measurements of MOF-74(Mg) bulk material (see Figure 6-40) is in very good agreement with the ones of the corresponding MOF-74(Mg) thin films. This confirms excellent access of guests into the oriented MOF-74(Mg) film.

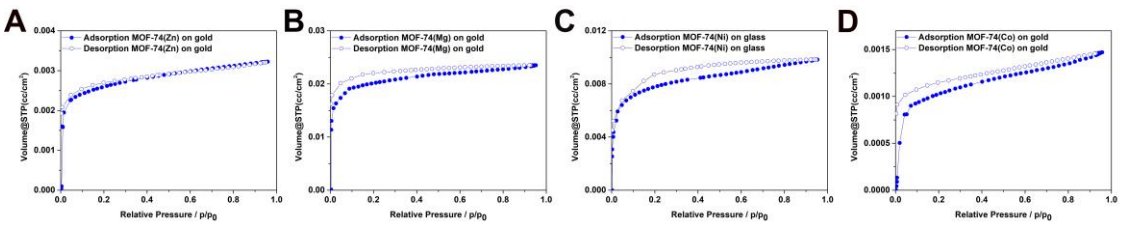

Figure 6-5: Krypton sorption isotherms of activated MOF-74(M = Zn, Mg, and Co) films grown on gold and of MOF-74(Ni) films grown on glass, measured at 77 K.

6.4.5 Optical properties of the MOF-74(M) films

After confirming the porosity, we examined the optical properties of the MOF-74(M) films grown on quartz by using UV-Vis absorption and PL spectroscopy (Figure 6-6). The UV-Vis spectra were measured in transmission mode. For all examined MOF-74(M) thin films, the absorption bands are located in the UV and blue part of the visible spectral regions. MOF-74(Zn and Mg) have an absorption onset between 458 and 453 nm and MOF-74(Ni and Co) between 460 and 466 nm (see Figure 6-6 C, D and Figure 6-41). Assuming a direct band gap, Tauc plots were calculated from the absorption spectra, yielding optical band gaps of about 2.8 eV for all the examined MOFs (see Figure 6-42). MOF-74(Zn) shows an absorption maximum at 406 nm, MOF-74(Mg) at 393 nm, MOF-74(Ni) at 396 nm, and MOF-74(Co) at 398 nm; this absorption band is attributed to the integrated DOT building block, which exhibits a similar absorption profile (see Figure 6-43). PL of the MOF-74(M) films on quartz was measured with a 378 nm excitation source (see Figure 6-6 C, D). The PL spectra of MOF-74(Zn) and MOF-74(Mg) show rather narrow emission bands with emission maxima at 476 and 487 nm, respectively, which are similar to the emission band of the solid DOT linker at 481 nm (see Figure 6-43). MOF-74(Ni and Co) films on quartz also show a second weaker emission band at 690 nm (see Figure 6-44).

However, the total emission profiles of MOF-74(Ni and Co) films exhibit relatively low intensity, therefore we focused on the PL study of the oriented MOF-74(Zn and Mg) films. TCSPC PL traces of MOF-74(Zn) and MOF-74(Mg) were recorded at the respective emission maxima of 476 and 487 nm (Figure 6-6 E, F). The MOFs show similar relaxation behaviour, which can be described by a biexponential decay. The first decay components give rise to lifetimes of τ_1 = 19 and 20 ps, while the second decay component are τ_2 = 161 and 168 ps for MOF-74(Zn) and MOF-74(Mg), respectively. The fractional distribution of decay lifetimes is similar for the two MOFs. The short lifetime decay channels are contributing 89% to the overall emission in MOF-74(Zn) and MOF-74(Mg), while the longer lifetime component has only a contribution to the overall emission of 11% in both MOFs. Furthermore, we performed confocal PL mapping experiments on the films with horizontally oriented MOF-74(Zn) and orthogonally oriented MOF-74(Mg) grown on gold. The confocal PL maps are presented in Figure 6-6 A, B, exhibiting a rather homogeneous emission over the whole examined film surface, underlining an even spread of MOF crystals on the substrate. The PL energies were found to be uniform within the investigated MOF-74(Zn) and MOF-74(Mg) films, and the emission profiles of both films seem to be decoupled from its crystal orientation.

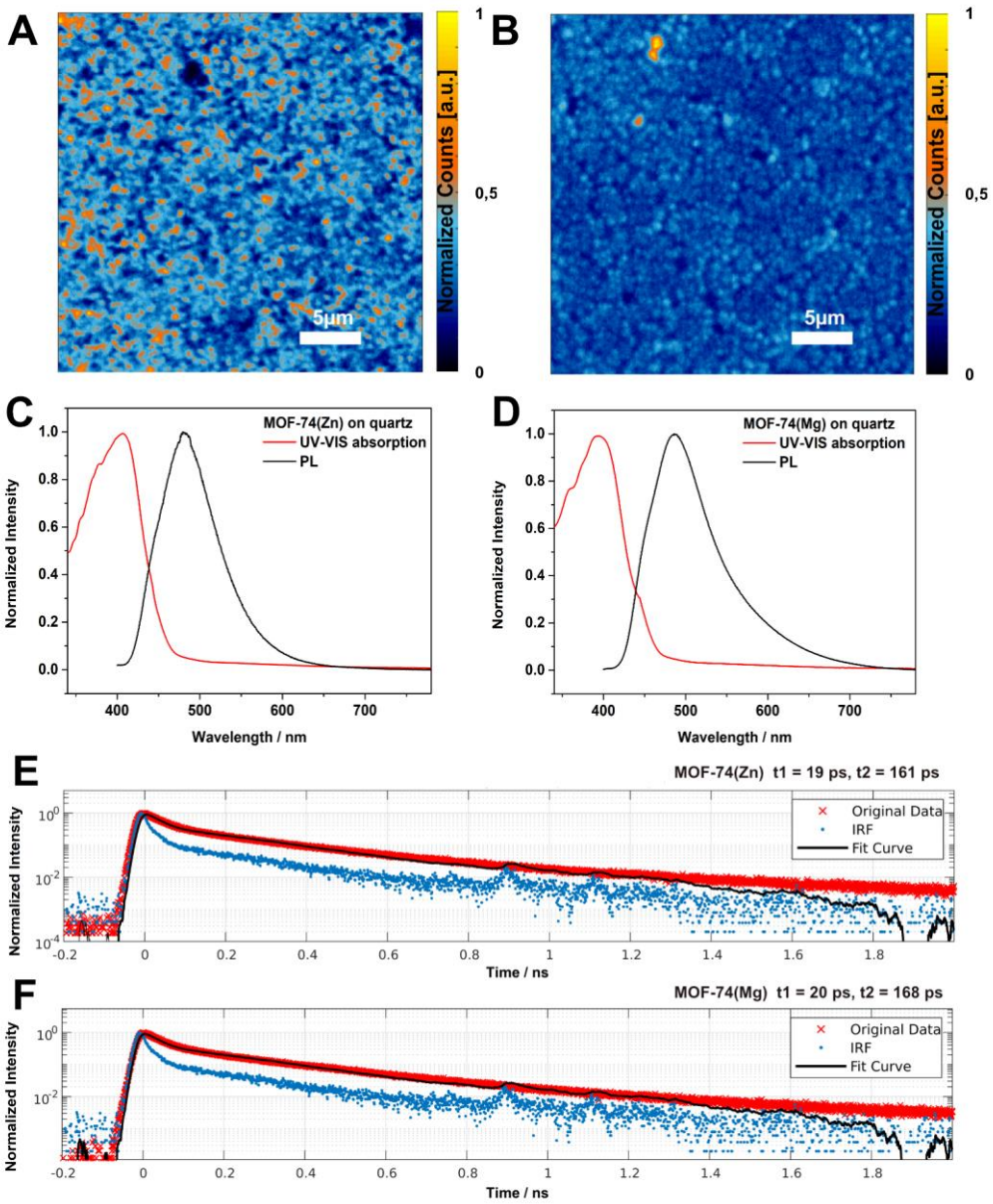

Figure 6-6: (A),(B) Confocal PL mapping of oriented MOF-74(Mg) film measured on an area of 30 μm x 30 μm and MOF-74(Zn) on gold, measured on an area of 30 μm x 30 μm. (C),(D) UV-Vis absorption spectra of MOF-74(M = Zn and Mg) grown on quartz substrates (red line) and PL spectra of MOF-74(M = Zn and Mg) measured with 378 nm excitation (black line). The time-correlated single photon counting (TCSPC) PL traces of (E) MOF-74(Zn) and (F) MOF-74(Mg) grown on gold were recorded at the respective emission maximum of each MOF. The lifetimes were obtained from biexponential fits (solid black lines) to the data (red scatter). The instrument response function is plotted in blue (scatter).

6.5 Conclusion

In this study we report the on-surface growth of crystalline MOF-74(M= Zn, Mg, Ni and Co) thin films through VAC, resulting in a homogeneous surface coverage, film thicknesses ranging between 250 nm and 3 μm and different crystallite orientations. The VAC synthesis for the four MOFs was successfully transferred to different substrates, i.e., gold, glass, quartz and silicon. We establish that MOF-74 based on different metal ions grows according to substantially different

growth modes on these surfaces. Hence, highly crystalline MOF-74(Zn) film was grown on the respective substrates, where the crystallographic *c*-axis of the MOF crystallites is oriented preferentially horizontally to the substrate. In contrast, highly crystalline MOF-74(Mg) was grown on glass and gold substrates with the crystallographic *c*-axis aligned nearly orthogonally to the substrate. Moreover, we report the synthesis of highly crystalline MOF-74(Co) and MOF-74(Ni) thin films on glass, quartz, gold, and silicon without a preferential crystallite orientation. Guest access into the pore systems of MOF-74(Zn, Mg, and Co) on gold, as well as MOF-74(Ni) on glass, serving as representatives of the series, was confirmed by krypton sorption measurements. Notably, MOF-74(Mg) films were shown to be highly porous with a relative surface area reaching 975 cm^2/cm^2 (normalized to geometric surface area), making these MOF films attractive candidates for on-chip host-guest experiments. In addition, the remarkable nearly orthogonal channel orientation in the oriented MOF-74(Mg) film suggests its future integration into membranes for molecular separations based on molecular sieving effects. PL studies of the MOF-74(M) films on quartz show emission in the blue spectral region, with MOF-74(Zn and Mg) having similar PL lifetimes. Confocal PL mapping also confirmed the homogeneous coverage of MOF-74(Mg) and MOF-74(Zn) on gold.

Concluding, this work establishes vapor-assisted conversion as a powerful method for the growth of diverse MOF-74 thin films with tuneable crystal orientations. These findings are expected to open the door for the growth of well-defined thin films of other MOF-74 analogs with sterically more demanding integrated organic linkers leading to interesting optical or electrical properties and greater pore apertures, thus enabling the design of diverse thin film devices for applications such as chemical sensing or optoelectronics.

6.6 References

(1) Yaghi, O. M.; Li, H. Hydrothermal Synthesis of a Metal-Organic Framework Containing Large Rectangular Channels. *J. Am. Chem. Soc.* **1995**, *117*, 10401–10402.

(2) Stock, N.; Biswas, S. Synthesis of metal-organic frameworks (MOFs): routes to various MOF topologies, morphologies, and composites. *Chem. Rev.* **2012**, *112*, 933–969.

(3) Deng, H.; Grunder, S.; Cordova, K. E.; Valente, C.; Furukawa, H.; Hmadeh, M.; Gándara, F.; Whalley, A. C.; Liu, Z.; Asahina, S.; Kazumori, H.; O'Keeffe, M.; Terasaki, O.; Stoddart, J. F.; Yaghi, O. M. Large-pore apertures in a series of metal-organic frameworks. *Science* **2012**, *336*, 1018–1023.

(4) Scheurle, P. I.; Mähringer, A.; Jakowetz, A. C.; Hosseini, P.; Richter, A. F.; Wittstock, G.; Medina, D. D.; Bein, T. A highly crystalline anthracene-based MOF-74 series featuring electrical conductivity and luminescence. *Nanoscale* **2019**, *11*, 20949–20955.

(5) AlKaabi, K.; Wade, C. R.; Dincă, M. Transparent-to-Dark Electrochromic Behavior in Naphthalene-Diimide-Based Mesoporous MOF-74 Analogs. *Chem* **2016**, *1*, 264–272.

(6) Hirofumi, M.; Akira, S.; Yusuke, M.; Yoshinori, I. Polycarboxylic acid containing condensed aromatic ring, crystalline network complex using same, and gas storage material. *WO 2017006638 A1* **2017**.

(7) Xu, G.; Nie, P.; Dou, H.; Ding, B.; Li, L.; Zhang, X. Exploring metal organic frameworks for energy storage in batteries and supercapacitors. *Mater. Today* **2017**, *20*, 191–209.

(8) Yang, D.-A.; Cho, H.-Y.; Kim, J.; Yang, S.-T.; Ahn, W.-S. CO 2 capture and conversion using Mg-MOF-74 prepared by a sonochemical method. *Energy Environ. Sci.* **2012**, *5*, 6465–6473.

(9) Zheng, J.; Vemuri, R. S.; Estevez, L.; Koech, P. K.; Varga, T.; Camaioni, D. M.; Blake, T. A.; McGrail, B. P.; Motkuri, R. K. Pore-Engineered Metal-Organic Frameworks with Excellent Adsorption of Water and Fluorocarbon Refrigerant for Cooling Applications. *J. Am. Chem. Soc.* **2017**, *139*, 10601–10604.

(10) Lazaro, I. A.; Forgan, R. S. Application of zirconium MOFs in drug delivery and biomedicine. *Coord. Chem. Rev.* **2019**, *380*, 230–259.

(11) Sun, C.-Y.; Qin, C.; Wang, X.-L.; Su, Z.-M. Metal-organic frameworks as potential drug delivery systems. *Expert Opin Drug Deliv.* **2013**, *10*, 89–101.

(12) Hod, I.; Bury, W.; Karlin, D. M.; Deria, P.; Kung, C.-W.; Katz, M. J.; So, M.; Klahr, B.; Jin, D.; Chung, Y.-W.; Odom, T. W.; Farha, O. K.; Hupp, J. T. Directed growth of electroactive metal-organic framework thin films using electrophoretic deposition. *Adv. Mater.* **2014**, *26*, 6295–6300.

(13) Meek, S. T.; Greathouse, J. A.; Allendorf, M. D. Metal-organic frameworks: a rapidly growing class of versatile nanoporous materials. *Adv. Mater.* **2011**, *23*, 249–267.

(14) Ben-Mansour, R.; Qasem, N. A. A.; Habib, M. A. Adsorption characterization and CO2 breakthrough of MWCNT/Mg-MOF-74 and MWCNT/MIL-100(Fe) composites. *Int. J. Energy Environ. Eng.* **2018**, *9*, 169–185.

(15) Caskey, S. R.; Wong-Foy, A. G.; Matzger, A. J. Dramatic tuning of carbon dioxide uptake via metal substitution in a coordination polymer with cylindrical pores. *J. Am. Chem. Soc.* **2008**, *130*, 10870–10871.

(16) Fracaroli, A. M.; Furukawa, H.; Suzuki, M.; Dodd, M.; Okajima, S.; Gándara, F.; Reimer, J. A.; Yaghi, O. M. Metal-organic frameworks with precisely designed interior for carbon dioxide capture in the presence of water. *J. Am. Chem. Soc.* **2014**, *136*, 8863–8866.

(17) Hod, I.; Sampson, M. D.; Deria, P.; Kubiak, C. P.; Farha, O. K.; Hupp, J. T. Fe-Porphyrin-Based Metal–Organic Framework Films as High-Surface Concentration, Heterogeneous Catalysts for Electrochemical Reduction of CO2. *ACS Catal.* **2015**, *5*, 6302–6309.

(18) Ricco, R.; Wied, P.; Nidetzky, B.; Amenitsch, H.; Falcaro, P. Magnetically responsive horseradish peroxidase@ZIF-8 for biocatalysis. *ChemComm.* **2020**, *56*, 5775–5778.

(19) Wang, L. J.; Deng, H.; Furukawa, H.; Gándara, F.; Cordova, K. E.; Peri, D.; Yaghi, O. M. Synthesis and characterization of metal-organic framework-74 containing 2, 4, 6, 8, and 10 different metals. *Inorg. Chem.* **2014**, *53*, 5881–5883.

(20) Xiang, S.; He, Y.; Zhang, Z.; Wu, H.; Zhou, W.; Krishna, R.; Chen, B. Microporous metal-organic framework with potential for carbon dioxide capture at ambient conditions. *Nat. Commun.* **2012**, *3*, 954.

(21) Pentyala, V.; Davydovskaya, P.; Pohle, R.; Urban, G.; Yurchenko, O. Mg-MOF74 and Co-MOF74 as Sensing Layers for CO_2 Detection. *Procedia Eng.* **2014**, *87*, 1071–1074.

(22) Campbell, M. G.; Dincă, M. Metal-Organic Frameworks as Active Materials in Electronic Sensor Devices. *Sensors* **2017**, *17*, 1108.

(23) Luo, J.; Li, Y.; Zhang, H.; Wang, A.; Lo, W.-S.; Dong, Q.; Wong, N.; Povinelli, C.; Shao, Y.; Chereddy, S.; Wunder, S.; Mohanty, U.; Tsung, C.-K.; Wang, D. A Metal–Organic Framework Thin Film for Selective Mg^{2+} Transport. *Angew. Chem.* **2019**, *131*, 15457–15461.

(24) Yi, F.-Y.; Chen, D.; Wu, M.-K.; Han, L.; Jiang, H.-L. Chemical Sensors Based on Metal-Organic Frameworks. *ChemPlusChem* **2016**, *81*, 675–690.

(25) Wuttke, S.; Median, D. D.; Rotter, J. M.; Begun, S.; Stassin, T.; Ameloot, R.; Oschatz, M.; Tsotsalas, M. Bringing Porous Organic and Carbon-Based Materials toward Thin-Film Applications. *Adv. Funct. Mater.* **2018**, *28*, 1801545.

(26) Cruz, A. J.; Stassen, I.; Krishtab, M.; Marcoen, K.; Stassin, T.; Rodriguez-Hermida, S.; Teyssandier, J.; Pletincx, S.; Verbeke, R.; Rubio-Gimenez, V.; Tatay, S.; Mart-Gastaldo, C.; Meersschaut, J.; Vereecken, P. M.; Feyter, S. de; Hauffman, T.; Ameloot, R. Integrated Cleanroom Process for the Vapor-Phase Deposition of Large-Area Zeolitic Imidazolate Framework Thin Films. *Chem. Mater.* **2019**, *31*, 9462–9471.

(27) Dolgopolova, E. A.; Shustova, N. B. Metal–organic framework photophysics: Optoelectronic devices, photoswitches, sensors, and photocatalysts. *MRS Bull.* **2016**, *41*, 890–896.

(28) Bétard, A.; Zacher, D.; Fischer, R. A. Dense and homogeneous coatings of CPO-27-M type metal–organic frameworks on alumina substrates. *CrystEngComm* **2010**, *12*, 3768.

(29) Lee, D.-J.; Li, Q.; Kim, H.; Lee, K. Preparation of Ni-MOF-74 membrane for CO2 separation by layer-by-layer seeding technique. *Microporous Mesoporous Mater.* **2012**, *163*, 169–177.

(30) Rezaei, F.; Lawson, S.; Hosseini, H.; Thakkar, H.; Hajari, A.; Monjezi, S.; Rownaghi, A. A. MOF-74 and UTSA-16 film growth on monolithic structures and their CO2 adsorption performance. *Chem. Eng. J.* **2017**, *313*, 1346–1353.

(31) Zhao, Z.; Zuhra, Z.; Qin, L.; Zhou, Y.; Zhang, L.; Tang, F.; Mu, C. Confinement of microporous MOF-74(Ni) within mesoporous γ-Al2O3 beads for excellent ultra-deep and selective adsorptive desulfurization performance. *Fuel Process. Technol.* **2018**, *176*, 276–282.

(32) P.J. Jodlowski, G. Kurowski, K. Dymek, R.J. Jedrzejczyk, P. Jelen, L. Kuterasinski, A. Gancarczyk, A. Wegrzynowicz, T. Sawoszczuk, M. Sitarz. *Microporous Mesoporous Mater.* **2020**, *303*, 110249.

(33) Yuan, H.; Tao, J.; Li, N.; Karmakar, A.; Tang, C.; Cai, H.; Pennycook, S. J.; Singh, N.; Zhao, D. On-Chip Tailorability of Capacitive Gas Sensors Integrated with Metal-Organic Framework Films. *Angew Chem Int Ed* **2019**, *58*, 14089–14094.

(34) Campbell, J.; Tokay, B. Controlling the size and shape of Mg-MOF-74 crystals to optimise film synthesis on alumina substrates. *Microporous Mesoporous Mater.* **2017**, *251*, 190–199.

(35) Chaudhari, A. K.; Souza, B. E.; Tan, J.-C. Electrochromic thin films of Zn-based MOF-74 nanocrystals facilely grown on flexible conducting substrates at room temperature. *APL Mater.* **2019**, *7*, 81101.

(36) Zhou, S.; Wang, S.; Xu, H.; Zhao, J.; Wang, J.; Li, Y. An electrochromic supercapacitor based on an MOF derived hierarchical-porous NiO film. *Nanoscale* **2020**, *12*, 8934–8941.

(37) Zhou, W.; Xue, Z.; Liu, Q.; Li, Y.; Hu, J.; Li, G. Trimetallic MOF-74 Films Grown on Ni Foam as Bifunctional Electrocatalysts for Overall Water Splitting. *ChemSusChem* **2020**, *13*, 5647–5653.

(38) Virmani, E.; Rotter, J. M.; Mähringer, A.; Zons, T. von; Godt, A.; Bein, T.; Wuttke, S.; Medina, D. D. On-Surface Synthesis of Highly Oriented Thin Metal-Organic Framework Films through Vapor-Assisted Conversion. *J. Am. Chem. Soc.* **2018**, *140*, 4812–4819.

(39) Mähringer, A.; Jakowetz, A. C.; Rotter, J. M.; Bohn, B. J.; Stolarczyk, J. K.; Feldmann, J.; Bein, T.; Medina, D. D. Oriented Thin Films of Electroactive Triphenylene Catecholate-Based Two-Dimensional Metal-Organic Frameworks. *ACS Nano* **2019**, *13*, 6711–6719.

(40) Mähringer, A.; Rotter, J. M.; Medina, D. D. Nanostructured and oriented metal-organic framework films enabling extreme surface wetting properties. *Beilstein J. Nanotechnol.* **2019**, *10*, 1994–2003.

(41) Mähringer, A.; Hennemann, M.; Clark, T.; Bein, T.; Medina, D. D. Energy Efficient Ultra-high Flux Separation of Oily Pollutants from Water with Superhydrophilic Nanoscale Metal-Organic Framework Architectures. *Angew. Chem. Int. Ed.* **2021**, *60*, 5519–5526.

(42) Dana D. Medina, Julian M. Rotter, Yinghong Hu, Mirjam Dogru, Veronika Werner, Florian Auras, John T. Markiewicz, Paul Knochel, and Thomas Bein. Room Temperature Synthesis of Covalent-Organic Framework Films through Vapor-Assisted Conversion. *J. Am. Chem. Soc.* **2015**, *137*, 1016–1019.

(43) Zhou, Z.; Mukherjee, S.; Warnan, J.; Li, W.; Wannapaiboon, S.; Hou, S.; Rodewald, K.; Rieger, B.; Weidler, P. G.; Wöll, C.; Fischer, R. A. Porphyrin based metal–organic framework films: nucleation and growth. *J. Mater. Chem. A* **2020**, *8*, 25941–25950.

(44) Warfsmann, J.; Tokay, B.; Champness, N. R. Synthesis of MIL-53 thin films by vapour-assisted conversion. *CrystEngComm* **2020**, *22*, 1009–1017.

(45) Jiang, Z. GIXSGUI : a MATLAB toolbox for grazing-incidence X-ray scattering data visualization and reduction, and indexing of buried three-dimensional periodic nanostructured films. *J. Appl. Cryst.* **2015**, *48*, 917–926.

(46) Webber, T. E.; Desai, S. P.; Combs, R. L.; Bingham, S.; Lu, C. C.; Penn, R. L. Size Control of the MOF NU-1000 through Manipulation of the Modulator/Linker Competition. *Cryst. Growth Des.* **2020**, *20*, 2965–2972.

(47) Forgan, R. S. Modulated assembly of metal-organic frameworks. *Chem. Sci* **2020**, *11*, 4546–4562.

(48) Thommes, M.; Kaneko, K.; Neimar K, A. V.; Olivier, J. P.; Rodriguez-Reinoso, F.; Rouquerol, J.; Sing, K. S. W. Physisorption of gases, with special reference to the evaluation of surface area and pore size distribution (IUPAC Technical Report). *Pure Appl. Chem.* **2015**, *87*, 1051–1069.

6.7 Supporting information

6.7.1 Reported methodologies of publications in the field of MOF-74(M) film synthesis

Table 6-1:

	method	metal ions	thickness	substrate	alignment	application
Bétard *et al.*[1]	reactive mother solutions, solvothermal synthesis	Zn, Mg, Ni, Co	80 µm (Zn), over 10 µm	ultrathin amorphous alumina	not stated	not stated
Lee *et al.*[2]	layer-by-layer seeding technique	Ni	10 – 25 µm	α-alumina	not stated	not stated
Rezaei *et al.*[3]	slightly modified layer-by-layer film synthesis protocol	Ni	~10 µm	cordierite monoliths	not stated	not stated
Zhao *et al.*[4]	solvothermal reaction	Ni	not stated	in the channels of γ-alumina	not stated	not stated
Luo *et al.*[5]	wet chemistry approach	Mg	202 nm	gold coated silicon	not stated	selective Mg^{2+} transport
Jodlowski *et al.*[6]	in-situ growth, solvothermal reaction	Zn, Ni, Co	40 µm (Zn), 10 µm (Ni), 20 µm (Co)	FeCrAl plates, FeCrAl gauze, NiCr foams	perpendicular oriented (Co; Zn) (according to SEM)	catalyst for oxidation of cyclohexene
Yuan *et al.*[7]	in-situ growth, solvothermal reaction	Mg	7 µm	inter-digitated electrodes	not stated	gas sensing
Campbell *et al.*[8]	one-step solvothermal reaction	Mg	tuneable thickness, 1 – 20 µm	tubular alumina porous substrate	not stated	not stated

	method	metal ions	thickness	substrate	alignment	application
Chaudhari *et al.*[9]	dip coating	Zn	not stated	Zn-coated ITO-PET	not stated	intercalation of guest molecules for electro-chromism
Zhou *et al.*[10]	in-situ growth, solvothermal reaction	Ni	not stated	ITO; nickel foam	not stated	preparation of NiO films through an-nealing
Zhou *et al.*[11]	in-situ growth, solvothermal reaction	trimetallic MOF: $Mn_{0.52}Fe_{0.71}Ni$	not stated	nickel foam	not stated	electro-catalyst for wa-ter splitting

6.7.2 Characterization metods

X-ray analysis

X-ray diffraction (XRD) analyzes were performed on a *Bruker D8* diffractometer in Bragg-Brentano geometry with Ni-filtered Cu K_α (λ = 1.54060 Å) radiation operating at 40 kV and 30 mA with a position-sensitive detector (*LynxEye*).

Two-dimensional grazing incidence wide angle X-ray scattering (2D GIWAXS) data were collected using an Anton-Paar Saxspace system equipped with Cu K_α microfocus source operated at 50 kV and 1 mA and an Eiger Dectris R 1M 2D detector.

Scanning electron microscopy (SEM)

SEM images were recorded on an *FEI Helios NanoLab G3 UC* electron microscope with an acceleration voltage of 2 kV. For the cross-section analysis substrates were partially cut and broken manually to reveal fresh cross-sections. Prior to SEM analysis the samples were coated with a thin carbon layer by carbon fiber flash evaporation in high vacuum.

Transmission electron microscopy (TEM)

TEM images were collected on an FEI Titan Themis 60-300 microscope at an acceleration voltage of 300 kV. The MOF film layer on top of the substrate was carefully removed with a sharp blade and mounted onto a copper grid supporting a thin electron transparent carbon film.

UV-Vis spectroscopy

Photophysical characterization of as-prepared MOF thin films on 2.0 cm x 1.5 cm quartz substrates was performed in transmission mode with a *PERKIN ELMER UV VIS/NIR Lambda 1050* spectrophotometer equipped with a 150 mm InGaAs integrating sphere. Diffuse reflectance spectra were collected with a Praying Mantis (Harrick) accessory and were referenced to barium sulphate powder as white standard.

Photoluminescence (PL) spectroscopy

PL measurements were performed on a *PicoQuant FluoTime 300* time-correlated single photon counting (TCSPC) setup. Steady-state spectra and time-resolved histograms were acquired using a 378 nm laser (*PicoQuant LDH-P-C-375*). Residual laser scattering was removed using a 400 nm dielectric long pass (*Thorlabs FELH0400*) in the beam path of the emitted light, which was detected under magic angle (54.7°) on a photomultiplying tube (*PicoQuant PMA 192*). The microscopic images were measured using Nikon-based confocal microscope and a Nikon objective with a numerical aperture of 0.95. As excitation laser-source a 405 nm pulsed PicoQuant diode was used and in the detection beam pass a long pass 490 filter (FEL 490 Thorlabs) was installed filtering out the residual laser light. For the detection, an avalanche photo diode (Laser Components) was used.

Contact angle measurements

Contact angle measurements were performed on an attension instrument from Biolin Scientific. A droplet of water was placed on the substrate, while recording the images. The image analysis was carried out with the software “one attension” using a Young-Laplace analysis mode and an air-to-water interface. The water volume of one droplet was between 50 to 60 µL.

Atomic force microscopy

AFM measurements were performed using a NANOINK atomic force microscope in tapping mode with a scan rate of 0.2 Hz, a proportional gain of 50 and an integral gain of 32. The scanned area was 5.02 µm x 5.02 µm and 1 μm^2.

Nitrogen Sorption

Ad- and desorption measurements were performed on an *Autosorb 1* (*Quantachrome instruments, Florida, USA*) with nitrogen of 99.9999% purity at 77.3 K. The samples were activated (dried) under high vacuum at 120 °C for at least 12 h. Evaluation of ad- and desorption isotherms was carried out with the *AsiQwin v.3.01* (*Quantachrome instruments, Florida, USA*) software.

For BET calculations, pressure ranges of the nitrogen isotherms were chosen with the help of the BET assistant in the *AsiQwin* software. In accordance with the ISO recommendations, multipoint BET tags equal to or below the maximum in V x (1-p/p_0) were chosen.

Krypton sorption

Krypton sorption experiments were performed with a Quanatchrome Autosorb *iQ* (*Quantachrome instruments, Florida, USA*) at 77.3 K, assuming a saturation vapor pressure of p_0 = 217 Pa for Krypton.

Prior to the measurement, the MOF films were activated under high vacuum at 120 °C for at least 12 h. For the measurement, the substrates covered with MOF-74(M) films were cut into small pieces and put into the measurement tube. The total surface area of the films was 30 cm^2, exhibiting MOF layer thicknesses determined by SEM. Evaluation of ad- and desorption isotherms was carried out with the *AsiQwin v.3.01* (*Quantachrome instruments, Florida, USA*) software. For the BET surface area calculation, a saturation vapor pressure of the supercooled liquid (321 Pa at 77.3 K) and a molecular cross-sectional area of 0.205 nm^2 were assumed.[12,13]

6.7.3 Experimental

6.7.3.1 General

All materials were purchased from *Sigma Aldrich, Acros or TCI Europe* in the common purities *purum, puriss* or *reagent grade.* The materials were used as received without additional purification and handled in air unless otherwise noted.

The water utilized in the synthesis was subjected to a *Merck-Milipore Mili-Q* purification system prior to use.

6.7.3.2 Substrates

The preparation of the gold-substrates is based on the procedure described by Hinterholzinger *et al.* Seven microscope glass slides (Menzel, 76 mm x 26 mm) were washed with a 1:100 mixture of Hellmanex III and water, water and finally ethanol. Oxygen plasma cleaning (Diener electronic, Plasma-Surface-Technology) for 30 min was conducted, prior to the mounting of the glass slides in a vacuum deposition unit installed in a glove box (MBraun Labmaster Pro SP) equipped with an Inficon SQC-310C deposition controller. A layer of 10 nm titanium and then a layer of 40 nm gold were thermally deposited under high vacuum onto the microscope glass slides. Afterwards, the microscope slides were cut into 1.2 cm x 1 cm pieces. These substrates were directly used for the MOF film preparation.

The glass substrates were prepared by cutting microscope glass slides (Menzel, 76 mm x 26 mm) into 1.2 cm x 1.0 cm pieces. Afterwards they were washed with a 1:100 mixture of Hellmanex III and water, rinsed with water and finally ethanol and dried under a nitrogen flow.

The silicon wafers (Si[100]; Ø 20 cm; 0.6 mm thick) from Siegert Wafer were cut into 1.2 cm x 1.0 cm pieces and used without further purification.

Thermal atomic layer deposition of ZnO thin films was carried out in a *Picosun R-200 Advanced Reactor* at 250 °C and approximately 6 hPa. The carrier/purge gas was nitrogen (air Liquide, 99.999%). Microscope slides were used as substrates without pretreatment. The precursors diethyl zinc (DEZ, Strem, 95%) and water (Millipore, *Q-grade*) were held in stainless steel cylinders at 18 °C during the process. One ALD cycle consisted of a 0.1 s DEZ pulse, 6 s purge, 0.1 s water pulse and 8 s purge. The gas flow in both precursor lines was constant at 100 sccm each. For 73 nm thick films a growth rate of 0.098 nm/ cycle with a non-uniformity of 1.1% across a 20 cm wafer was determined by spectroscopic ellipsometry (*J. A. Woollam M-2000*) on Si(100) witness substrates with native oxide. The ZnO layer was represented by a Cauchy model layer.

6.7.3.3 Film formation *via* vapor-assisted conversion (VAC)

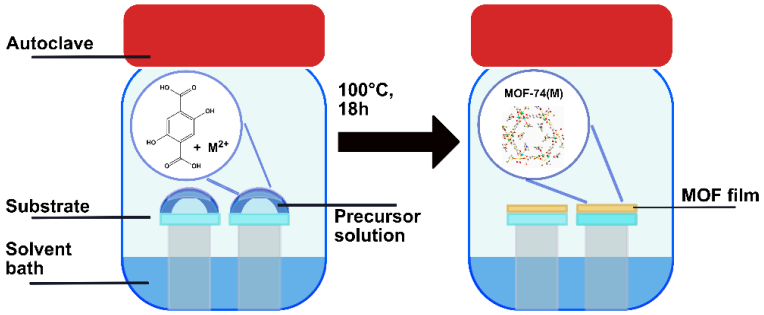

Figure S6-7: Schematic representation of the MOF-74(M) thin film synthesis via vapor-assisted conversion.

For the film formation using VAC, a glass bottle (Schott Duran, borosilicate 3.3, ISO4796, 100 mL) with a PBT cap equipped with a Teflon seal was used. The bottom part of the bottle was filled with 14 Raschig-rings (10 mm x 10 mm, soda-lime glass) to obtain an elevated flat platform for the substrate. A mixture of DMF/ EtOH/ H_2O was filled into the bottle (5 mL). Afterwards, a substrate (1.2 cm x 1 cm) was placed on top of the Raschig-rings and fully coated with a drop of freshly prepared MOF precursor solution. The bottle was closed and was transferred into a pre-heated oven where it was kept for the specified time. Afterwards the bottle was removed from the oven and allowed to cool down to room temperature before the substrate was removed and dried under reduced pressure. For the precursor solution, 2,5-dihydroxyterephthalic acid was dissolved in a DMF/ EtOH/ H_2O mixture by ultrasonic treatment. If desired, benzoic acid was added to this

solution. The metal precursor was added to the solution and dissolved by applying ultrasonic treatment

6.7.3.4 Thin film formation *via* vapor-assisted conversion (VAC)

Table 6-2: Synthesis conditions for MOF-74(Zn) films *via* VAC

Exp.	**Precursor solution**				**Droplet Volume**	**Substrate**	**Temp-erature**	**Reaction time**	**Vapor source**
	2,5-dihy-droxy ter-ephthalic acid	$Zn(OAc)_2$	Benzoic acid*	DMF					DMF
1	0.95 mg 4.8 mmol	1.76 mg 9.6 mmol	100 µL	2.2 mL	50 µL	glass	100 °C	18 h	5 mL
2	0.95 mg 4.8 mmol	1.76 mg 9.6 mmol	100 µL	2.2 mL	100 µL	quartz	100 °C	18 h	5 mL
3	0.95 mg 4.8 mmol	1.76 mg 9.6 mmol	50 µL	2.2 mL	50 µL	gold	100 °C	18 h	5 mL
4	0.95 mg 4.8 mmol	1.76 mg 9.6 mmol	50 µL	2.2 mL	40 µL	silicon	100 °C	18 h	5 mL

*Benzoic acid (1.02 mmol; 124 mg) was dissolved in DMF (2 mL)

Table 6-3: Synthesis conditions for MOF-74(Zn) films *via* ZnO conversion

Exp.	Precursor solution				Droplet Volume	Substrate	Temp-erature	Reaction time	Vapor source	
	2,5-dihydroxy tereph-thalic acid	$Zn(OAc)_2$	THF	H_2O					THF	H_2O
5	0.95 mg 4.8 mmol	-	1.1. mL	1.1 mL	100 µL	70 nm ALD ZnO on glass	110 °C	18 h	2.5 mL	2.5 mL

Table 6-43: Synthesis conditions for MOF-74(Mg) films *via* VAC

Exp.	Precursor solution					Droplet Volume	Sub-strate	Temp-erature	Reaction time	Vapor source
	2,5-dihdroxy tereph-thalic acid	$Mg(NO_3)_2 \cdot 6\ H_2O$	Benzoic acid*	DMF	EtOH					
6	0.95 mg 4.8 mmol	2.45 mg 9.6 mmol	50 µL	2.2 mL		100 µL	glass	100 °C	18 h	5 mL DMF
7	0.95 mg 4.8 mmol	2.45 mg 9.6 mmol	50 µL	2.2 mL		100 µL	quartz	100 °C	18 h	5 mL DMF
8	0.95 mg 4.8 mmol	2.45 mg 9.6 mmol		1.6 mL	0.6 mL	50 µL	gold	100 °C	18 h	5 mL DMF/ EtOH (1: 0.28)
9	0.95 mg 4.8 mmol	2.45 mg 9.6 mmol	50 µL	2.2 mL		100 µL	silicon	100 °C	18 h	5 mL DMF

*Benzoic acid (1.02 mmol; 124 mg) was dissolved in DMF (2 mL)

Table 6-5: Synthesis conditions for oriented MOF-74(Mg) films on gold *via* VAC

Exp.	**Precursor solution**						**Droplet Volume**	**Substrate**	**Temperature**	**Reaction Time**	**Vapor source**
	2,5-dihdroxy tereph-thalic acid	$Mg(NO_3)_2$ 6 H_2O	Ben-zoic acid*	DMF	EtOH	H_2O					DMF/ EtOH/ H_2O
10	1.9 mg 9.6 mmol	4.9 mg 19.2 mmol	75 µL	1.94 mL	0.13 mL	0.13 mL	200 µL	gold	100 °C	28 h	5 mL (1:0.06 : 0.06)

Table 6-6: Synthesis conditions for MOF-74(Ni) films *via* VAC

Exp.	**Precursor solution**					**Droplet Volume**	**Sub-strate**	**Temp-erature**	**Reaction time**	**Vapor source**
	2,5-dihydroxy terephthalic acid	$Ni(NO_3)_2$ · 4 H_2O	DMF	EtOH	H_2O					DMF/ EtOH/ H_2O
11	0.95 mg 4.8 mmol	2.79 mg 9.6 mmol	2.0 mL	0.1 mL	0.1 mL	100 µL	glass	100 °C	18 h	5 mL (1:0.04 :0.04
12	0.95 mg 4.8 mmol	2.79 mg 9.6 mmol	2.0 mL	0.1 mL	0.1 mL	100 µL	quartz	100 °C	18 h	5 mL (1:0.04 :0.04
13	0.95 mg 4.8 mmol	2.79 mg 9.6 mmol	0.73 mL	0.73 mL	0.73 mL	100 µL	silicon	100 °C	18 h	5 mL (1:1:1)

Exp.	**Precursor solution**			**Droplet Volume**	**Substrate**	**Temperature**	**Reaction time**	**Vapor source**
	2,5-dihydroxy terephthalic acid	$NiCl_2$ · 6 H_2O	DMF					DMF
14	0.95 mg 4.8 mmol	2.28 mg 9.6 mmol	2.2 mL	50 µL	gold	110 °C	18 h	5 mL

Table 6-7: Synthesis conditions for MOF-74(Co) films *via* VAC

Exp.	Precursor solution					Droplet Volume	Sub-strate	Temp-erature	Reaction time	Vapor source
	2,5-dihy-droxy ter-ephthalic acid	$Co(OAc)_2$	DMF	EtOH	H_2O					
15	0.95 mg 4.8 mmol	2.39 mg 9.6 mmol	2.2 mL			100 µL	glass	100 °C	18 h	5 mL DMF
16	0.95 mg 4.8 mmol	2.39 mg 9.6 mmol	2.2 mL			100 µL	quartz	100 °C	18 h	5 mL DMF
17	0.95 mg 4.8 mmol	2.39 mg 9.6 mmol	0.73 mL	0.73 mL	0.73 mL	100 µL	silicon	110 °C	18 h	5 mL DMF/ EtOH/ H_2O (1:1:1)
	2,5-dihy-droxy ter-ephthalic acid	$CoCl_2 \cdot 6H_2O$	DMF	EtOH	H_2O					
18	0.95 mg 4.8 mmol	2.28 mg 9.6 mmol	2.1 mL		0.1 mL	50 µL	gold	100 °C	18 h	5 mL DMF/ H_2O (1:0.044))

6.7.3.5 MOF-74 bulk material synthesis

MOF-74(Zn)[14]

2,5-dihydroxy-1,4-benzenedicarboxylic acid (0.019 g, 0.096 mmol) and zinc nitrate tetrahydrate, $Zn(NO_3)_2 \cdot 4\ H_2O$ (0.053 mg, 0.203 mmol) were dissolved in DMF (2 mL), 2-propanol (0.1 mL) and water (0.1 mL). The resulting mixture was sonicated until complete dissolution of the educts was achieved and it was kept in a culture tube at 105 °C for 1 day. The resulting precipitate was washed with DMF (2 x 10 mL) and ethanol (1 x 10 mL) and dried under reduced pressure.

MOF-74(Mg)[15]

2,5-dihydroxy-1,4-benzenedicarboxylic acid (0.111 g, 0.559 mmol) and magnesia nitrate hexa-hydrate, Mg(NO3)2·6 H2O (0.475 mg, 1.85 mmol) were dissolved in a 15:1:1 (44.1 mL : 295 µL : 295 µL) mixture of DMF-ethanol-water (50 mL). The resulting mixture was sonicated until complete dissolution of the educts was achieved and it was kept in a Teflon sealed 100 mL Schott

Duran glass bottle at 125 °C for 1 day. The resulting precipitate was washed with DMF (2 x 10 mL) and methanol (1 x 10 mL) and dried under reduced pressure.

MOF-74(Ni)[15]

2,5-dihydroxy-1,4-benzenedicarboxylic acid (0.478 g, 2.41 mmol) and nickel nitrate hexahydrate, $Ni(NO_3)_2 \cdot 6\ H_2O$ (2.378 mg, 8.178 mmol) were dissolved in a 1:1:1 (666 µL : 666 µL : 666 µL) mixture of DMF-ethanol-water (200 mL). The resulting mixture was sonicated until complete dissolution of the educts was achieved and it was kept in three Teflon sealed 100 mL Schott Duran glass bottles at 100 °C for 1 day. The resulting precipitate was washed with DMF (2 x 10 mL) and methanol (1 x 10 mL) and dried under reduced pressure.

MOF-74(Co)[15]

2,5-dihydroxy-1,4-benzenedicarboxylic acid (0.482 g, 2.43 mmol) and cobalt nitrate hexahydrate, $Co(NO_3)_2 \cdot 6\ H_2O$ (2.377 g, 8.67 mmol) were dissolved in a 1:1:1 (666 µL : 666 µL : 666 µL) mixture of DMF-ethanol-water (200 mL). The resulting mixture was sonicated until complete dissolution of the educts was achieved and it was kept in three Teflon sealed 100 mL Schott Duran glass bottles at 100 °C for 1 day. The resulting precipitate was washed with DMF (2 x 10 mL) and methanol (1 x 10 mL) and dried under reduced pressure.

6.7.4 Additional thin film characterization

6.7.4.1 Additional characterization of MOF-74(Zn) films

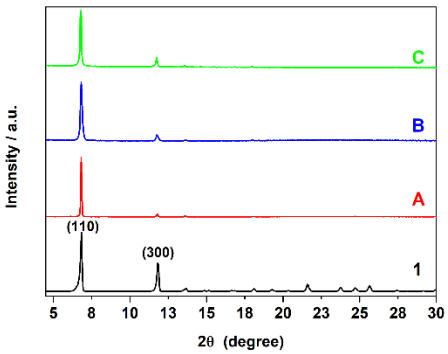

Figure 6-8: XRD patterns of (1) MOF-74(Zn) bulk material and of MOF-74 (Zn) thin films obtained by VAC with $Zn(OAc)_2$ as metal source, DMF as solvent and benzoic acid as modulator, grown on (A) gold, (B) glass and (C) silicon surfaces (see Table 6-2).

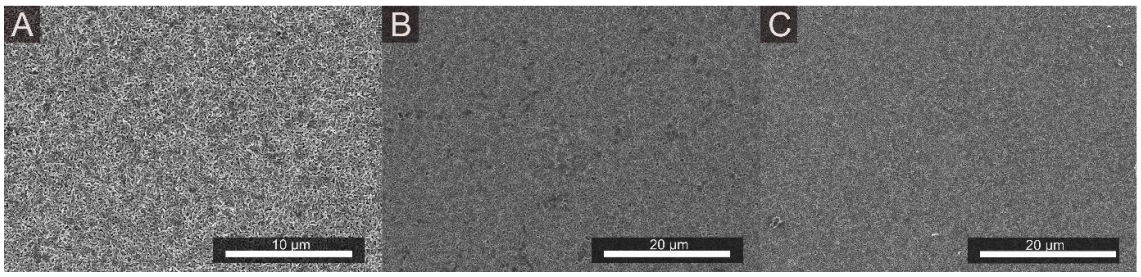

Figure 6-9: Low-magnification SEM top-view (top) and large-scale SEM cross-section images (bottom) of MOF-74(Zn) thin films grown on (A) gold, (B) glass and (C) silicon surfaces, obtained by VAC.

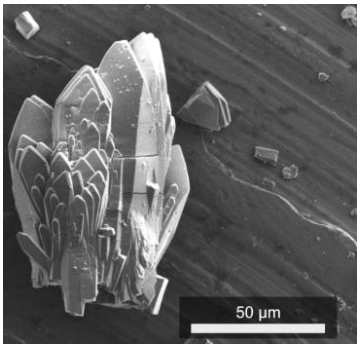

Figure 6-10: Scanning electron microscopy image of MOF-74(Zn) bulk material.

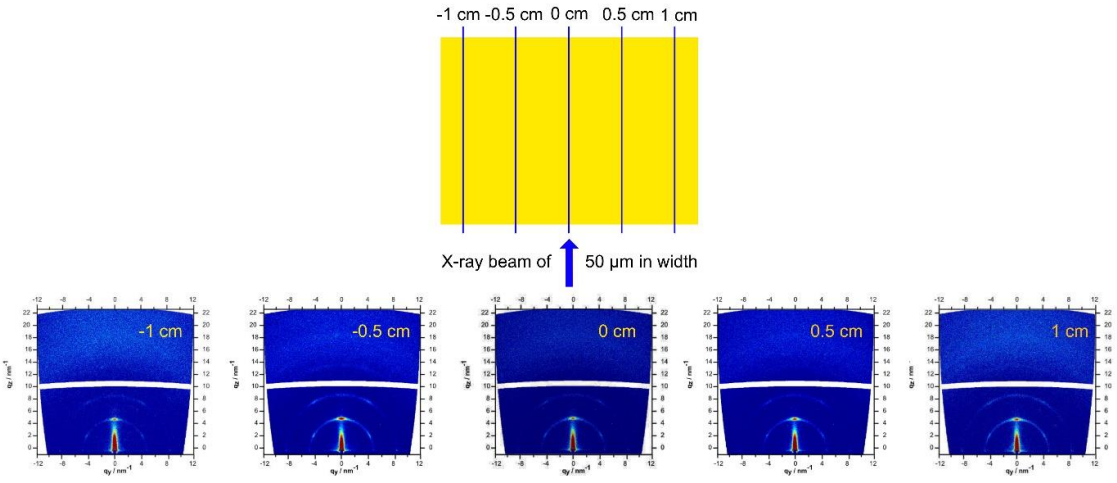

Figure 6-11: Illustration of the 2D GIWAXS line scan experiment (top) and 2D GIWAXS patterns of MOF-74(Zn) on gold (bottom), showing a high degree of orientation along the substrate.

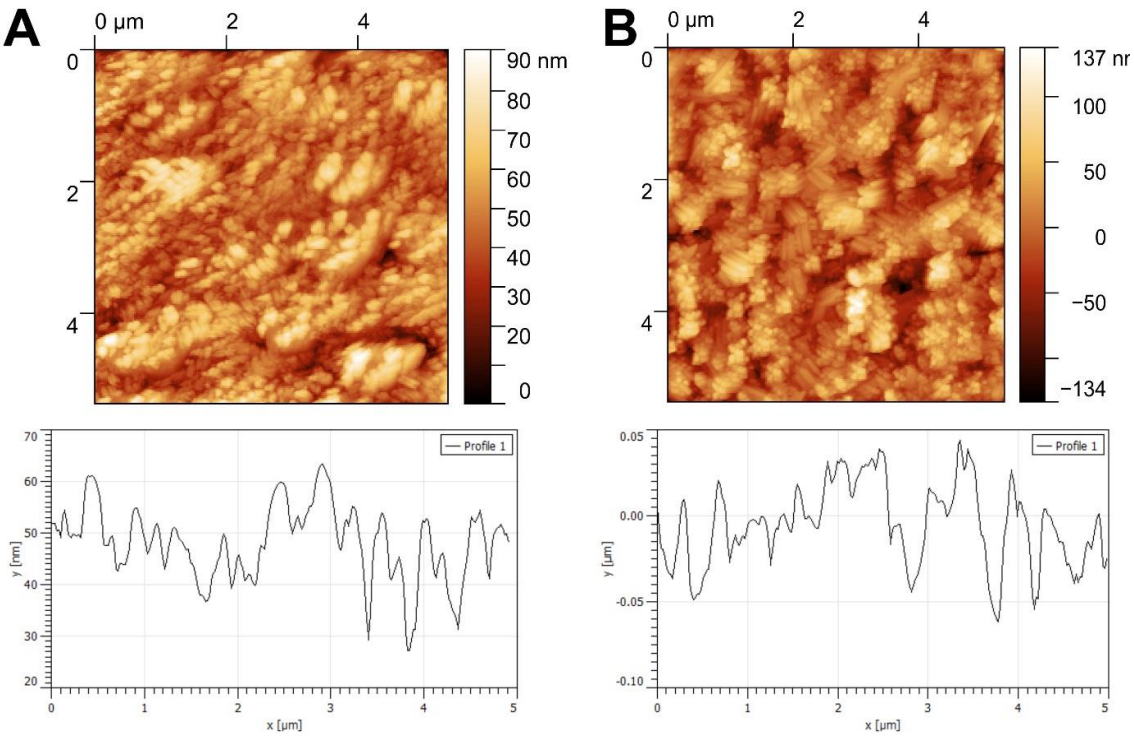

Figure 6-12: AFM measurements performed on a 5 µm x 5 µm area, displaying AFM topography image with a color bar displaying the film heights, as well as the corresponding height profile of a MOF-74(Zn) thin film on (A) a gold substrate and (B) on a glass substrate. The RMS (S_q) and R_q were calculated to be 11.5 nm and 11.1 nm for (A) and 33.6 nm and 33.1 nm for (B).

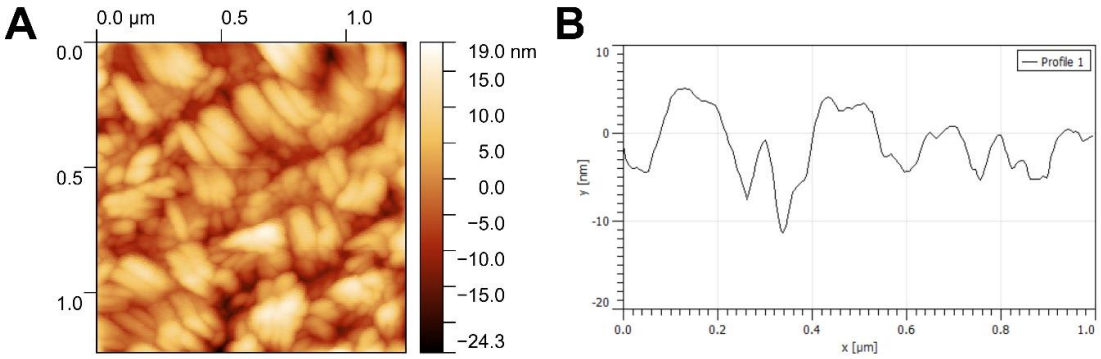

Figure 6-13: AFM measurements performed on a 1 µm x 1 µm area, displaying (A) AFM topography image with the corresponding (B) height profile of a MOF-74(Zn) thin film on a gold substrate. The RMS (S_q) and R_q were calculated to be 5.3 nm and 5.2 nm.

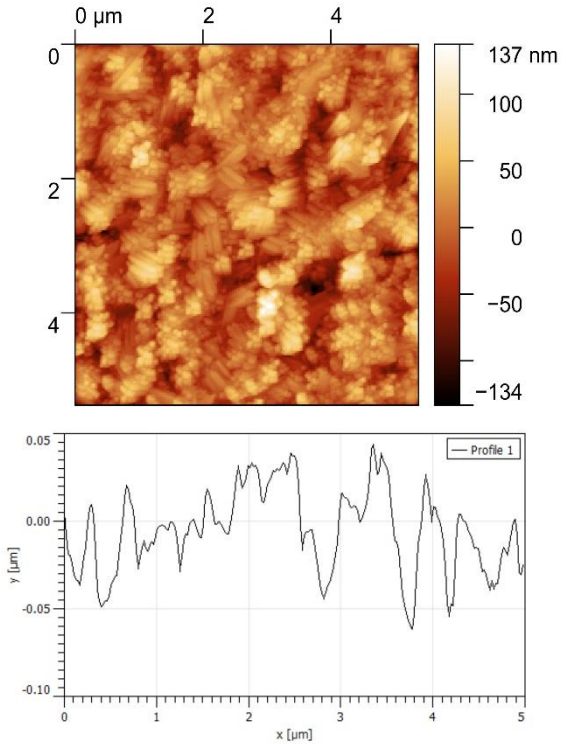

Figure 6-14: AFM measurements performed on a 5 µm x 5 µm area, displaying AFM topography images with the corresponding height profile of a MOF-74(Zn) thin film on a silicon substrate. The RMS (S_q) and R_q were calculated to be 33.1 nm and 33.6 nm.

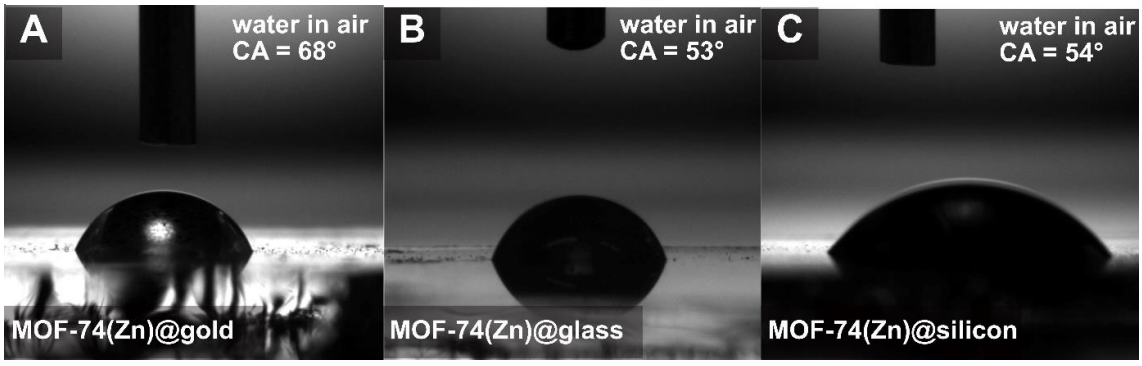

Figure 6-15: Water contact angle (WCA) measurements in air of MOF-74(Zn) grown on (A) gold, (B) glass, (C) silicon.

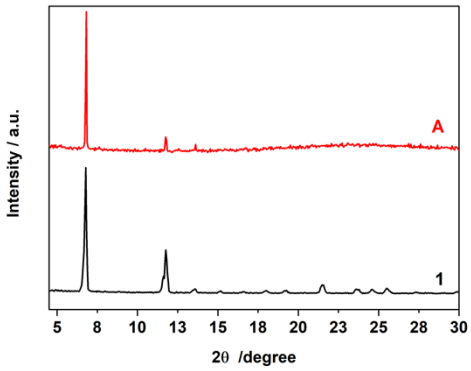

Figure 6-16: XRD patterns of MOF-74 (Zn) bulk material (1) and of a MOF-74 (Zn) thin film obtained by the conversion of a 70 nm ALD ZnO layer (A) in a THF/ H_2O mixture as solvent (see Table).

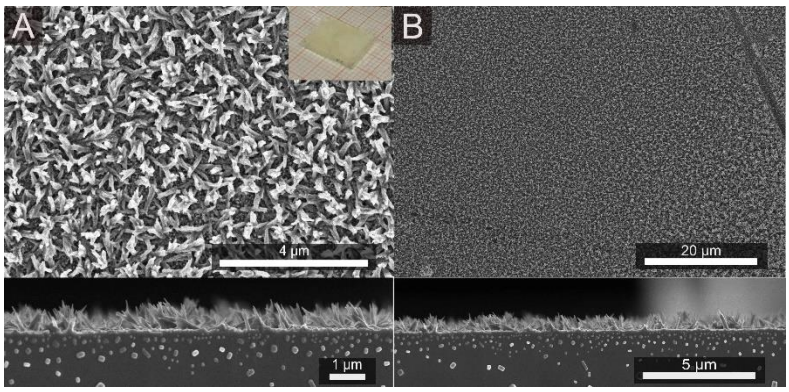

Figure 6-17: SEM top-view and cross-section images of a MOF-74(Zn) thin film grown on a 70 nm ALD ZnO layer as seed layer and metal precursor, obtained by VAC. (A) High-magnification and (B) low-magnification. Photo image of the thin film is shown as inset in (A).

6.7.4.2 Additional characterization of MOF-74(Mg) films

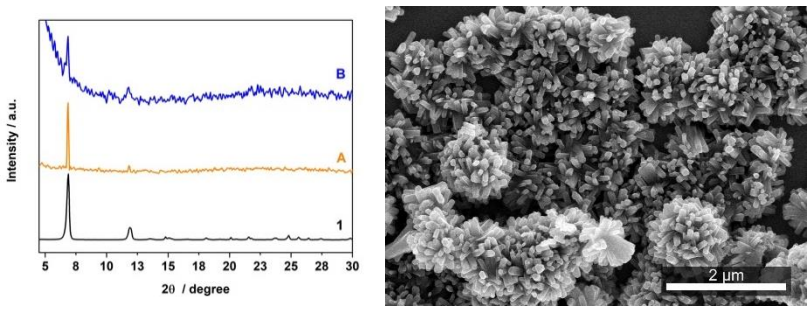

Figure 6-18: (Left) XRD patterns of (1) MOF-74(Mg) bulk material and of MOF-74(Mg) thin films grown on a (A) gold surface (unoriented) with $Mg(NO_3)_2$ 6 H_2O as metal precursor and a DMF/ EtOH solvent mixture and (B) a silicon surface with DMF as solvent and benzoic acid as modulator (see Table 6-43-4). (Right) SEM image of MOF-74(Mg) grown on silicon, obtained by VAC.

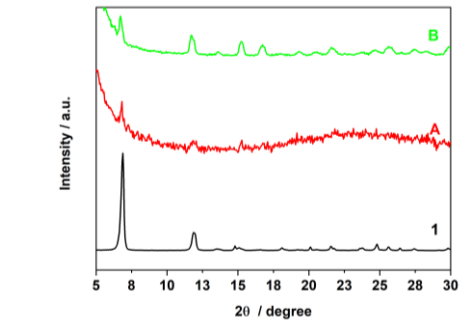

Figure 6-19: XRD pattern of MOF-74(Mg) (1) bulk material and of MOF-74(Mg) thin films grown on (A) glass with $Mg(NO_3)_2$ 6 H_2O as metal precursor, DMF as solvent and benzoic acid as modulator and (B) on gold surface (oriented) with a DMF/ EtOH/ H_2O solvent mixture and benzoic acid modulator (see Table 6-43-4 and Table).

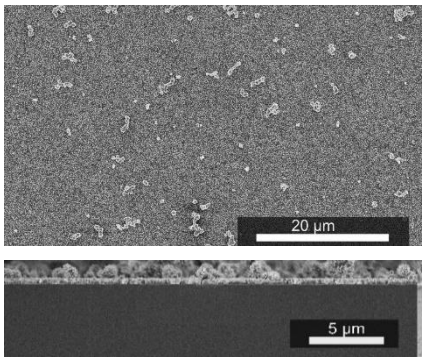

Figure 6-20: Low-magnification SEM top-view and cross-section images of a MOF-74(Mg) thin film grown on glass surfaces (oriented), obtained by VAC.

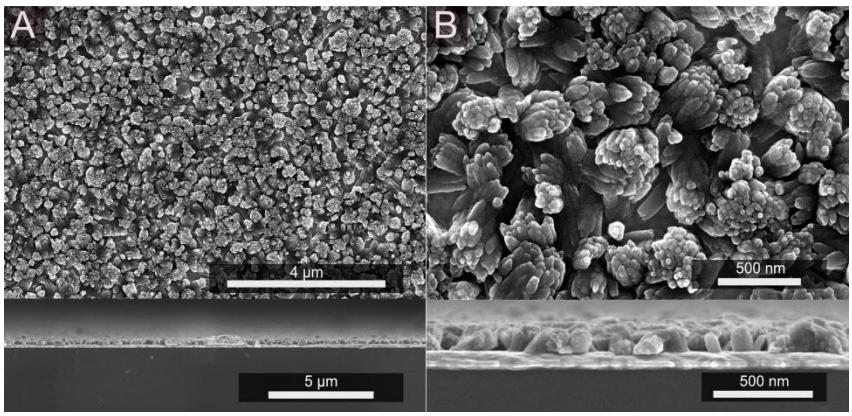

Figure 6-21: (A) Low-magnification (B) and high-magnification SEM top-view and cross-section images of a MOF-74(Mg) thin film grown on a gold surface (nonoriented), obtained by VAC.

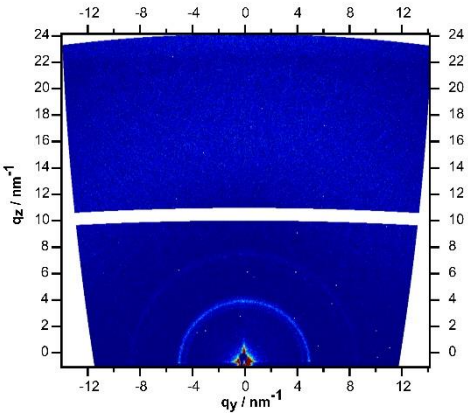

Figure 6-22: 2D GIWAXS patterns of a MOF-74(Mg) thin film grown on gold (nonoriented).

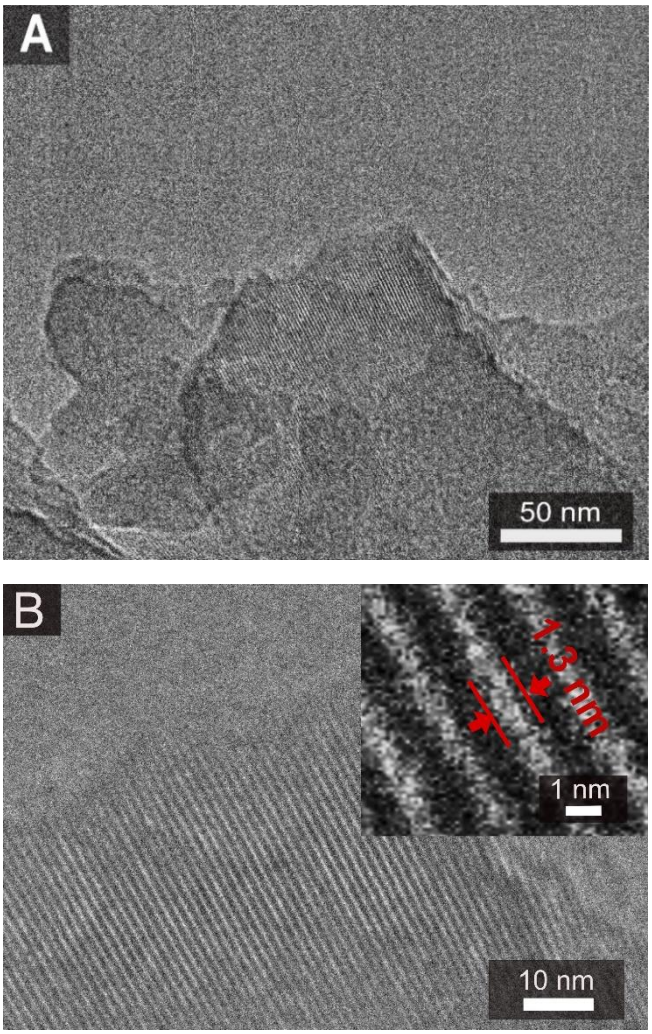

Figure 6-23: (A) TEM micrograph of MOF-74(Mg) materials, grown on gold substrates (removed from substrate), in a side view. (B) a close up of (A), showing lattice fringes with interplanar spacings of (110) planes as inset.

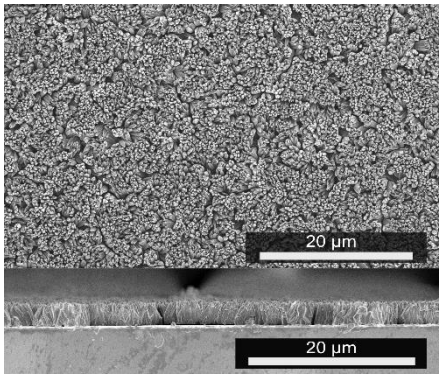

Figure 6-24: Low-magnification SEM top-view and cross-section images of a MOF-74(Mg) film grown on gold surfaces (oriented), obtained by VAC.

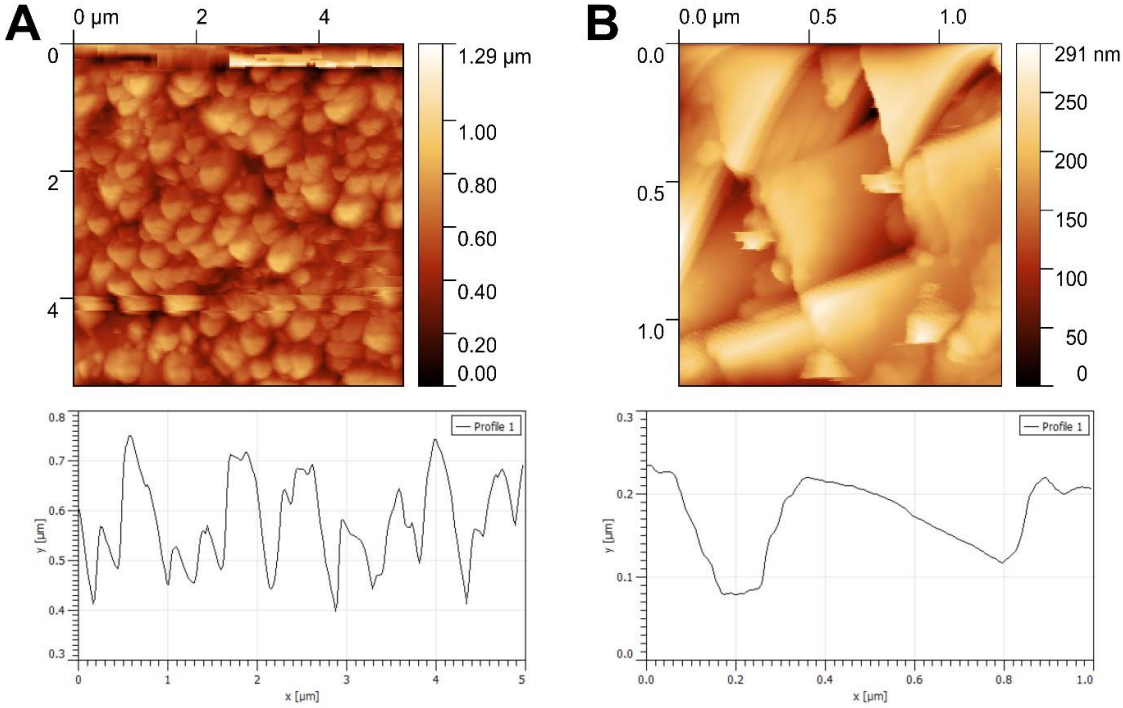

Figure 6-25: AFM measurements performed on an (A) 5 µm x 5 µm area and (B) 1 µm x 1 µm area, displaying AFM topography images with the corresponding height profile of a MOF-74(Mg) thin film on gold. The RMS (S_q) and R_q were calculated to be for (A) 54 nm and 52 nm, for (B) 35 nm and 33 nm.

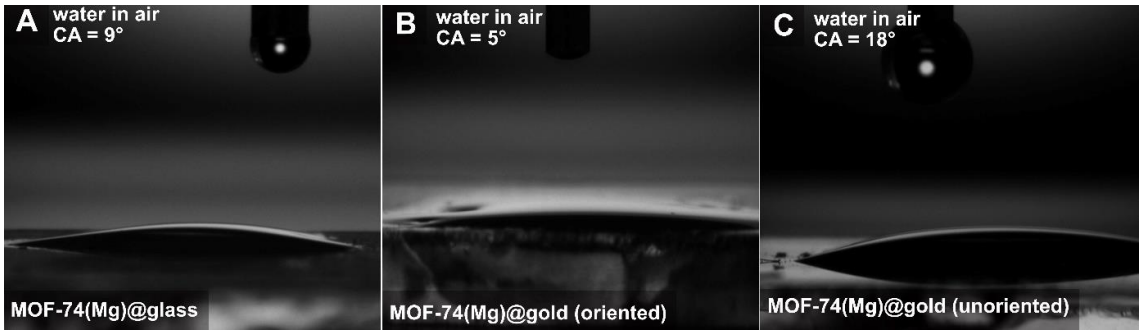

Figure 6-26: WCA measurements in air with water as test liquid of (A) MOF-74(Mg) grown on glass, (B) MOF-74(Mg) grown on gold (oriented) and (C) MOF-74(Mg) grown on gold (unoriented).

6.7.4.3 Time dependent monitoring of MOF-74(Zn, Mg) film growth

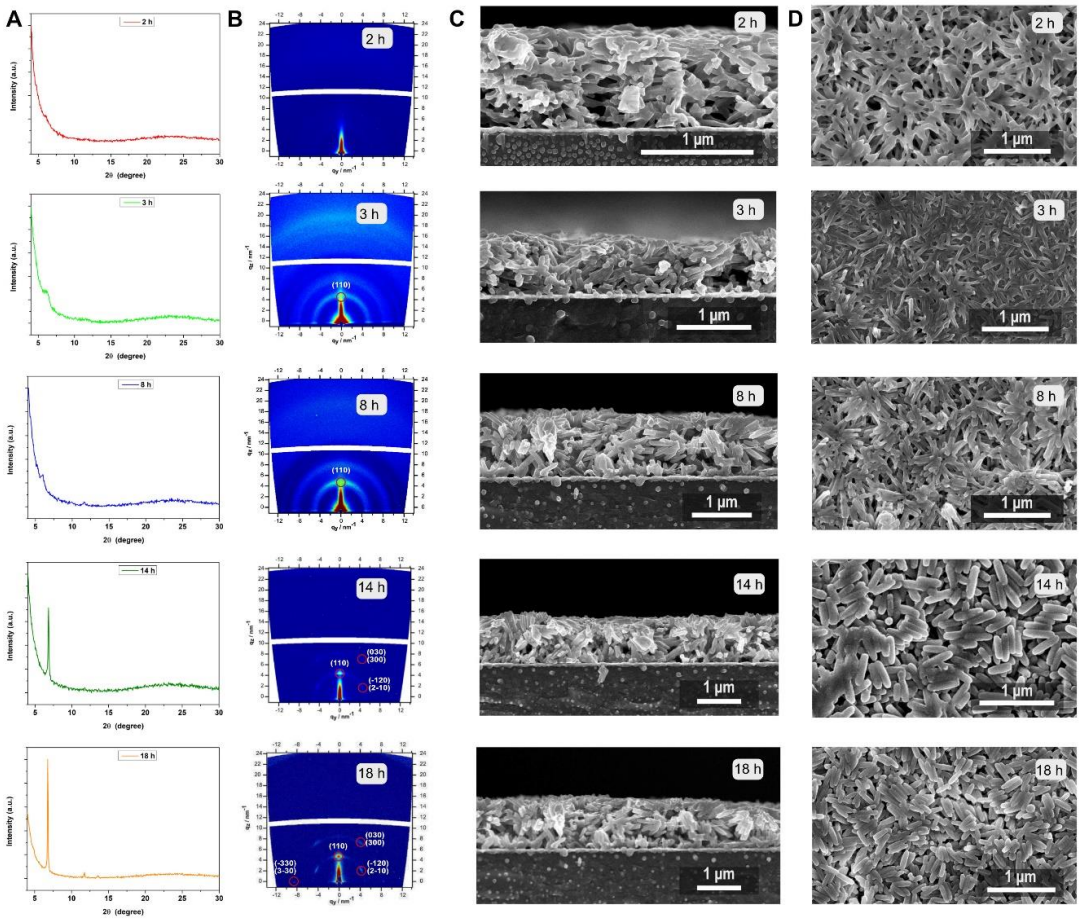

Figure 6-27: Time-dependent MOF-74(Zn) growth experiments on a gold substrate with a droplet volume of 100 µL via VAC. (A) XRD patterns. (B) 2D GIWAXS patterns. (C) SEM top-view and (D) SEM cross-section images.

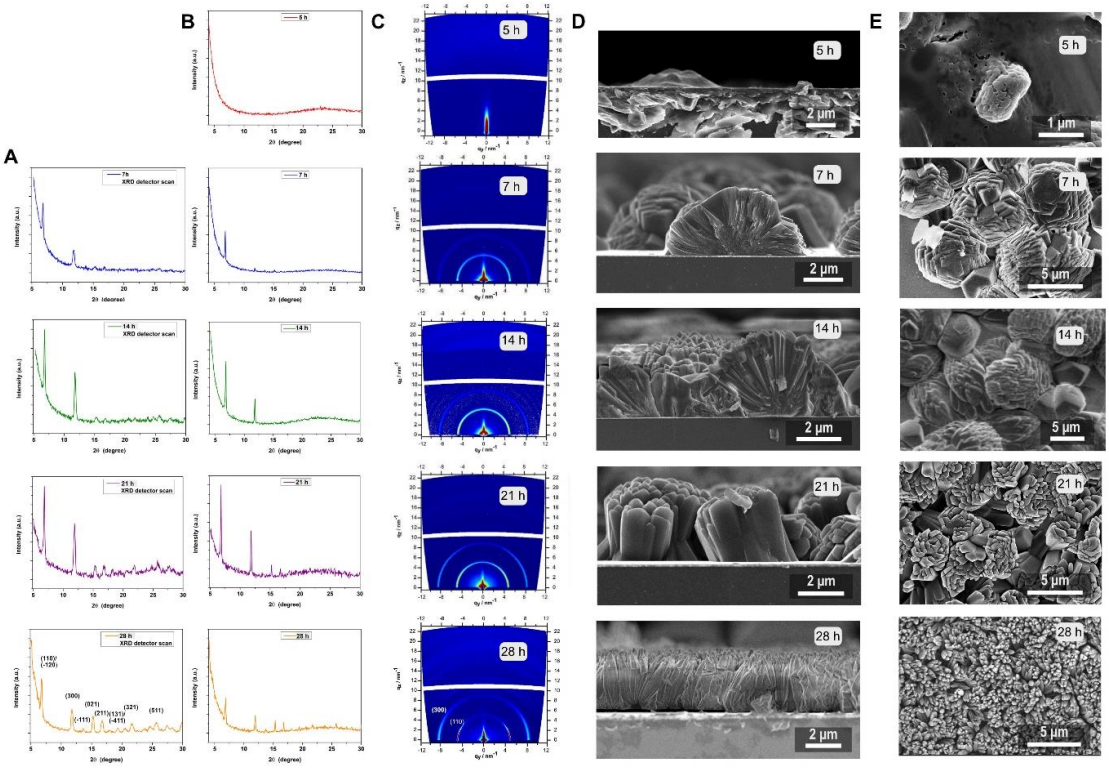

Figure 6-28: Time-dependent MOF-74(Mg) growth experiments on a gold substrate with a droplet volume of 100 µL *via* VAC. (A) XRD patterns. (B) 2D GIWAXS patterns. (C) SEM top-view and (D) SEM cross-section images.

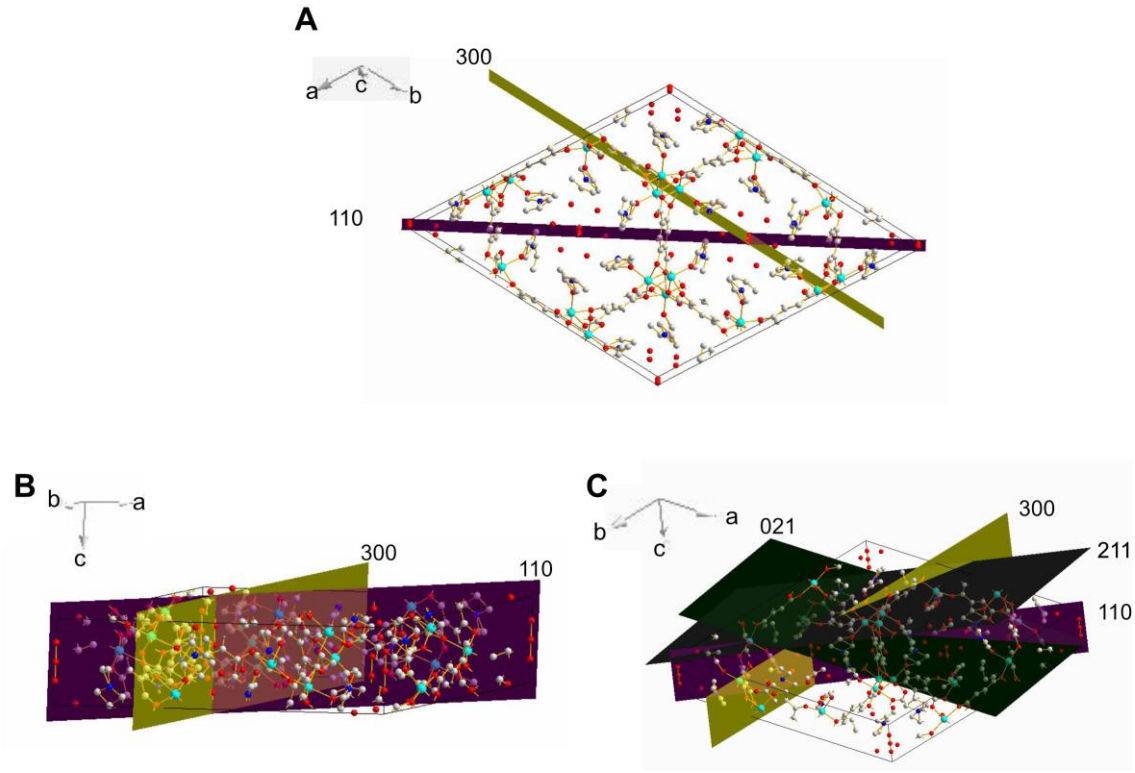

Figure 6-29: Crystal structure of MOF-74[14] with displayed lattice planes in different orientations of the unit cell.

6.7.4.4 Additional characterization of MOF-74(Co) films

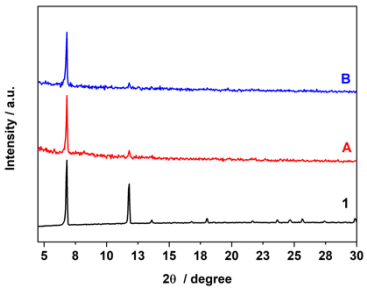

Figure 6-30: X-ray diffraction patterns of (1) MOF-74(Co) bulk material and of MOF-74 (Co) thin films grown on (A) glass with $Co(OAc)_2$ as metal precursor and DMF as solvent, (B) silicon with a DMF/ EtOH/ H_2O solvent mixture (see 6-7).

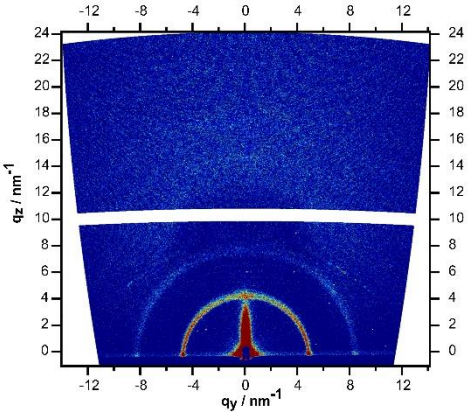

Figure 6-31: 2D GIWAXS patterns of a MOF-74(Co) thin film grown on gold.

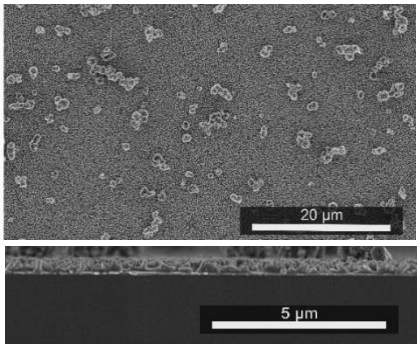

Figure 6-32: Low-magnification SEM top-view images (top) and low-magnification SEM cross-section images (bottom) of a MOF-74(Co) thin film grown on a gold surface with $CoCl_2$ 6 H_2O as metal precursor and a DMF/ H_2O solvent mixture, obtained by VAC (see Table).

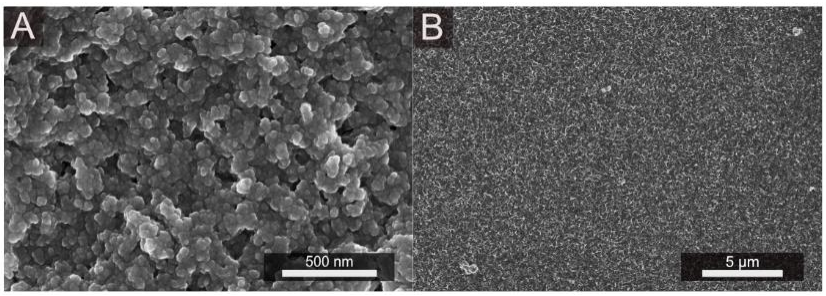

Figure 6-33: SEM top-view images of MOF-74 (Co) thin films grown on (A) glass and (B) silicon surfaces, obtained by VAC.

6.7.4.5 Additional characterization of MOF-74(Ni) films

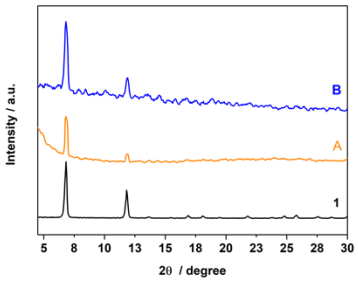

Figure 6-34: X-ray diffraction patterns of (1) MOF-74 (Ni) bulk material and of MOF-74(Ni) thin films grown on (A) gold with $NiCl_2 \cdot 6H_2O$ as metal precursor and DMF as solvent, and (B) silicon with $Ni(NO_3)_2 \cdot 4H_2O$ as metal precursor and a DMF/ EtOH/ H_2O solvent mixture, obtained by VAC (see Table 6-6).

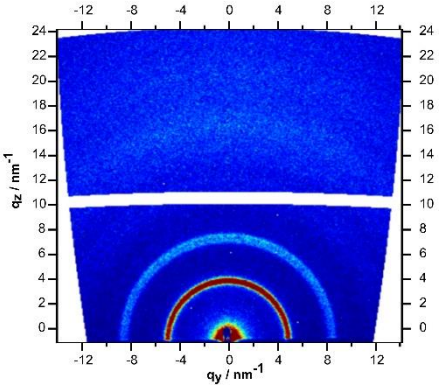

Figure 6-35: 2D GIWAXS patterns of MOF-74(Ni) thin film grown on glass.

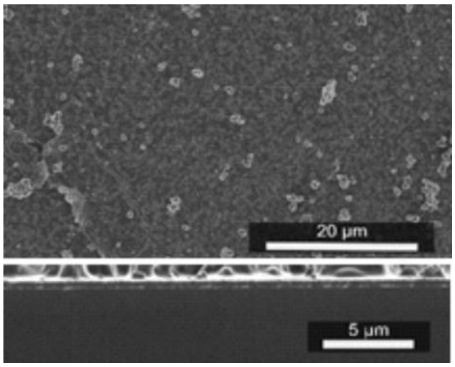

Figure 6-36: Low-magnification SEM top-view images (top) and low-magnification SEM cross-section images (bottom) of an MOF-74(Ni) thin film grown on a glass surface with $Ni(NO_3)_2 \cdot 4H_2O$ as metal precursor and a DMF/ EtOH/ H_2O solvent mixture, obtained by VAC (seeTable).

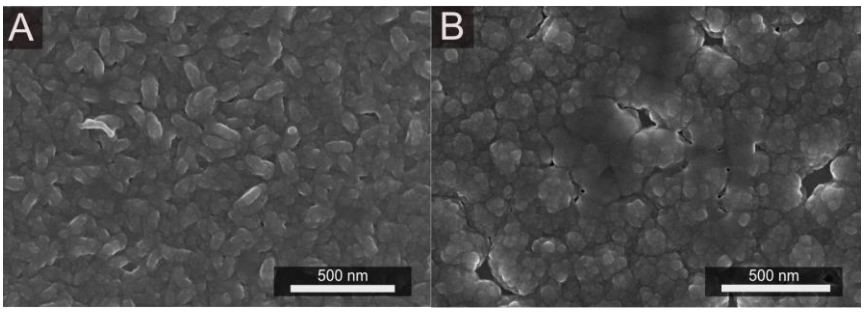

Figure 6-37: SEM top-view images of MOF-74(Ni) thin films grown on (A) gold and (B) silicon surfaces, obtained by VAC.

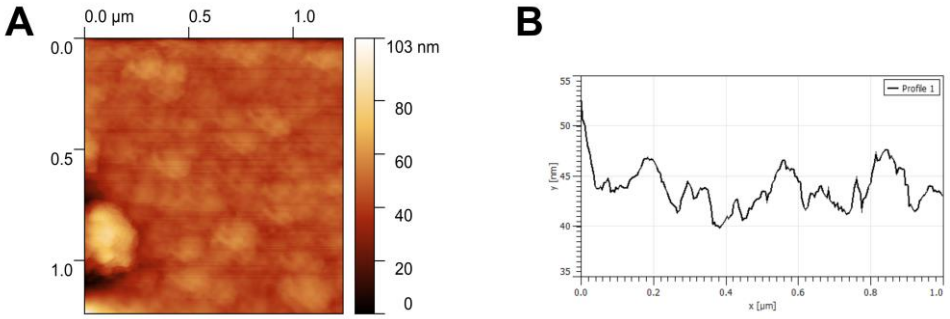

Figure 6-38: AFM measurements of MOF-74(Ni) thin films on glass substrates performed on (A) 1 µm x 1 µm film area and displaying AFM topography images with (B) the corresponding height profile. The RMS (S_q) and R_q were calculated to be 18.5 nm and 10.3 nm (A).

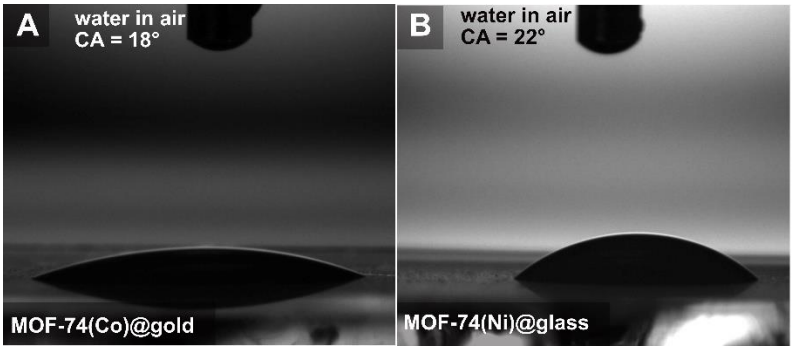

Figure 6-39: WCA measurements in air of (A) MOF-74(Co) grown on gold and (B) MOF-74(Ni) grown on glass.

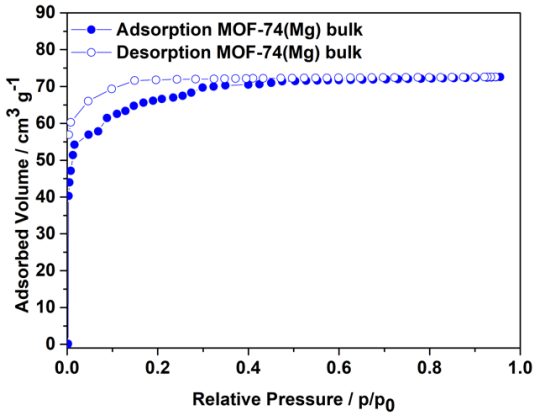

Figure 6-40: Krypton sorption isotherm of degassed MOF-74(Mg) bulk material at 77.3 K.

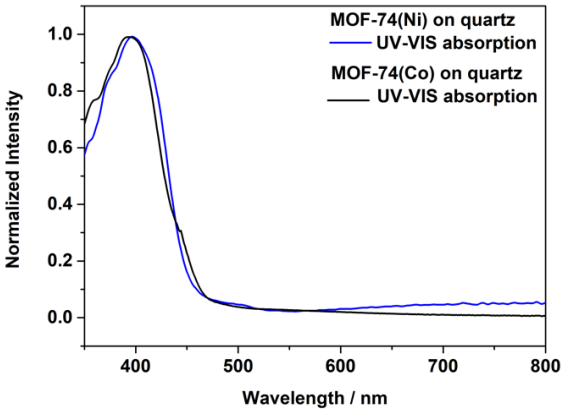

Figure 6-41: UV-Vis absorption spectra of MOF-74(M = Ni, Co).

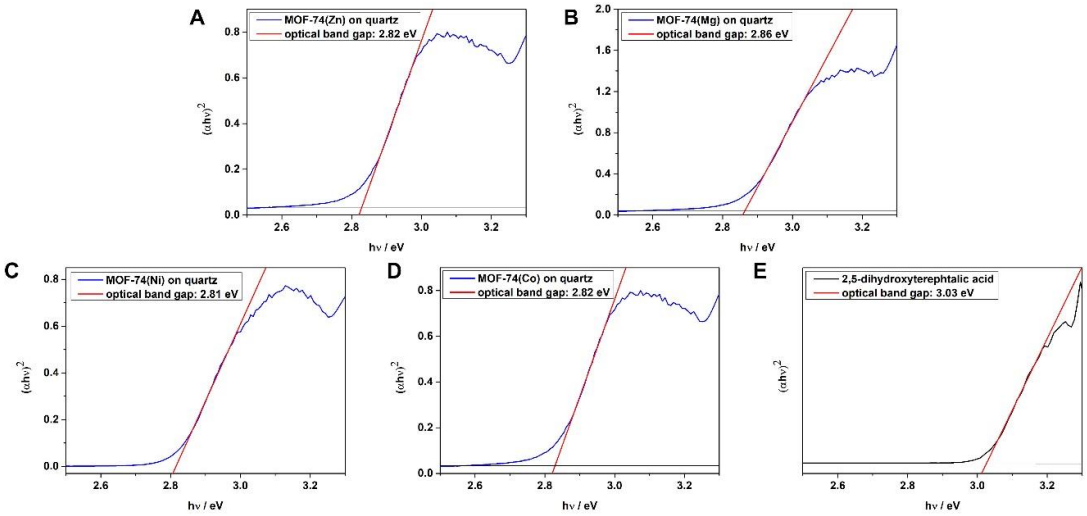

Figure 6-42: Tauc plots of (A) MOF-74(Zn), (B) MOF-74(Mg), (C) MOF-74(Ni), (D) MOF-74(Co) grown on quartz glass and of (E) 2,5-dihydroxyterephthalic acid measured in solution, assuming a direct band gap.

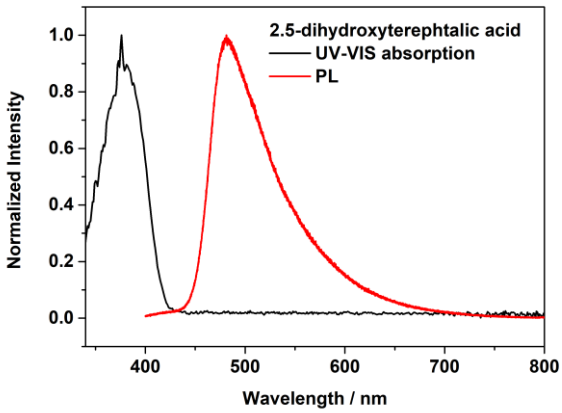

Figure 6-43: UV-Vis absorption spectrum of 2,5-dihydroxyterephthalic acid dissolved in MeOH (black line) and the photoluminescence spectrum (PL) measured as solid with 378 nm excitation (red line).

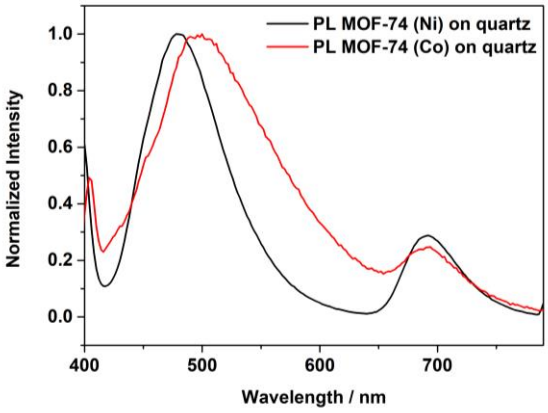

Figure 6-44: Photoluminescence (PL) spectra of MOF-74(M = Ni, Co) thin films measured with 378 nm excitation.

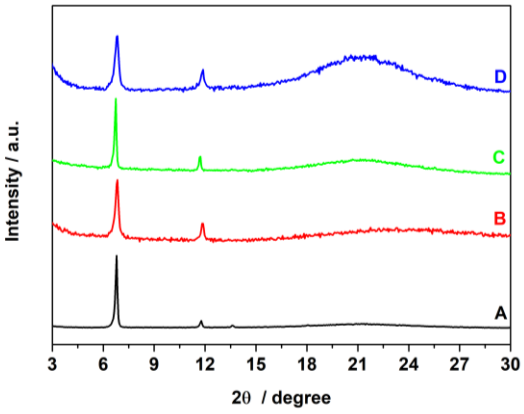

Figure 6-45: X-ray diffraction patterns of (A) MOF-74(Zn), (B) MOF-74(Mg), (C) MOF-74(Ni) and (D) MOF-74(Co) thin films on quartz, all obtained by VAC.

6.7.4.6 Data reduction plots of the 2D GIWAXS diffraction analysis

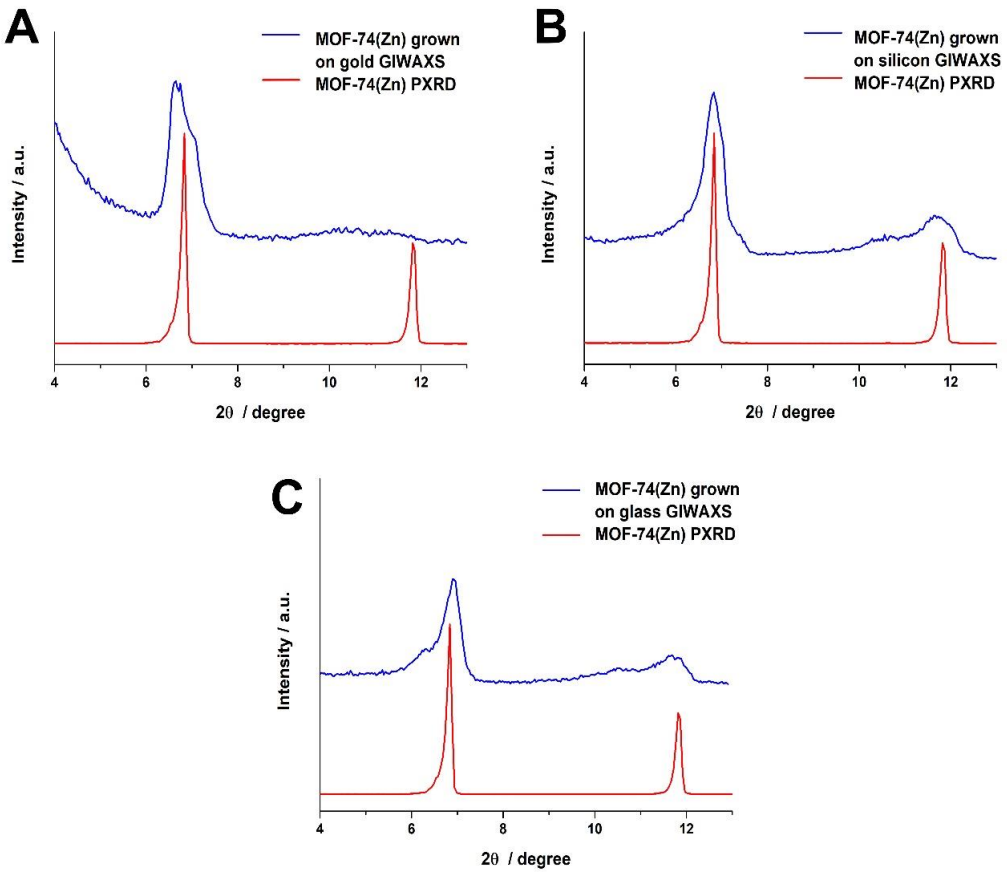

Figure 6-46: 1D plots of the 2D GIWAXS diffraction patterns of (A) MOF-74(Zn) grown on gold, (B) MOF-74(Zn) grown on silicon and (C) MOF-74(Zn) grown on glass, given in Figure 6-2 and the powder diffraction patterns of the corresponding bulk materials (red). The patterns confirm the formation of crystalline MOF-74 materials as the crystalline phase on the substrates.

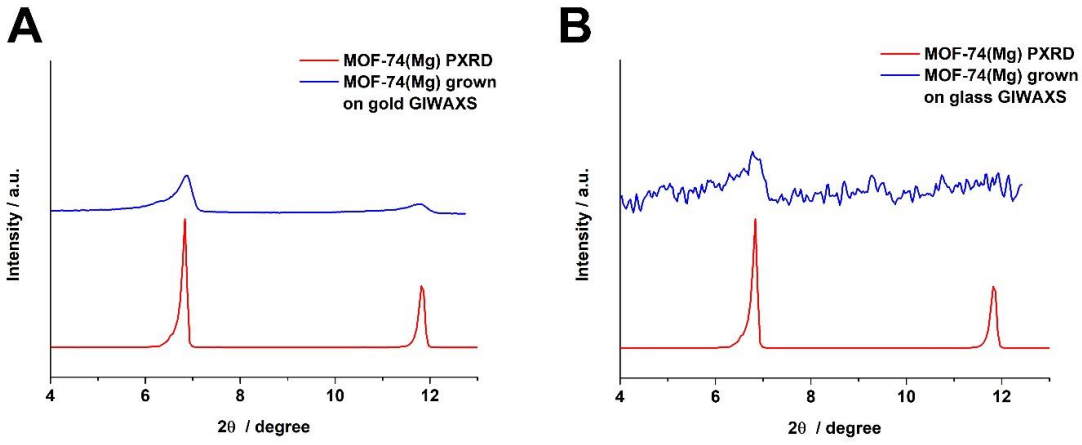

Figure 6-47: 1D plots of the 2D GIWAXS diffraction patterns of (A) MOF-74 (Mg) grown on gold (oriented), (B) MOF-74(Mg) grown on glass given in Figure S5, and the powder diffraction patterns of the corresponding bulk materials (red). The patterns confirm the formation of crystalline MOF-74 materials as the crystalline phase on the substrates.

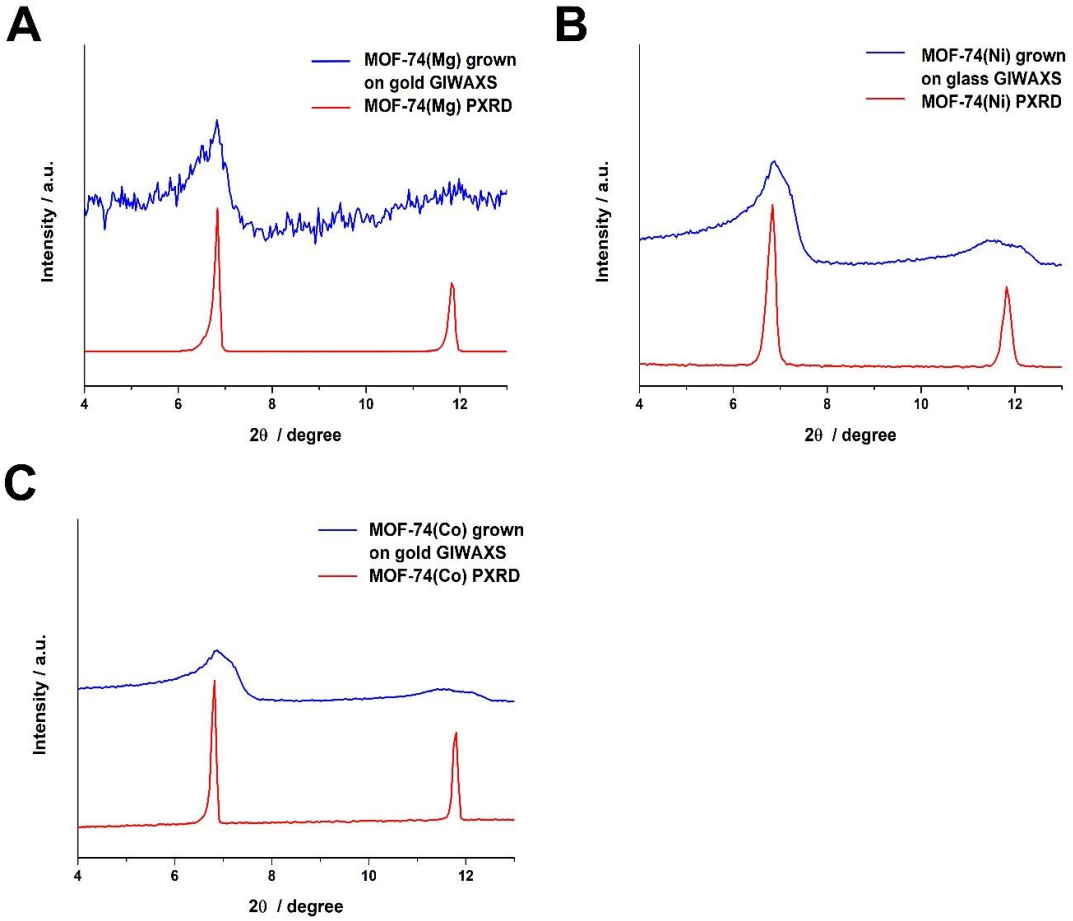

Figure 6-48: 1D plots of the 2D GIWAXS diffraction patterns of (A) MOF-74(Mg) grown on gold (unoriented), (B) of MOF-74(Ni) grown on glass, (C) MOF-74(Co) grown on gold and the powder diffraction patterns of the corresponding bulk materials (red). The patterns confirm the formation of crystalline MOF-74 materials as the crystalline phase on the substrates.

6.7.4.7 Additional contact angle measurements

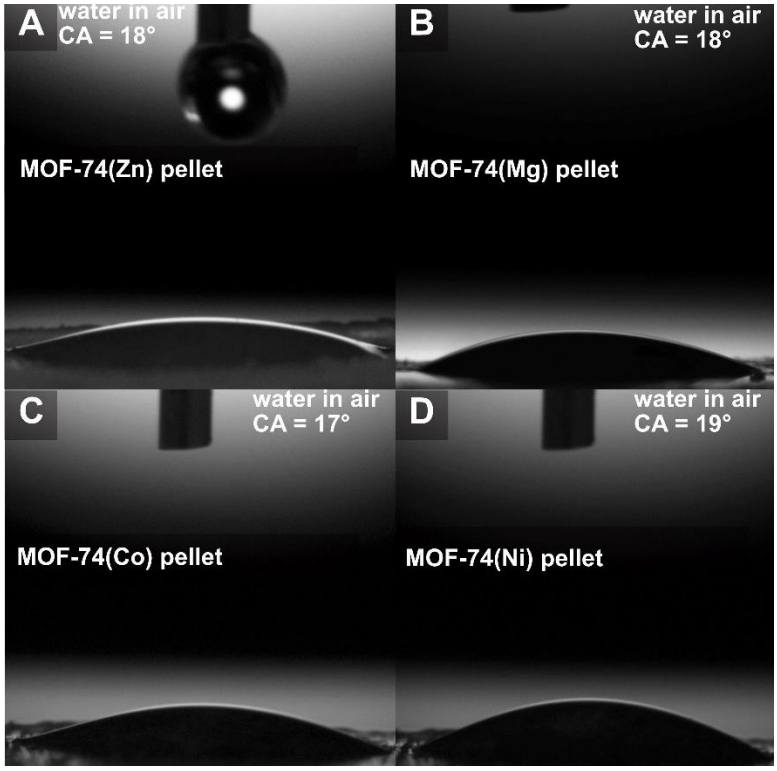

Figure 6-49: WCA measurements in air of a (A) MOF-74(Zn) pressed pellet, (B) MOF-74(Mg) pressed pellet, (C) MOF-74(Co) pressed pellet and (D) MOF-74(Ni) pressed pellet.

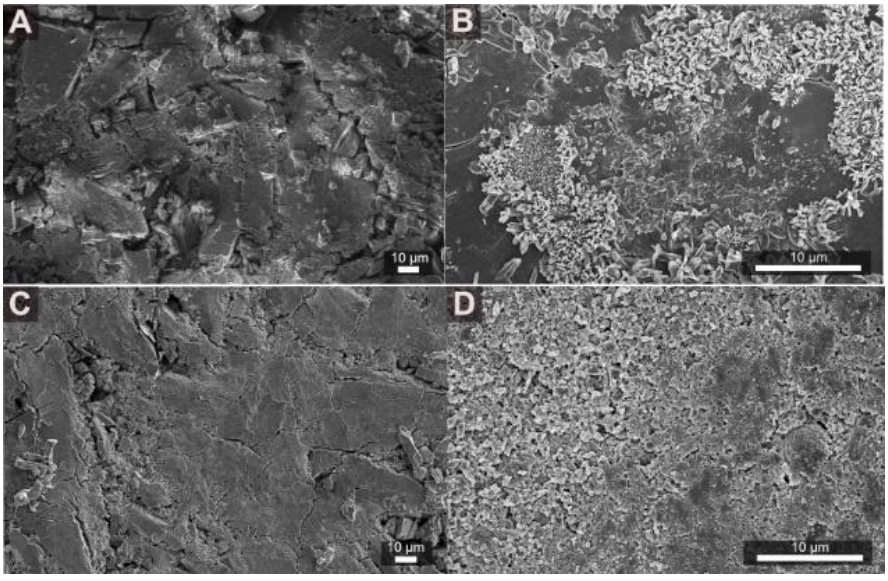

Figure 6-50: SEM images of pressed pellets of (A) MOF-74(Zn), (B) MOF-74(Mg), (C) MOF-74(Ni) and (D) MOF-74(Co) bulk material (1 cm diameter, thickness 500 µm, 100 mg activated MOF).

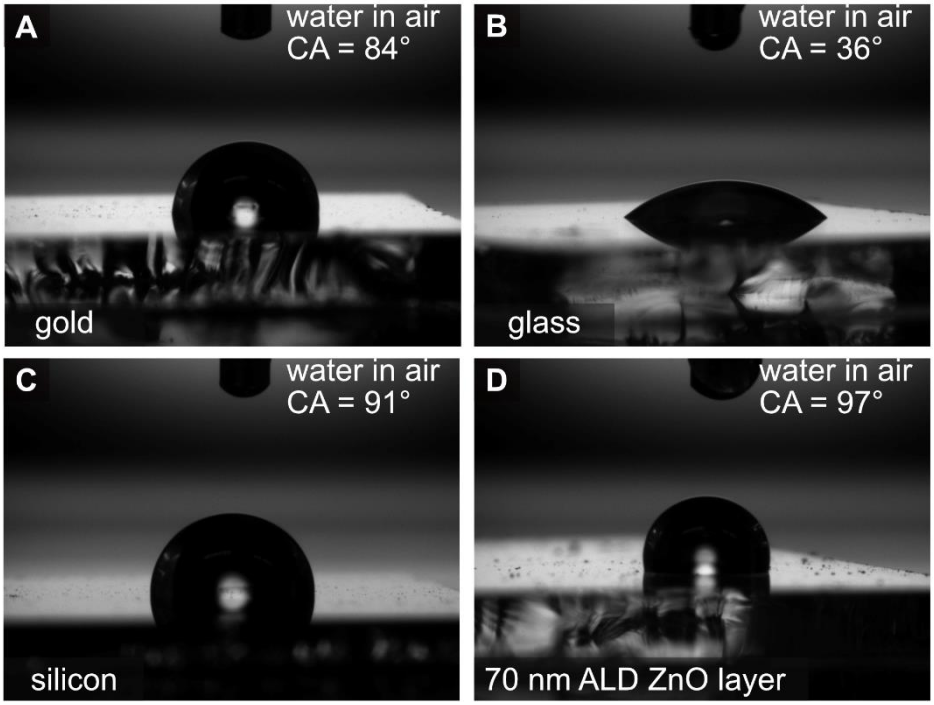

Figure 6-51: WCA measurements in air on (A) a bare gold surface, (B) on a bare glass surface, (C) on a bare silicon surface and (D) on a 70 nm ALD ZnO layer.

6.7.4.8 Characterization of the MOF-74(M) bulk material

XRD analysis

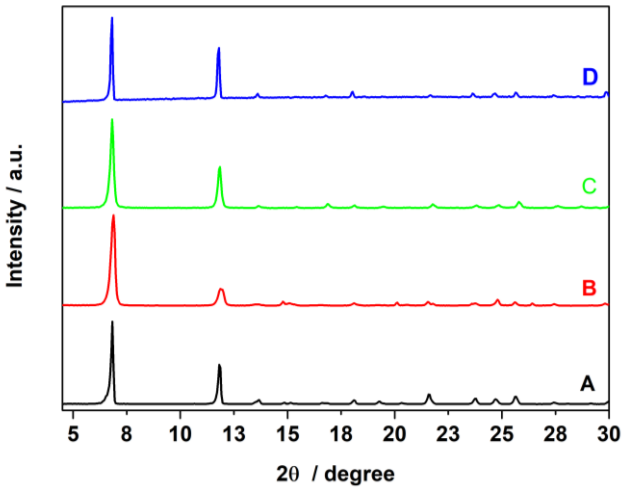

Figure 6-52: XRD patterns of (A) MOF-74(Zn), (B) MOF-74(Mg), (C) MOF-74(Ni) and (D) MOF-74(Co) bulk materials.

SEM analysis

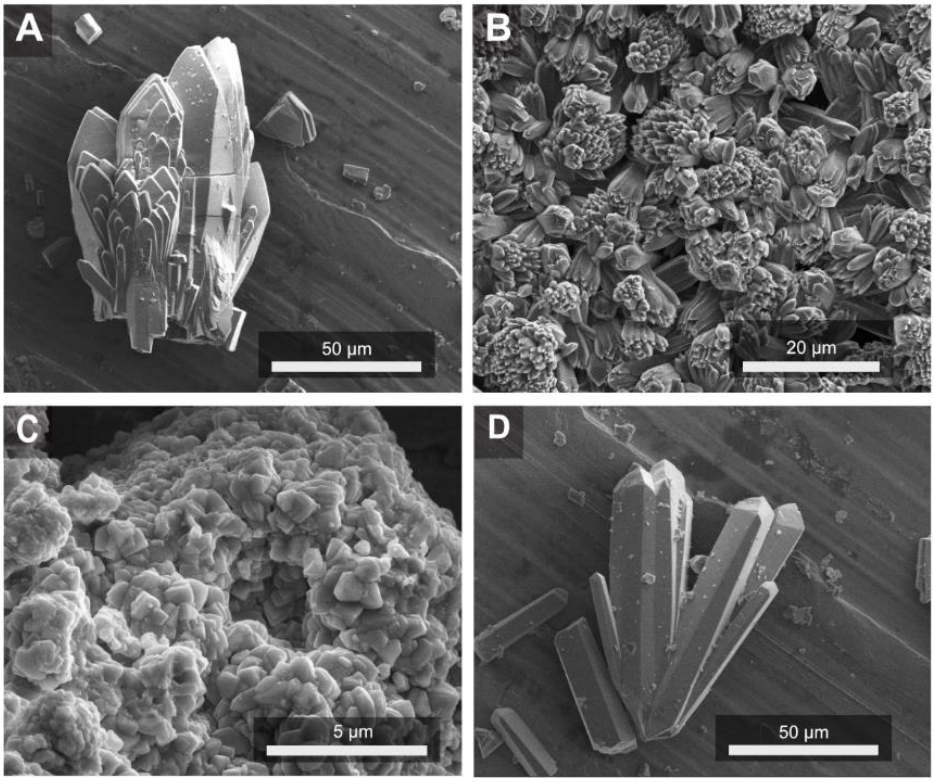

Figure 6-53: SEM images of (A) MOF-74(Zn), (B) MOF-74(Mg), (C) MOF-74(Ni) and (D) MOF-74(Co) bulk materials.

6.7.5 References

(1) Bétard, A.; Zacher, D.; Fischer, R. A. Dense and homogeneous coatings of CPO-27-M type metal–organic frameworks on alumina substrates. *CrystEngComm* **2010**, *12*, 3768–3772.

(2) Lee, D.-J.; Li, Q.; Kim, H.; Lee, K. Preparation of Ni-MOF-74 membrane for CO2 separation by layer-by-layer seeding technique. *Microporous Mesoporous Mat.* **2012**, *163*, 169–177.

(3) Rezaei, F.; Lawson, S.; Hosseini, H.; Thakkar, H.; Hajari, A.; Monjezi, S.; Rownaghi, A. A. MOF-74 and UTSA-16 film growth on monolithic structures and their CO2 adsorption performance. *Chem. Eng. J.* **2017**, *313*, 1346–1353.

(4) Zhao, Z.; Zuhra, Z.; Qin, L.; Zhou, Y.; Zhang, L.; Tang, F.; Mu, C. Confinement of microporous MOF-74(Ni) within mesoporous γ-Al2O3 beads for excellent ultra-deep and selective adsorptive desulfurization performance. *Fuel Process. Technol.* **2018**, *176*, 276–282.

(5) Luo, J.; Li, Y.; Zhang, H.; Wang, A.; Lo, W.-S.; Dong, Q.; Wong, N.; Povinelli, C. ; Shao, Y.; Chereddy, S.; Wunder, S.; Mohanty, U.; Tsung, C.-K.; Wang, D.. A Metal-Organic Framework Thin Film for Selective Mg2+ Transport. *Angew. Chem.* **2019**, *43*, 15457–15461.

(6) Jodlowski, P.J.; Kurowski, G.; Dymek, K.; Jedrzejczyk, R.J.; Jelen, P.; Kuterasinski, L.; Gancarczyk, A.; Wegrzynowicz, A.; Sawoszczuk, T.; Sitarz, M.. In situ deposition of M(M=Zn; Ni; Co)-MOF-74 over structured carriers for cyclohexene oxidation - Spectroscopic and microscopic characterisation. *Microporous Mesoporous Mat.* **2020**, *303*, 110249.

(7) Yuan, H.; Tao, J.; Li, N.; Karmakar, A.; Tang, C.; Cai, H.; Pennycook, S. J.; Singh, N.; Zhao, D. On-Chip Tailorability of Capacitive Gas Sensors Integrated with Metal-Organic Framework Films. *Angew. Chem. Int. Ed.* **2019**, *58*, 14089–14094.

(8) Campbell, J.; Tokay, B. Controlling the size and shape of Mg-MOF-74 crystals to optimise film synthesis on alumina substrates. *Microporous Mesoporous Mat.* **2017**, *251*, 190–199.

(9) Chaudhari, A. K.; Souza, B. E.; Tan, J.-C. Electrochromic thin films of Zn-based MOF-74 nanocrystals facilely grown on flexible conducting substrates at room temperature. *APL Mater.* **2019**, *7*, 081101.

(10) Zhou, S.; Wang, S.; Xu, H.; Zhao, J.; Wang, J.; Li, Y. An electrochromic supercapacitor based on an MOF derived hierarchical-porous NiO film. *Nanoscale* **2020**, *12*, 8934–8941.

(11) Zhou, W.; Xue, Z.; Liu, Q.; Li, Y.; Hu, J.; Li, G. Trimetallic MOF-74 Films Grown on Ni Foam as Bifunctional Electrocatalysts for Overall Water Splitting. *ChemSusChem* **2020**, *13*, 5647–5653.

(12) Lowell, S.; Shields, J.E.; Thomas, M.A.; Thommes, M.; *Characterization of Porous Solids and Powders SurfaceArea, Pore Size and Density*; Springer Netherlands: Dordrecht, 2006; pp 71 - 80.

(13) McClellan, A. L.; Harnsber, H. F. Cross-Sectional Areas of Molecules Adsorbed on Solids Surfaces. *J. Colloid Interface Sci.* **1967**, *23*, 577–599.

(14) Rosi, N. L.; Kim, J.; Eddaoudi, M.; Chen, B.; O'Keeffe, M.; Yaghi, O. M. Rod packings and metal-organic frameworks constructed from rod-shaped secondary building units. *J. Am. Chem. Soc.* **2005**, *127*, 1504–1518.

(15) Caskey, S. R.; Wong-Foy, A. G.; Matzger, A. J. Dramatic tuning of carbon dioxide uptake via metal substitution in a coordination polymer with cylindrical pores. *J. Am. Chem. Soc.* **2008**, *130*, 10870–10871.

7 A cubic coronene-based MOF

This chapter is based on the following article:

An electrically conducting 3D coronene-based metal-organic framework

Patricia I. Scheurle[a, b, †], Laura Frey[a, b, †], Markus Döblinger[a, b], Marta Martínez-Abadía[c], Andre Mähringer[a, b], Lena Harms[e], Gunter Wittstock[e], Aurelio Mateo-Alonso[c], Thomas Bein[a, b], Dana D. Medina[a, b]. *Manuscript in preparation.*

[a]Department of Chemistry, Ludwig-Maximilians-Universität (LMU), Butenandtstr. 11 (E), 81377 Munich, Germany.

[b]Nanosystems Initiative Munich (NIM) and Center for NanoScience (CeNS), Schellingstr. 4, 80799 Munich, Germany.

[c]POLYMAT, University of the Basque Country UPV/EHU. Avenida de Tolosa 72, E-20018 Donostia-San Sebastián, Spain

[e]School of Mathematics and Science, Department of Chemistry, Carl von Ossietzky University of Oldenburg, 26111 Oldenburg (Germany)

†The authors contributed equally to this work.

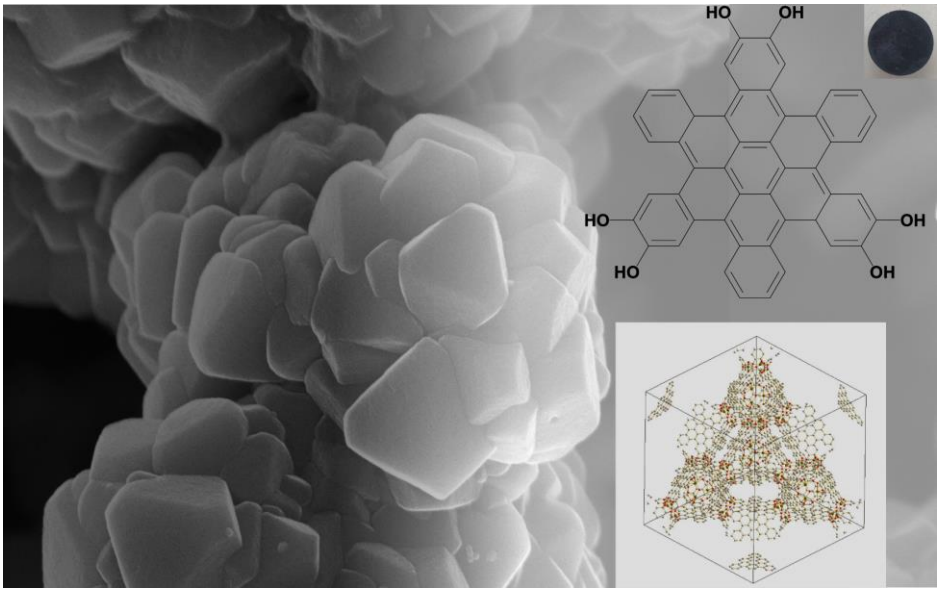

7.1 Abstract

A novel cubic mesoporous metal-organic framework (MOF) was synthesized through the reaction between hexahydroxy-cata-hexabenzocoronene and Fe^{III} ions. The highly crystalline MOF features broad absorption over the whole visible and near infrared region. An electrical conductivity of 10^{-6} S cm^{-1} was measured on a pressed pellet.

7.2 Introduction

Metal-organic frameworks are highly crystalline and porous materials with very attractive features enabling diverse applications such as gas storage, gas separations, heterogeneous catalysis, and drug delivery.[1–4] In recent years, the intriguing property of electrical conductivity was added as new feature of a select small number of MOFs.[5–7] In combination with high crystallinity and porosity, it enables new applications like charge storage and chemical sensing.[8–10]

Especially 2D-layered MOF structures were found to exhibit electrical conductivity, where charge migration can occur *via* through-space and through-bond mechanisms.[6,11] The MCAT-1 series is a prominent 2D MOF family in this respect, exhibiting high electrical conductivity values, for example between 1.5 Scm^{-1} and 0.1 Scm^{-1} (Cu-CAT-1, exfoliated flake/single crystal, 2-point-probe method).[12,13] This particular 2D MOF family is built from hexahydroxytriphenylene (HHTP) ligands connected through bivalent metal ions such as Co^{II}, Ni^{II} and Cu^{II}. It crystallizes in a hexagonal symmetry and features BET surface areas of up to 350 m^2/g.[12]

While 2D MOFs can show intriguing electronic properties, they often feature relatively low porosity. On the other hand, electrically conducting and porous 3D MOFs are still rare.[14–16] The first 3D M-CAT named Fe-CAT-5 was synthesized by Yaghi and co-workers in 2015; in this MOF HHTP organic linkers form a 2-fold interpenetrating network together with iron ions.[17] Additionally, the rare-earth metal ions La^{III}, Nd^{III}, Ho^{III} and Yb^{III} also form 3D frameworks with HTTP.[18] In these crystal structures, the planar ligands are interconnected with the metal ions and exhibit different stacking distances depending on their ionic radii. Within this group of lanthanide-HHTP MOFs, an electrical conductivity of up to 0.05 S cm^{-1} could be achieved. The rare-earth metal ions Y^{III} and Eu^{III} led to the formation of a cubic, porous structure, with electrical conductivities reaching 10^{-5} S/cm.[19] Recently our group reported a new 3D Fe-HHTP MOF, crystallizing in a cubic geometry with the space group F*32*.[20] It shows an electrical conductivity of 10^{-3} S/cm (van der Pauw method, pellet) and features a BET surface area of 1490 m^2 g^{-1}. Moreover, it exhibits a broad optical absorption from 475 nm to 1900 nm, and theoretical modeling indicated the structure to be an efficient electron conductor with continuous charge-carrier pathways throughout the structure.

The “through-bond” charge transfer is the common charge-carrier transport pathway in highly porous 3D MOFs. Due to the isotropic charge-carrier transport pathways in cubic MOF structures, they are promising platforms for the construction of highly porous electroactive MOFs.

Besides HHTP, another attractive trigonal planar building block is based on the coronene core. Using this polycyclic aromatic hydrocarbon as a building block is of special interest for the synthesis of highly ordered structures, since the rigid nodes can guide the stacking of framework layers. To date, only a few coronene-based 2D MOFs have been reported; for example, Dong *et. al.* showed a perthiolated coronene-based Fe-MOF that exhibits high electrical conductivity of 10 S/cm and a BET surface area of 210 m^2 g^{-1}.[21] Chen *et al.* also synthesized a perthiolated coronene-based Ni-MOF showing a similar electrical conductivity. However, using a coronene-based core for the synthesis of a 3D framework with a defined structure has not been reported yet.

Here we present the synthesis of a new 3D MOF that is constructed with the trigonal planar building block 2,3,10,11,18,19-hexahydroxy-cata-hexabenzocoronene (HBC) with Fe^{II}-ions, named Fe-Coronene-MOF. It crystallizes in a cubic geometry, similar to the Fe-HHTP-MOF[19], which was predicted by structral analysis with PXRD and TEM. The Fe-Coronene-MOF features mesopores and a broad optical absorption over the whole visible and near infrared spectrum. The iron-valency was studied by means of ^{57}Fe Mössbauer and X-ray photoelectron spectroscopy (XPS) measurements, showing the presence of high-spin Fe^{III} in the structure. Two-point probe electrical conductivity measurements give values of around 10^{-6} S/cm. Cyclic voltammetry measurements were performed to study the redox behavior of the Fe-Coronene-MOF electrochemically.

7.3 Results and discussion

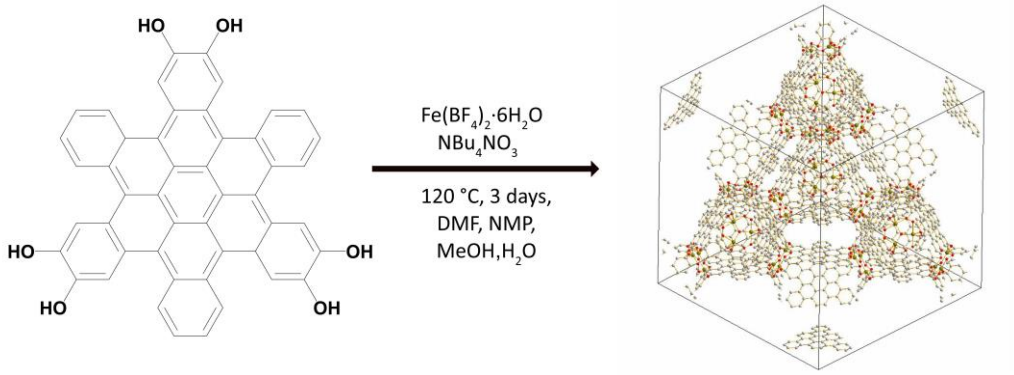

Figure 7-1: Synthesis scheme of the solvothermal reaction of 2,3,10,11,18,19-hexahydroxy-cata-hexabenzocoronene (HBC) with $Fe(BF_4)_2 \cdot 6H_2O$ as iron precursor, forming the cubic Fe-Coronene-MOF.

Fe-Coronene-MOF was synthesized under solvothermal reaction conditions (see Figure 7-1). The metal precursor $Fe(BF_4)_2 \cdot 6H_2O$, the ligand 2,3,10,11,18,19-hexahydroxy-cata-hexabenzocoronene (HBC) and the crystallization agent tetrabutylammonium nitrate NBu_4NO_3 were dissolved in *N*,*N*-dimethylformamide (DMF), methanol (MeOH), *N*-methyl-2-pyrrolidone (NMP) and water under argon atmosphere. The reaction mixture was sealed under inert conditions and ultrasonically treated until complete dissolution of the reagents was observed. It was heated in a preheated oven at 120 °C for 72 h. After cooling down to room temperature, the reaction product was washed with DMF and degassed under dynamic vacuum prior to analysis, yielding a black microcrystalline powder (for more details see SI).

In the powder X-ray diffraction (PXRD) pattern, sharp reflections up to high 2Θ values confirm the formation of a highly crystalline material (see Figure 7-2 A). Distinct reflections at 3.5, 6.8, 7.2, 7.6, 8.2, 9.0, 10.8, 12.3, 13.7° 2Θ are visible in the PXRD pattern. In the scanning electron microscopy (SEM) images, tetrahedral and faceted intergrown crystallites can be observed, with edge-to-edge distances of 600 – 900 nm. They exhibit typical angles of 72° between facets of the tetrahedra (Figure 7-2 B). The diffraction pattern of the MOF powder fits well with the one predicted from the simulated model structure, which indicates a cubic crystal system (Figure 7-2 A). It exhibits a lattice constant of a = 42.6 Å using the X-cell program and the reflex module from Material Studio 2017. With the program EXPO2014, the structure could be solved by simulated annealing in the space group $F4_132$. However, for future Rietveld refinements, a PXRD pattern with much higher signal-to-noise ratio will be needed. The most prominent reflection at 3.5° 2Θ corresponds to the (111) reflection, which is in good accordance with the *d*-spacing of 25 Å, detected by TEM (Figure 7-9 Figure 7-9).

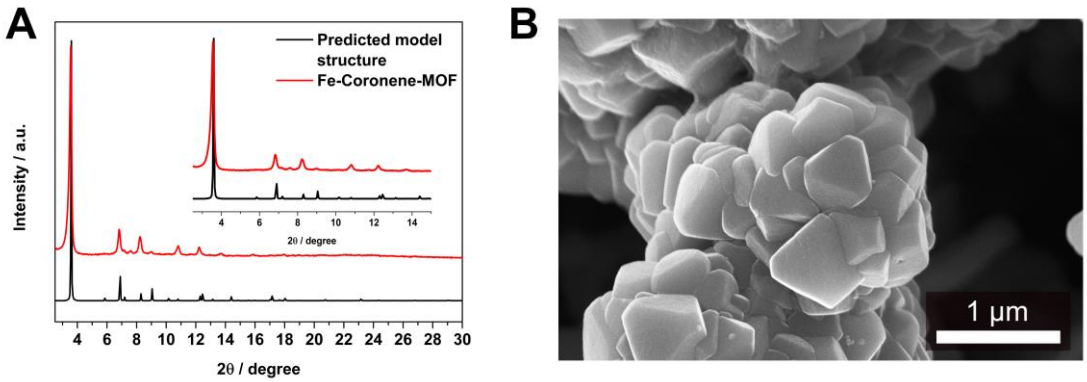

Figure 7-2: (A) A Experimental and predicted powder X-ray diffraction pattern of the Fe-Coronene-MOF, with a zoom-in as inset. (B) SEM image of intergrown tetrahedral crystallites with a size of 600 – 900 nm.

TEM analysis shows large crystalline domains with diameters of 350-450 nm. The Fourier transforms (FFT) from the images of two exemplary crystallites indicates a cubic structure (Figure 7-3

insets), similar to the previously reported Fe-HHTP-MOF[19] and agree well with the lattice constant from the PXRD pattern. Compositional EDX analysis shows the presence of Fe, O and C, with residual amounts of nitrogen.

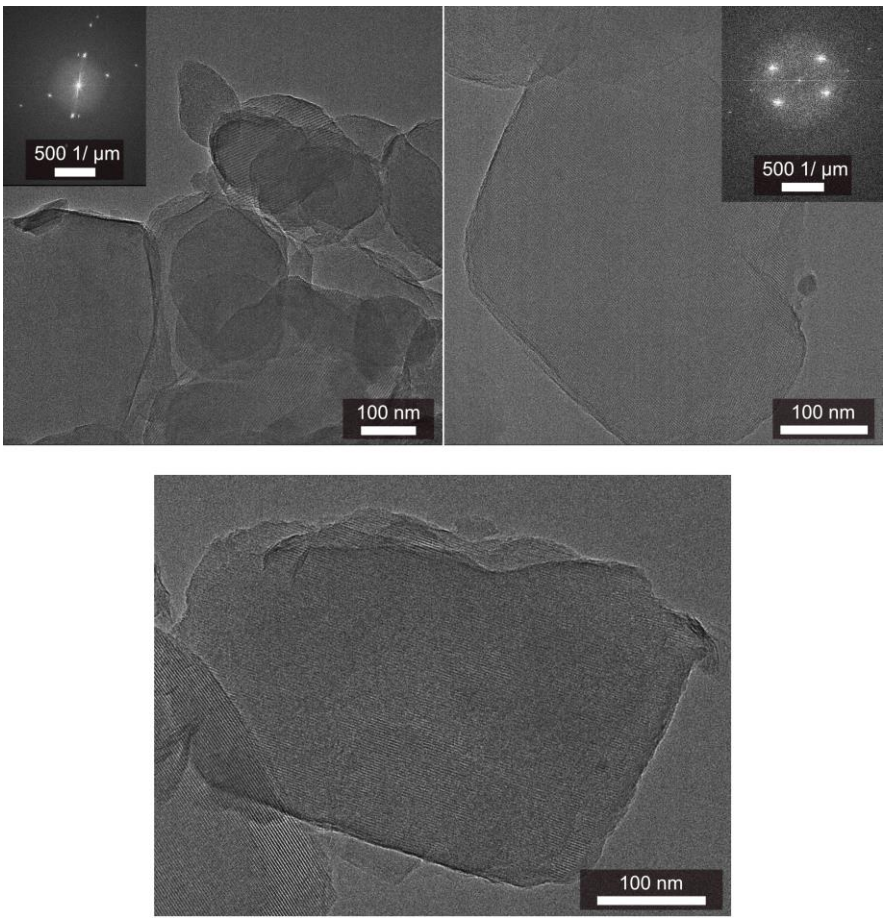

Figure 7-3: TEM images of MOF crystallites. Insets: FFT from the image of the respective crystallite.

In the structure model, two coronene moieties are bridged by one iron atom, whereby three iron bis-coronene complexes form a trimeric geometry, which is stabilized by a central oxygen atom. The oxo-trimers are the extended vertices defining an open supertetrahedron, whereby the connecting coronene moieties are the faces, with each of them being linked to three iron oxo-trimers (Figure 7-10, Figure 7-11). Connecting the corners of the supertetrahedra to four other supertetrahedra, a porous 3D architecture is formed. As a supertetrahedron is the basic building unit, the structure can be described by a diamond (4-c dia) topology. To further study the composition and the potential presence of guest molecules in the MOF structure, X-ray photoelectron spectroscopy (XPS) experiments were performed (Figure 7-12, Figure 7-13). The measured boron spectrum shows no signal, excluding the presence of impurities coming from the metal precursor $Fe(BF_4)_2 \cdot 6H_2O$. The measured nitrogen spectrum shows a weak signal that is probably related to residual DMF or NMP in the pores. The reference XPS spectrum of the N 1s region of tetrabutylammonium nitrate excludes its presence in the Fe-Coronene-MOF (Figure 7-13).

Nitrogen sorption analysis show a IUPAC[22] type *IV(a)* isotherm, with a sharp first nitrogen uptake at relatively low partial pressures (p/p_0 < 0.1 and up to 75 cm^3 g^{-1}) and a second one up to 160 cm^3 g^{-1} (Figure 7-4). The desorption curve shows a small hysteresis, which can be attributed to capillary condensation typical for mesopores. However, the rest of the desorption curve overlaps with the adsorption curve, underlining a reversible gas sorption process. The BET surface area was measured to be 463 m^2 g^{-1}. Quenched solid density functional theory (QSDFT) calculations reveal a pore size distribution showing two pore sizes of 1.2 nm and 3.3 nm. This is in good accordance with the simulated structure model (Figure 7-11).

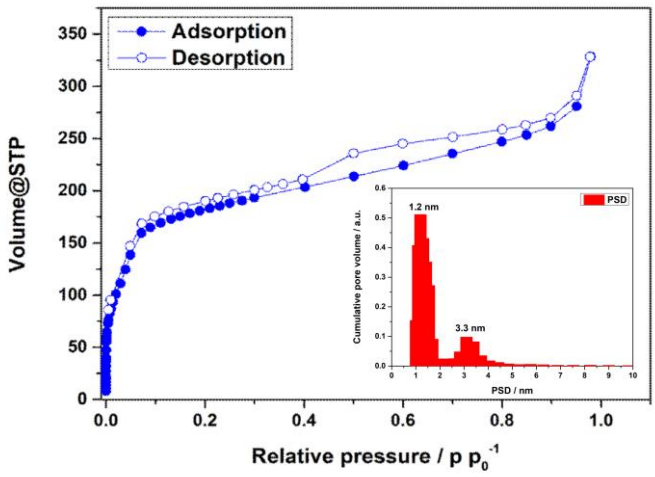

Figure 7-4: Nitrogen sorption analysis of the Fe-Coronene-MOF. The pore size distribution is shown as inset, which was obtained by quenched solid density functional theory (QSDFT).

To study the optical properties of the Fe-Coronene-MOF, we performed UV-Vis-NIR absorption measurements of powder samples in a diffuse reflectance geometry and constructed the spectrum using the Kubelka-Munk equation (Figure 7-5 A). It features a broad absorption over the whole visible spectrum up to the near IR region, with maxima at 430 nm and 680 nm and an absorption onset at 1200 nm. The spectrum corresponds to the black colour of the MOF powder. A direct band gap of 1.39 eV was calculated by means of a Tauc plot, using the onset in the near infrared (Figure 7-5 B). Photoluminescence of the MOF powder (laser excitation at 375 nm) was not observed.

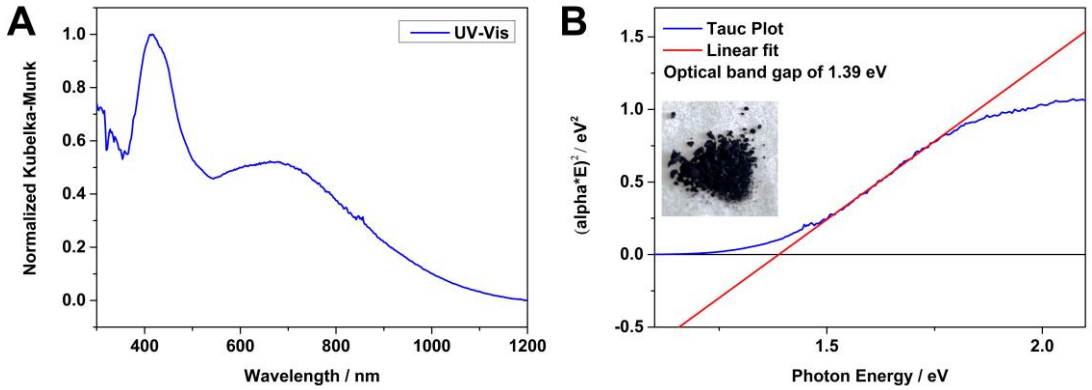

Figure 7-5: (A) UV-Vis-NIR spectrum of the Fe-Coronene-MOF, obtained in diffuse-reflectance mode. (B) Tauc plot, assuming a direct band gap, shows a band gap of 1.39 eV for the Fe-Coronene-MOF.

The iron valency of the Fe-Coronene-MOF was examined by X-ray photoelectron spectroscopy (XPS). The recorded Fe2p signal of the XPS measurement shows a peak splitting into two broad $Fe2p_{3/2}$ and $Fe2p_{1/2}$ peaks (Figure 7-6 A). The fitting of each peak by four components agrees well with the reported interpretation of signals from high-spin Fe^{III}. An XPS scan at the end of all measurements shows a small change in the recorded iron spectra, which can be attributed to the reduction of a small amount of iron during the measurements (Figure 7-6 B). The gradual reduction by secondary electrons during X-ray irradiation in the course of the measurement and by the use of a flood gun for charge compensation is a commonly observed phenomenon in XPS measurements of coordination networks.

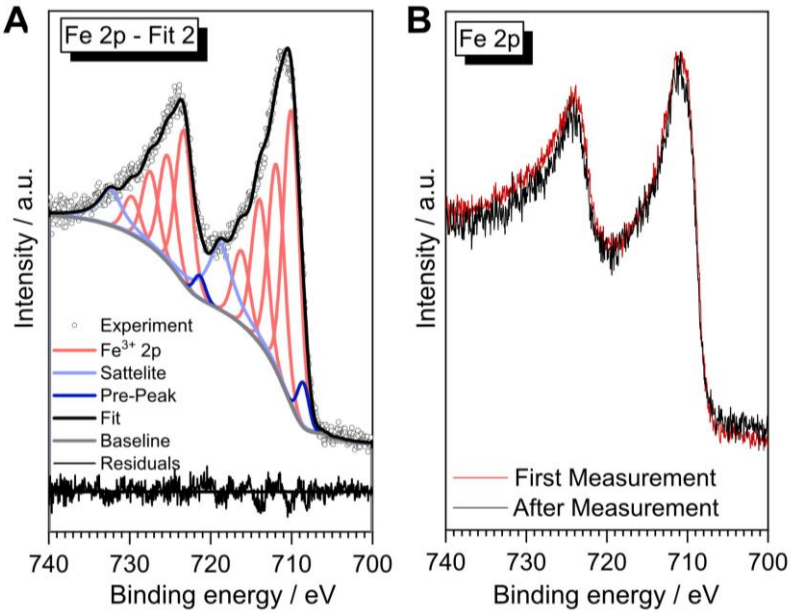

Figure 7-6: (A) XPS data of the Fe 2p region. The open circles visualize the experimental data points, the fit and residuals as solid black lines and the multiplet components as red lines. (B) XPS data of the Fe 2p region of the first measurement (red) and at the end of all other measurements (N 1s, B 1s, survey scan).

To investigate the electrical conductivity of the Fe-Coronene-MOF, we used two-point probe measurements of crystalline pelletized powder samples (Figure 7-7). The thickness of the pellets was measured with a slide gauge to be 450 µm. Applying voltage in the range of -3 to 3 V provided a linear ohmic resistance curve, which was fitted by a linear regression, giving an electrical conductivity of 3 x 10^{-6} S/cm.

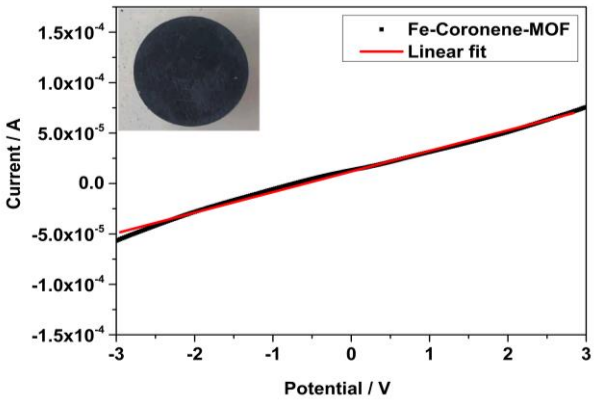

Figure 7-7: *I-V* curve of a pressed pellet of the Fe-Coronene-MOF, measured via the two-point probe measurement. A photo image of a pressed pellet is shown as an inset.

To get better insights regarding the electrochemical behavior of the Fe-Coronene-MOF and to determine the oxidation potential, we performed cyclic voltammetry (CV) (Figure 7-8, Figure 7-16). For the measurement, we pressed a mixture of MOF bulk material with active carbon into a stainless steel mesh. The CV measurement was performed in a typical three-electrode setup, with tetrabutylammonium hexafluorophosphate as the electrolyte in argon-purged anhydrous DMF. The Fe-Coronene-MOF shows an oxidation behavior that is stable during two cycles. One quasi-reversible redox couple is visible in the CV curve, having its onset at 0.43 eV. With the CV data in hand, the oxidation onset potential against the HOMO energy of ferrocene can be used for the calculation of the absolute energy of the valence band edge against the vacuum scale (Figure 7-16 B). The energy of the conduction band edge can then be determined by adding the absolute energy of the valence band to the optical band gap energy. The absolute valence band energy is determined by using the oxidation onset potential of the MOF and correlating this to the vacuum energy of the ferrocene HOMO energy of 4.8 eV and to the oxidation onset of ferrocene under the used measurement conditions. A conduction band energy minimum of -3.2 eV and a valence band energy maximum of -4.7 eV were calculated for the Fe-Coronene-MOF.

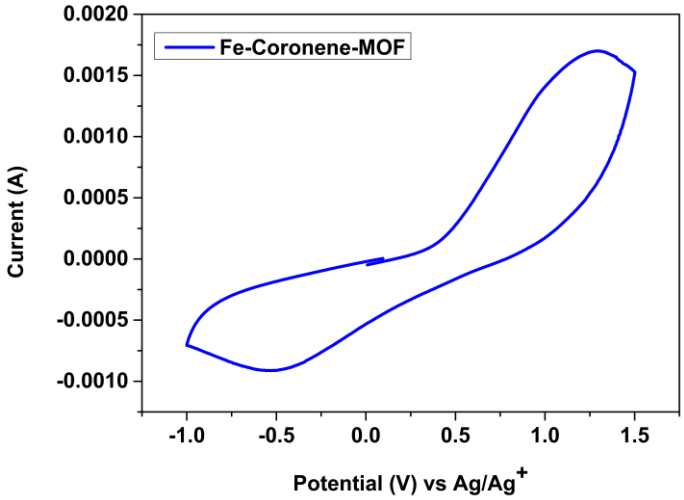

Figure 7-8: Voltammogram of the Fe-Coronene-MOF as bulk material, pressed in a stainless steel mesh. It was measured in a solution of 0.1 M tetrabutylammonium hexafluorophosphate ($TBAPF_6$) in DMF versus Ag/Ag^+ (in V) with a scan rate 0.1 V/s under argon atmosphere.

7.4 Summary and outlook

Here, we demonstrated the successful synthesis of a novel cubic ferric coronene framework named Fe-Coronene-MOF. It was obtained as a black powder in a solvothermal synthesis. SEM images reveal a morphology of intergrown tetrahedral crystallites with a size of 600 – 900 nm. The PXRD pattern of the simulated model with the cubic space group $F4_132$ matches well with the recorded diffraction pattern. According to the simulated model, iron-connected supertetrahedra form a diamond-like topology. The Fe-Coronene-MOF is mesoporous and shows an electrical conductivity of 10^{-6} S cm^{-1}. Due to its black colour, it features an absorption over the whole visible spectrum up to the near IR region, with a band gap of 1.39 eV. The ferric character was confirmed by means of XPS, showing the presence of high-spin Fe^{III} in the framework. This has to be confirmed by ^{57}Fe Mössbauer measurements. Due to its black colour, we plan to perform spectral reflectance measurements in the future. Furthermore, we plan to do a Rietveld refinement of the PXRD pattern in order to confirm the initially developed structural model.

7.5 References

(1) Sun, C.-Y.; Qin, C.; Wang, X.-L.; Su, Z.-M. Metal-organic frameworks as potential drug delivery systems. *Expert Opin Drug Deliv* **2013**, *10*, 89–101.

(2) Bao, Z.; Yu, L.; Ren, Q.; Lu, X.; Deng, S. Adsorption of CO2 and CH4 on a magnesium-based metal organic framework. *J. Colloid Interface Sci.* **2011**, *353*, 549–556.

(3) Millward, A. R.; Yaghi, O. M. Metal-organic frameworks with exceptionally high capacity for storage of carbon dioxide at room temperature. *J. Am. Chem. Soc.* **2005**, *127*, 17998–17999.

(4) Bavykina, A.; Kolobov, N.; Khan, II S.; Bau, J. A.; Ramirez, A.; Gascon, J. Metal-organic frameworks in hetereogeneous catalysis: recent progress, new trends, and future perspectives. *Chem. Rev*., **2020**, *120*, 8469–8535.

(5) Sun, L.; Campbell, M. G.; Dincă, M. Electrically Conductive Porous Metal-Organic Frameworks. *Angew. Chem.* **2016**, *55*, 3566–3579.

(6) Xie, L. S.; Skorupskii, G.; Dinca, M. Electrically Conductive Metal−Organic Frameworks. *Chem. Rev.* **2020**, *120*, 8536–8580.

(7) Medina, D. D.; Mähringer, A.; Bein, T. Electroactive Metalorganic Frameworks. *Isr. J. Chem.* **2018**, *58*, 1089–1101.

(8) Yi, F.-Y.; Chen, D.; Wu, M.-K.; Han, L.; Jiang, H.-L. Chemical Sensors Based on Metal-Organic Frameworks. *ChemPlusChem* **2016**, *81*, 675–690.

(9) Mähringer, A.; Jakowetz, A. C.; Rotter, J. M.; Bohn, B. J.; Stolarczyk, J. K.; Feldmann, J.; Bein, T.; Medina, D. D. Oriented Thin Films of Electroactive Triphenylene Catecholate-Based Two-Dimensional Metal-Organic Frameworks. *ACS Nano* **2019**, *13*, 6711–6719.

(10) Bi., S.; Banda, H.; Chen, M.; Niu, L.; Chen; Wu, T.; Wang, J.; Wang, R.; Feng, J.; Chen, T.; Dinca, M.; Kornyshev, A. A.; Feng, G. Molecular understanding of charge storage and charging dynamics in supercapacitors with MOF electrodes and ionic liquid electrolytes. *Nat. Mater.* **2020**, *19*, 552–558.

(11) Xie, L. S.; Alexandrov, E. V.; Skorupskii, G.; Proserpio, D. M.; Dincă, M. Diverse π-π stacking motifs modulate electrical conductivity in tetrathiafulvalene-based metal-organic frameworks. *Chem. Sci.* **2019**, *10*, 8558–8565.

(12) Hmadeh, M.; Lu, Z.; Liu, Z.; Gándara, F.; Furukawa, H.; Wan, S.; Augustyn, V.; Chang, R.; Liao, L.; Zhou, F.; Perre, E.; Ozolins, V.; Suenaga, K.; Duan, X.; Dunn, B.; Yamamto, Y.; Terasaki, O.; Yaghi, O. M. New Porous Crystals of Extended Metal-Catecholates. *Chem. Mater.* **2012**, *24*, 3511–3513.

(13) Day, R. W.; Bediako, D. K.; Rezaee, M.; Parent, L. R.; Skorupskii, G.; Arguilla, M. Q.; Hendon, C. H.; Stassen, I.; Gianneschi, N. C.; Kim, P.; Dincă, M. Single Crystals of Electrically Conductive Two-Dimensional Metal-Organic Frameworks: Structural and Electrical Transport Properties. *ACS Cent. Sci.* **2019**, *5*, 1959–1964.

(14) Xie, L. S.; Sun, L.; Wan, R.; Park, S. S.; DeGayner, J. A.; Hendon, C. H.; Dincă, M. Tunable Mixed-Valence Doping toward Record Electrical Conductivity in a Three-Dimensional Metal-Organic Framework. *J. Am. Chem. Soc.* **2018**, *140*, 7411–7414.

(15) Park, J. G.; Aubrey, M. L.; Oktawiec, J.; Chakarawet, K.; Darago, L. E.; Grandjean, F.; Long, G. J.; Long, J. R. Charge Delocalization and Bulk Electronic Conductivity in the Mixed-Valence Metal-Organic Framework Fe(1,2,3-triazolate)2(BF4) x. *J. Am. Chem. Soc.* **2018**, *140*, 8526–8534.

(16) Darago, L. E.; Aubrey, M. L.; Yu, C. J.; Gonzalez, M. I.; Long, J. R. Electronic Conductivity, Ferrimagnetic Ordering, and Reductive Insertion Mediated by Organic Mixed-Valence in a Ferric Semiquinoid Metal-Organic Framework. *J. Am. Chem. Soc.* **2015**, *137*, 15703–15711.

(17) Nguyen, N. T. T.; Furukawa, H.; Gándara, F.; Trickett, C. A.; Jeong, H. M.; Cordova, K. E.; Yaghi, O. M. Three-Dimensional Metal-Catecholate Frameworks and Their Ultrahigh Proton Conductivity. *J. Am. Chem. Soc.* **2015**, *137*, 15394–15397.

(18) Skorupskii, G.; Trump, B. A.; Kasel, T. W.; Brown, C. M.; Hendon, C. H.; Dincă, M. Efficient and tunable one-dimensional charge transport in layered lanthanide metal-organic frameworks. *Nat. Chem.* **2020**, *12*, 131–136.

(19) Skorupskii, G.; Dincă, M. Electrical Conductivity in a Porous, Cubic Rare-Earth Catecholate. *J. Am. Chem. Soc.* **2020**, *142*, 6920–6924.

(20) Mähringer, A.; Döblinger, M.; Hennemann, M.; Gruber, C.; Fehn, D.; Scheurle, P. I.; Hosseini, P.; Santourian, I.; Schirmacher, A.; Rotter, J. M.; Wittstock, G.; Meyer, K.; Clark, T.; Bein, T.; Medina, D. D. An electrically conducting three-dimensional iron-catecholate porous framework. *Angew. Chem.* **2021**.

(21) Dong, R.; Zhang, Z.; Tranca, D. C.; Zhou, S.; Wang, M.; Adler, P.; Liao, Z.; Liu, F.; Sun, Y.; Shi, W.; Zhang, Z.; Zschech, E.; Mannsfeld, S. C. B.; Felser, C.; Feng, X. A coronene-based semiconducting two-dimensional metal-organic framework with ferromagnetic behavior. *Nat. Commun.* **2018**, *9*, 2637.

(22) Thommes, M.; Kaneko, K.; Neimark, A. V.; Olivier, J. P.; Rodriguez-Reinoso, F.; Rouquerol, J.; Sing, K. S.W. Physisorption of gases, with special reference to the evaluation of surface area and pore size distribution (IUPAC Technical Report). *Pure Appl. Chem.* **2015**, *87*, 1051–1069.

7.6 Supporting information

7.6.1 Characterization methods

Nuclear magnetic resonance (NMR)

NMR spectra were recorded on *Bruker AV400* and *AV400 TR* spectrometers. The chemical shifts are expressed in parts per million and calibrated using residual (undeuterated) solvent peaks as an internal reference (^{1}H-NMR: DMSO-d_6: 2.50; ^{13}C-NMR: DMSO-d_6: 39.52). The data for ^{1}H-NMR spectra are written as follows: s = singlet, d = doublet, t = triplet, q = quartet, m = multiplet.

X-ray diffraction

X-ray diffraction (XRD) studies were performed on a *Bruker D8* diffractometer in Bragg-Brentano geometry with Ni-filtered Cu K_α (λ = 1.54060 Å) radiation operating at 40 kV and 30 mA with a position-sensitive detector (*LynxEye*).

Scanning electron microscopy (SEM)

SEM images were recorded on an *FEI Helios NanoLab G3 UC* electron microscope with an acceleration voltage of 2 kV from a field emission gun. For the cross-section analysis substrates were partially cut and broken manually to reveal fresh cross-sections. Prior to SEM analysis the samples were coated with a thin carbon layer by carbon fiber flash evaporation in high vacuum.

Transmission electron microscopy (TEM)

TEM images were collected on an *FEI Titan Themis 60-300* microscope at an acceleration voltage of 300 kV. Powder samples were prepared by crushing the particles with a razor blade and subsequently depositing the powder onto a copper grid supporting a thin electron transparent carbon film.

Nitrogen sorption

Ad- and desorption measurements were performed on an *Autosorb 1* (*Quantachrome Instruments, Florida, USA*) with nitrogen of 99.9999% purity at 77.3 K. The samples were activated (dried) under high vacuum at 120 °C for at least 12 h. Evaluation of ad- and desorption isotherms was carried out with the *AsiQwin v.3.01* (*Quantachrome Instruments, Florida, USA*) software.

For BET calculations, pressure ranges of the nitrogen isotherms were chosen with the help of the BET assistant in the *AsiQwin* software. In accordance with the ISO recommendations, multipoint BET tags equal to or below the maximum in V x (1-p/p_0) were chosen.

Electrical conductivity measurements

Two-point probe measurements of crystalline pellets were carried out with a Metrohm Autolab PGStat302N potentiostat and an in-house constructed dc-conductivity measurement cell by recording *I–V* curves between -5 to +5 V by an AUTOLAB 302N. The distance between the electrodes (circular, with a diameter of 4 mm) was equivalent to the thickness of the pellet, which was measured to be 800 μm.

Preparation of Fe-Coronene-MOF pellets

MOF pellets with 1 cm diameter (obtained from several identical batches) for electrical conductivity measurements were fabricated with 60 mg of the respective MOF bulk material with a standard *Paul-Weber* KBr Press with 45 kg/cm^2 pressure.

UV-Vis spectroscopy

UV-Vis spectra were recorded using a PERKIN ELMER UV VIS/NIR Lambda 1050 spectrophotometer equipped with a 150 mm InGaAs integrating sphere. Diffuse reflectance spectra were collected with a Praying Mantis (Harrick) accessory and were referenced to barium sulphate powder as white standard.

X-ray photoelectron spectroscopy

XPS was performed using an ESCALAB 250 Xi instrument (Thermo Fisher, East Grinsted, UK) with monochromatized Al Kα (hν = 1486.6 eV) radiation focused to a spot of 500 micron diameter at the surface of the samples. Spectra were measured with pass energies of 200 eV for survey scans and 10 eV for high-resolution regions. Charging was compensated by use of an internal electron flood gun. Peak fitting was performed by the software Avantage, version 5.9904 (Thermo Fisher) using a Shirley background ("Smart Shirley") and a convolution of Gaussian and Lorentzian functions for each signal component. All spectra were referenced to remaining adventitious carbon at 284.8 eV.

7.6.2 Experimental

7.6.2.1 General

All materials were purchased from *Sigma Aldrich, Acros or TCI Europe* in the common purities *purum, puriss* or *reagent grade.* The materials were used as received without additional purification and handled in air unless otherwise noted. The water utilized in the synthesis was subjected to a *Merck-Milipore Mili-Q* purification system prior to use.

7.6.2.2 Synthetic procedures

7.6.2.3 HBC ligand

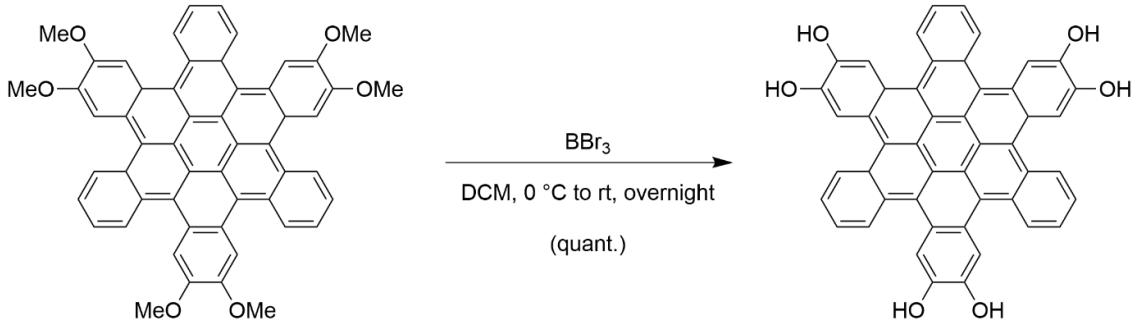

HBC

2,3,10,11,18,19-Hexahydroxy-cata-hexabenzocoronene (HBC) was synthesized according to a previously reported procedure.[1] 2,3,10,11,18,19-hexamethoxy-cata-hexabenzocoronene (30 mg, 0.038 mmol) was dissolved in 3 mL of dry dichloromethane. The solution was cooled to 0 °C and 3 mL of BBr_3 (1M solution in dichloromethane) were added. Afterwards, the solution was allowed to warm to room temperature and stirred under argon overnight. After the reaction was complete, water was added to quench the reaction and the solvent was mostly removed using an argon flow. The resulting precipitate was filtered and finally dried under reduced pressure to give HBC as a light green solid with quantitative yield (26.63 mg). ^{1}H NMR (400 MHz, $(CD_3)_2CO$): δ = 9.32-9.24 (m, 6H), 8.74 (s, 6H), 7.89-7.81 (m, 6H).

7.6.2.4 Fe-Coronene-MOF synthesis

Freshly synthesized HBC (11.0 mg, 15.8 mmol), $Fe(BF_4)_2 \cdot 6H_2O$ (21.0 mg, 62.2 mmol) and tetrabutylammonium nitrate (10.0 mg, 41.2 mmol) were suspended in DMF (1.75 mL), NMP(125 µL), MeOH (125 µL), H_2O (125 µL) and mesitylen (50 µL) under argon atmosphere. The resulting mixture was sonicated until complete dissolution of the educts was achieved and it was kept in a culture tube at 120°C for 3 days. The resulting precipitate was washed with DMF

(3 x 20 mL) and activated at 120 °C to remove the less volatile solvents to obtain a black crystalline powder.

7.6.3 Characterization

7.6.3.1 Transmision electron microscopy

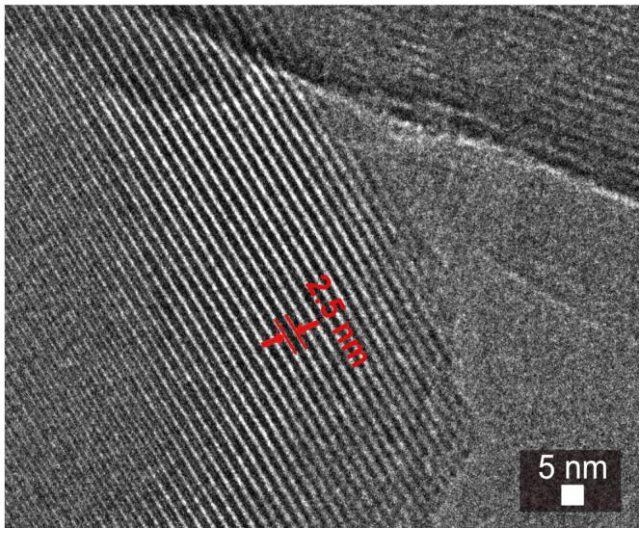

Figure 7-9: TEM image of the Fe-Coronene-MOF, showing a distance of 2.5 nm between the lattice fringes, which is in good accordance with the first reflection at 3.5° 2Θ in the PXRD pattern (Figure 7-2 A).

7.6.3.2 Images of the simulated structure of the Fe-Coronene-MOF

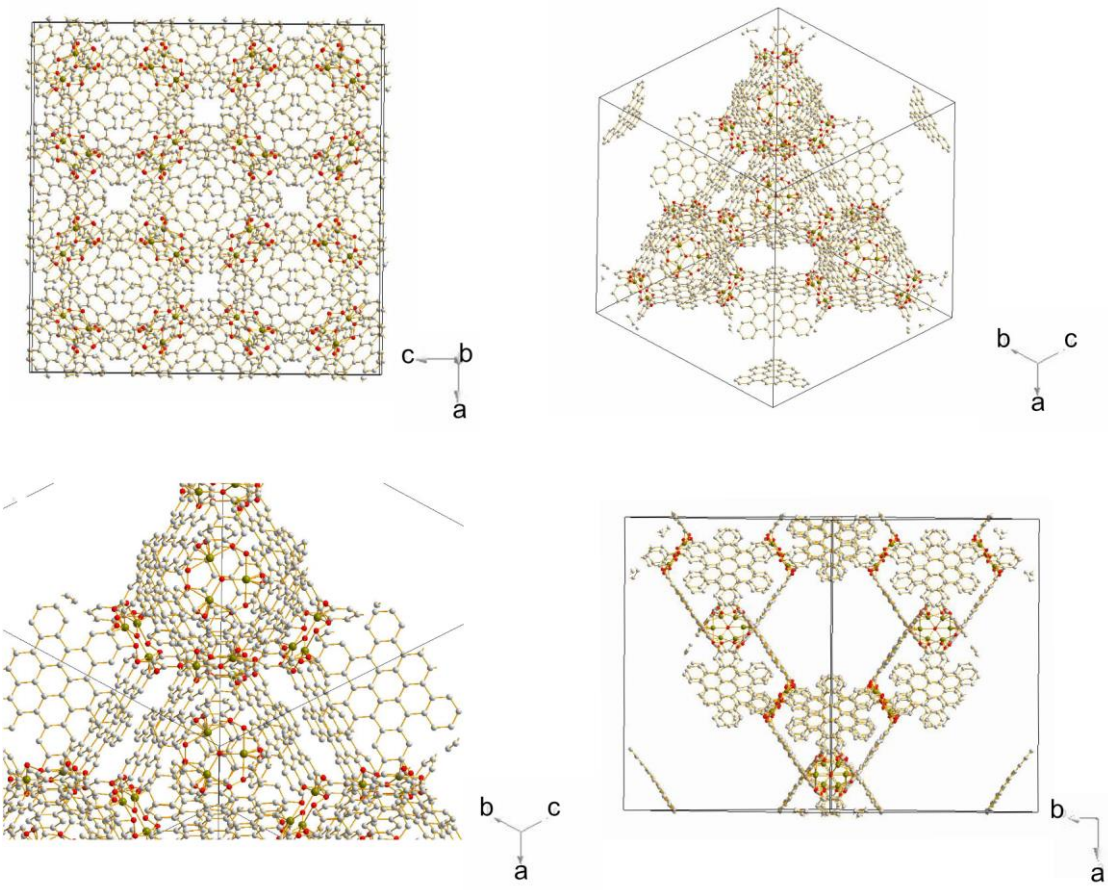

Figure 7-10: Images of the simulated model structure of the Fe-Coronene-MOF in different viewing directions.

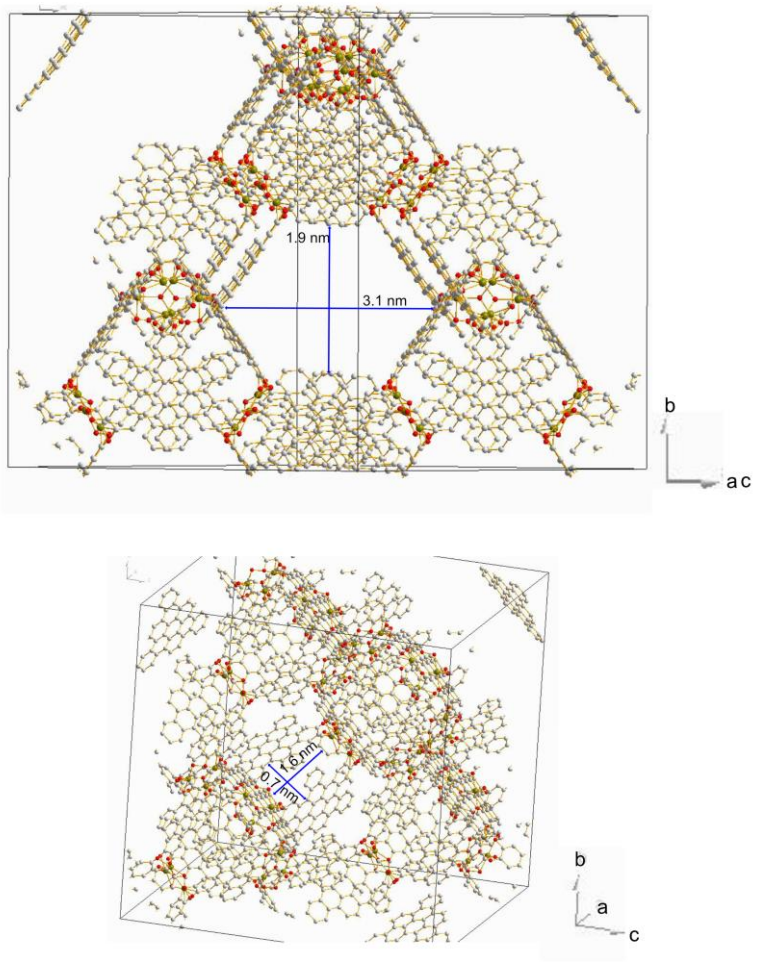

Figure 7-11: Images of the simulated model structure of the Fe-Coronene-MOF in different viewing directions, visualizing a bigger and a smaller pore.

7.6.3.3 X-ray photoelectron spectroscopy

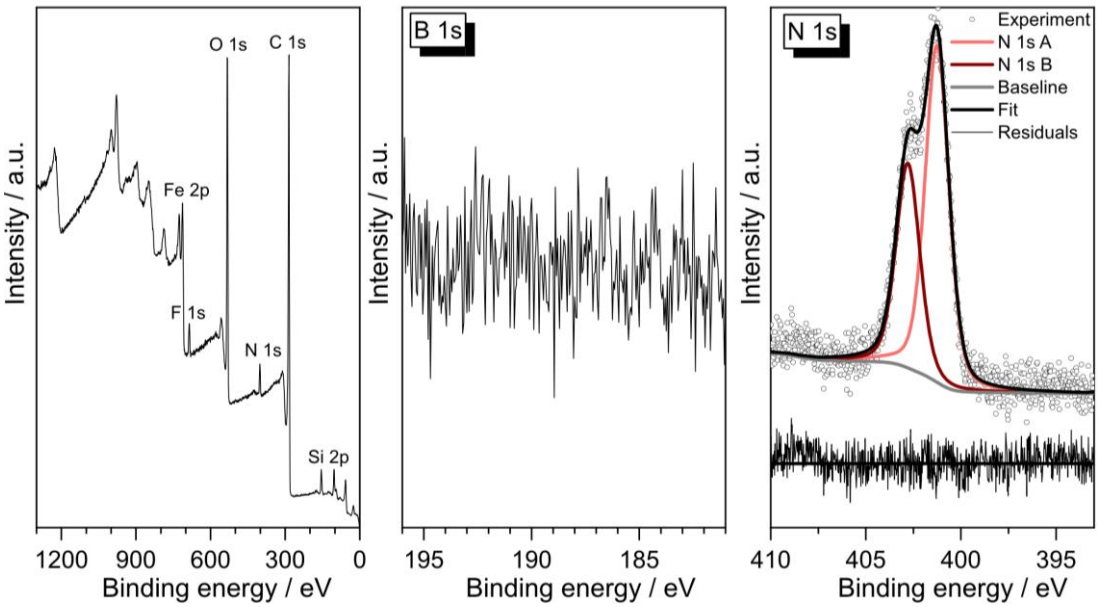

Figure 7-12: XPS analysis of Fe-Coronene-MOF. (A) Survey scan of the sample. (B) B 1s spectrum of the Fe-Coronene-MOF. No boron impurity coming from the iron precursor could be detected. (C) N 1s spectrum of the Fe-Coronene-MOF. Two types of nitrogen, which are not nitrate, because it would be expected at 407.4 eV^2, were detected. We attribute the signals to residual DMF and NMP in the sample.

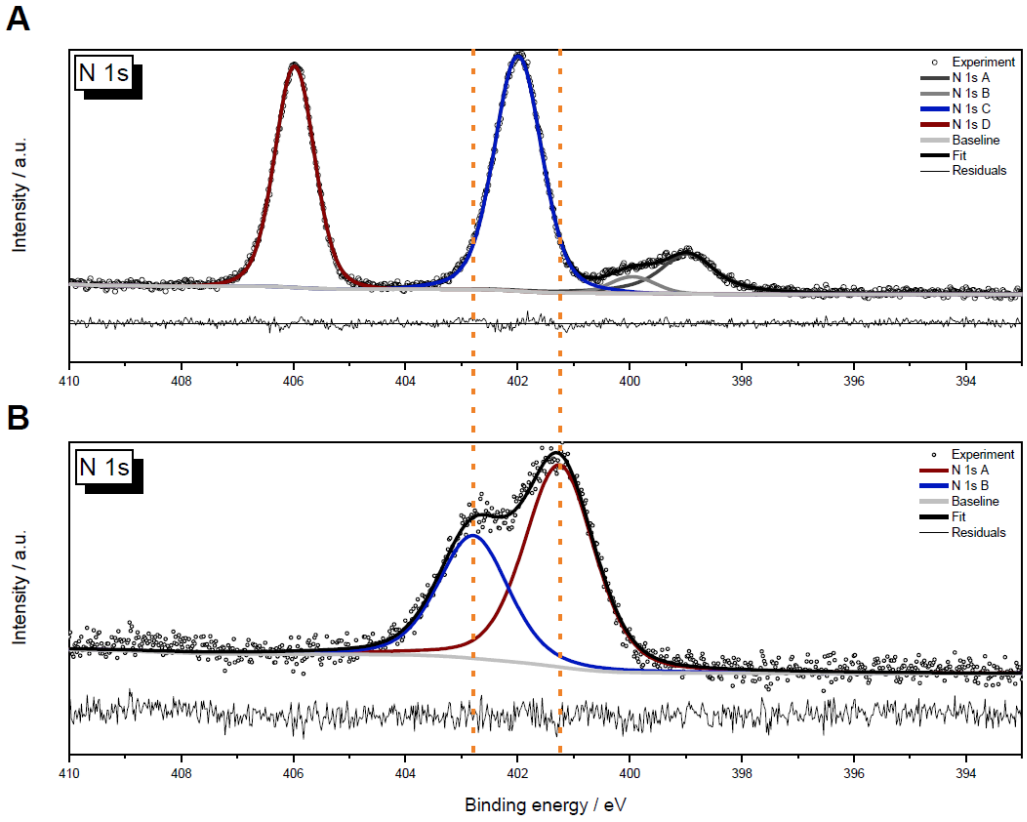

Figure 7-13: High-resolution XP spectra of the N 1s region of (A) tetrabutylammonium nitrate and (B) the Fe-Coronene-MOF. The N 1s signals of tetrabutylammonium nitrate shown in (A) are not present in the N 1s spectrum of the Fe-Coronene MOF, confirming its absence.

7.6.3.4 Scanning electron microscopy

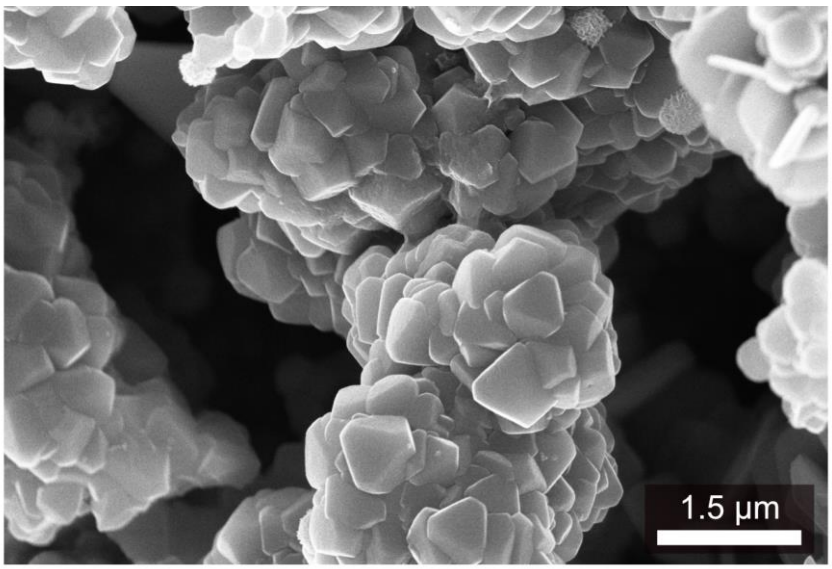

Figure 7-14: SEM image of intergrown tetrahedral crystallites with a size of 600 – 900 nm.

7.6.3.5 UV-Vis spectroscopy

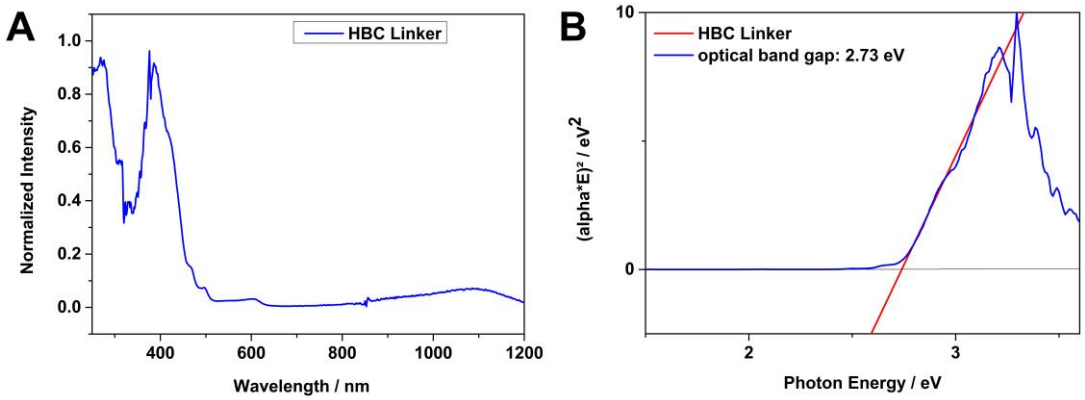

Figure 7-15: (A) UV-Vis-NIR spectrum of the HBC ligand. (B) Tauc plot of the HBC ligand, indicating a direct band gap of 2.7 eV.

7.6.3.6 Cyclic voltammetry

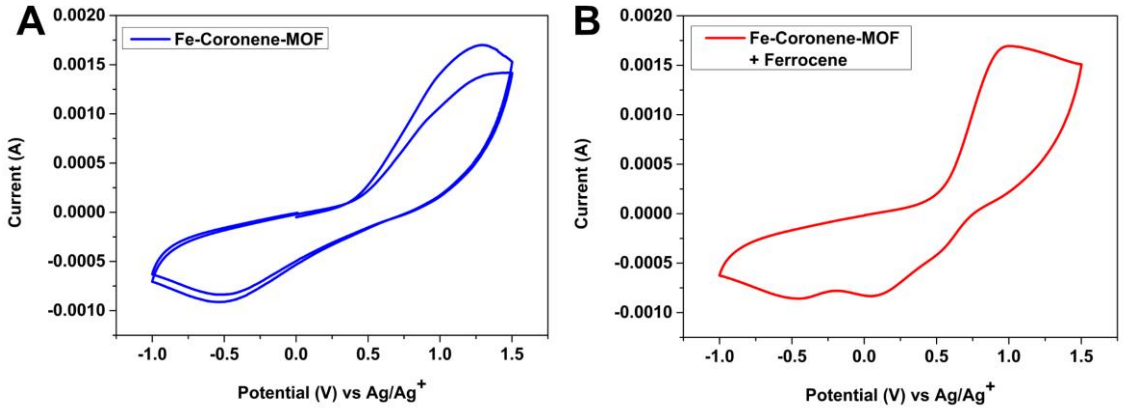

Figure 7-16: Cyclic voltammograms of the (A) Fe-Coronene-MOF and (B) of the Fe-Coronene-MOF with the addition of ferrocene. Measurements were performed under nitrogen.

Table 7-1: Positions of the reduction onsets in V, the HOMO/LUMO levels and of the optical band gap of the Fe-Coronene-MOF. Position of the oxidation onset in V, the HOMO/LUMO level and of the optical band gap of the Fe-Coronene-MOF.

MOF	E_{ox1}^{onset} (V)	HOMO (eV)	LUMO (eV)	Optical Eg (eV)
Fe-Coronene-MOF	0.43	-4.7	-3.3	1.39

Calculated from: $E_{HOMO} = -(E_{ox1}^{onset} + 4.8 - E_{Fc/Fc+})$, $E_{LUMO} = E_{HOMO} + E_g$

7.6.4 References:

(1) Martínez-Abadía, M.; Stoppiello, C. T.; Strutynski, K.; Lerma-Berlanga, B.; Martí-Gastaldo, C.; Saeki, A.; Melle-Franco, M.; Khlobystov, A. N.; Mateo-Alonso, A. A Wavy Two-Dimensional Covalent Organic Framework from Core-Twisted Polycyclic Aromatic Hydrocarbons. *J. Am. Chem. Soc.* **2019**, *141*, 14403–14410.

(2) Swift, A., Paul, A. J.; Vickerman, J. C. Investigation of the surface activity of corrosion inhibitors by XPS and time-of-flight SIMS. *Surf. Interface Anal.* **1993**, *20*, 27-35.

8 Conclusion and outlook

This thesis was focused on the fabrication and characterization of novel electroactive metal-organic frameworks (MOFs), which are mainly based on the MOF-74 topology. This includes the synthesis of functionalized organic ligands exhibiting interesting (opto)electronic properties, followed by the formation of MOFs with diverse divalent metal ions. In addition, the synthesis of high-quality MOF-74(M) thin films was developed, which is crucial for the fabrication of device-type technologies based on electroactive MOFs.

In the first project of this thesis (Chapter 3) we exchanged the original 2,5-dihydroxyterephthalic acid ligand with a longer and electron-richer organic ligand containing an anthracene core. The anthracene-based ligand was functionalized with para-carboxy and ortho-hydroxy groups, to enable the formation of the MOF-74 topology with five different divalent metal ions (Zn^{2+}, Mg^{2+}, Ni^{2+}, Co^{2+}, Mn^{2+}). Due to the longer linear linker molecule, we were able to expand the pore size and to increase the surface area of the ANMOF-74 family (anthracene-based MOF-74). Moreover, the electron-rich ligand led to an increase in electrical conductivity by up to six orders of magnitude, compared to the respective pristine MOF-74(M). The incorporation of the anthracene-based ligand not only improved the electrical properties of the MOF, but also altered the optical properties. Notably, ANMOF-74(Zn) showed a broad emission over the whole visible spectrum, making it an attractive potential candidate as LED material. In summary, the incorporation of an electron-rich anthracene-based linker molecule into the MOF-74 topology enabled us to modulate the (opto)electronic properties of the respective MOFs, and among other features increased their electrical conductivity.

By applying our concept of the incorporation of electron-rich linker molecules into the MOF-74 topology, we further expanded the anthracene-based ligand with ethyne groups, which is discussed in Chapter 4. Together with Mn^{2+}, a crystalline ethyne-anthracene based MOF-74 (EAMOF-74) was formed, exhibiting a pore size of 3 nm. The optical band gap could be lowered to 2.49 eV and the photoluminescence (PL) was shifted to the green spectral region, in comparison to ANMOF-74(Mn). Notably, this MOF exhibits a twisted rod-like morphology with left- and right-rotations occurring at the same frequency. A helical morphology is a rare phenomenon for MOFs and was previously only reported once for MOF-74-II superstructures.

The fifth chapter of this thesis deals with the incorporation of a functionalized perylene diimide (PDI) based ligand into the MOF-74 topology. The ligand contained para-hydroxy and ortho-carboxy groups and formed three crystalline PDI-based MOF-74 analogs with the divalent metal

ions Zn^{2+}, Mg^{2+}, Ni^{2+}. The stacking of the PDI cores along the crystal *c*-axis enabled π-π-interactions. Furthermore, the series displayed ohmic behaviour and featured electrical conductivity values in the range of 10^{-7} S/cm. The incorporation of the PDI-based ligand also influenced the optical properties of the MOF series, leading to an optical band gap of around 2.1 eV and photoluminescence in the orange and red spectral regions. The reduction potentials of the MOF series were analyzed by CV measurements, revealing HOMO/LUMO levels of -6.1 eV and -4.0 eV, respectively. In the crystal structure, the PDI cores stack along the *c*-axis, enabling π-π-stacking between the ligands. In principle, this allows for a "through-space" charge transport along the PDI stacks, besides the "through-bond" transport along the metal coordination spheres.

For the implementation of MOFs into device-type technologies for applications like chemical sensing, optoelectronics or electrochemical energy storage, the synthesis of thin, homogeneous and crystalline films on various substrates is of key importance. In this context, Chapter 6 addresses the synthesis of MOF-74(M = Zn^{2+}, Mg^{2+}, Ni^{2+}, Co^{2+}) thin films on various substrates like glass, quartz, gold and silicon. For the film fabrication we used the vapor-assisted conversion (VAC) strategy, which enabled a controlled film growth regarding film thickness, morphology and crystallite orientation. We obtained crystalline but non-oriented MOF-74(Co) films on all substrates. With MOF-74(Ni) we achieved crystalline, densely packed and non-oriented films. Notably, MOF-74(Zn) films grown on glass, gold and silicon showed a preferential crystallite orientation with the crystallographic *c*-axis aligned horizontally to the surface, which was confirmed by 2D GIWAXS measurements. In contrast, MOF-74(Mg) grown on glass and gold featured a preferential crystallite orientation with the crystallographic *c*-axis aligned orthogonally to the surface. As a result, we could demonstrate, for the first time, the synthesis and characterization of preferentially oriented MOF-74 films on non-modified substrates. In addition, all MOF-74(M) films offer on-surface permanent porosity and pore accessibility, which is an important feature for surface-based technologies and on-chip host guest experiments. For the photophysical characterization by means of UV-Vis, photoluminescence spectroscopy and TCSPC, the MOFs were grown on quartz substrates.

The last research chapter of the thesis (Chapter 7) deals with the synthesis of a novel mesoporous cubic Fe-Coronene-MOF. The MOF comprises hexahydroxy-cata-hexabenzocoronene (HBC) supertetrahedral units and Fe^{III} ions, forming a diamond topology. The Fe valency was studied by XPS, which we plan to complete by ^{57}Fe-Mössbauer measurements (in collaboration) in the future. Due to its black color the MOF showed a broad absorption over the whole visible and near-infared spectral region. To get even better insights regarding the quantitative optical absorption capabilities of the MOF, we plan to perform total hemispherical reflectance measurements in the

future (in collaboration). The electrical conductivity was studied on crystalline pressed MOF pellets by two-point probe measurements, which revealed values of 10^{-6} S/cm.

In conclusion, this thesis focuses on different approaches towards tailoring the electrical and optical properties of MOFs, especially those with the MOF-74 topology, by the development of functionalized organic building blocks. Furthermore, the growth of different MOF-74 films was studied, aiming at a future implementation into device-type technologies. The combination of high crystallinity, luminescence, as well as high electrical conductivity embedded in a stable porous MOF matrix also broadens the scope for potential practical applications, such as chemical sensing or metalorganic photovoltaic devices. In the future, additional research on these intriguing complex materials should also focus on understanding and ultimately controlling charge-carrier mobility and charge-carrier transport pathways, which constitute fundamental characteristics determining the electrical conductivity in MOFs.

9 Appendix

9.1 Publications

Scheurle, P. I.; Mähringer, A.; Biewald, A.; Hartschuh, A.; Bein, T., Medina, D. D., MOF-74 films obtained through vapor-assisted conversion – impact on crystal orientation and optical properties. *Chem. Mater*. **2021**, *3*, 5896-5904.

Mähringer, A.; Döblinger, M.; Hennemann, M.; Gruber, C.; Fehn, D.; Scheurle, P. I.; Hosseini, P.; Santourinian, I.; Schirmacher, A.; Rotter, J. M.; Wittstock, G.; Meyer, K.; Clark, T., Bein, T., Medina, D.D. An electrically conducting three-dimensional iron-catecholate porous framework. *Angew. Chem.* **2021**, *133*, 18213-18220.

Scheurle, P. I‡.; Mähringer, A.‡; Jakowetz, C.; Hosseini, P.; Richter, A. F.; Wittstock, G.; Medina, D. D.; Bein, T., A highly crystalline anthracene-based MOF-74 series featuring electrical conductivity and luminescence. *Nanoscale* **2019**, *11*, 20949-20955.

Short, G. N.; Nguyen, H. T. H.; Scheurle, P. I.; Miller, S.A. Aromatic polyesters from biosuccinic acid. *Polymer Chemistry* **2018**, *9*, 4113-4119.

‡The authors contributed equally to this work

9.2 Conference contributions

Oral Presentations

- MOF-74(M) films obtained through vapor-assisted conversion – impact on crystal orientation and optical properties

  FEZA **2021**, Online

- Electroactive MOF-74 Analogs

  SolTech Workshop **2020**, Online

Poster Presentations

- MOF-74(M) films obtained through vapor-assisted conversion – impact on crystal orientation and optical properties

  EuroMOF **2021**, Online

- MOF-74(M) films obtained through vapor-assisted conversion – impact on crystal orientation and optical properties

  COORNETs summer school **2021**, Online

- A highly crystalline anthracene-based MOF-74 series featuring electrical conductivity and luminescence

  EuroMOF **2019**, Paris, France.

- Electroactive MOF Networks

  Proposal Review Colloquium COORNETs **2019**, Garching, Germany.

- A highly crystalline anthracene-based MOF-74 series featuring electrical conductivity and luminescence

  Center for NanoScience (CeNS) workshop **2019**, Venice, Italy.

- A highly crystalline anthracene-based MOF-74 series featuring electrical conductivity and luminescence. (Poster Prize)

  Nanosystems Initiative Munich (NIM) summer retreat **2019**, Seeon, Germany.

- Synthesis and characterization of highly crystalline MOF-74 thin films

  Center for NanoScience (CeNS) workshop **2018**, Venice, Italy.

- Synthesis and characterization of highly crystalline MOF-74 thin films

  Nanosystems Initiative Munich (NIM) summer retreat **2018**, Spitzingsee, Germany.

- Highly oriented MOF films through vapor-assisted conversion. (Poster Prize)

  docMOF **2018**, Burghausen, Germany.